FIGURE 263.—Assumed performance characteristics for negative values of pressure coefficient for all stages.
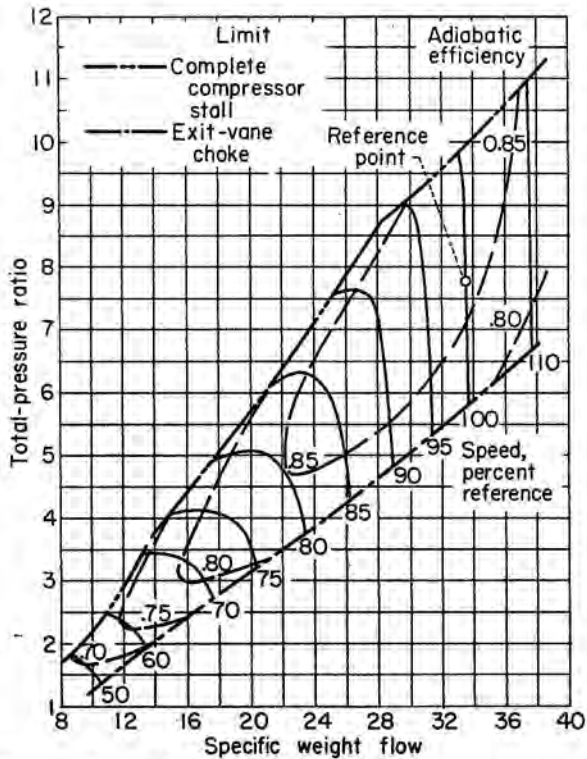
seriously affect the performance of all stages in the compressor. Therefore, the occurrence of abrupt stall in the multistage compressor can logically be taken as the lower limit of usable range at that speed. As pointed out in chapter XII, discontinuities in overall performance of the compressor may result in compressor surge; and, thus, the complete-compressor-stall limit may also be considered to be the surge limit of the compressor. As noted in figure 264, this limit does not exhibit the customary dip or kink at intermediate speeds. If surge were assumed to occur at the maximum-pressure-ratio points as in reference 248, the general trends would be unchanged.
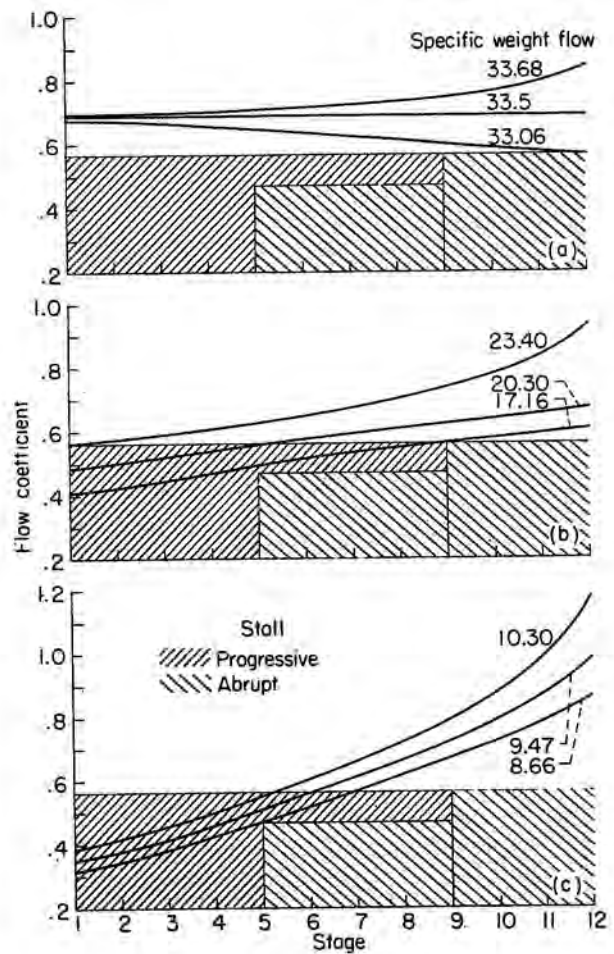
(a) Speed, 100 percent of reference.
(b) Speed, 80 percent of reference.
(c) Speed, 50 percent of reference.

FIGURE 265.—Stagewise variation of flow coefficient for case I.

FIGURE 264.—Computed over-all performance for case 1.

Variation of stage flow coefficients.—In order to illustrate the stages that are stalled at various inlet flows and speeds, the stage flow coefficient is plotted against stage number (fig. 265) for several values of inlet flow at speeds of 100, 80, and 50 percent of the reference value. The heavily shaded area on these plots represents the range of progressive stall, and the lightly shaded area represents the range of abrupt stall with the associated discontinuity of stage pressure coefficient (fig. 262).

At 100 percent of reference speed (fig. 265(a)), flow-coefficient variations are shown for the reference-point specific flow of 33.5, the approximate exit-vane choke flow of 33.68, and the complete-compressor-stall flow of 33.06. The variation of flow coefficient in the front stages is small, and thus the specific-weight-flow range at this speed is also small. The maximum change in flow coefficient occurs in the last stage, and complete compressor stall results from abrupt stall of this stage.

As the speed is reduced to 80 percent of the reference value, the flow coefficients decrease for the entrance stage and increase for the exit stage, as shown in figure 265(b). At this speed, the first stage operates in the progressive-stall range even at the maximum specific weight flow of 23.40. Complete compressor stall results from stall of the ninth stage at a specific weight flow of 17.16. It should also be noted that the number of stages operating in the progressive-stall range increases from one to eight as the flow is decreased from the exit-vane choke value of 23.40 to the complete-compressor-stall value of 17.16.

As the speed is further decreased to 50 percent of the reference value (fig. 265(c)), the front stages move deeper into stall and the rear stages closer to choking flow. Complete compressor stall results from occurrence of abrupt stall in the fifth stage. From five to seven stages operate in the progressive-stall range at all flows.

A comparison of figures 265 (a), (b), and (c) shows that at high speeds complete compressor stall results from abrupt stall of the rear stages; and, as speed is reduced, earlier stages in the compressor instigate complete compressor stall. As shown by the variation of stage flow coefficient and by the assumed abrupt-stall limits (fig. 265), complete compressor stall will only be instigated by stages 5, 9, and 12 for this example.

In order to define more clearly the relation of stage stall to compressor speed and flow, the individual stage stall limits are cross-plotted on the computed performance map in figure 266. This figure shows that progressive stall exists in from one to eight stages for all speeds below 80 percent of the reference value and for the low-flow portion of the flow range at speeds of 85 and 90 percent. It should be noted that, near the complete-compressor-stall point at 90-percent speed (fig. 266), nearly all the stages stall at approximately the same value of specific weight flow. In fact, stages 2 to 5 stall at a slightly higher value of inlet flow than stage 1. As pointed out in chapter XI, rotating stall is a prevalent source of compressor blade vibration. Therefore, this range of operation where progressive stall exists is extremely important with respect to engine reliability.

In general, the computed progressive-stall limits of this hypothetical compressor (fig. 266) are verified by experimental studies of rotating stall in multistage compressors. The speeds at which this type stall are encountered are somewhat
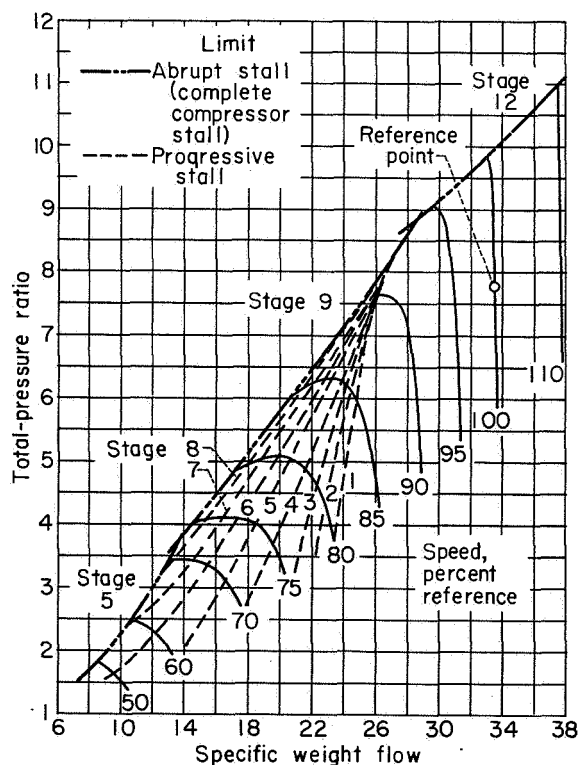

FIGURE 266.—Relation of stage stall and over-all compressor performance for case I.

higher than discussed in chapter XI. The speed at which inlet-stage stall first occurs, however, would be a function of stage characteristics as well as design-point matching. For this example, all stages were assumed to have identical characteristics up to the stall point and were matched at a constant value of flow coefficient of 0.69. Mach number effects, which were ignored in this analysis, may also vary the speed at which inlet-stage stall is first encountered. As can be seen from the stage curves of figure 261, a reduction in rotational speed, which corresponds to a reduction in stage-inlet Mach number, results in an increase in the maximum obtainable flow coefficient of the exit stage of a multistage compressor. Correspondingly, a decrease in inlet Mach number of the first stage would tend to decrease the flow coefficient at which stall of this stage is encountered. Both of these effects would tend to decrease the speed at which first-stage stall is encountered in the multistage compressor but would not alter the trends indicated by the computed compressor performance.

The lines of abrupt stall (fig. 266) show that, for speeds up to 70 percent of the reference value, complete compressor stall results from abrupt stall of the fifth stage; for speeds of 75 to 90 percent, from abrupt stall of the ninth stage; and for speeds of 95 percent and higher, from abrupt stall of the twelfth stage. The resulting complete-compressor-stall limit, however, is free of the normal dip or kink that is frequently encountered in high-pressure-ratio multistage compressors.

CASE II

Case II was computed to evaluate the effects of small discontinuities resulting from interaction effects in the first few stages of a multistage compressor, and also to evaluate the effects of unstalling hysteresis of the inlet stage. Interaction effects were assumed to exist in the first four stages. The detailed flow studies of the 10-stage research compressor discussed in chapter XI reveal that flow fluctuations of rotating stall increased through the first four stages and then decreased through the remaining stages. Therefore, the assumption of interaction effects in four stages appeared reasonable. The magnitude of the decrease in performance was arbitrarily chosen.

The stage characteristics used for stages 1 to 4 of case II are given in figure 267. These stage performance characteristics were obtained by arbitrarily modifying the pressure-coefficient characteristics used in case I and computing the modified efficiency curves assuming no change in the actual work input from that of case I. A small discontinuity in the performance of stage 1 was assumed as shown in figure 267(a). The unstalling hysteresis effect is also indicated in this figure. Stall recovery was assumed to occur at a flow coefficient of 0.60, whereas stall originally occurred at a flow coefficient of 0.565. To evaluate interaction effects, stages 1 to 4 were assumed to operate on the lower or stalled portions of their performance curves (fig. 267) whenever any of these stages encountered stall. The stage performance characteristics for stages 5 to 12 were identical to those of case I (figs. 262 (b) and (c)).

Performance with front stages unstalled.—The calculated performance map for case II for the condition of no stall in the front stages is presented in figure 268(a). This performance map is identical to the high-speed part of the map for case I (figs. 264 and 266) except for the complete-compressor-stall limit at speeds below 95 percent of the reference value. In case II the stall of one of the front stages leads to a discontinuity of over-all performance because of the assumed interaction effects. Thus, an envelope of the progressive-stall limits for case I (fig. 266) represents the complete-compressor-stall limit for case II for speeds from 80 to approximately 95 percent of reference speed. No operation with the front stage unstalled is obtainable below 80-percent speed.

Performance with first stage stalled.—The computed performance for case II for the condition of stall in the first stage and interactions in stages 2 to 4 is shown in figure 268(b) for speeds of 50 to 95 percent of the reference speed. The upper limit of flow for speeds of 85, 90, and 95 percent of the reference value was determined by the unstalling flow coefficient for the first stage. At 95-percent speed, the front-stage unstalling limit intersects the ninth-stage stall-limit line (fig. 268(b)). Therefore, this was the maximum speed for which calculations of performance with the front stage stalled were made. Complete compressor stall at speeds of 50 to 70
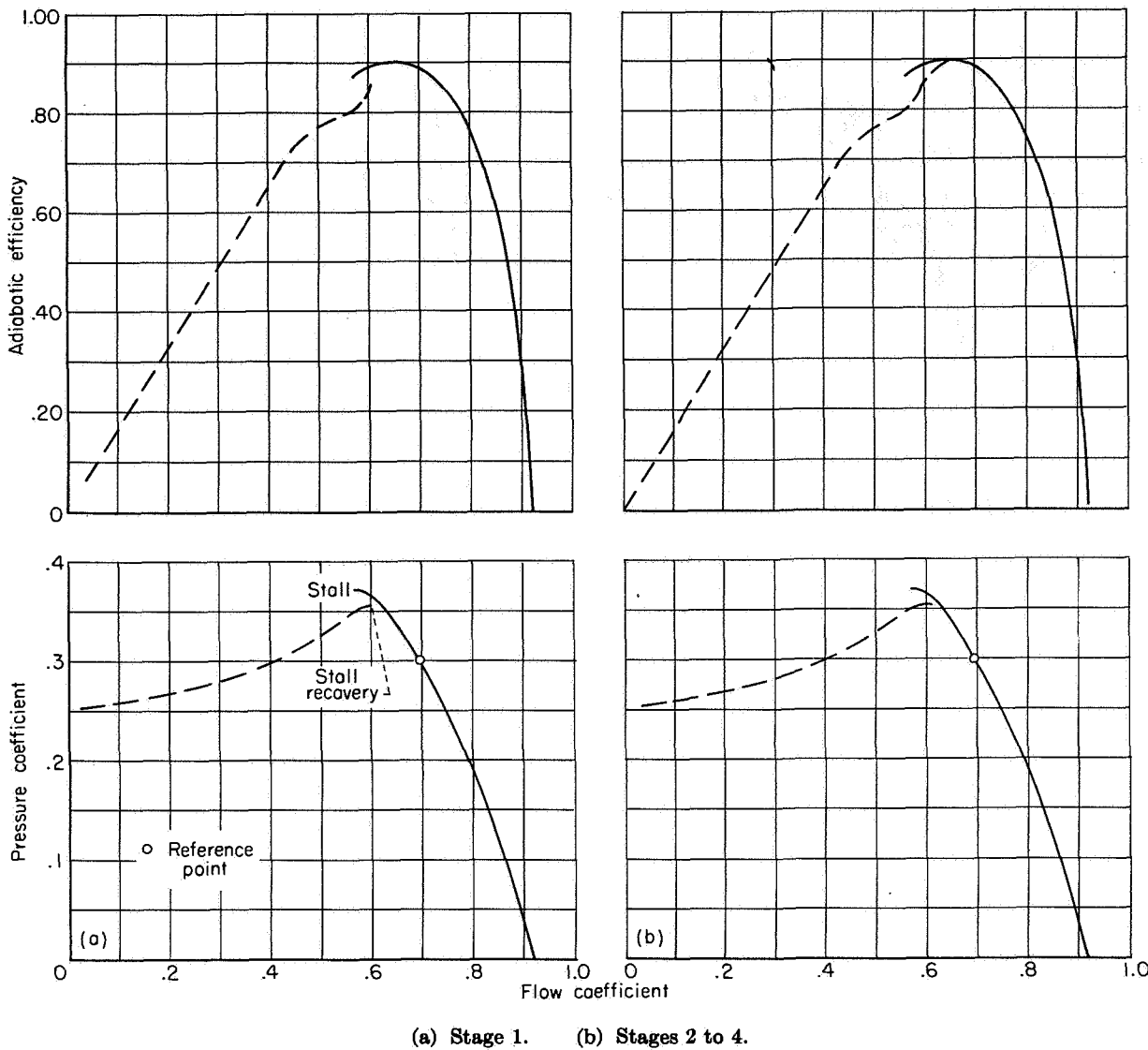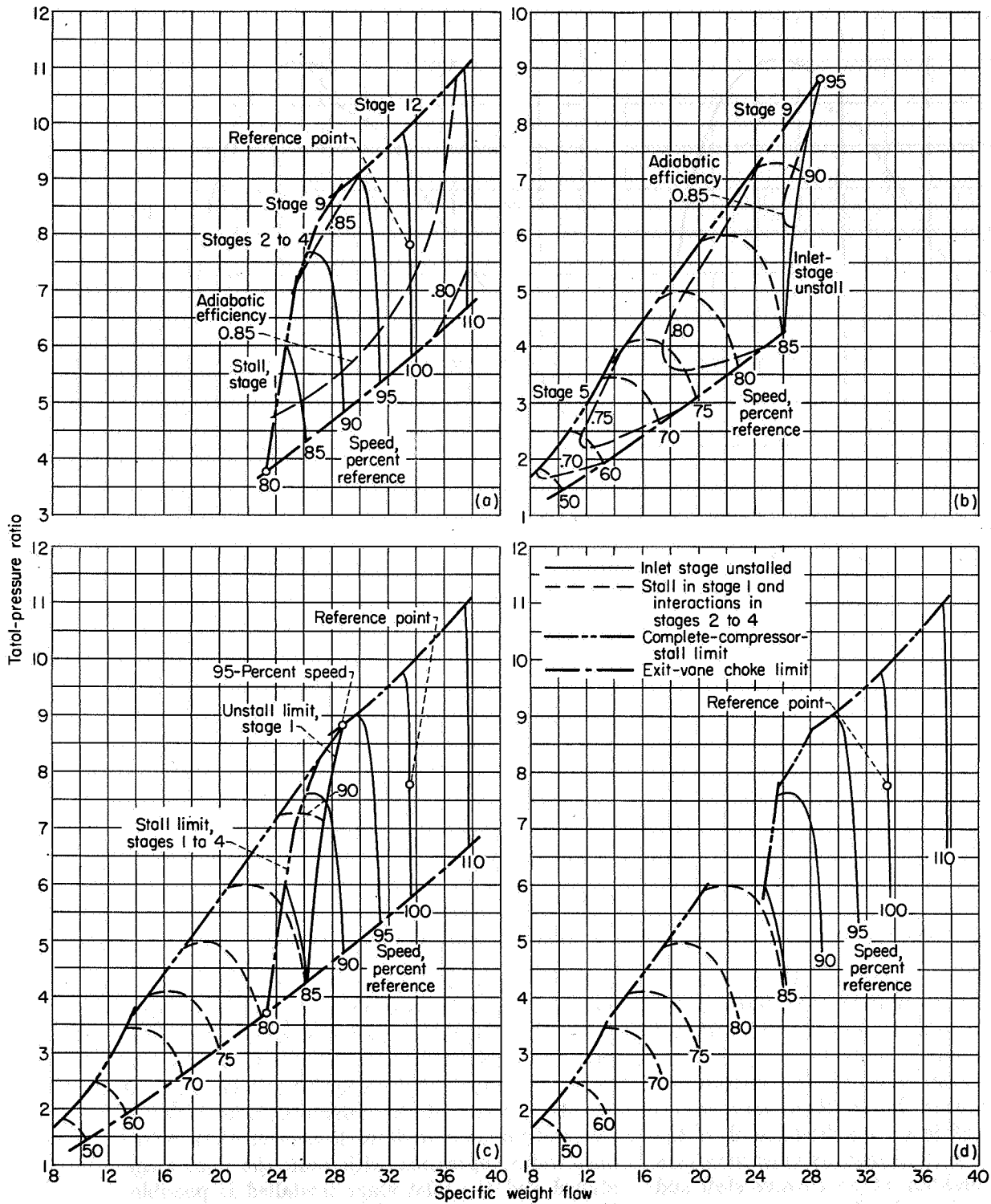
(a) Stage 1.   (b) Stages 2 to 4.

FIGURE 267.—Assumed performance characteristics for stages 1 to 4 for case II.

percent results from discontinuities due to the occurrence of abrupt stall of the fifth stage; and at speeds of 75 to 95 percent, from abrupt stall of the ninth stage.

The efficiencies for case II at intermediate speeds are somewhat lower than for case I. This decrease in efficiency is a direct result of the decrease in pressure coefficient assumed for stages 1 to 4 for the condition of progressive stall and stage interaction effects in these stages.

Complete performance map.—The complete performance map for case II is obtained by superimposing the performance maps for operation with the inlet stage unstalled and the performance

map for operation with the inlet stage stalled and interactions in stages 2 to 4 (figs. 268 (a) and (b)). The resulting performance in terms of pressure ratio against specific weight flow is given in figure 268(c) for a range of speeds from 50 to 110 percent of the reference value. For a range of speeds from 80 to 95 percent of the reference value, operation with both the inlet stage stalled and the inlet stage unstalled is possible. Thus, in this intermediate-speed range, the existence of double performance curves and two complete-compressor-stall or surge points at a given speed is indicated. The double curves of this analysis were obtained as a result of a

(a) Front stage unstalled.   (b) Front stage stalled and interactions in stages 2 to 4.
(c) Composite performance (superimposition of   (d) Transition from stalled to unstalled inlet
figs. 268(a) and (b)).   stage on exit-vane choke line.

FIGURE 268.—Computed over-all performance for case II.

small discontinuity in the performance characteristics of the first stage and interactions in stages 2 to 4. These results are verified by the multiple performance curves obtained in the experimental investigations reported in references 292 and 293.

It should be noted that, for the computations of case II, a small discontinuity in the pressure-coefficient curve of stage 1 was assumed. Similar results would be obtained, however, if the performance of stage 1 were assumed to be continuous, provided discontinuities of stage performance as a result of interaction were assumed for any of the following stages.

Transition from stalled to unstalled operation of inlet stage.—Reference 293 indicates multiple values of surge-point performance for intermediate-speed operation. In these tests, the particular surge point obtained depended upon the schedule of speed and flow that preceded the occurrence of surge. The double-valued curves of figure 268(c) and the dependence of compressor performance on the manner in which a particular operating point is approached indicate the necessity of studying the transition from compressor operation with the inlet stage stalled to operation with the inlet stage unstalled.

The usual operating schedule in compressor-component testing is to start at maximum or choke flow for a given speed and increase the throttling in successive steps until surge is obtained. Since compressor operation at maximum flow at low and intermediate speeds is normally set by the choke of the exit vanes, transition from stalled to unstalled operation of the inlet stage can be considered to occur along the exit-vane choke limit of figure 268 (c). Thus, as the compressor speed is increased, the choking limit of the exit vanes will prevent unstalling of the inlet stages for this case until a speed of 85 percent of the reference value is attained. Unstalling of the inlet stage and alleviation of the resulting interaction effects will result in a transient change of operation from the exit-vane choke point on the dashed speed curve to the exit-vane choke point on the solid speed curve. For this example, the specific weight flow increases from 26 to 26.3 and the pressure ratio from 4.23 to 4.30. The efficiency is not changed appreciably. For the purposes of this chapter, the transient conditions following unstalling of

the inlet stage are not considered, and the compressor operation is assumed to change discontinuously from that for inlet stage stalled to that for inlet stage unstalled.

The type of over-all performance map obtained from the normal compressor-component rating techniques described is given in figure 268 (d). For speeds up to 85 percent of the reference value, the compressor would operate with the front stage stalled; and for speeds above 85 percent, with the front stage unstalled. Therefore, both branches of the performance curve are given at this crossover speed of 85 percent of the reference value.

Complete-compressor-stall limit.—The complete-compressor-stall limit will follow the discontinuity points of the dashed speed curves up to the crossover speed and the discontinuity point on the solid curves above this speed. Thus, a stall-limit line faired through these points exhibits the dip common to most high-pressure-ratio axial-flow compressors. As indicated by this analysis of case II, however, two discrete stall-limit lines exist, the low-speed stall limit representing the mode of operation with the front stages stalled and the high-speed stall limit representing the mode of operation with no stages stalled. Since these two stall-limit lines may overlap in the intermediate-speed range where multiple performance characteristics may exist, a continuous stall-limit line should not be faired through the stall points for the complete range of speeds. In presentation of experimental data, however, the compressor stall or surge line is faired through a finite number of points and is generally considered a continuous function of flow, pressure ratio, and speed.

The analysis of case II shows that the dip in the compressor stall or surge limit that is experimentally found to exist for intermediate-speed operation of high-pressure-ratio multistage compressors can be simulated by assuming a small discontinuity in the performance characteristics of the inlet stage and interaction effects in stages 2 to 4. Similar results would be obtained from any combination of discontinuous performance characteristics of the inlet stages. For example, the performance characteristics of the first stage of the 16-stage compressor reported in reference 253 were continuous, but discontinuities did exist in the characteristics of a few stages after the first. It should also be noted that relatively continuous

stage characteristics will result in a fairly smooth surge or stall-limit line, as indicated in reference 257.

The transition from the complete-compressor-stall limit for operation with the inlet stage stalled to that for operation with the inlet unstalled depends on the manner in which this limit is approached. If the compressor-discharge throttling is sufficient to cause the compressor to operate appreciably above the exit-vane choke limit as speed is increased, unstalling of the front stage may not be achieved until a speed appreciably greater than 85 percent of the reference value is attained. In the range of speeds from 85 to 95 percent of the reference value, the complete-compressor-stall limit may follow that of figure 268(b). But, if the speed is first increased above the value for unstalling of the inlet stage and then reduced, complete compressor stall may occur on the limit of figure 268(a) for speeds of 80 to somewhat over 90 percent of the reference value. Thus, for case II, double-valued compressor stall points at a given speed may be obtained for the range of speeds from 80 to 95 percent of reference speed, as indicated in figure 268(c). As previously discussed, this phenomenon has been observed in experimental studies of multistage axial-flow-compressor performance. For cases where unstalling of groups of stages or alleviation of interaction effects occurs stepwise, even more than two compressor performance characteristic curves may be obtained at a given value of speed.

For maximum engine acceleration, the compressor operating line in an engine will be very close to the surge or stall limit at low and intermediate speeds. Thus, the intermediate-speed complete-compressor-stall limit obtained by normal compressor rating techniques may not be representative of the complete-compressor-stall or surge limit obtained during engine acceleration. Therefore, when multiple operating curves exist at any compressor speed, performance evaluations must include all possible operating conditions. This may be done by approaching a given operating point by varying compressor speed at each of several fixed system throttle settings, as well as by variation of throttle settings at a fixed speed. Speed changes must include both increases and decreases in rotational speed. An operating technique such as this will give performance maps of the type shown in figure 268(c) for those cases

where multiple performance curves exist for a given compressor rotational speed. The data of reference 293 indicate six separate performance curves at approximately 75 percent of design speed. For this compressor, the performance characteristic that exhibited no stall in the inlet stages was easily duplicated. Points on the performance characteristics for the condition of stall in the inlet stages were in general duplicable, but minor variations in the method of approach to this particular speed would result in operation on different curves of the separate performance characteristics for the condition of stall in the inlet stages. Thus, estimation of the compressor performance in the actual engine based on compressor-component tests may be difficult for this intermediate-speed range. During component testing of compressors, however, it is desirable to evaluate all possible performance characteristics in this intermediate-speed range where multiple characteristics may exist.

Effect of unstalling hysteresis.—For case II a hysteresis effect was assumed in the unstalling characteristic of the inlet stage. This had no effect on the general trend of complete-compressor-stall characteristics, except with respect to the speed at which transition from stalled to unstalled operation of the inlet stage was achieved. For no hysteresis effect, unstalling of the inlet stage along the exit-vane choke line (fig. 208(b)) would be achieved at 81.5 percent of reference speed rather than at 85 percent as for the case with hysteresis. Possible discontinuities in the complete-compressor-stall limit and the potential of double-valued points between speeds of 80 to 93 percent can be seen from figure 268(c).

Part-speed efficiency.—At 85-percent speed, the transition speed, the maximum computed efficiency for operation with no stage stalled was 0.86; whereas the maximum efficiency was 0.84 at this speed for the condition of inlet stage stalled and interactions in stages 2 to 4. This small difference in computed efficiency simply reflects the small changes in stage performance that were assumed to result from inlet-stage stall and the attendant interactions (fig. 267). Thus, no conclusive results can be obtained from these computed efficiencies. Interaction effects or sharp decreases in stage efficiency as a result of stage stall will, however, affect compressor efficiency adversely.

CASE III

In order to evaluate more serious interaction effects, calculations were made for case III that assumed the same conditions in stages 1 to 4 as for case II and, in addition, assumed large interaction effects in stages 5 to 8. The modified performance curves for these middle stages are given in figure 269. As for stages 1 to 4, the pressure-coefficient curve for stages 5 to 8 was arbitrarily modified and the efficiency curve was computed from the pressure coefficient by assuming no change in total work input for the stage. The magnitude of discontinuity of pressure coefficient is representative of that for an abrupt type of stage stall. When progressive stall existed in stage 1, stages 5 to 8 were assumed to operate on the dashed curves of figure 269. The performance of stages 9 to 12 was identical to that for case I.
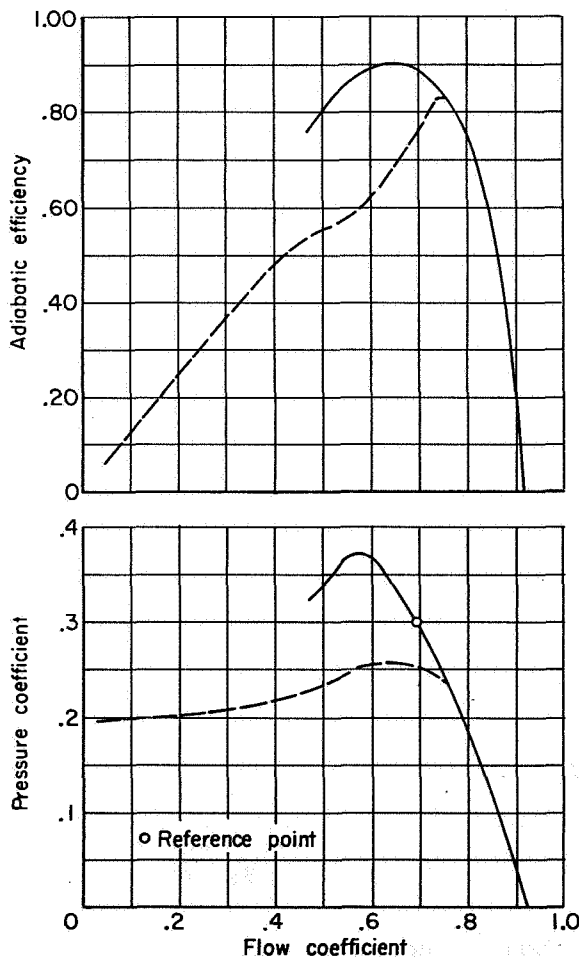

FIGURE 269.—Assumed performance characteristics for stages 5 to 8 for case III.

The performance of this case for the condition of unstalled operation of the inlet stage is identical to that for case II (fig. 268(a)). For the condition of stall of the inlet stage, however, the performance is markedly changed (fig. 270(a)).

Complete performance map.—The complete computed compressor performance map for case III (fig. 270(b)) is obtained by superimposing figures 268(a) and 270(a). As in case II, the multiple performance curves at speeds above 80 percent of the reference value indicate the necessity of varying the mode of testing in component rating so that all possible compressor operating conditions can be evaluated.

Transition from stalled to unstalled operation of inlet stage.—For case III, if compressor speed is increased along the exit-vane choke limit, inlet-stage unstalling will be effected at 94 percent of the reference speed. At this speed the transient change in computed pressure ratio would be from 4.85 to 5.2, the change in specific weight flow would be from 28.3 to 30.9, and the change in efficiency from 0.71 to 0.81. Thus, for large interaction effects, unstalling of the inlet stage is occompanied by relatively large increases in weight flow, pressure ratio, and efficiency. The transition speed of 94 percent is shown in figure 270(b) for both the condition of stall in the inlet stage and interactions in stages 2 to 8 and the condition of no stall in the inlet stage and no interactions. If interaction effects of the magnitude assumed for this case do exist and the compressor operating characteristic follows a throttling line close to the complete-compressor-stall limit, unstalling of the inlet stage may not be achieved even at design speed. By increasing the speed to a value above that for unstalling of the inlet stage and then decreasing the speed, stall-free operation might be obtained down to 80 percent of the reference speed at low values of pressure ratio.

Complete-compressor-stall limit.—For the high-speed portion of the compressor map where no stages are stalled (fig. 268(a)), at speeds above 95 percent of the reference value, complete compressor stall results from abrupt stall of the twelfth stage; and at speeds of 80 to approximately 95 percent, from stall of stages 1 to 4 and the attendant stage interactions. For the operating conditions where stall in the inlet stage and interactions in stages 2 to 8 exist (fig. 270(a)), complete compressor stall for speeds up to 95 percent of the

reference value results from abrupt stall of the ninth stage, and for higher speeds, from abrupt stall of the twelfth stage.

The complete-compressor-stall-limit line indicated for case III for the normal component rating technique can be obtained from figure 270(b). This stall-limit line would follow the complete-compressor-stall-limit points for the dashed speed curves (fig. 270(a)) up to 94 percent of reference speed. In this speed range the compressor would operate with the first stage stalled and interactions in stages 2 to 8. For speeds above 94 percent, the stall-limit line will follow the complete-compressor-stall-limit points for the solid speed curves, which represent a condition of stall-free operation for all stages.

Effect of unstalling hysteresis.—If the hysteresis effect on unstalling of the inlet stage were neglected, the first stage in this case would become unstalled at 91.5 percent of reference speed for operation along the exit-vane choke limit. The general trend of performance and complete-compressor-stall limit would, however, be unchanged. The effect of inlet-stage unstalling hysteresis is to increase the speed at which the inlet stage becomes unstalled regardless of the throttling or compressor operating line.

Part-speed efficiency.—As can be seen from a comparison of figures 264 and 270(a), interactions of the magnitude assumed for case III result in large reductions in efficiency for operation with stall in the inlet stages. The computed values indicate a reduction in efficiency of about 15 percent compared with about 2 percent for case II. Thus, the low part-speed efficiencies exhibited by some multistage axial-flow compressors may result from severe interaction effects.

Multiple-valued performance characteristics.—Both cases II and III indicate the potential of two separate curves in this general speed range. If at any given value of speed the potential of different degrees of deterioration of stage performance due to interactions is considered, then more than two performance curves may be obtained. For example, if the characteristics for 85-percent speed are considered for cases I to III, the performance characteristics shown in figure 271 are obtained. Curve I represents a condition of unstalled operation for all stages; curve II, a condition of stall in the inlet stages and inter-
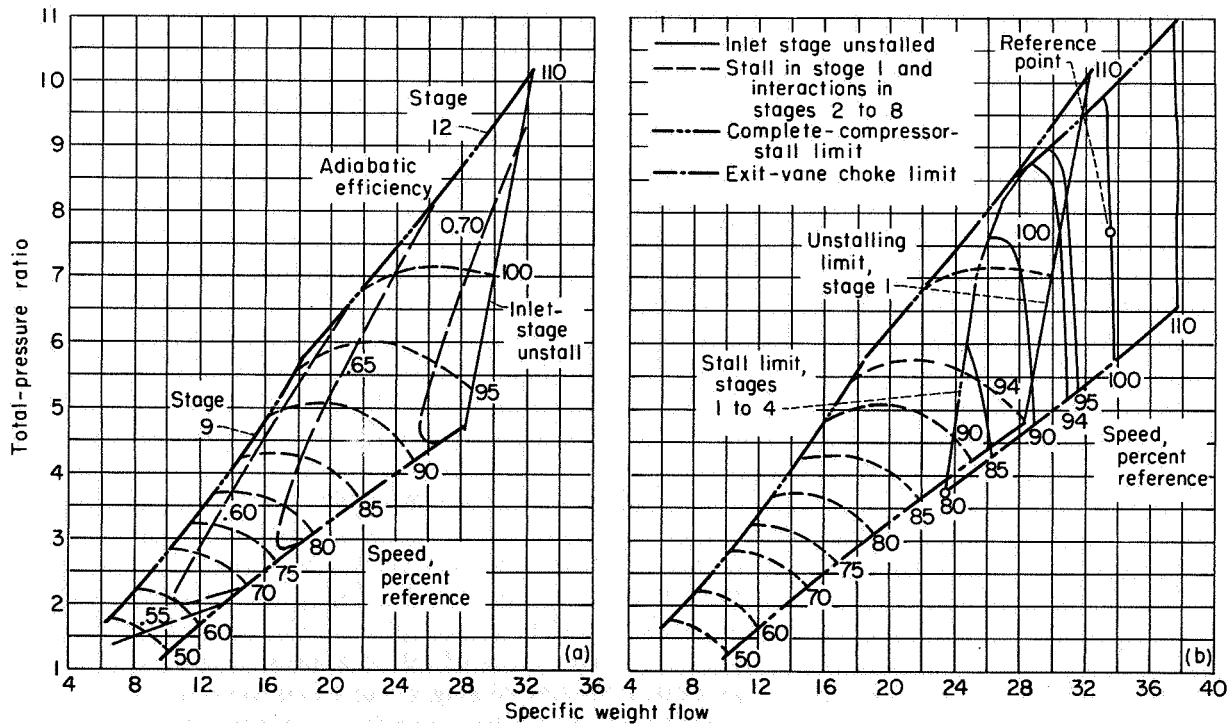
(a) Front stage stalled and interactions in stages 2 to 8.

(b) Composite performance (superimposition of figs. 268(a) and 270(a)).

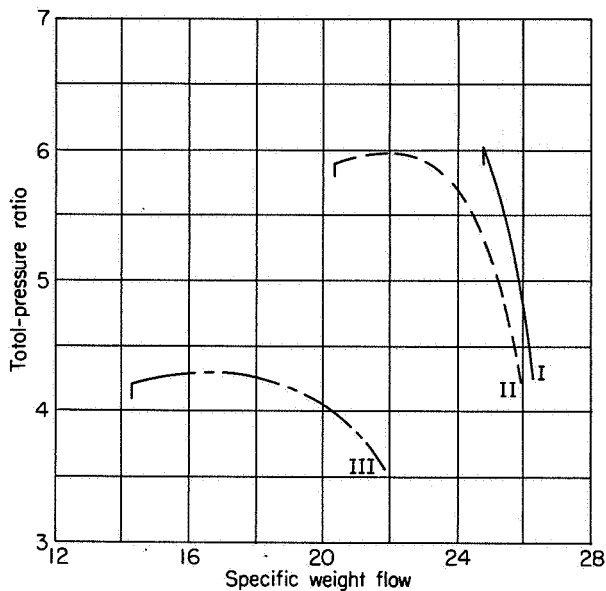FIGURE 270.—Computed over-all performance for case III.

FIGURE 271.—Comparison of computed performance at 85-percent speed for cases I to III.

actions in stages 2 to 4 as obtained for case II; and curve III, a condition of stall in the inlet stages and interactions in stages 2 to 8 as obtained for case III. Such variations in performance may be a result of changes in the number of stages that exhibit this deterioration of performance or changes in the magnitude of the performance deterioration of each stage that is affected. Variations of stall interaction effects, therefore, will result in a multiplicity of over-all performance characteristics at a given speed; and the compressor flow, pressure ratio, and efficiency will increase with decreasing severity of stall and interaction effects. The particular performance obtained will depend on the previous history of speed and flow as well as the hysteresis effect accompanying changes of stall pattern in any given compressor. Needless to say, flow distortions at the compressor inlet can aggravate these adverse effects.
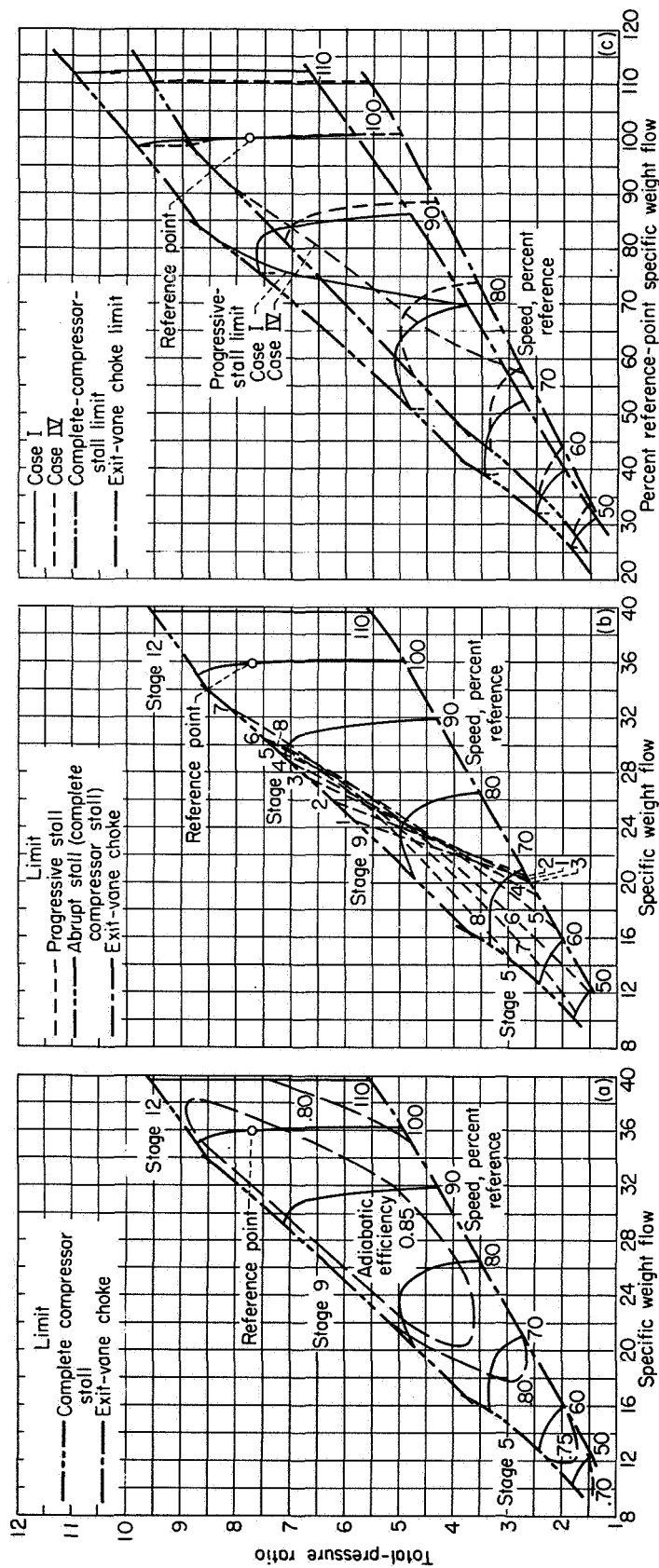
CASE IV

Since part-speed performance problems of high-pressure-ratio axial-flow compressors can be attributed to stalling of the inlet stages as a result of flow limitations of the rear stages, some improvement in part-speed performance may be expected by matching the front stages near their choking value of flow coefficient and the rear stages near their stalling value of flow coefficient. This stage-matching compromise is equivalent to matching

the compressor stages for some speed lower than the design value, as suggested in reference 248. In addition to improving part-speed performance, such compromises in stage matching may reduce the speed at which progressive stall is encountered and thus decrease the potential of blade vibrations excited by rotating stall. To evaluate these potentials, case IV was computed. In this case, the reference-point flow coefficients of the stages were varied as shown in table VIII(b) from a value of 0.760 in the inlet stage to a value of 0.630 in the twelfth stage. The principal purpose of this study was to investigate variations of stage operation with speed. Therefore, no interactions were considered. The stage characteristics used for the individual stages were identical to those for case I (fig. 262).

Computed over-all performance.—The computed over-all performance map for case IV is given in figure 272(a) as a plot of over-all total-pressure ratio against specific weight flow. For this case as for case I, complete compressor stall was assumed to occur when abrupt stage stall was encountered in any stage. Complete compressor stall for case IV results from abrupt stall of the fifth stage for speeds of 50, 60, and 70 percent of the reference value, from abrupt stall of the ninth stage for speeds of 80 and 90 percent, and from abrupt stall of the twelfth stage for 100 and 110 percent. These results are similar to those for case I.

The peak efficiencies calculated for case IV varied from approximately 0.74 at 50 percent of reference speed to a maximum of 0.87 at 90-percent speed, and decreased to 0.85 at the reference speed.

Stage progressive-stall limits.—In order to determine the speed at which various stages reach the flow coefficient for progressive stall (0.565), the progressive-stall limits for stages 1 to 8 are cross-plotted on the computed performance map in figure 272(b). This figure shows that the first stage is stalled over almost the entire flow range at 70 percent of reference speed, and over only the low-flow portion of the compressor flow range at 80-percent speed. The first-stage stall limit intersects the complete-compressor-stall limit at approximately 85 percent of reference speed. Consideration of the stall limits of stages 2 to 7 indicates that at 90-percent speed stage 7 is the first stage to encounter progressive stall. In the range of approximately 70- to 85-percent speed,

(a) Over-all performance.

(b) Stage stall limits.

(c) Comparison of stall limits for cases I and IV.

FIGURE 272.—Computed over-all performance for case IV.

several of the front stages approach stall almost simultaneously at a weight flow somewhat higher than that for first-stage stall. At the higher values of pressure ratio at intermediate speeds, the general effect of the stage-matching compromise was to transfer the progressive-stall problem from the front stages towards the middle stages of the compressor.

No interaction effects were considered in this analysis. However, as pointed out previously, stages operating near the stalling value of flow coefficient are very susceptible to deteriorations of performance induced by flow fluctuations resulting from stall of adjacent stages. Therefore, serious interaction effects may be expected where simultaneous stall of several stages occurs (fig. 272(b)). Furthermore, the stages with higher hub-tip ratio, such as stages 5 to 7 of case IV, are more apt to exhibit an abrupt stall than are the stages with low hub-tip ratio, such as stages 1 to 3. At speeds of 80 to 90 percent, therefore, interaction effects may instigate abrupt stall of one of the middle stages of the case IV compressor and thereby limit the flow range at these speeds.

Comparison of cases I and IV.—A comparison of the efficiencies of case I (fig. 264) and case IV (fig. 272(a)) indicates no appreciable variations of the over-all compressor efficiency due to the stage-matching compromises of case IV. It should be noted, however, that in case I the stages were not matched at the peak-efficiency points (see fig. 262). Compared with a compressor for which all stages were matched at the peak-efficiency points, the compromise of case IV would have decreased the overall compressor efficiency at high speeds and increased it at low speeds.

The increase in first-stage flow coefficient for case IV resulted in an increased specific weight flow from 33.5 for case I to 35.9 for case IV. Thus, for a given weight-flow requirement, the compromised matching would permit the use of a slightly smaller compressor diameter.

In order to compare the complete-compressor-stall limits and stage progressive-stall limits for cases I and IV, these performance maps are superimposed in figure 272(c). This figure is plotted as pressure ratio against percent of reference-point specific weight flow in order to compare compressors of equivalent flow capacities. Comparison of the complete-compressor-stall limits shows that the compromise of stage matching (case IV) gave a

marked decrease in the attainable pressure ratio at all speeds. It can also be seen from figure 272(c) that the percentages of reference-point specific weight flow at the lower speeds are higher for case IV than for case I. At the overspeed condition, however, the condition is reversed, and case I indicates the higher percentage of reference-point flow.

The progressive-stall limits shown in figure 272(c) represent the envelope of the progressive-stall limit for stages 1 to 8 as given in figures 264 and 272(b). A comparison of these limits for cases I and IV indicates that, along the exit-vane choke limit, the speed at which progressive stall is encountered is decreased from 80-percent speed for case I to slightly less than 70-percent speed for case IV. Along the complete-compressor-stall limit, however, progressive stall occurs at somewhat higher speeds for the compromise matching design (case IV) than for case I. During engine operation at part speed, the compressor will normally operate in the high-pressure-ratio range at any given speed. As shown in figure 272(c), the stage-matching compromise used for case IV gave no effective reduction in the speed at which progressive stall might be encountered during engine operation but merely transferred the instigation of this stall from the first stage to one of the middle stages of the compressor.

From the comparison of the computed performance of cases I and IV, it is obvious that the compromise in stage matching used in case IV does not improve the progressive-stall limit appreciably but decreases the complete-compressor-stall margin. Since this compromise in stage matching does not result in a marked decrease in the speed at which rotating stall could be encountered, it would not appreciably alter the potential blade-vibration problem associated with rotating stall.

CASE V

Since the compromise matching of case IV indicated a severe decrease in the pressure ratio estimated for complete compressor stall, the effect of an additional stage was considered. This hypothetical compressor, designated case V, is identical to that of case IV except for the addition of a thirteenth stage. The stage characteristics assumed for this added stage were the same as for stages 9 to 12 (fig. 262(c)). As in case IV, no stage interaction effects were considered in case V. The details of the stage matching and stage
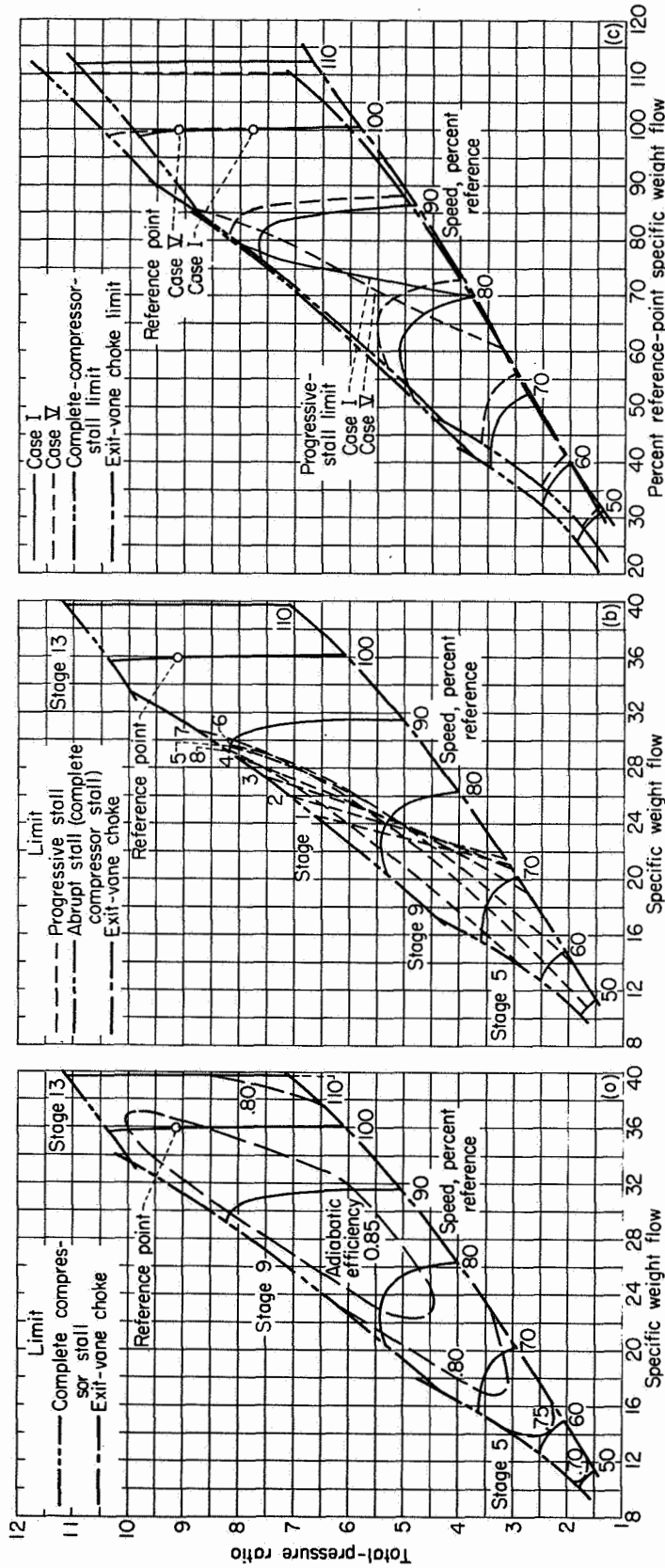
(a) Over-all performance.

(b) Stage stall limits.

(c) Comparison of stall limits for cases I and V.

FIGURE 273.—Computed over-all performance for case V.

reference-point performance characteristics for this case are given in table VIII(b).

Computed over-all performance.—Figure 273(a) presents the computed over-all performance for case V as a plot of over-all total-pressure ratio against specific weight flow. The reference-point total-pressure ratio indicated in this figure is 9.1 as compared with 7.73 for case IV. Complete compressor stall at speeds of 50, 60, and 70 percent of the reference value results from abrupt stall of the fifth stage; at speeds of 80 and 90 percent, from abrupt stall of the ninth stage; and at speeds of 100 and 110 percent, from abrupt stall of the thirteenth stage.

The peak efficiencies computed for case V varied from 0.70 at 50 percent of reference speed to 0.85 at reference speed with a maximum of 0.87 at 90-percent speed.

Stage progressive-stall limits.—The stage progressive-stall limits for case V are cross-plotted on the over-all performance map in figure 273(b). Progressive-stall limits for stages 1 to 8 are shown in this figure, and the results are similar to those for case IV (fig. 272(b)). At 90 percent of reference speed for case V, the seventh stage encounters progressive stall at a flow only slightly higher than that for complete compressor stall.

At 80-percent speed, stages 3 to 6 encounter progressive stall almost simultaneously at a flow about halfway between the exit-vane choke limit and the complete-compressor-stall limit; and at 70-percent speed, stages 1 to 4 are stalled at the exit-vane choke limit.

Comparison of cases I and V.—Comparison of the efficiencies of case I (fig. 264) and case V (fig. 273(a)) shows that the stage-matching compromise and the addition of a thirteenth stage have little effect on the computed over-all efficiency. The addition of the thirteenth stage resulted in a higher reference-point pressure ratio (9.1 for case V compared with 7.75 for case I). Because the efficiency contours are displaced towards higher pressure ratios, the case V compressor indicates a computed efficiency of approximately 0.84 at a pressure ratio of 7.75 as compared with a value of 0.86 for case I at the same pressure ratio.

The comparison of complete-compressor-stall limits for cases I and V are presented in figure 273(c), which gives a plot of pressure ratio against percent of reference-point specific weight flow.

As in case IV, the specific weight flow for case V was 35.9 pounds per second per square foot of annulus area as compared with 33.5 for case I. Figure 273(c) indicates that case I has a slightly better complete-compressor-stall margin at speeds of 50 to 70 percent of the reference value; the two compressors exhibit about the same complete-compressor-stall limit at speeds of 80 to 90 percent; and case V has a slightly better stall limit at 100- and 110-percent speed.

The envelope lines of the stage progressive-stall limits for stages 1 to 8 are also plotted in figure 273(c). These limits indicate that along the exit-vane choke limit case I encounters progressive stall at 80 percent of reference speed, whereas case V encounters progressive stall at about 72-percent speed. Along the complete-compressor-stall limit, both cases I and V encounter progressive stall at somewhat over 90 percent of reference speed. Thus, the compromise of stage matching and the addition of a stage (case V) do not decrease the speed at which progressive stall is encountered in the vicinity of the complete-compressor-stall limit. Therefore, the potential of blade vibrations excited by progressive stall would be equally as critical for a compressor such as case V as for one such as case I.

Figure 273(c) also shows that the compromised compressor (case V) has a slightly higher percentage of reference-point flow at lower than reference speed and a slightly lower percentage at higher than reference speed than does the compressor of case I.

This comparison indicates that, with respect to complete-compressor-stall and progressive-stall limits, the original 12-stage hypothetical compressor (case I) is comparable with the 13-stage compressor with modified stage matching (case V). For a given design flow, the case V compressor would be slightly smaller than that for case I, but this advantage is offset by the necessity of a extra stage in order to maintain the complete-compressor-stall margin for the compressor with compromised stage matching.

CONCLUDING REMARKS

PART-SPEED PERFORMANCE PROBLEMS

The analysis reported herein was made to study the effects of various stage stall and interaction characteristics on the part-speed efficiency, inter-

mediate-speed complete-compressor-stall characteristics, and multiple-valued performance characteristics of high-pressure-ratio multistage axial-flow compressors. In addition, the range of conditions where progressive rotating stall exists was considered as a range of potential blade vibrations. Effects of compromising stage matching to favor part-speed performance have also been considered. Because of the simplifying assumptions used, the results obtained represent only a first approximation. The qualitative results, however, are generally in agreement with trends observed experimentally.

This analysis indicates that multiple-valued multistage performance curves will be obtained if stall of the inlet stage results in discontinuities of that stage or of one or more of the succeeding stages. Discontinuities of these succeeding stages may be a result of interaction effects due to unsteady flow initiated by progressive stall of the first stage. The particular operating point of the compressor at the speeds where multiple curves exist depends on the manner in which that operating point is approached. More than two performance curves may be obtained at a given speed if the number of stages affected by interaction varies or if the severity of interactions varies.

The dip obtained in the experimentally determined surge or complete-compressor-stall-limit lines of high-pressure-ratio axial-flow compressors apparently is merely a result of transition from compressor operation with the front stages stalled to operation with these stages unstalled. The intermediate-speed limit obtained by normal component test techniques may not be representative of that obtained in an engine at the same speed. Furthermore, the engine complete-compressor-stall limit obtained during accelerations may be different from that obtained during decelerations.

This analysis indicates that extremely poor part-speed efficiencies cannot be attributed entirely to stage mismatching but can to a large extent be attributed to stage interactions or deterioration of stage performance due to unsteady flow resulting from rotating stall originating in the inlet stages. The magnitude of interaction effects for each stage and the number of stages affected will determine the reductions in performance at low and intermediate speeds.

Hysteresis effects in the unstalling characteristics of the first stage do not alter the existence of double-valued performance curves at intermediate speeds. The existence of large unstalling hysteresis in combination with severe discontinuities in stage performance may prevent unstalling of the inlet stages until very high speeds are obtained.

With respect to part-speed efficiency and intermediate-speed complete compressor stall, this study indicates the desirability of stages having continuous characteristics at their stall points. It should be noted that these stage characteristics must be maintained when the stage is operating in the flow environment of the multistage compressor. Stages of this type generally have a progressive stall that originates at one end of the blade and gradually increases in severity as the flow coefficient is decreased. Design of such stages depends on a better knowledge of the effects of unsteady flow and of radial maldistribution of flow, which result from off-design operation of adjacent stages. The stage data and over-all compressor performance characteristics obtained from the 10-stage compressor of reference 257, however, indicate that these desirable stage characteristics can to a degree be achieved. Although the use of stages having progressive stall may alleviate the part-speed efficiency and complete-compressor-stall problems, it would not alleviate the potential of blade vibrations excited by rotating stall.

Increasing the stall-free range of operation of the inlet stages would, of course, increase the range of stall-free operation of the multistage compressor. Since the part-speed problem in the multistage compressor results from flow limitations of the exit stages, stage range with respect to off-design performance can best be evaluated on the basis of flow range at the discharge rather than that at the inlet of the stage. Therefore, devices or design improvements that would increase the stage-loading limit or flow range must be evaluated to determine the potential gains in effective stage range.

More complete data on effects of stage design and blading geometry on stage stall characteristics, as well as a better understanding of stage interactions due to radial maldistribution of flow and unsteady flow as encountered in multistage compressors, are required in order to obtain a more quantitative evaluation of part-speed performance.

STAGE-MATCHING COMPROMISES

One proposed technique of improving part-speed performance is to compromise stage matching to favor low-speed operation of the compressor. The analysis of this technique indicates that such compromises severely reduce the complete-compressor-stall margin unless additional stages are used. The higher flow coefficients of entrance stages may permit the use of a slightly smaller compressor for a given flow capacity, but this advantage would be offset by the necessity of an additional stage to obtain the required complete-compressor-stall margin. Furthermore, no gain in the range of speeds where no rotating stall exists is obtained except near the exit-vane choke limit. Stage compromises tend to result in progressive stall in the middle stages at speeds above that for stall of the inlet stage. Thus, the potential for abrupt stall, interaction effects, and poor intermediate-speed complete-compressor-stall characteristics would be greater for the compromised design. No reduction in the potential of blade vibration excited by rotating stall is indicated. Furthermore, stage-matching compromises to favor part-speed performance would definitely restrict the obtainable overspeed performance of any compressor.

VARIABLE GEOMETRY

Inlet baffles.—As indicated in chapter XI, the use of adjustable inlet blockage either in the form of baffles or ramps may disrupt the periodic nature of rotating stall and thus present a potential solution to the blade-vibration problem. Preliminary tests of a hub baffle (ref. 20) indicate that the use of such a baffle may also result in some improvement in the complete-compressor-stall or surge margin at low speeds. In addition, baffles may be used at high speeds to reduce the compressor mass flow and therefore to act as a thrust-spoiling device.

Adjustable blading.—Adjustable inlet guide vanes and adjustable stator blades have also been proposed as variable-geometry features for alleviation of part-speed performance problems and improvement of flexibility of engine operation. The satisfactory application of such adjustable blading, however, depends on a knowledge of the variations of stage matching and radial distribution of flows that result from blade adjustment. As indicated in references 296 and 297, closing the inlet guide vanes reduces both the flow coefficient and the pressure coefficient of the first stage. This change in pressure coefficient tends to moderate the decrease in first-stage flow coefficient so that the flow coefficient of the second stage is not appreciably altered. The operation of middle and latter stages, therefore, tends to be primarily a function of compressor speed and throttling rather than of inlet-guide-vane position. Thus, closing the inlet guide vanes results in an appreciable reduction in flow but only a small reduction in over-all pressure ratio for the compressor. This, in general, improves the complete-compressor-stall-limit or surge-limit characteristics. Of course, when the guide vanes are opened, the converse is true. References 296 and 297 also point out that closing the inlet guide vanes alters the radial variation of loading of the first rotor as a result of the establishment of radial equilibrium of static pressure. This radial variation of loading is in the direction of increasing the value of flow coefficient at which tip stall is encountered and thus would tend to reduce the effectiveness of guide-vane adjustment in relieving the part-speed operating problem. Furthermore, alterations in radial distribution of flow and blade loading may affect the stalling characteristics of the individual stages. Adjustable inlet guide vanes have, however, been effectively used as a means of improving engine acceleration characteristics, and adjustable guide vanes and stators provide a potential technique for improving the flexibility of high-pressure-ratio compressor operation without sacrificing design-point performance. The added weight and complexity of the engine and its control system must be considered, however.

Compressor air bleed.—Compressor-discharge bleed has been used effectively to alter the matching of the compressor and turbine at part speed so as to avoid serious intermediate-speed complete-compressor-stall problems (ref. 22). This technique, however, does not eliminate the potential of blade vibrations instigated by rotating stall. Interstage air bleed in the multistage compressor has the potential of effectively altering the matching of the inlet and exit stages and thus appreciably reducing the speed at which rotating stall is encountered, as well as improving the complete-compressor-stall or surge margin at intermediate

speeds. The computed effects of bleed on a 16-stage compressor (ref. 23) indicate improvements in efficiency at part speed even when the compressor is charged with the work added to the bleed air. Care must be exercised in design of bleed ports to avoid resonance with adjacent blades and to avoid serious distortions of flow distribution in the vicinity of the bleed ports. The use of interstage bleed will add some weight and complexity to the turbojet engine but, in general, offers improvement in regard to intermediate-speed complete-compressor-stall or surge margins and to blade-vibration problems resulting from rotating stall.

CHAPTER XIV

THREE-DIMENSIONAL COMPRESSOR FLOW THEORY AND REAL FLOW EFFECTS

By Howard Z. Herzig and Arthur G. Hansen

The discrepancies observed between the actual flows in an axial-flow compressor and theoretical simplified design flows increase in magnitude and diversity with the trend toward more compact compressors. The research into design procedures to reduce these discrepancies is reviewed and discussed. The improved design procedures are arbitrarily classified into two categories. One category includes investigations that successively extend the design procedures from the simplified-radial-equilibrium axially symmetric designs to the complex complete three-dimensional design. The second category includes individual studies of more restricted problems such as secondary flows, radial variation of circulation, entropy, or enthalpy. Such research leads to more adequate correction factors for use with simplified design procedures.

INTRODUCTION

One of the most important problems in the aerodynamic design of compressors is that of expressing the design flow equations in forms that are at once simple enough and accurate enough. The equations and their solutions should be simple enough that the designer can see the relative significance of the variables he is free to specify, and it must be possible to solve the relations quickly. The latter is important because it is frequently necessary to compute many compressor designs in order to select the one most suitable for a particular application. The equations and their solutions must represent the fluid motion accurately enough that the discrepancies between predicted and measured flow conditions are acceptably small.

The equations of motion for the flow of a real fluid in an axial-flow compressor are nonlinear three-dimensional equations and to date have proved mathematically intractable. Accordingly, designers have evolved the use of various assumptions to obtain reduced linear flow equations for

which solutions can be obtained. Such procedures are necessarily conditional upon obtaining physically valid flow descriptions by their use.

In practice, the aerodynamic design of subsonic compressors has usually been based on two principal assumptions: (1) axially symmetric flow and (2) blade-element flow. The axially symmetric flow assumption is primarily a mathematical device that reduces the general flow equation from a three-dimensional to a two-dimensional system. In order to linearize and further simplify the flow equations, several auxiliary flow assumptions are made, such as considering the flow to be nonviscous and time-steady. Additional assumptions often made within the axial-symmetry approach include simple radial equilibrium and constant entrophy radially.

The assumption of blade-element flow enables the designer to use the performance data (obtained chiefly from two-dimensional-cascade investigations, ch. VI) in the compressor blading design. In fine, the over-all advanced compressor design requires a combined approach. It is necessary to simplify the mathematical problem in order to obtain solutions readily; and it is likewise necessary to use empirical information obtained in related investigations in order to correct, as far as possible, for the discrepancies between the real and the design flows in the compressor.

In the past, suitable compressors have been designed by this simplified design procedure. Experience has taught that, by adhering to well-established limits on inlet relative flow Mach numbers, blade-turning and -loading parameters, wheel speeds, pressure ratios, and others, designers can consistently produce satisfactory compressors. From a practical point of view, these results justify the axial-symmetry and blade-element-flow approach to the design of such compressors (ch. III), herein called "conservative compressors."

365

However, with the present requirements of compact engines, it becomes necessary to increase the airflow-handling capacity and the stage pressure ratios while maintaining or even improving the efficiency if possible. Therefore, the Mach numbers, wheel speeds, and blade loading must be allowed to rise while the hub-tip radius ratio, the axial length per stage, and the number of stages must go down. Thus, the higher compressor performance requirements make it desirable to exceed the design limits earlier found advisable for conservative compressor design. In addition, such problems as blade-row interference, unsteady-flow phenomena, and off-design performance may become increasingly important.

Changing design conditions in order to meet increased compressor performance requirements, of course, requires corresponding adjustments in design techniques. These follow several courses. Particular flow problems may be attacked by intensive theoretical and experimental studies limited to the specific problem at hand. Such studies are directed toward learning enough about the nature of the flow process involved and the magnitudes of the effects to enable this information to be incorporated into the design approach. Results of such studies have made available modified theoretical design procedures in which one or more of the auxiliary simplifying assumptions (e.g., simplified radial equilibrium) can be avoided (refs. 236, 244, and 298 to 301). These have been called "improved" axially symmetric designs. Or, the information may take the form of new empirical design criteria or blade shapes, that is, new blade-loading and flow Mach number criteria. The diffusion factor is a pertinent example (ref. 9).

Eventually, the trend toward high power output with efficiency and compactness results in a condition wherein the discrepancies between the real and the design flows may no longer be encompassed by quantitative correction factors and improved axial-symmetry theories. In order to obtain physically valid descriptions of such real flows, further advanced design approaches must be found. The three-dimensional-flow theory of reference 242 is cited as an example.

In view of the importance to compressor designers of finding satisfactory solutions for these design problems, it is hardly surprising that there should exist an already extensive and now rapidly growing body of related literature. This chapter summarizes and reviews some of this literature and includes examples of improved axisymmetric design theories as well as examples of further advanced design approaches. Because of increasing importance, blade-row interference effects and time-unsteady effects are also discussed, despite the fact that only crude beginnings have been made toward solutions of these complex problems.

SYMBOLS

The following symbols are used in this chapter:

$D/D\tau$	differentiation with respect to time following the motion
$\mathscr{F}$	magnitude of $\overline{\mathscr{F}}$
$\overline{\mathscr{F}}$	blade force acting on gas particles per unit mass of gas
H	total or stagnation enthalpy per unit mass of gas, $h+(V^2/2)$
h	static enthalpy per unit mass of gas, $u+(p/\rho)$
I	modified total enthalpy, $h+\dfrac{(V')^2}{2}-\dfrac{U^2}{2}=$ $H-\omega(rV_\theta)$
n	polytropic compression exponent
p	static or stream pressure
Q	external heat added to gas per unit mass per unit time
R	gas constant
r	radius
S	entropy per unit mass of gas
t	static or stream temperature
U	magnitude of $\overline{U}$
$\overline{U}$	vector velocity of rotor blades at radius r
u	internal energy per unit mass of gas
V	magnitude of $\overline{V}$
$\overline{V}$	absolute vector velocity of gas
V'	magnitude of $\overline{V}'$
$\overline{V}'$	vector velocity of gas relative to rotor blade
z	coordinate along axis
Γ	circulation
γ	ratio of specific heats
$\overline{\zeta}$	absolute vorticity vector
η_p	polytropic efficiency
θ	angular distance
μ	viscosity
ν	kinematic viscosity
ρ	mass density
τ	time

Φ viscous dissipation of energy per unit volume of gas per unit time

ω angular velocity of rotor

Subscripts:

r radial direction

z axial direction

θ tangential direction

DESIGN ASSUMPTIONS

The chief desideratum in compressor design is to perceive the most advantageous compromise between ease of obtaining possible design solutions and magnitude of the resulting inaccuracies. It is clear that the present trend toward higher-power-output, more compact, and yet more efficient compressors requires shifting the compromise point in the direction of fewer simplifying assumptions, despite the increased complexity of the calculation procedures involved. The first prerequisite, however, is a better understanding of the physical significance of the various design assumptions and their ranges of applicability.

AXIAL SYMMETRY

The assumption of axially symmetric flow is one of the two most important assumptions used in axial-flow-compressor design. By this assumption, all the partial derivatives of the gas properties with respect to the angular coordinate are taken equal to zero. The system of flow equations is thereby reduced to a two-dimensional system, in which the gas properties are functions of the axial and radial coordinates only. Basically, this is equivalent to assuming the three-dimensional flow through a blade row can be represented sufficiently accurately, at a measuring station between blade rows, by a circumferential average of the flow conditions at each radial position. Symmetry about the axis of rotation does, of course, obtain for the limiting case of an infinite number of blades. Thus, one way of envisioning axially symmetric flow is to consider the flow as being restricted to hypothetical flow surfaces, as follows: Consider the number of blades in the blade row to increase without bound, in such fashion that the ratio of the spacing to blade thickness remains constant. Then the spacing between blades approaches zero, and the thickness of the blades approaches zero, so that the two blade surfaces and the space between them ap-

proach a mean surface. The streamlines are confined to such a mean surface.

Mathematically, the assumption serves to simplify the calculation problems. Physically, the assumption of axial symmetry, at least between the blade rows, is somewhat justified, because in a compressor, where adjacent blade rows rotate relative to each other, the blade-row incidence angles can be correct only for an average exit flow from the preceding blade row. As to design, the assumption of axial symmetry enables the designer to fix his attention on the radial distribution of the gas properties at a station between blade rows by averaging out the gas-property variations in the circumferential direction.

Simple radial equilibrium.—An auxiliary simplifying assumption that has been found convenient is the assumption of simple radial equilibrium. The condition of simple radial equilibrium further simplifies the flow equations by considering radial accelerations due to curvature of the streamlines in the radial-axial plane equal to zero. Physically, this assumption does not mean that radial velocity components are zero, but that the acceleration due to curvature of the flow path is negligible.

As the trend shifts toward higher aspect ratios or toward transonic and supersonic compressors, this assumption becomes increasingly inappropriate for two reasons: (1) The requirement of high mass flow per unit frontal area in such compressors necessitates low hub-tip radius ratios in the first stages, with attendant high curvature of the annulus walls and large aspect ratios. High pressure ratios per stage generally mean tapered passages. (2) Main-flow radial displacement due to boundary-layer accumulations, especially in the stator hub regions, may assume sizable proportions at the higher Mach numbers as a result of secondary flows. These factors combine to qualify seriously the physical validity of the simple-radial-equilibrium condition.

Constant entropy radially.—Another auxiliary simplifying assumption often used for compressor design is that the radial variation of entropy is zero. Radial variation of entropy depends upon viscous dissipation of energy and upon radial variations of heat transfer to or from the compressor. In the absence of cooling, the heat transfer to or from a compressor is negligible. The entropy gradient can be considered negligible

in the inlet stages at all radii except in the blade end regions.

In conservative compressors, therefore, the assumption of zero variation of entropy radially is reasonable, at least for the inlet stage (ref. 49 and ch. VIII). Flow conditions that result in increased losses and corresponding entropy rises result in increased secondary-flow effects. The attendant redistribution of increased-entropy fluids leads to nonnegligible radial entropy variations. In general, this is the physical situation, at least in the rear stages of compressors. In these stages, if constant entropy radially is not assumed, agreement between design and actual flow conditions may be considerably improved.

BLADE-ELEMENT FLOW

The assumption of blade-element flow is an important assumption used in conjunction with the axisymmetric approach. Both theoretical and experimental considerations are involved. Underlying the assumption of blade-element flow is the physical assumption that stream surfaces through a blade row are largely undistorted and that the fluid, by and large, remains on nearly conical surfaces, independent of the radial gradients. This assumption implies that the flow about any blade section or element remains the same regardless of whether the section is in a two-dimensional cascade or in an arbitrary rotor configuration.

The blade-element characteristics are obtained from measurements made on similar blade sections, usually in two-dimensional cascades (ch. VI). Strong efforts are made to eliminate the distorting influences of the end-wall boundary layers by means of various devices such as porous-wall boundary-layer suction, and so forth. Empirical correlation formulas are thus obtained for the flows about the blade sections for wide ranges of blade-setting angles, solidities, and flow velocities. In recognition of the influence of three-dimensional flows and the wall boundary layers in annular configurations, experimental data are likewise taken from tests in such configurations (ch. VII). Correlations are obtained for the performance of the blade sections at various radial positions spanwise. Empirical loss factors are thus developed to account for the viscous losses that arise in flow through a blade row. As a result of continuing experiments, there is a large growing body

of such information and data on compressor blade rows available for use (chs. IV to VII).

When large deviations from the physical assumption of flow on conical surfaces independent of radial gradients occur, the flow estimations based on blade-element flow become correspondingly more inaccurate. At higher inlet Mach numbers and increasing stage pressure ratios, stream surface distortions also increase, from secondary-flow boundary-layer displacement phenomena, for example. Under these conditions the combined assumptions of axial symmetry and blade-element theory may no longer give a satisfactory, physically valid flow picture at a given measuring station. Considerable research is being devoted at present to obtaining more insight into the nature of the losses that result from flow through a blade row and to obtaining better methods of accounting for the losses than is afforded by current blade-element-flow theories.

IMPROVED DESIGN THEORIES

High-output compact axial-flow compressors, in order to outperform conventional compressors, must be designed to operate at higher relative flow Mach numbers, wheel speeds, and blade loading, with lower hub-tip radius ratios and axial length per stage, and with fewer stages. Experience indicates that under these conditions the real flows in compressor configurations are different locally from those predicted by the simplified design methods to an extent which suggests that the simplifying assumptions therein may be qualitatively as well as quantitatively wrong for such applications. The quantitative differences arise from augmented boundary-layer phenomena such as viscous losses, separation effects, clearance effects, secondary-flow effects, and others as well. The qualitative differences include large distortions in the mainstream flow surfaces. Near sonic velocities, the secondary-flow distribution may change drastically from that at subsonic flow conditions (ch. XV), with resulting large local accumulations of low-energy fluids that give rise to local blockage effects. Likewise, near sonic velocities, small changes in flow area mean large changes in flow Mach number.

Thus, even minor deviations from predicted flow directions and expected boundary-layer behavior (due to secondary-flow effects or to three-dimensional effects, e.g.) can cause large deviations

from design flow conditions. As a result of these deviations, measurements in compressors, particularly in the blade end regions, show the following major discrepancies from design predictions based on two-dimensional-cascade data (chs. VI and VII): (1) Integrated total-pressure losses across the blade row are greater than predicted from blade-element theory, (2) flow directions deviate from those predicted at the blade-row exit, and (3) the operating range of angle of attack (without sharp rise in losses) is different from that predicted. The measurements further indicate that these blade end-region effects may account for half the observable losses.

To the designer seeking to achieve high-performance compressors, this increasing inability to approximate satisfactorily the real flows in actual compressors by means of idealized flows through simple configurations, with corrections for the anticipated differences between the real and the simulated cases, presents problems that must be solved. The importance of incorporating progressively more complete solutions of the flow equations into compressor design procedures has led to a series of experimental and theoretical investigations. The research toward improved compressor design procedures falls roughly into two categories. One phase of this research has been devoted to lifting the restrictions on the design flow calculations—that is, using a more exact basis for design. The results of these investigations appear in reports for proposed design procedures such as improved axisymmetric, quasi-three-dimensional- and three-dimensional-flow solutions. Another phase of the research has been to make a series of individual studies of more restricted problems within a chosen over-all design approach.

The succeeding sections of this chapter present brief reviews and discussions of some of the investigations into both aspects of the compressor design problem. A brief section is devoted to the timewise variations of the gas properties in compressors exclusive of the surging and stalling phenomena (see chs. XI to XIII).

COMPRESSOR DESIGN THEORIES

BASIC EQUATIONS

Following reference 236, the state of a gas in motion may be specified in terms of its velocity $\overline{V}$ and two thermodynamic properties, enthalpy per unit mass H and entropy per unit mass S. These are defined by

$$H = h + \frac{V^2}{2} = u + \frac{p}{\rho} + \frac{V^2}{2} \qquad (374)$$

and

$$t\, dS = du + p\, d\rho^{-1} \qquad (375)$$

The equation of state for a perfect gas is

$$p = \rho R t \qquad (376)$$

As given in reference 236, the Navier-Stokes equation of motion for a real fluid with constant viscosity is

$$\frac{D\overline{V}}{D\tau} = \overline{\mathscr{F}} - \frac{1}{\rho}\nabla p + \frac{\mu}{\rho}\left[\nabla^2\overline{V} + \frac{1}{3}\nabla(\nabla\cdot\overline{V})\right] \qquad (377)$$

The energy equation is

$$\frac{Du}{D\tau} + p\,\frac{D\rho^{-1}}{D\tau} = Q + \frac{\Phi}{\rho} \qquad (289)$$

The continuity equation is

$$\frac{\partial\rho}{\partial\tau} + \nabla\cdot(\rho\overline{V}) = 0 \qquad (290)$$

The six preceding equations are combined to give general flow equations (378) to (381).

Equilibrium equation.—The equilibrium equation

$$\nabla H = \overline{\mathscr{F}} + t\nabla S + \overline{V}\times(\nabla\times\overline{V}) - \frac{\partial\overline{V}}{\partial\tau}$$

$$+ \nu\left[\nabla^2\overline{V} + \frac{1}{3}\nabla(\nabla\cdot\overline{V})\right] \qquad (378)$$

expresses the instantaneous gradient of total enthalpy at a measuring station in terms of blade force, viscous forces, velocity, entropy gradient, and so forth. For design purposes, the desired velocity diagram and thermodynamic properties of the gases are determined at measuring stations between successive blade rows. In such locations, the blade force $\overline{\mathscr{F}}$ is zero, and the flow is generally presumed time-steady; that is, $\partial V/\partial\tau$ is zero. The last term in equation (378), in the brackets, represents the results of viscous action. In reasonably efficient flow, at least through the main flow except in thin boundary-layer regions, this term is small. Therefore, for design purposes, the last term is considered negligible.

The flow at the measuring station is considered inviscid. Physically, this is equivalent to assuming that the variations in velocity caused by viscous effects in the fluid in the spaces between the blade rows are small compared with the variations in velocity at those stations which are the results of viscous dissipation within the blade rows upstream. This appears in general to be a reasonable assumption. At any rate, the correction factors used to account for boundary-layer effects can accommodate such viscous losses as may arise in the space between blade rows.

Equation (378) thus becomes

$$\nabla H = t\nabla S + \overline{V} \times (\nabla \times \overline{V}) \qquad (378a)$$

where $\nabla \times \overline{V}$ is the absolute vorticity $\overline{\zeta}$ of the fluid. Thus, the modified equilibrium equation

$$\nabla H = t\nabla S + \overline{V} \times \overline{\zeta} \qquad (378b)$$

shows how the gradient in total enthalpy at a measuring station is related to the gradient of entropy and the absolute vorticity of the fluid. The aerothermodynamic equations for rotating blade rows can be expressed more conveniently in terms of relative velocity vector $\overline{V}'$, entropy S, and a quantity I in place, respectively, of absolute velocity vector $\overline{V}$, entropy S, and total enthalpy H. The relative quantities I and $\overline{V}'$ are defined as follows (ref. 301):

$$I = h + \frac{(V')^2}{2} - \frac{U^2}{2} = H - \omega(rV_\theta) = H - UV_\theta$$

In cylindrical coordinates, with z-axis (of machine) parallel to $\overline{\omega}$,

$$\overline{V} = \overline{V}' + \overline{\omega} \times \overline{r}$$

The modified equilibrium equation for a rotating system can thus be written

$$\nabla I = t\nabla S + \overline{V}' \times \overline{\zeta} \qquad (378c)$$

Energy equation.—The energy equation is

$$\frac{DH}{D\tau} = Q + \frac{\Phi}{\rho} + \frac{1}{\rho}\frac{\partial p}{\partial \tau} + \overline{V}$$

$$\cdot \left\{ \overline{\mathscr{F}} + \nu \left[\nabla^2 \overline{V} + \frac{1}{3}\nabla(\nabla \cdot \overline{V}) \right] \right\} \qquad (379)$$

The substantial derivative $D/D\tau$ indicates that the variation in total enthalpy of a particle along its streamline path from station to station is expressed by equation (379); whereas, equation (378) is used to define the variations in total enthalpy from streamline to streamline at a fixed station. The rate of change of total enthalpy per unit mass of fluid along a streamline is seen in equation (379) to be a function of the rate of external heat addition Q, the rate of viscous dissipation of useful energy along the path Φ/ρ, the rate of work done by the blades, measured by $\overline{V} \cdot \overline{\mathscr{F}}$, and the viscous effects on the velocity distributions as measured by the last term $\nu[\nabla^2\overline{V} + \frac{1}{3}\nabla(\nabla \cdot \overline{V})]$. In the case of steady real flow through a rotor, the $\overline{V} \cdot \overline{\mathscr{F}}$ is the predominating term on the right side of equation (379). For the real flow through a stator blade row, all the terms on the right side are usually small enough to be ignored.

For nonviscous flow, the energy equation becomes

$$\frac{DH}{D\tau} = Q + \frac{1}{\rho}\frac{\partial p}{\partial \tau} + \overline{V} \cdot \overline{\mathscr{F}} \qquad (379a)$$

and there is the additional relation that the blade force is normal to the blade surface (normal to the relative velocity of the fluid),

$$(\overline{V} - \overline{U}) \cdot \overline{\mathscr{F}} = 0$$

Thus, the energy equation for nonviscous flow through a stator in absolute quantities is written

$$\frac{DH}{D\tau} = Q + \frac{1}{\rho}\frac{\partial p}{\partial \tau} \qquad (379b)$$

Correspondingly, in terms of relative quantities, the energy equation for nonviscous flow through a rotor is written

$$\frac{DI}{D\tau} = Q + \frac{1}{\rho}\frac{\partial p}{\partial \tau} \qquad (379c)$$

According to this equation, for steady adiabatic flow the entropy and the quantity I remain constant along relative streamlines through the rotor. For steady relative flow, the rate of change of I along a streamline is proportional to the change of Q along the streamline. In addition to their convenience mathematically in finding the flows through rotating blade rows, the relative quantities help greatly in clarifying physical occurrences in nonviscous fluid flows in rotating turbomachines.

In compressors, the external heat exchange Q is small. If Q is neglected, for inviscid steady flow, equation (379) becomes

$$\frac{DH}{D\tau} = \overline{V} \cdot \overline{\mathscr{F}} \qquad (379d)$$

which is equivalent to (ref. 236)

$$\frac{DH}{D\tau} = \omega \frac{D(rV_\theta)}{D\tau} \qquad (379e)$$

that is, the rate of change of enthalpy along a streamline (work done on the gas) is equal to the angular speed of the blades multiplied by the rate of change of angular momentum about the compressor axis of the particle along the streamline. In terms of relative quantities,

$$\frac{DI}{D\tau} = \frac{DH}{D\tau} - \omega \frac{D(rV_\theta)}{D\tau} = 0 \qquad (379f)$$

Maintaining the quantity I constant is a more concise but equivalent way of expressing that the rate of change of total enthalpy H along a streamline is equal to the angular speed of the blade multiplied by the rate of change of whirl of the gas streamline as it passes through the rotor. This is Euler's turbine equation.

For conventional compressors, the rotors are often designed to add the same amount of energy to the gas at all sections radially; that is, H is kept radially constant through the machine for design purposes. For free-vortex distribution and addition of whirl, I is radially constant throughout the machine.

Entropy equation.—The entropy equation

$$\frac{DS}{D\tau} = \frac{Q}{t} + R \frac{\Phi}{p} \qquad (380)$$

indicates that the rate of change of entropy along a streamline depends only upon the rate of external heat addition and the rate of viscous dissipation of useful energy. As observed earlier, Q, the external heat-exchange rate, can be considered zero for compressors.

The first two terms in equation (379) are thus seen to be a measure of rate of entropy change along a streamline:

$$t \frac{DS}{D\tau} = Q + \frac{\Phi}{\rho}$$

Continuity equation.—The continuity equation

$$\nabla \cdot \overline{V} + \frac{1}{\gamma - 1} \frac{D \ln t}{D\tau} - \frac{D}{D\tau} \left(\frac{S}{R} \right) = 0 \qquad (381)$$

which is the last of the general flow equations presented herein, expresses the continuity relation in terms of divergence of velocity, rate of change of temperature function, and rate of change of entropy.

AXISYMMETRIC-FLOW THEORY

In order to simplify the analysis, the flow about the axis of rotation is usually assumed symmetrical. As has been discussed previously, this is often interpreted physically as assuming that the number of blades is allowed to increase without limit in such a way as to keep the total circulation constant, and accordingly the flow approaches the axisymmetric solution as a limit. Mathematically, the action of the blades can be computed by representing the blades by a volume distribution of forces in the flow equations. The magnitude of the force at a point is obtained by maintaining the product of the number of blades and the resultant force constant at any point on a blade as the number of blades is increased. The resultant force is the difference between the forces on the two sides of the blade. The flow follows stream surfaces, and the derivatives in the equations refer to changes of the fluid properties on the stream surfaces. This kind of solution, which gives average values in the circumferential direction, is usually valid when the departure from that average is small. For incompressible frictionless flow, when the blades are thin and the solidity fairly high, the solution can be considered as applying to the mean stream surface between two blades based on mass-flow considerations (ref. 5).

Equilibrium equation: All partial derivatives of gas properties with respect to time and angular position are taken as zero for steady axisymmetric flow. With this simplification and neglecting the viscosity effects, the radial, tangential, and axial components of equation (378) become

$$\frac{\partial H}{\partial r} = \mathscr{F}_r + t \frac{\partial S}{\partial r} + \frac{V_\theta}{r} \frac{\partial (rV_\theta)}{\partial r} + V_z \frac{\partial V_z}{\partial r} - V_z \frac{\partial V_r}{\partial z} \qquad (382a)$$

$$0 = \mathscr{F}_\theta - \frac{V_r}{r} \frac{\partial (rV_\theta)}{\partial r} - V_z \frac{\partial V_\theta}{\partial z} \qquad (382b)$$

and

$$\frac{\partial H}{\partial z}=\mathcal{F}_z+t\,\frac{\partial S}{\partial z}+V_r\,\frac{\partial V_r}{\partial r}-V_r\,\frac{\partial V_z}{\partial r}+V_\theta\,\frac{\partial V_\theta}{\partial z}$$

(382c)

Equation (382a) is the radial-equilibrium equation. At a station between blade rows, $\mathcal{F}_r$ is zero. For the usual assumption of constant entropy radially, the second term on the right side is taken to be zero. The fifth term represents the effect of radial motion on the condition of radial equilibrium and is neglected (ch. VIII) for the assumption of simplified radial equilibrium. The simplified-radial-equilibrium equation is thus generally written as follows for design purposes:

$$\frac{\partial H}{\partial r}=\frac{V_\theta}{r}\,\frac{\partial(rV_\theta)}{\partial r}+V_z\,\frac{\partial V_z}{\partial r}$$

or, by differentiating and combining,

$$\frac{\partial H}{\partial r}=\frac{1}{2}\frac{\partial V_z^2}{\partial r}+\frac{1}{2}\frac{\partial V_\theta^2}{\partial r}+\frac{V_\theta^2}{r}$$

(382d)

Energy equation.—From equation (379) for steady axially symmetric viscous flow and the assumption that heat generated by frictional work remains in the stream, $DH/D\tau$ can be written as

$$\frac{DH}{D\tau}=Q+\omega\,\frac{D(rV_\theta)}{D\tau}$$

in which Q is generally considered zero. This same relation was previously derived for frictionless steady flow (eq. (379e)).

Entropy equation.—For axially symmetric flow, equation (380) becomes

$$\frac{DS}{D\tau}=\frac{Q}{t}+\frac{\nu}{t}\left\{2\left(\frac{\partial V_r}{\partial r}\right)^2+2\left(\frac{V_r}{r}\right)^2+2\left(\frac{\partial V_z}{\partial z}\right)^2\right.$$

$$+\left(\frac{\partial V_\theta}{\partial z}\right)^2+\left(\frac{\partial V_r}{\partial z}+\frac{\partial V_z}{\partial r}\right)^2$$

$$\left.+\left[r\,\frac{\partial\left(\frac{V_\theta}{r}\right)}{\partial r}\right]^2-\frac{2}{3}\left[\frac{1}{r}\frac{\partial(rV_r)}{\partial r}+\frac{\partial V_z}{\partial z}\right]^2\right\}$$

(383a)

For the frictionless case,

$$\frac{DS}{D\tau}=\frac{Q}{t}$$

(383b)

Continuity equation.—For axisymmetric flow, equation (381) becomes

$$\frac{1}{r}\frac{\partial(rV_r)}{\partial r}+\frac{\partial V_z}{\partial z}+\frac{1}{\gamma-1}\left(V_r\,\frac{\partial\ln t}{\partial r}+V_z\,\frac{\partial\ln t}{\partial z}\right)$$

$$-V_r\,\frac{\partial\left(\frac{S}{R}\right)}{\partial r}-V_z\,\frac{\partial\left(\frac{S}{R}\right)}{\partial z}=0$$

(384)

IMPROVED FLOW THEORIES

Design theories have been presented that dispense with several of the flow assumptions made for the simplified axisymmetric designs. The first of these (ref. 236) used a modified equation (382a) for the radial-equilibrium condition (see ch. VIII for details) in lieu of equation (382d), the simplified-radial-equilibrium condition. In succeeding reports (refs. 298 to 300), the theories are extended to finite numbers of blades. In reference 301, a through-flow theory is developed; and the effects of blade thickness are considered in references 127 and 302.

Radial-equilibrium condition.—The preceding analysis, as developed in reference 236, has led to the development of six equations with eight independent variables, namely V_θ, V_r, V_z, $\mathcal{F}_\theta$, $\mathcal{F}_r$, $\mathcal{F}_z$, H, and S. Of these equations ((379e), (382a), (382b), (382c), (383a), and (384)), five are independent. For nonviscous flow, the following relation must hold:

$$(\overline{V}-\overline{U})\cdot\overline{\mathcal{F}}=0$$

(385)

as discussed earlier. This provides a sixth independent equation to replace equation (379e). For this case, equation (383b) is used instead of equation (383a).

For viscous flow, a sixth independent relation is developed (ref. 236) for the rate of change of entropy along a streamline, in terms of n, the polytropic exponent of the flow process:

$$\frac{DS}{D\tau}=R\,\frac{n-\gamma}{(n-1)(\gamma-1)}\left(V_r\,\frac{\partial\ln t}{\partial r}+V_z\,\frac{\partial\ln t}{\partial z}\right)$$

(386)

where

$$n=\frac{1}{1-\frac{1}{\eta_p}\frac{\gamma-1}{\gamma}}$$

and η_p is the assumed design polytropic efficiency.

For the design problem, two degrees of freedom are thus available. Accordingly, the desirable

variation of two of the gas properties, one of which is usually V_θ, can be specified; and the variation of the other gas properties and the blade force can then be determined theoretically.

Current design procedure is to specify desired gas conditions at stations in the gaps between blade rows only, where the blade-force terms are zero. One of the two available degrees of freedom in going from one such station to the next is taken up by the blade section selected. Accordingly, except at the first-stage inlet, there is only one condition at each station that the designer can specify.

No general analytical solution is presented in reference 236, but two numerical methods of solution are suggested. In one method, the design equations are written as finite-difference equations and applied to successive closely spaced axial stations. The second method employs only three stations per stage but assumes the shape of the radial-flow paths between stations. This method is considerably simpler to apply than the first. In reference 236, with assumed sinusoidal radial-flow paths, a form of the radial-equilibrium equation is developed which shows that the effects of radial motion are functions of the radial displacement, the square of the axial velocity, and the square of the blade-row aspect ratio.

Summarizing briefly the results and conclusions of reference 236, an investigation was conducted into the radial motion of the flow in a turbomachine by means of an axial-symmetry theory that does not assume simplified radial equilibrium. Blade aspect ratio had an important effect on the radial motion. The amount of radial motion depended also upon the passage taper, hub-tip ratio, speed of the main flow and design type (velocity diagram). Thus, for large blade-row aspect ratio or high axial velocity even with a small amount of radial displacement, the effect of radial motion may be large (i.e., a large oscillatory radial motion may be expected within the blade row). In reference 236, radial entropy gradients were neglected. Under certain conditions (ref. 49), these gradients have been shown to be important.

The results of a simplified analysis by the methods of reference 236, assuming sinusoidal flow paths through the blade row, are found in reference 241 to compare favorably with the re-

sults obtained by improved axisymmetric and three-dimensional analyses.

The analysis presented in reference 236, while it gives much useful information concerning the flow within blade rows, does not readily yield information concerning the flow just upstream or just downstream of such blade rows. The distribution of flow properties near a blade row is considered as an individual study in references 238 and 303. The problem is treated as an investigation into the matter of the flow near a blade row rather than with regard to design, and therefore is discussed in this chapter in the section SOME ASPECTS OF THREE-DIMENSIONAL FLOWS.

Finite blade spacing.—The design theories are extended from the blade systems with infinitesimal blade spacing (i.e., axially symmetric) to systems with finite blade spacing in an interesting series of reports (refs. 298 to 300). The procedure requires the axisymmetric solution for the flow as a first step. Reference 298 first presents the axisymmetric solution for the complete inverse (design) problem; that is, neither the blade shapes nor the wall geometry is specified in advance. The axial-flow-compressor designer starting with a reference streamline does specify the desired radial variation of the axial velocity component V_z (as in ref. 298) and an enthalpy function $\int dp/\rho$. By integration of the continuity equation (for isentropic flow in refs. 298 and 299), the radial velocity component V_r is obtained. The tangential velocity component V_θ is next obtained from the energy equation. The continuous force field that replaces the blade system in axially symmetric solutions can then be calculated from the Euler dynamic equations for axially symmetric flow. The infinitesimally spaced blades (stream surfaces) can be computed by use of the streamline equations

$$\frac{\partial r}{\partial z} = \frac{V_r}{V_z}$$

$$\frac{r\partial \theta}{\partial r} = \frac{V_\theta}{V_r}$$

$$\frac{r\partial \theta}{\partial z} = \frac{V_\theta}{V_z}$$

and the inlet conditions. Thus, the compression ratio, the form of the airfoils, and the flow around them can be determined.

When the cascade of blades with infinitesimal spacing and axially symmetric flow is replaced by a cascade of blades with finite spacing, the flow can no longer be considered circumferentially uniform. The uniform force field, which in the equations replaced the effects of the blades in the axially symmetric case, is in turn replaced in the equations by the asymmetric inertia and pressure terms, the $\partial/\partial\theta$ terms, that had earlier been neglected. Changing the force field and adding circumferentially asymmetric terms means that the streamlines of flow must change as well. One set of "mean" stream surfaces, considered to be halfway between the finite-spacing blades, is assumed "frozen," that is, unchanged. All the other streamlines shift and deform. This means the velocity and pressure terms must also change.

Corrective terms are to be found, which are to be added to the axisymmetric flow in order to obtain the asymmetric flow in the spaces between blades. These corrective terms are obtained as a power-series development for the flow-variable changes in terms of a spacing parameter ψ, the angular distance from the frozen streamline surfaces. Recurrence formulas are developed for these corrective terms, and an iteration process is set up for the desired solution. For simplicity, it is assumed that the changes in the flow variables are small enough that only terms linear in ψ need be kept. This is equivalent to assuming a linear pressure variation across each passage.

Thus, when the radial variations of a velocity component and of an enthalpy (pressure) function are prescribed, the steady, nonviscous three-dimensional flow through a cascade of blades with finite spacing can be found. For the two-dimensional solution (ref. 300), only the enthalpy function need be prescribed. While airfoils of finite thickness can be designed in this way, the numerical example of reference 300 is actually for a cascade of line (zero-thickness) airfoils with shapes approximating closely the streamlines found for the axisymmetric solution and with small lift coefficients. A further extension to the viscous-flow case is made in the appendix of reference 300. The methods developed in references 298 to 300 are instructive, as they indicate that the blade-to-blade variations with finite numbers of blades of finite thickness can be treated as perturbations on a mean, "frozen" streamline. However, in the nonviscous case (e.g., ref. 300),

the Bauersfeld condition, that for a nonviscous fluid the force field must be perpendicular to the streamlines defining the blade surfaces, was not considered. And in the treatment of the viscous-flow case (appendix of ref. 300), it was not possible in the one-step perturbation method to satisfy some boundary conditions and obtain closure of the nose and trailing edges of the blades.

In a series of reports (refs. 304 to 306), a treatment of the viscous flow through infinitely many thin blades is developed and extended, using the frozen-streamline notion, to develop the theory for an iteration process for the viscous, laminar, incompressible flow through blade rows with a finite number of blades of finite thickness. The application of this considerably more complex procedure greatly improves the solutions and makes possible the closure of the blade surface at the nose and trailing edge. Even with this procedure, however, it is necessary to relax the boundary condition of zero velocity (no slip) at the blade surfaces in order to linearize the problem sufficiently for possible solutions.

Through-flow theory.—A further generalization beyond the simplified axisymmetric-flow approach, the through-flow theory (ref. 301), considers the flow along an arbitrary surface $S(r,\theta,z)=C$. Retaining the blade force terms $\overline{\mathscr{F}}$ in the equations of motion partially takes into account the circumferential variations of pressure (enthalpy) and density. The development of the analysis presents a unified theory; that is, the direct and inverse problems are solved for compressible flow, either subsonic or supersonic, for arbitrary blade and wall shapes, and for high-solidity, thin blades. A principal equation is developed from the continuity equation, the equation of motion in the radial direction, and through use of a stream function. Two main groups of designs are considered. In the first group the designer prescribes the variation of the angular momentum. This group includes the free-vortex type, the wheel type, the symmetrical-velocity-diagram type, and so forth. In the second group of designs a relation between the tangential and axial velocities is prescribed. This group includes such radial-blade-element configurations as are found in high-speed centrifugal and mixed-flow impellers.

Criteria are established for both groups to determine whether the principal equation is elliptic or hyperbolic, roughly whether the flow is subsonic or

supersonic. Two methods are presented for solving the elliptic case. In one method the equations can be expressed in difference form and solved either by relaxation procedures or by a suggested iterative procedure if a high-speed large-scale digital computing machine is available. The relaxation procedure, for which the machine can also be used, is preferred. The other method suggested, machine solution of the set of simultaneous equations by a matrix process, is much quicker, especially when a number of solutions is to be found. The details of this matrix method are given in reference 129.

Blade thickness.—In standard design procedures, the axisymmetric solutions provide "meanline" information that can then be corrected for the effects of blade thickness by use of experimental data. A simple extension of the through-flow theory (ref. 301) incorporates some of the blade-thickness effects directly in the design procedure. For blades that are not thin, an approximate blade thickness factor b is included in the definition of the stream function. Better physical understanding of the significance of such a blade thickness-correction factor is obtained (refs. 127 and 302) by analyses of the effects of blade thickness on flow along a mean streamline on a blade-to-blade flow surface.

In a thick-bladed turbine configuration (in order to emphasize the effects) with subsonic incompressible flows, the mean streamline based on mass flow in the channel has less curvature than either the mean channel line or the mean camber line. The variation in the axial component of flow is nonlinear across the channel; the specific mass flow $\rho V'_z$ along the mean streamline is about 4 percent higher than that obtained by a one-dimensional calculation based on channel-width reduction. Furthermore, the influence of blade thickness extends a short distance upstream and downstream of the channel. The tangential velocity on the mean streamline rises above its inlet value before the leading edge and decreases rapidly at first through the channel and then more slowly to a value below its exit value for some distance downstream of the trailing edge.

For compressible flows, the mean streamline approximates the position of the mean channel line better than for incompressible flows but still has a lower curvature. The effects of blade thickness on tangential velocities of the mean

stream and on specific mass flow are similar to, albeit somewhat larger than, the corresponding effects in the incompressible case. The variation in specific mass flow was higher than that given by the one-dimensional calculations based on channel width, and the effect was observed outside the channel.

For supersonic flows (ref. 302) in a configuration with higher solidity and thinner blades, the mean streamline conformed more closely to the mean camber line than for the other cascade with lower solidity and thicker blades. The analysis using the thickness-correction factor b shows that the specific mass flow along the mean streamline increased an average of 9 percent more than anticipated from a one-dimensional calculation. Comparison of the specific mass flow in the axial direction with the variation in channel width likewise showed a 9-percent increase on the average in specific mass flow axially over the area reduction. This increase, it will be noted, is more than twice the value obtained for the previous subsonic cases. The variations of axial and tangential velocity components on the mean streamline are correspondingly increased.

For the symmetrical nozzle configurations (no turning), the increase in specific mass flow along the mean streamline at supersonic flow conditions was about 8 percent higher than expected from a one-dimensional calculation.

THREE-DIMENSIONAL THEORY

A general three-dimensional, nonviscous, compressible-flow theory is developed in reference 242 for subsonic and supersonic turbomachines with finite numbers of blades of finite thickness. The theory is applicable to axial-, radial-, or mixed-flow turbomachines for both the direct and inverse problems. Such a theory may be required for low hubtip radius ratios and for highly loaded stages with high inlet Mach numbers, where two-dimensional solutions may be inadequate.

As in earlier reports, the equations of motion, energy, and continuity are expressed in terms of the velocity components, entropy, and the quantity I (a modified total enthalpy). Estimated entropy changes due to shock waves, heat transfer (turbine cooling), and viscous effects can be accommodated in the calculations.

Analysis.—A three-dimensional-flow solution is obtained by combining solutions for mathemati-

cally two-dimensional flows on two different kinds of intersecting relative stream surfaces (fig. 274). A stream surface S_1 of the first kind is one traced out by fluid particles initially, at some axial position, on a circumferential circular arc of fixed radius about the axis of the machine. The blade-to-blade variations of flow can be computed on such surfaces (which extend from the suction surface of one blade to the pressure surface of the adjacent blade) in an essentially two-dimensional fashion. Suitable stream functions are defined that facilitate the solutions.

FIGURE 275.—Twist of flow surfaces in axial-flow channel.

FIGURE 274.—Intersecting S_1 and S_2 surfaces in blade row.

These S_1 surfaces will in general be twisted (fig. 275); that is, the flows are not restricted to surfaces of revolution as in quasi-three-dimensional solutions developed elsewhere. The S_1 surfaces can be modified and redefined in order to cope with the large circumferential derivatives that result from cases of large surface twist. Complications arise in regions where, because of secondary flows, for example, particles leave the walls and flow onto the blade surface, or, as is more likely, leave the blade surface and flow onto the wall or even out into the passage. In these regions it is necessary to approximate a solution

by assuming that the flow follows the hub and casing walls.

A relative stream surface of the second kind S_2 is one traced out by fluid particles which, at some axial position, were initially along a radial or nearly radial line. The most important S_2 surface is the one that starts midway between two blades (fig. 274) and divides the mass flow in the channel between the blades into two approximately equal parts. The through-flow solution obtained for large numbers of thin blades is a special case of S_2 stream surface solution. The problems of surface twist and complications near the boundaries for S_2 surfaces are similar to those already described for S_1 surfaces.

In general, the three-dimensional solutions for both the direct and inverse problems employ the solutions on both these two kinds of surfaces. The correct solution on one kind of surface often requires information obtained from solutions of the other kind. For example, determination of flow on S_1 surfaces requires information concerning the radial variation of the velocity components that is obtained from solutions along the S_2 surfaces. Consequently, iterative solutions between the two kinds of surfaces may be required. However, the computations are essentially two-dimen-

sional and can be handled by present computa tional techniques. A general method is provided for solving the flow equations manually or by high-speed digital machine computations.

In the direct problem, the solution starts with an assumed flow surface and proceeds with successive alternate solutions on the two kinds of flow surfaces until a satisfactory approximation is obtained. The better the first approximation, the shorter the computation.

The process is usually shorter for the inverse problem. The calculation begins on the mean S_2 surface on which the designer has one degree of freedom and an estimated blade thickness distribution B to specify. After the solution on this S_2 surface has been obtained, the blade coordinates are determined by extending the solution circumferentially.

Initial approximations.—The computations of the general theory for three-dimensional flows can be shortened materially by starting the iteration procedure with a reasonably good first approximation of the detailed flow variation. Reference 307 presents a quick approximate solution for the two-dimensional, compressible, subsonic, non-viscous flow past arbitrary turbomachine blades on arbitrary surfaces of revolution.

The first step in this particular solution is to estimate a mean streamline shape and the specific mass flow (product of velocity and density) along it. (For alternative methods, see ch. IV.) Equations for the flow along stream filaments of revolution are then solved to obtain values of the density and velocity components separately and of their derivatives in the circumferential direction. Next a Taylor series expansion in the circumferential direction using these values, together with mass-flow integrations, provides calculated blade shapes. Finally, an iteration procedure is set up in which the variance between the calculated blade shapes and the actual blade shapes provides the information required as a starting point for the second cycle. According to reference 307, depending upon the configuration and the original estimates, the detailed flow variations can be suitably obtained in two to four computation cycles.

Solutions on flow surfaces S_1 and S_2.—The three-dimensional analysis of reference 242 can provide a clearer understanding of the flows uncomplicated by viscous, secondary-flow effects than was obtainable from the simplified solutions.

More complete knowledge about the effects of the main stream on the development of viscous boundary layers may then aid in understanding the secondary-flow behavior in the turbomachines.

The practical utility of the more accurate flow representation of reference 242 depends, of course, upon its susceptibility to accurate and quick computation. Reference 130 is an investigation of the mechanics of obtaining solutions for the principal flow equations of the general three-dimensional-flow theory.

It will be recalled that the three-dimensional solution was obtained by combinations of mathematically two-dimensional solutions on two kinds of intersecting relative stream surfaces, designated S_1 and S_2. The principal flow equations for both kinds of surfaces are similar, and the methods of successive approximations used for their solution are similar. If it can be shown that the solution on one of the surfaces converges readily, the solution on the other should converge as well. Reference 130 evaluates three methods for obtaining solutions on the S_2 surfaces: (1) a relaxation method using a hand-operated desk calculator, (2) a matrix method on an IBM card-programmed electronic calculator, and (3) a matrix method on a Univac. The actual machine analyzed was a single-stage axial-flow turbine, but the results are equally meaningful to compressor design. Free-vortex variation in tangential velocity and cylindrical bounding walls were specified to reduce radial-flow effects. The blades are quite long, however, with hub-tip radius ratio of 0.6.

For both relaxation and matrix solutions, the nonlinear partial differential principal equation is replaced by a number of finite-difference equations representing the principal equation at the number of grid points in the flow region. The equations are solved by a method of successive approximations. The accuracy of such solutions depends upon the grid size (number of points), the degree of the polynominal representation used, the size of the residuals accepted, and the number of successive cycles completed for convergence.

Convergence was readily obtained in all cases of the investigation. The indications are that the matrix methods were quicker and somewhat more accurate than the relaxation solutions. In any event, the calculations were feasible and not overly difficult for the solution of the flow on a flow

surface, one step in the over-all three-dimensional-flow solution.

Information concerning the detailed flow distribution (ref. 307) and particularly concerning the relations of the pressure gradients and blade shape to radial-flow components (ref. 130) is discussed in the next main section of this chapter.

Evaluation and relation to previous methods.—Because of the complexity of the over-all three-dimensional design theory, very little has been recorded about experience in its use. Little information is available concerning the convergence of the iteration procedures or the magnitudes of the random errors of the computational methods. At present, this three-dimensional theory may serve best as a useful guide for evaluating experimental data.

As noted in reference 242, the through-flow solution (ref. 301) can be considered as a limiting case for the more general three-dimensional solution. It may be regarded, for example, as the solution for the flow along the S_2 mean stream surface that divides the mass flow equally when the circumferential variation of the velocity components approaches zero. Thus, the through-flow solution serves to indicate trends when the effects resulting from having a finite number of blades are small or constant. In this connection, the use of a blade thickness factor, based on information about blade thickness effects such as obtained, for example, in references 127 and 302, should improve the solutions considerably.

The effects of compressibility, spanwise variation of circulation $V_\theta r$, and radial components $\mathcal{F}_r$, or distributed-force vector $\overline{\mathcal{F}}$ upon the radial variations of gas state in a single-stage and in a seven-stage subsonic compressor with symmetrical velocity diagram are studied in reference 241. The results of these studies are presented briefly in the next main section. The investigation includes a brief discussion of the comparison between simplified-radial-equilibrium solutions and the solutions according to reference 236, while employing solutions obtained by means of the through-flow and three-dimensional theories (refs. 301 and 242, respectively) as criteria for accuracy. In this comparison, at axial stations in front of and behind the rotor of the single-stage compressor the simplified-equilibrium solution and the limiting solutions of reference 236 (zero and infinite aspect ratios) produced rather poor

approximations to more complete solutions. The simple approximation to the streamline path suggested in reference 236, with an assumed sinusoidal path through the rotor, gave a good approximation to the three-dimensional solution in the case investigated in reference 303.

SOME ASPECTS OF THREE-DIMENSIONAL FLOWS

The formidability of the complete three-dimensional design theory makes its application to compressor design somewhat impractical at this time. Nevertheless, considerable information about the three-dimensional aspects of the actual fluid behavior in compressors is required for design purposes. Such information has been obtained most successfully from many experimental and theoretical studies, each directed and confined to a particular phase of the real flow. By restricting the scope of a particular study, the investigator can make sweeping assumptions that simplify his solutions greatly. He need only be careful that his assumptions do not qualify the particular aspects of the flow being investigated. In the following subsections, several such phases of the over-all three-dimensional-flow behavior are described briefly, such as the effects of radial variations of circulation and of blade loading, radial components of flow within and between the blade rows, the effects of compressibility and of blade-force components, and some secondary-flow effects. Only steady-flow phenomena are considered here. The time-unsteady flows are considered in the next main section of this chapter.

RADIAL-FLOW VARIATIONS

In order to facilitate the investigations of the effects of radial variation of circulation, the flows are generally assumed axially symmetric and nonviscous, with constant entropy and enthalpy radially at the inlet. Even for these conditions, the solutions for the governing equations are simple only for the incompressible case of vortex distribution of the tangential velocity component, that is, constant circulation spanwise. For this condition only, the flow is two-dimensional and the streamlines all lie on cylindrical surfaces. For conditions of inconstant circulation radially, according to Prandtl's theory, vortices trail from the blades with their vorticity vectors downstream in the flow direction. The flow equations are then nonlinear, nonhomogeneous partial differential equa-

tions; and the flow itself is no longer confined radially to cylindrical surfaces. The aerodynamic advantages to be gained by use of nonvortex designs (i.e., lower relative velocities in the case of solid-body rotation design) must be weighed against the radial-flow components that arise, which can be calculated only with difficulty. Nevertheless, the aerodynamic advantages associated with nonvortex designs have frequently been beneficial enough to outweigh any detrimental effects.

Radial-flow shifts.—The radial-flow displacement that occurs within blade rows, both rotating and stationary, is discussed in reference 236. Here the use of a sinusoidal approximation to the probable flow path was suggested in a calculation procedure based on this kind of assumed curve. For a subsonic single-stage and a subsonic seven-stage compressor designed for symmetrical velocity diagram at all radii, reference 241 compares the simplified-radial-equilibrium solution, the assumed sinusoidal-flow-path solution (single stage only) (ref. 236), the through-flow solution (ref. 301), and the three-dimensional solution (ref. 242). Using references 301 and 242 as criteria, reference 241 found that, in the single-stage compressor, the sinusoidal-flow-path assumption gave answers that agreed closely with the more complete solutions. The simplified-radial-equilibrium solution did not agree well.

One conclusion reached in reference 241 is that, while compressibility does not change the streamline shapes very much, it does affect the velocity components a great deal. Another conclusion is that the gas undergoes an oscillatory radial motion in passing through the compressor. The period of the oscillatory motion is equal to the length of a stage. The gas (e.g., ref. 241) shifts inward through the inlet guide vanes and the first rotor and then outward in the first stator, the effects of this oscillatory motion being greatest in high-aspect-ratio stages. In general, the shift through the guide vanes, if present, is always inward. The shift through the rotor depends upon the particular velocity diagram and may be inward (for velocity distribution that is wheel type in the direction of the rotor rotation), may not shift (free vortex), or may be outward (wheel type in opposite direction to rotor rotation). In a velocity-diagram analysis, reference 221 shows that for inward radial shift in a rotor the negative radial gradients

of the axial velocity components behind the rotor lead to undesirable diffusion factors at the rotor tip and high stator-inlet Mach numbers.

By choosing a wheel-type flow distribution at the rotor inlet counter to the rotor direction with vortex distribution in the rotor, a radially outward shift in mass flow may be obtained. This should lead to more favorable distributions of diffusion factor and Mach number.

Reference 130 points out that the axial component of velocity is constant radially for free-vortex blading only for the case of simplified radial equilibrium. In the more general case, including, for example, the effects of radial variation of entropy and enthalpy, considerable radial variation of the axial velocity components results for both incompressible and compressible flows. In all such cases described in reference 130 (turbine configurations), there was a negative radial gradient of axial velocity ahead of the rotor.

Reference 130 indicates that the actual path within the blade row may be far from sinsoidal and depends upon such factors as radial twist of the stream (due to $\mathscr{F}_r$, radial component of the distributed-force term) and compressibility of the gas.

Flow near blade rows.—Reference 238 provides information about the flow near a blade row, just upstream or just downstream. It is first noted in reference 238 that the three-dimensional nonviscous incompressible-flow solution is simple only for the case of vortex distribution of the tangential velocity component. For this condition, the blade circulation spanwise is constant and there are no radial components or axial variations. For varying circulation spanwise, it is still possible to calculate the difference between the axial velocity profiles far upstream and far downstream of the blade row fairly readily by neglecting radial transport of vorticity shed from the blades. But to determine the velocity distribution of the flow field near the blade rows is a more difficult problem, involving nonlinear, nonhomogeneous, partial differential equations.

In reference 238, the flow is considered nonviscous, incompressible, and axially symmetric, with no inner- or outer-shroud taper. It is further assumed that there is no self-transport of vorticity; that is, the vorticity is transported only by the mean velocity and not by its own induced velocity. This last qualification reduces the

problem to the solution of a linear, nonhomogeneous, partial differential flow equation. The solutions thus obtained provide an approximation to the velocity field for any blade-loading distribution. The results are useful, then, for such conditions in which self-transport is negligible—that is, for moderate-turning, high-solidity configurations.

For the particular case where the blade chord approaches zero (actuator disk), the linearized partial differential equation describing the tangential velocity component becomes homogeneous as well and can be solved directly by using the given boundary conditions. Physically, this assumption is equivalent to requiring the change in mean tangential component through a blade row to occur as a discontinuity (the actuator disk) in a plane normal to the axis at a chosen axial location. By appropriately choosing the location for the discontinuous jump in tangential velocity (the axial and radial velocity components remaining continuous throughout), the direct solution for the homogeneous case is shown to be a useful approximation to the more exact solution for the case of finite nonzero blade chord, except near the lifting line, where large radial velocities and axial velocity gradients are generated.

For both the finite blade chord and the discontinuous approximation, the linerarized flow equations make possible the attainment of the incompressible solution for a multistage turbomachine by superposition of the flows for the individual blade rows. Exponential approximations are developed for rapid estimations of the velocity-component distributions, which provide an even simpler method of approximating the flow through a turbomachine. These approximations were sufficient for the particular case calculated in reference 238 to estimate the general order of the velocity components and were sufficiently to make these relations useful in estimating the interference of adjacent blade rows.

An illustrative example is calculated in reference 238, which assumes a linearly increasing circulation distribution from root to tip. The calculations indicate sizable changes in axial velocity profile both upstream and downstream of the blade row. The linearized approximation used (with the blade loading similar at all radii and assuming no radial force components) makes possible the separation of the velocity components

into the series of terms associated with the blades considered stationary and the additional terms due to rotation effects. Thus, the radial velocity disturbances, important principally as they affect the axial and tangential velocity components, are analyzed. An interesting asymmetrical behavoir is observed. The induced effects associated with the stationary blade attain their maximum downstream of the blade midchord position axially; the disturbances associated with rotation obtain their maximum upstream.

Reference 308 describes two physically possible types of nonviscous incompressible flow for a special case of the "actuator-disk" theory, the limiting case of a cascade of blades with negligible chord, discussed as an approximation to the more exact solution of reference 238. As before, only the tangential velocity components have a discontinuity at the actuator-disk section, the radial and axial components being continuous throughout. Axial symmetry, neglible heat transfer, and isentropic flow are assumed. The basic equations employed are Euler's equation of motion, the continuity equation, and the thermodynamic entropy and energy equations. As shown by a numerical example, the exact solutions to the problems as formulated here may match desired turbomachine flow conditions sufficiently closely to provide useful approximations of interest to designers. [Note that ξ and ζ should be interchanged in eqs. (9) to (11) in ref. 308.]

Radial adjustment and blade-row interference.—The shape of a stream surface as it passes through the stages of an axial turbomachine is investigated in reference 303 with the use of the exponential approximation to the linearized flow solution developed in reference 238. Attention is directed to the flow near the blade row and the manner in which the transition is made from the far-upstream to the far-downstream velocity profile. For the configuration investigated in reference 241, it was found that the radial velocity requires more than two axial chord lengths upstream of the inlet guide vanes and downstream of the stator before becoming negligible. Reference 303 establishes a relation between the aspect ratio of the blades and the rate of radial adjustment. The radial adjustment ranges from nearly complete by the time the trailing edge of low-aspect-ratio blades (=1.0) is reached, to almost negligible radial adjustment at the trailing edges

of high-aspect-ratio blades (=3.0). This information is then brought to bear on the dual problems of the mutual interference of neighboring blade rows and the three-dimensional flows in an axial turbomachine at off-design conditions. Briefly, for blade aspect ratios of 1.0 or less, the effects on the velocity distribution of interference between adjacent blade rows are negligible, and distortion of the design axial velocity profile at off-design operation is small. The effects of off-design operation may increase considerably with higher blade aspect ratio, while the interference between adjacent blade rows may become a predominant influence for aspect ratios over 3.0.

SECONDARY-FLOW EFFECTS

General discussion.—The three-dimensional behavior of a real fluid is intimately associated with the three-dimensional boundary-layer behavior of that fluid. The tendencies of the boundary layers to accumulate locally, to develop large radial and cross-channel flows in a complex of motions generally termed secondary flows, are discussed in chapter XV. Detailed experimental information on secondary-flow patterns is presented in chapter XV, together with the results of the more important theoretical developments. The present chapter is concerned chiefly with the overall flow picture; only the broad aspects of secondary flows are considered here.

The flow through a blade grid is considered as flow through individual channels or curved ducts in reference 309, and three distinct boundary-layer phenomena are discussed: (1) the cross-channel displacement leading to thickened boundary-layer regions at the suction surface of the passage, (2) the different behavior of boundary layer when adhering to a solid surface as contrasted with detached boundary layers such as wakes, and (3) the effect of centrifugal acceleration inducing radial components of motion affecting especially the boundary layers of moving blade rows. A criterion of radial stability is developed indicating that "stability of compressible flow depends not only upon the radial distribution of total energy, as is the case for incompressible flow, but also upon the temperature distribution." With this criterion, the radial displacement of boundary layer in turbomachines is analyzed for various conditions of flow circulation and boundary-layer distribution.

In reference 310, the secondary flows are attributed largely to trailing-edge vortices shed as a result of spanwise variation of circulation along the blades and nonuniform inlet approach velocities (see ch. XV for discussion of passage vortices). Reasonable orders of magnitude of three-dimensional losses are estimated by the methods of reference 310 for the very conservative flow conditions assumed. A practical extension of this investigation is provided in the guide-vane analysis of reference 43. End-wall boundary layers are shown to cause deviations of the real flow from blade-element-flow considerations. Some of the effects noted are first underturning and then overturning in the boundary layer as the end wall is approached, a general decrease in circulation and turning angle along the blade in the boundary-layer regions, and large induced losses in the guide-vane end regions. A calculation procedure for quantitative estimations of the mean flow variations induced by the end-wall boundary-layer effects is set up in which the distribution along the blades is represented by a system of vortices, the effects of which are calculated by the method of images, with use of an empirical correlation factor. The closing section of reference 43 considers several aspects of the secondary-flow problem, from the designer's viewpoint, in some detail.

The more complex flow situation in rotor blading is considered in reference 310. The effects of tip clearance and relative blade to wall motion are discussed in very general terms, as is boundary-layer displacement of the type noted in reference 309. The action of secondary flows under certain conditions to prevent stalling and to enable blades to operate above the two-dimensional stalling limit is brought out. The work-done factor and the induced-drag coefficient are connected on the basis of these secondary-flow considerations. Finally, the conclusion is reached that ordinarily (conservative, subsonic turbomachines) the primary flow conditions and primary losses are still due to two-dimensional blade-section performance. Experimental evidence (ch. XV and ref. 311) indicates that the secondary-flow-induced losses assume considerably more importance with higher flow velocities and larger turning angles.

An interesting analysis is developed in reference 312 of the relation between the secondary flows and the main flow characterized by radially varying blade circulation and rotational incoming flow.

References 312 and 244 present a clear, understandable physical picture of three-dimensional flows in turbomachines.

Commentary.—Despite the great amount of research already devoted to the study of secondary flows in turbomachinery, empirical information, useful to designers, concerning the actual flows within the blade rows themselves is still largely lacking. Most analyses to date provide information and devise design procedures about the flows encountered at stations between the blade rows. For design purposes, the nature of the flows in the blade rows themselves is almost invariably assumed. References 302 and 304 give evidence that the flow patterns within the blade rows are quite complex, that large stream surface distortions can and do exist. These results must be considered to qualify the conclusions reached from analyses (e.g., ref. 244) based on assumed simple flow configurations in the passages between stations.

TIME-UNSTEADY FLOW

A theory of nonstationary motion around airfoils is presented in reference 313. The purpose of the paper is to present the theory originally developed by Birnbaum, Wagner, Küssner, Glauert, and Theodorsen in relatively uncomplicated mathematical forms. A remarkably clear exposition of the fundamental conceptions of the two-dimensional circulation theory of airfoils is presented first. The report shows how a "wake of vorticity" is produced if the circulation around the airfoil is a timewise variable. The induced vorticity distributions over a thin airfoil are presented for such wake vortices at various distances in the wake ξ from the midpoint of the airfoil.

Formulas for the lift and momentum are next obtained for the thin airfoil, and here it is seen that the simple Joukowski formula $L = \rho V\Gamma$ no longer will do. Instead, the expression for the lift consists of three parts:

$$L = L_0 + L_1 + L_2$$

where

$$L_0 = \rho u \Gamma_0$$

$$L_1 = -\rho \frac{d}{d\tau} \int_{-1}^{1} \gamma_0(x) x \, dx$$

$$L_2 = \rho u \int_{1}^{\infty} \gamma(\xi) \, d\xi / \sqrt{\xi^2 - 1}$$

and

u velocity of motion of airfoil (or of gust of wind past airfoil)

Γ_0 circulation resulting from vorticity $\gamma_0(x)$

$\gamma_0(x)$ vorticity bound to airfoil that would be produced by airfoil motion (or by gust) if instantaneous velocity were maintained permanently

x coordinate along blade rearward from mid-chord position

$\gamma(\xi)$ vorticity in wake

The quasi-steady lift L_0 is that which would be produced if the instantaneous velocity and angle of attack were permanently maintained. The lift L_1 represents the forces acting on a body in an ideal fluid when no circulation is produced because of the reaction of the accelerated fluid masses. It is obtained by integrating over the surface the "impulsive pressures" $\rho \frac{\partial \varphi}{\partial \tau}$ (where φ is the instantaneous potential function). The lift L_2 represents the contributions to the lift from the wake itself, and contains the wake effects. A corresponding formulation is obtained for the moment:

$$M = M_0 + M_1 + M_2$$

In these formulas, L_0 and M_0 as well as L_1 and M_1 require only solutions of steady-state problems by usual methods. The wake contributions L_2 and M_2 can be interpreted physically as the differences between the instantaneous and the final values of lift and moment for a case in which the quasi-steady lift and moment undergo a sudden change. Hence, L_2 and M_2 can be called the "deficiencies" caused by the nonuniformity of the motion of the airfoil or of the fluid velocity.

These general results were then applied to an oscillating airfoil and to an airfoil entering a vertical gust with various velocity profiles. The general expressions for the lift and moment developed by von Kármán and Sears (ref. 313) are applied in reference 314 to a series of alternating up and down gusts, sinusoidally distributed. The magnitude of the lift decreases as the frequency of the gusts increases. As in reference 313, the lift is shown to act, always, at the quarter-chord point of the airfoil. These results are applied to a wind-tunnel fan blade operating just downstream of a set of prerotation vanes. The vanes produce periodical disturbances through which the fan

blades pass, which in turn give rise to periodical forces on the blades and perhaps vibrations of dangerous amplitudes. An approximate calculation is made in order to apply the results obtained, in which it is necessary to take the two-dimensional flow across some mean cross section representative of the blade and to consider that this mean section encounters flow conditions in its path that can be approximated by superimposing a sinusoidal variation of axial velocity on a uniform mean axial velocity. No dangerously large vibration amplitudes were calculated in the example given in reference 314.

The results derived in reference 314 for an airfoil moving through a stationary gust pattern are extended in references 315 and 316 by means of a simple generalization to provide formulas for calculating the unsteady aerodynamic quantities for a single stator row followed by a single rotor row. Because the blades are thin, slightly cambered, and lightly loaded, this configuration resembles a compressor more closely than a turbine. The flow is assumed incompressible and inviscid; the blade rows are represented by infinite cascades of two-dimensional blades. Each airfoil (ref. 315) is considered "to be acting in a velocity field induced by (a) its own wake, (b) the (variable) bound vortices of fellow members of its own blade row, (c) their wakes, (d) the (variable) bound vortices of members of the other blade row, and (e) their wakes."

In order to obtain a solution with reasonable ease, a scheme of successive approximations is followed:

(1) Assume first that the unsteady effect on the circulation of a blade is small compared with the steady circulation ordinarily considered by a designer.

(2) The first approximation to the unsteady effects on a typical stator blade $_r\Gamma^s(\tau)$ is calculated on the assumption that the only significant contribution arises from the steady circulation on the rotor blades $_0\Gamma^r$. For this first approximation, the unsteady rotor circulation $_r\Gamma^r(\tau)$ and the unsteady parts of the circulation of all the other stator blades and of all the vortex wakes except that of the chosen stator blade are neglected. "(Presumably this approximation breaks down for stator cascades of extremely large solidity, in which the adjacent blades are so close that their nonsteady circulation components induce large effects.)"

(3) In order to calculate the unsteady effects on a rotor blade, in this same first approximation process, the significant contributions are assumed to arise from the steady circulation about the stator blades $_0\Gamma^s$ and from the effects of the rotor blades passing through the vortex wakes shed by the stator blades.

The procedure thus far can considered as the first of a series of successive approximations. The second step might consider the additional effects of $_0\Gamma^r$ but, as noted in reference 315, would very likely be extremely difficult to calculate.

On the basis of this first-approximation scheme, then, a calculation is made for the unsteady velocity at a rotor or stator blade induced by the steady circulation distribution on the blades of the other row in motion relative to the blade in question. From this, the unsteady lift and moment of a stator or rotor blade can likewise be calculated. Investigations of numerical examples were made for configurations of thin, small-turning airfoils, with rotor and stator solidities fixed at unity, with a 50-percent reaction stage, and with the stagger angles $\alpha_r = \alpha_s = 45°$. The calculations were made for a range of the parameter b'/c_r (ratio of axial separation between trailing edge of stator row and leading edge of rotor row to rotor half-chord) and over a range of d_n/d_s (ratio of pitch of rotor blades to pitch of stator blades).

The results showed large increase of unsteady lift with decreasing b'/c_r, and appreciable change of lift with variation of d_n/d_s. In one case the unsteady part of the lift was as much as 18 percent of the steady lift and, for this approximation, is accordingly of practical importance. Also, the contribution of the stator wakes to the unsteady lift of the rotor blades was comparable in magnitude to the effects induced by the bound circulation of the stators themselves. The assumption made for the first approximation, namely that the unsteady effect on the circulation of a blade is much less than the steady circulation $|_r\Gamma| \ll |_0\Gamma|$, was checked and found to be reasonable. In addition, the authors find the power in the vortex wakes quite small. (The power is expressed as the ratio of the energy transferred to the wakes per unit time to the steady power required to turn the rotor.)

A further result is that the energy in the stator wake for the present cases is about 100 times as large as the energy in the rotor wake. Because the kinetic energy transferred to the vortex wakes due to periodic variation in circulation is proportional to $|_r\Gamma|^2$ (ref. 317), the squared amplitude of variation of circulation, and therefore the unsteady circulation on the stator blades, is about 10 times as large as that on the rotor blades.

The unsteady lift on both was about the same, however, for the example in reference 316 because of the differences in chordwise velocity distributions on the stator and rotor. In general, then, according to references 315 and 316, the induced circulation on a blade row due to the relative motion of an adjacent downstream row is considerably greater than that due to the effects of an adjacent upstream row.

SECONDARY FLOWS AND THREE-DIMENSIONAL BOUNDARY-LAYER EFFECTS

By Arthur G. Hansen and Howard Z. Herzig

A survey of experimental and theoretical research on secondary flows and three-dimensional boundary-layer flows as applicable to compressor flow phenomena is presented. The results of experimental research are used to construct a simple model of secondary flow in compressor blade rows.

The limitations of the application of present research on secondary flows to flow in a multistage compressor and indications of ways this research might be applied to current design considerations are also presented.

INTRODUCTION

The importance of boundary-layer development in relation to compressor design procedures is discussed in chapter III and in reference 318. As these references point out, there are no simple techniques that accurately account for viscous effects in current design systems. Instead, the effects of boundary layers are taken into account only by introducing some gross correction factors into calculations derived from nonviscous-flow theory. These correction factors, moreover, are based on empirical data and give only rough estimates of boundary-layer development. Nevertheless, this method of accounting for viscous-flow effects has proved relatively adequate for the design of compressors of the type currently in use. With the trend toward high-speed and high-mass-flow turbomachines, however, the influence of boundary layers becomes increasingly critical in design calculations. This is simply illustrated by noting the sensitivity of flow velocities in the transonic range to slight changes in boundary-layer-flow blockage.

It is important to recognize that a more satisfactory description of boundary-layer flow cannot come from refinements of the two-dimensional boundary-layer theory currently in use (ch. V). The reason is that boundary-layer behavior in blade rows of an actual turbomachine exhibits certain irreconcilable differences from boundary-layer behavior predicted by two-dimensional theory. Two-dimensional boundary-layer theory predicts characteristics of a boundary layer resulting from a mainstream flow that has no variation in its lateral direction. In an actual blade row, however, lateral variations of the main stream and the associated boundary layer cannot be ignored. The occurrence of secondary flows—that is, boundary-layer flows having components normal to the mainstream direction—often results in sizable displacements and accumulations of boundary-layer material. These flows arise principally from blade end clearance, blade-to-blade and radial pressure gradients, centrifugal-force effects, and relative motion between blade ends and annulus walls (refs. 311 and 318). Flows of this type have no counterpart in two-dimensional theory.

Losses occurring in blade end regions of compressor blade rows account for a sizable portion of the total measured loss (ch. VII). As blade end losses are principally the result of boundary-layer displacements and accumulations, it may be stated that future improvement of compressor efficiencies will depend significantly upon understanding the nature and causes of these boundary-layer phenomena and upon finding more realistic and accurate methods of accounting for them in design procedures.

For these reasons, the analysis of secondary flows has become the major problem associated with research on boundary-layer behavior in compressors. While many important aspects of secondary-flow phenomena have not as yet been investigated, considerable research progress has been made. This chapter presents an over-all review of both experimental and theoretical research and indicates its relevancy to compressor design.

At the present time, research on secondary flows has two immediate goals: (1) to find methods of reducing the magnitude of undesirable secondary-

flow disturbances in blade rows, and (2) to develop practical theories of secondary-flow behavior that the compressor designer can incorporate into design methods. In attaining these goals, three basic problems can be recognized: (1) isolating the factors that may cause secondary flows, (2) analyzing the types of secondary-flow components resulting from these factors, and (3) determining the contribution of these components to the total flow behavior. The factors that cause secondary flows are fairly well known and have been indicated previously. The state of knowledge concerning the characteristics of the associated secondary-flow components, however, leaves much to be desired. As will be evident from the discussions presented, most of the current knowledge is qualitative in nature. Adequate theories furnishing the quantitative information necessary for improving compressor designs are still to be formulated.

EXPERIMENTAL INVESTIGATION OF SECONDARY FLOWS

Because of the importance of the problem, many experimental and theoretical investigations of secondary flow in turbomachines are presented in current literature (surveys 212 to 240, ref. 319). In experimental research carried out at the NACA Lewis laboratory, flow-visualization techniques as well as total-pressure and flow-angle measurements were used in order to obtain an insight into the three-dimensional boundary-layer-flow patterns in typical axial-flow turbomachines. The results of the investigations (refs. 311 and 318) are presented here only for the over-all physical understanding of secondary-flow processes in turbomachines that they afford rather than for detailed compressor flow information.

The following discussion attempts to build up a concept of secondary-flow behavior in compressor blade rows by separate descriptions of the various types of secondary-flow components that can occur. In this regard, an analysis of secondary flows arising from cross-channel pressure gradients is first discussed. Next, the influence of radial pressure gradients that contribute to the local accumulation of boundary-layer material is analyzed. The size and locations of these accumulations depend upon the character of blade boundary layers, which are, in turn, a function of profile shapes; hence, some indication of the effect of blade profile shapes on secondary flows is

also included in the discussions. This is followed by a discussion of blade tip clearance and relative motion between blades and annulus walls. Finally, the influence of rotor-stator interaction on flow behavior is presented. Comprehensive descriptions of the methods employed to obtain the results can be found in references 311, 318, and 320.

The section is concluded with consideration of a model of the complete secondary-flow pattern as indicated by the experimental results and a discussion of ways certain aspects of secondary-flow theory might be applied to compressor design.

CROSS-CHANNEL FLOWS AND PASSAGE VORTEX FORMATION

Apparatus and procedure.—For simplicity, the study of secondary-flow components resulting from cross-channel pressure gradients was begun by visualization of the end-wall inlet boundary layer of a two-dimensional cascade at low air-speeds. It was intended, by using a smoke flow-visualization method (ref. 318), to isolate and to evaluate the effects of cross-channel gradients upon the wall boundary layer while eliminating such complicating considerations as radial flows and possible shock phenomena.

A sketch of the two-dimensional cascade rig is shown in figure 276. The cascade section was so designed that the solidity, angle of attack, aspect ratio, turning angle, and blade stagger angle could be varied quite readily. The two-dimensional cascades were used for tests at Mach numbers below 0.4. The boundary-layer flow was visualized by means of smoke introduced through a probe. The smoke flow-visualization method was used only at low mainstream velocities (about 30 ft/sec). At higher velocities, dispersion of the smoke due to turbulence made the method impracticable.

Passage vortex formation.—The overturning in the end-wall boundary layer of a two-dimensional cascade with no tip clearance is illustrated in
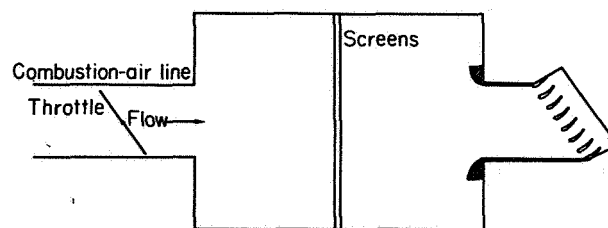

FIGURE 276.—Two-dimensional steady-flow cascade (ref. 318).

figure 277. The overturning results from imposition of the mainstream static-pressure gradients upon the low-momentum boundary-layer fluid. The smoke used to trace out the flow patterns was introduced at the wall by means of the probe. A downstream view of a boundary-layer streamline crossing a channel (fig. 278) shows that, as the streamline approaches the suction surface, it deflects spanwise and then rolls up into a vortex-type flow. (The insert shows the entire streamline pattern schematically.) Probe surveys showed that all the streamlines in the wall boundary layer converged to approximately the same region and rolled up into the flow vortex (fig. 279(a)). The pattern of vortex formation was such that, as the point of smoke introduction was shifted toward the suction side, the streamlines along the end wall exhibited increased spanwise deflection as they approached the region of convergence, where they rolled up into the central portions of the vortex, as shown schematically in figure 279(b).

This secondary-flow vortex is called the "passage vortex" in order to emphasize the fact that it is a passage wall and not a blade trailing-edge vortex due to circulation changes along the blade. The size and vorticity of the passage vortex increase

FIGURE 278.—Downstream view showing vortex formation resulting from roll-up of end-wall boundary layer. Smoke introduced on wall near blade pressure surface (ref. 318).

with increasing main-flow turning. When the turning is large enough (fig. 280), the outermost layer of the vortex may come from boundary-layer flow on the pressure surface that deflects onto the end wall and flows all the way across the channel until it reaches the suction surface.

At low airspeeds where smoke could be used, passage vortex formation was observed for other configurations, including cascades of NACA 65-(12)10 blades. At higher Mach numbers, surface indications, obtained by use of hydrogen sulphide traces on white lead paint, show that the cross-channel deflection pattern remains unchanged (ref. 318).

It should be noted that the cross-channel component of boundary-layer flow can be considered as a "double" boundary layer (fig. 281). The component normal to the main stream must have zero velocity at the wall, rise to some maximum value, and then fall to zero again in the main stream. The outer portion of this cross-channel boundary layer rolls up to form the passage vortex. The "sublayer" next to the wall has vorticity of the opposite sign to the outer portion, and when it rolls up produces vortices opposite in direction to passage vortices. Under these test conditions, the diffusion of vorticity forces from this sublayer was rapid enough to cause this portion of the

FIGURE 277.—Overturning in end-wall boundary layer due to secondary flow. Smoke introduced through probe on wall in passage at inlet (ref. 318).

boundary-layer vorticity to disappear rapidly. Photographs of this sublayer rollup are found in reference 320 and in the motion-picture supplement to that report.
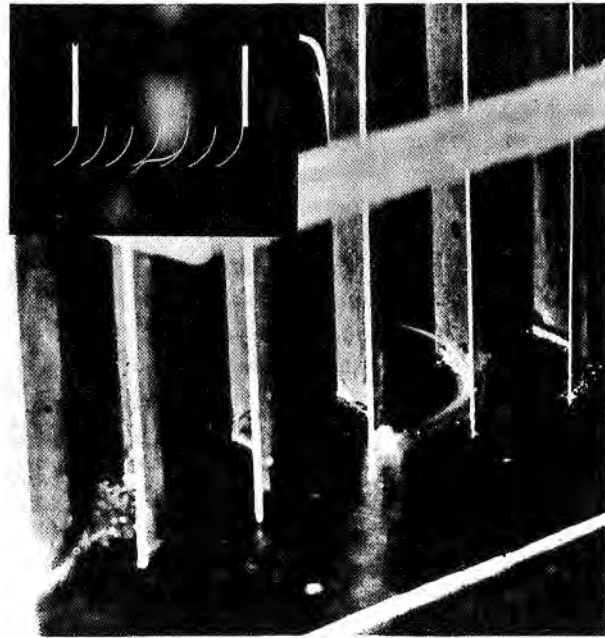

FIGURE 280.—Deflection of flow off blade pressure surface and across passage to roll up into outer layers of passage vortex (ref. 318).

(a)
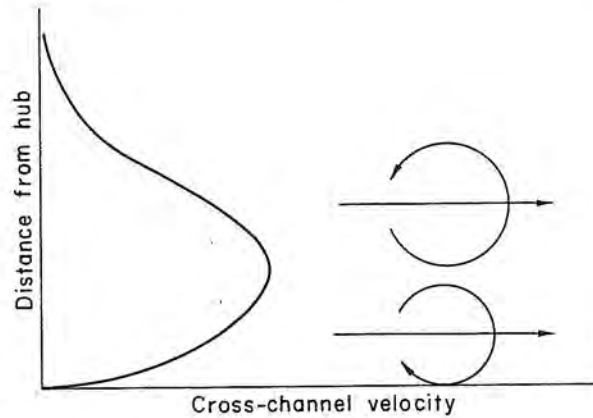

(b)

(a) Convergence of streamlines (ref. 318).
(b) Spanwise deflection and vortex roll-up.

FIGURE 279.—Passage vortex formation.

FIGURE 281.—Boundary-layer velocity and vorticity profiles for cross-channel component of boundary-layer flow (ref. 320).

Passage vortex behavior and effects.—Once the passage vortex has been formed, it tends to resist turning and does not follow subsequent mainstream turnings as it proceeds downstream. Figure 282 shows how, in tandem cascades, a vortex formed in the upstream cascade resists the turning in the downstream cascade. Test observers could see the passage vortex richochet off a pressure surface of the downstream cascade and cause flow separation in the region of impact.
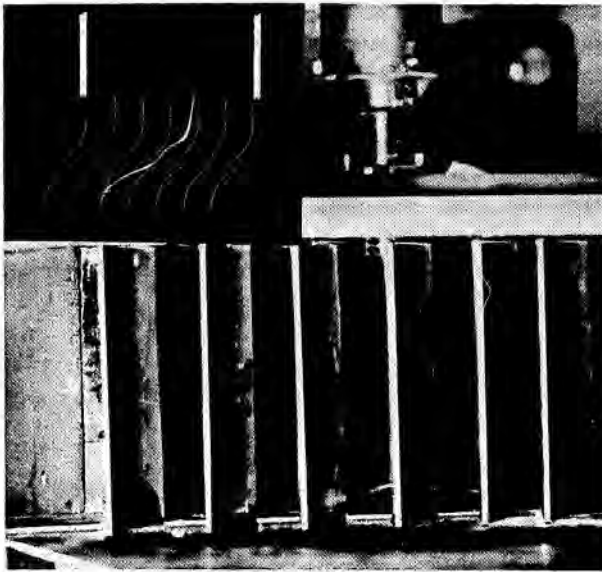
FIGURE 282.—Resistance to turning of passage vortex generated by upstream cascade causes it to strike pressure surface of blade in downstream cascade. Smoke introduced through probe on wall at inlet to upstream cascade (ref. 318).

The phenomenon has been observed in accelerating as well as decelerating cascades.

Thus, the accumulation of low-energy material near the suction surface of a turbomachine passage causes flow disturbances and losses leading to flow-angle deviations and poor angles of attack in subsequent blade rows. Furthermore, the vortex behavior as it passes downstream can lead to flow disturbances on the blade surfaces that it impinges upon and to additional losses there. This behavior may account for a large part of the losses variously attributed to secondary flows. The mixing action of the vortex behavior likewise represents a large deviation from the kind of simplified boundary-layer behavior assumed in design procedure.

RADIAL SECONDARY FLOWS IN STATORS

Just as the cross-channel pressure gradient imposed by the main stream causes cross-channel secondary flows, so the radial pressure gradient causes radial boundary-layer flows. Given a boundary-layer region extending from the inner to the outer shroud in a stator row, radial transport from the tip to the root regions can occur. The quantity of such transport depends upon the thickness of the radial boundary-layer region or flow path and the magnitude of the radial

pressure gradient (a function of mainstream turning and velocity).

In rotors, the flow picture is further complicated by the centrifugal forces on the rotor blade boundary layers. In general, for compressors where the blade speeds are higher than the mainstream tangential velocity component, the boundary layer will be forced radially outward (see ref. 319, section II–F).

Apparatus and procedure.—The effects of radial pressure gradients and higher flow Mach numbers were studied in an annular-cascade test unit, shown schematically in figure 283. The cascade blades investigated therein were of several types (ref. 311). However, attention is confined initially to the tests in a cascade of high-turning vortex blades designed for smooth two-dimensional blade surface velocity profiles. While these blades are not typical of those found in compressor units, the tests conducted provide sufficient information to formulate theories that apply to annular blade rows in general.

The annular cascade was used for a range of hub discharge Mach numbers up to about 1.5. As mentioned previously, smoke flow-visualization tests were unsatisfactory for flow velocities much in excess of 30 feet per second. Consequently, for high speeds, two other flow-visualization techniques were employed. In the first, the surfaces of the blade passages were painted with a lead carbonate base paint. Hydrogen sulfide gas (which has a density comparable to air) was then introduced into the boundary-layer region, and boundary-layer motion was indicated by the brown trace made by the reaction of the hydrogen sulfide with the paint. Unfortunately, this method provides indications of
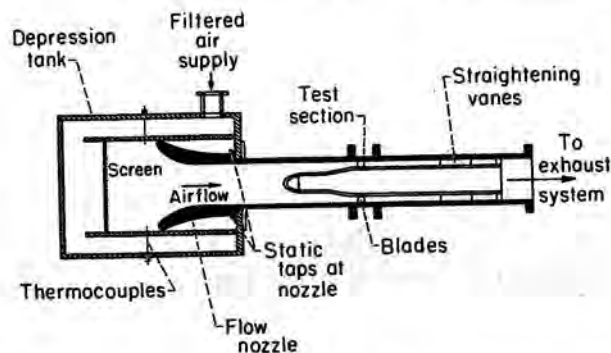

FIGURE 283.—Schematic view of annular-cascade test unit (refs. 311 and 318).

flows along boundaries only; and, because of the turbulence at higher Mach numbers, the traces indicate the flow paths of a region of the boundary layer instead of individual streamline paths. The second flow-visualization method was based on paint flow traces. The paint used was a lead carbonate paint deliberately made nondrying and capable of flowing with the surface flow gradients at the higher Mach numbers investigated.

Since hydrogen sulfide and paint traces can at best give indications of boundary flows directly on blade surfaces and annulus walls, the significance of these traces is interpreted only on the basis of previous information obtained either by the smoke visualization method or by quantitative measurements.

It should also be noted that total pressures, flow angles, and wall static pressures were measured at a discharge measuring station in the annular-cascade investigations. The measurements were made on three sets of blades and at two flow conditions for each set of blades. These flow conditions are designated, respectively, "lower Mach number" (high subsonic flow) and "higher Mach number" (supersonic flow). The measuring probes and hot-wire anemometers used are described in reference 311. Great care was taken in the fabrication and use of these instruments in order to make the results as reliable and accurate as possible. Nevertheless, because of the large pressure and angle gradients involved in the flow regions of chief interest in this report, the results are discussed in qualitative terms only.

Indications of radial flows based on downstream measurements.—Contours of loss in inlet kinetic energy for the annular cascade of vortex blades are presented in figure 284. The hub loss accumu-
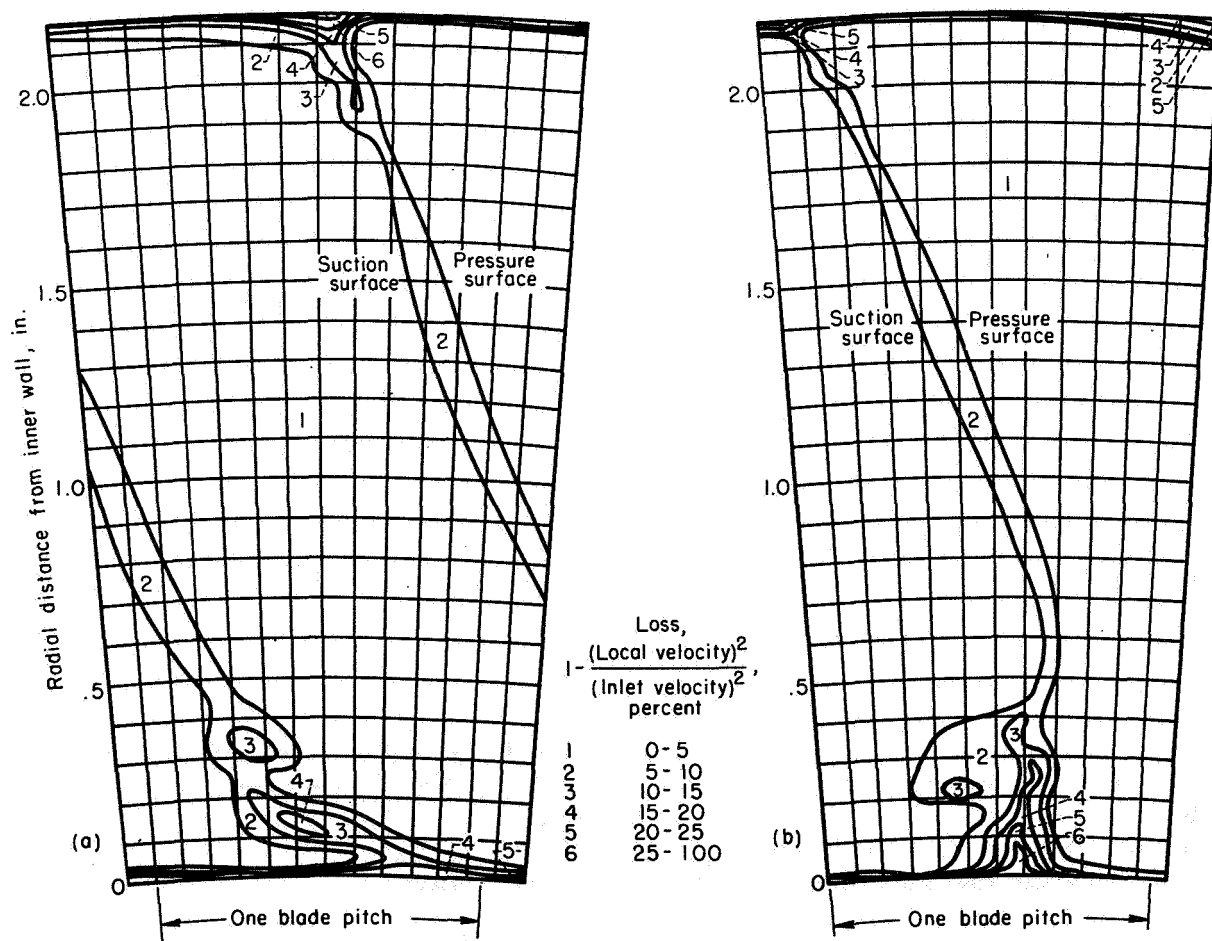
(a) Subsonic flow condition (lower Mach number).   (b) Supersonic flow condition (higher Mach number).

FIGURE 284.—Contours of kinetic-energy loss at exit measuring station of vortex blades (ref. 311).

lation is much larger than the outer-shroud loss accumulation for both the subsonic and supersonic flow conditions, despite the fact that the "wetted" area is greater in the outer half of the passages. This fact indicates radial flow of boundary-layer material. The decrease in outer-shroud loss core and the increase in inner-shroud core with increasing Mach number indicate the development of additional or larger paths for radial transport of low-energy fluid at the higher flow Mach number.

Visual indications of radial flows.—In the presence of a radial pressure gradient in the annular cascade, the radial transport of sizable quantities of low-energy material can be expected in blade boundary-layer regions having low viscous shear forces along the blade span. Such a path, for example, might be provided by the blade trailing-edge regions. Another possible radial pathway might be provided on the suction surface of each blade at supersonic flow conditions when a shock exists across the passage to cause thickening of the blade suction-surface boundary layer.

One method used to detect such paths was to apply narrow bands of paint on the suction surfaces of certain blades in the cascade. The paint traces found after a test then indicated paths along which low-energy material might be transported radially. Such traces are shown in figure 285. For this photograph, bands were painted on the suction surfaces of blades 1, 2, and 3 at the inner-shroud, midspan, and outer-shroud radial positions, respectively. Two such paths are shown in the figure, one at about midchord on the suction surface and the other along the blade trailing edge.

· **Evaluation of radial components of secondary flow.**—The existence of radial flow of low-energy material as indicated in the previous section was proved and the quantity of such flows at the supersonic flow condition was evaluated by the following rather simple device (ref. 311). Flow fences were fastened to the blades at the midspan position as in figure 286. The full flow fence (fig. 286(a)) was intended to interrupt radial flows both along the trailing edge and in the thickened boundary-layer region indicated in figure 285. The reduced flow fence (fig. 286(b)) was modified by being cut back so that it now affected only the trailing-edge radial flows. The results are presented in figure 287. Because of
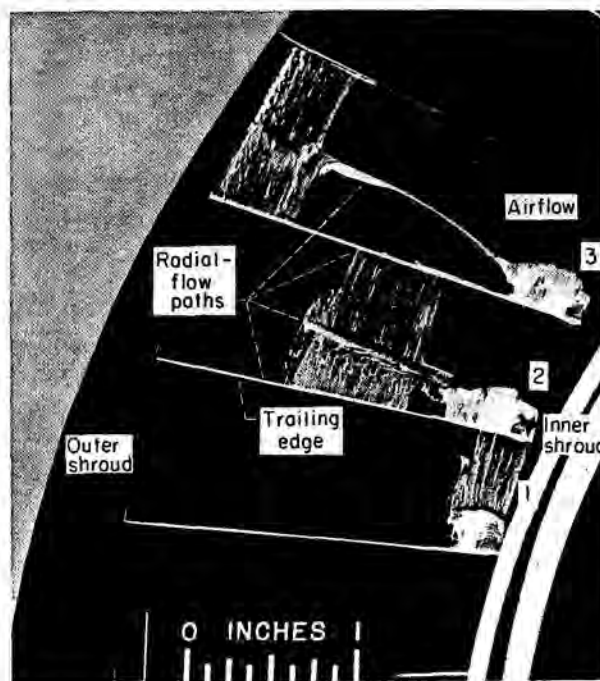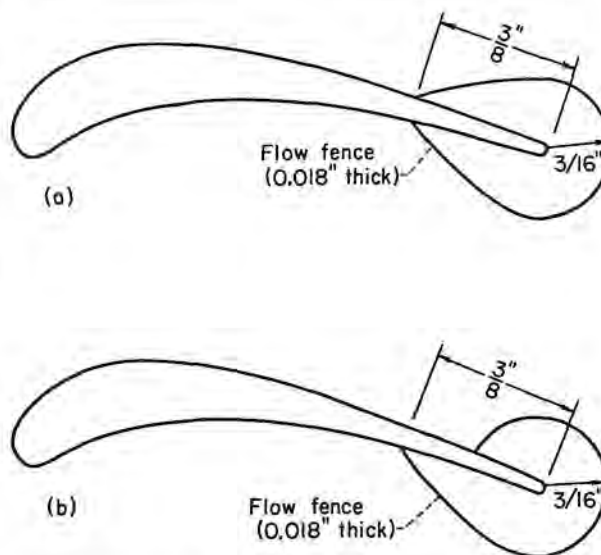

FIGURE 285.—Paint traces showing location of shock and radial flow in thickened boundary regions on suction surfaces of vortex blades (ref. 311).

(a) Flow fence to interrupt radial flow along blade trailing edge and in thickened boundary-layer region.

(b) Modified flow fence to interrupt radial flow along blade trailing edge only.

FIGURE 286.—Sketches of flow fences located on blades at midspan position (ref. 311).

(a) Full flow fence interrupts radial flow along trailing edge and along suction surface.

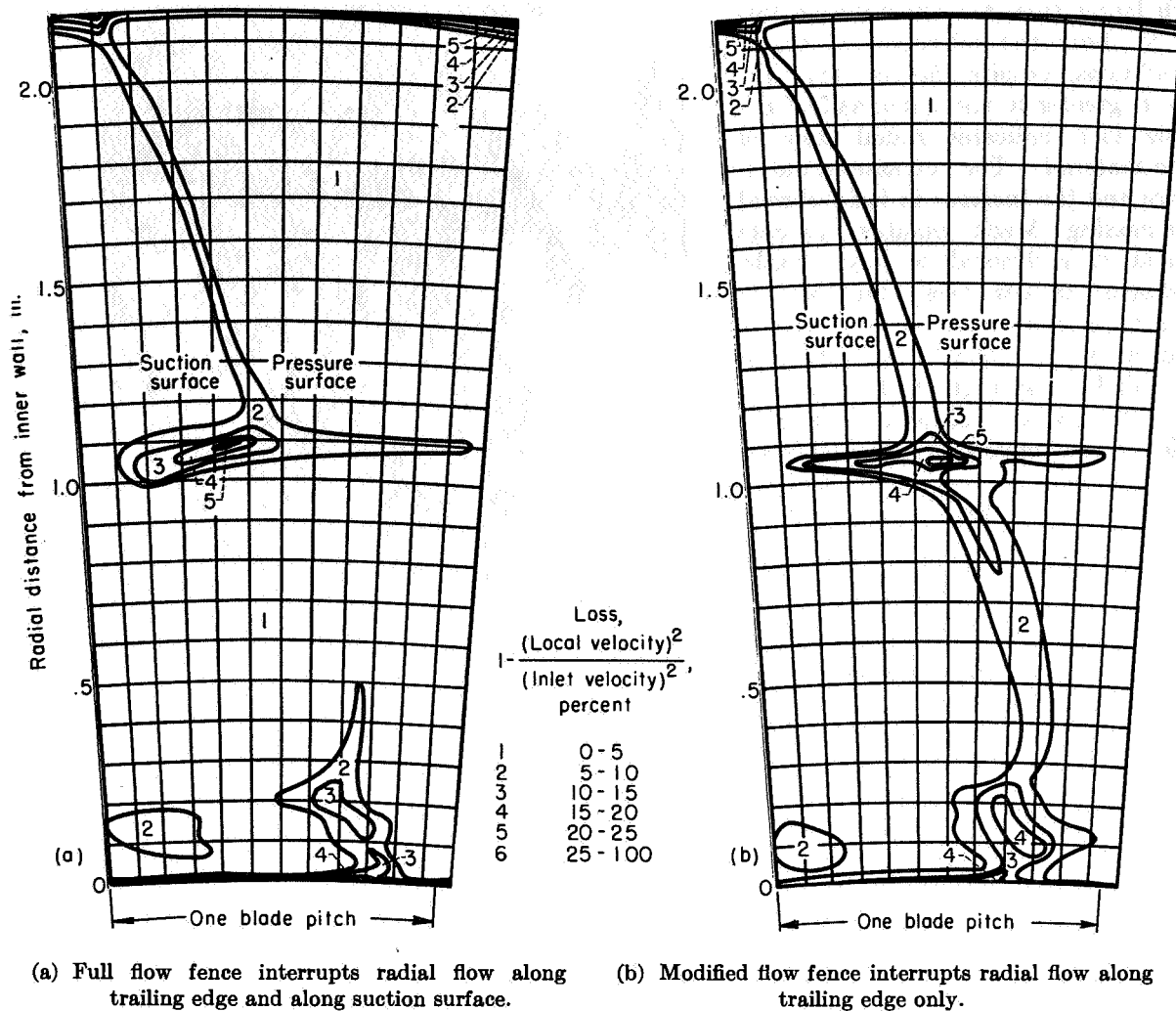(b) Modified flow fence interrupts radial flow along trailing edge only.

FIGURE 287.—Contours of kinetic-energy loss at exit of vortex blades, showing results of radial-flow fences. Higher Mach number (ref. 311).

possible losses due to the fences themselves, the reduction in inner-shroud loss core is used to measure the quantities of radial transport. At the supersonic flow condition for this set of vortex blades, radial transport of boundary layer accounted for 65 percent of the low-energy material in the inner-shroud loss core at the blade-exit station. Of this 65 percent, 35 percent came through along the trailing edge, and 30 percent through the thickened boundary-layer paths on the suction surfaces. Thus, radial transport of boundary-layer material may be considerable under certain conditions.

Loss accumulations and passage vortices.— Briefly, measurements downstream of a cascade of vortex blades at a high subsonic flow Mach num-

ber (fig. 284(b)) indicate the presence at the measuring plane of (1) a large accumulation of boundary-layer material near the hub corner, (2) a much smaller accumulation near the outer shroud, and (3) a well-defined wake between. The interpretation (ref. 311) is straightforward. Radially inward flow of boundary-layer material originating either on the outer shroud both upstream and within the cascade or on the blades themselves must, of necessity, take place somewhere upstream of the measuring plane. Most likely, radial-flow regions are on the suction surfaces of the blades and behind the trailing edges. At higher flow Mach numbers, the measured outer-shroud losses decrease further, the wake between remains nearly unchanged, and the inner-

shroud loss core increases further. There being little reason to assume smaller outer-shroud losses at the higher Mach numbers, it is concluded that increased radial flows must occur at the higher Mach numbers for these vortex blades. Judging from the relative sizes of the inner- and outer-shroud loss cores and the total absolute values of the losses, the radial-flow mechanism must serve to transport sizable quantities of boundary-layer material. The flow-fence tests on the vortex blades proved that this is the case and located the radial-flow paths behind the blade trailing edges and in a shock-thickened boundary-layer region along the blade suction surface.

The loss measurements at any position do not indicate the losses that actually develop at that radial position on the blade. Presumably, even in the radial-transport regions, through-flow components of the boundary-layer flow exist, and some of this material is shed and appears in the measured wakes at all radial postions. Since

there is no apparent increase in the measured wakes when the shock-thickened suction-surface radial-flow path is established, it might be speculated that little of the boundary-layer material from this radial-flow path is shed to contribute to the measured wakes.

For comparison with the preceding results obtained on vortex blades, tests were conducted on two sets of constant-discharge-angle blades at comparable flow conditions. For one set of these blades, designated set A, the measured results (fig. 288) indicate very closely the same kind of radial-flow mechanism as for the vortex blades for both the lower and higher flow Mach numbers. Thus, the differences in the circulation distribution of the vortex blades and the constant-discharge-angle blades are not potent factors affecting the over-all secondary-flow picture. There are no indications from measurements on either of these sets of blades that outer-shroud passage vortices are ever formed. For the other

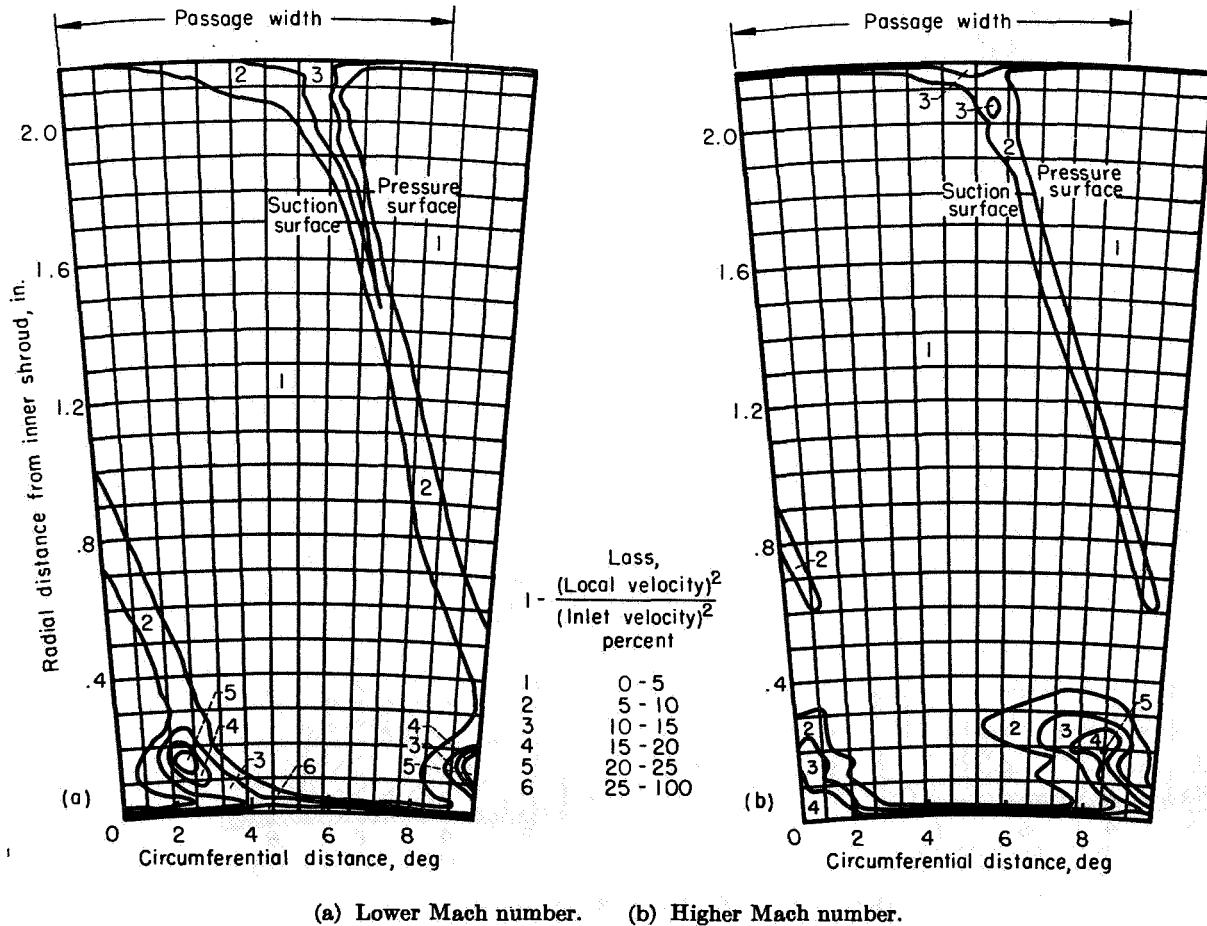(a) Lower Mach number.   (b) Higher Mach number.

FIGURE 288.—Contours of kinetic-energy loss at exit measuring station of constant-discharge-angle blades, set A (ref. 311).

set of constant-discharge-angle blades, designated set B, the measured loss distributions (fig. 289) appear quite different. At the lower flow Mach number in particular (fig. 289 (a)), the measured loss pattern near the outer shroud certainly implies the existence of a passage vortex. The different kind of loss pattern here requires further consideration to establish possible reasons for the differences.

The flow Mach numbers and inlet Reynolds numbers are the same for all three sets of blades. The over-all apparatus setup is the same. This means that the boundary-layer conditions at the inlets are the same, and measurements show that this is so (ref. 311). The main-flow turning is nearly the same for all three blades. As men-tioned, the circulation variation between the two types does not appear to be a significant factor.

One particular difference noted in reference 311, however, is that at the tip section there were definite peaks in the blade suction-surface velocity profile for set B. The other vortex blades and set A had fairly smooth suction-surface velocity profiles at the tips. All three sets of blades had fairly smooth suction-surface velocity profiles at midspan and near the hub. According to boundary-layer theory, velocity peaks and subsequent decelerations on a blade suction surface lead to relatively thick and perhaps even to separated boundary layers on the blades downstream of these peaks. By comparison, smooth velocity profiles are more likely to lead to thinner blade boundary
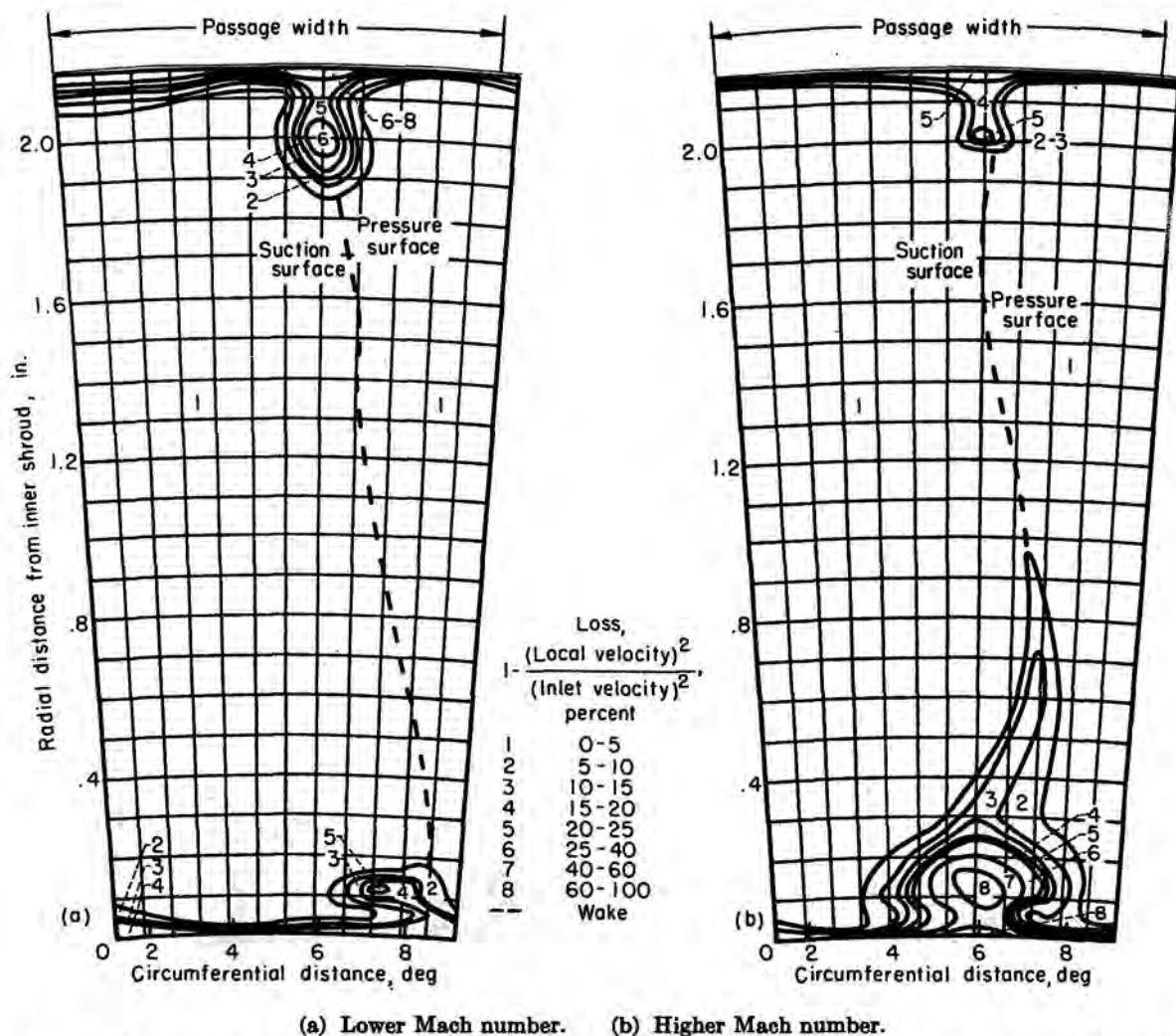

(a) Lower Mach number.　　(b) Higher Mach number.

FIGURE 289.—Contours of kinetic-energy loss at exit measuring station of constant-discharge-angle blades, set B (ref. 311).

layers. Smoke flow tests on the blades in question substantiated this predicted boundary-layer behavior, albeit at low Mach numbers.

Thus, it is a fair assumption that, all other things being equal, the boundary layer on the suction surface in the tip region for set B is likely to be thicker than for the other blades. On this account, reference 311 proposes that, when the cross-channel boundary-layer flow on the outer shroud encounters the relatively thicker blade boundary layer, rollup and passage vortex formation occur. The boundary-layer material on and near the annulus outer wall becomes entrained in this passage vortex. Judging from the size of the measured tip loss region, the passage vortex formation in this manner reduces the material available for secondary-flow radial transport. For the subsonic case (fig. 289(a)), the occurrence of this phenomenon could conceivably account for all the measured loss patterns observed: that is, (1) a large tip loss region, (2) a small hub loss region as compared with both the tip region of this blade and the hub regions of the other two blades (figs. 287(a) and 288(a)), and (3) smaller measured wakes between.

At the higher Mach number, once again the shock-thickened radial-flow path is formed, providing an additional path for boundary-layer removal to the inner-shroud region. This path is formed well up on the blade suction surface, nearer the point of passage vortex formation than is the blade trailing-edge region. This additional flow path may serve (ref. 311) to drain off some of the tip-region boundary-layer material before (or despite the fact that) it rolls up into the passage vortex. This criterion is somewhat borne out by the reduction in measured tip loss region at the higher flow Mach number and the great increase in measured hub loss region (fig. 289(b)). Again, if this criterion is correct, the radial flows through the thickened boundary-layer region on the blade suction surface appear to contribute little to the measured wake losses.

FLOW IN BLADE END REGIONS WITH CLEARANCE

In the blade passages of turbines and axial-flow compressors, large flow disturbances tend to occur in blade end regions. Furthermore, in passages having blade end clearance, the magnitude of the clearance has a direct influence on losses and flow behavior in the blade tip regions. In order to understand better the manner in which tip clear-

ance influences flow behavior, flow-visualization studies were made in two-dimensional cascades provided with tip clearance and in a two-dimensional cascade modified to provide relative motion between the blades and an end wall (ref. 318). This latter case was chosen to approximate more closely conditions that exist in an actual compressor or turbine.

Tip clearance.—The initial studies of blade tip-clearance regions were made in two-dimensional cascades having 0.060- and 0.014-inch tip clearances (1.7- and 0.4-percent span, respectively). These studies disclosed that flow along the blade pressure surface in the tip vicinity and in the wall boundary layer near the pressure surface deflected under the tip and formed a vortex lying against the suction surface (shown in fig. 290 for 0.060-in. clearance). Figure 291 shows that
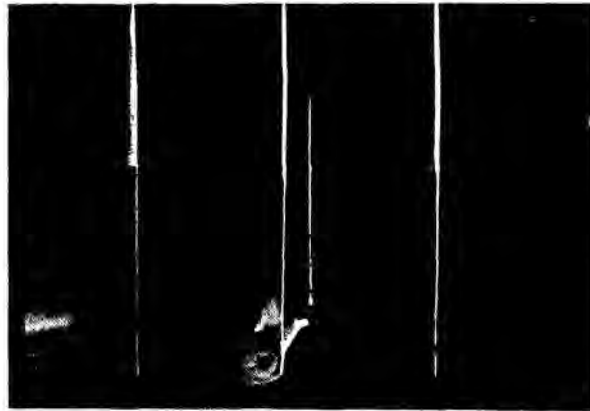

FIGURE 290.—Deflection of flow off pressure surface at blade end and through tip-clearance region to roll up as vortex near suction surface (ref. 318).

FIGURE 291.—Displacement of passage vortex by tip-clearance vortex (ref. 318).

the passage vortex previously described still exists; however, it has been displaced by the tip-clearance vortex. These two vortices rotate side by side in opposite directions with little apparent mixing. Furthermore, the formation of the tip-clearance vortex appeared to influence the magnitude of the passage vortex only to the extent that some of the flow on or near the blade pressure surface, which in the case of no tip clearance would have flowed into the passage vortex region, now becomes part of the tip-clearance vortex. Consequently, the formation of the two vortices, when tip clearance exists, constitutes a much larger flow disturbance in the blade end region than would exist with no clearance.

Relative motion between blades and wall.—In order to study flow in a blade end region when relative motion exists between the blades and an end wall, one of the end walls of a two-dimensional cascade was replaced by an endless moving belt (fig. 292), the direction and speed of which could be varied at will (see ref. 318). Smoke flow-visualization tests were conducted in this modified cascade for various wall speeds.

The test disclosed two interesting phenomena. The first was that a blade surface which was "leading" relative to the wall motion exerted a scraping effect on boundary layer entrained on the moving wall. One effect of this phenomenon was to impart a rolling motion to the boundary layer as it is piled up near the pressure surface (fig. 293).
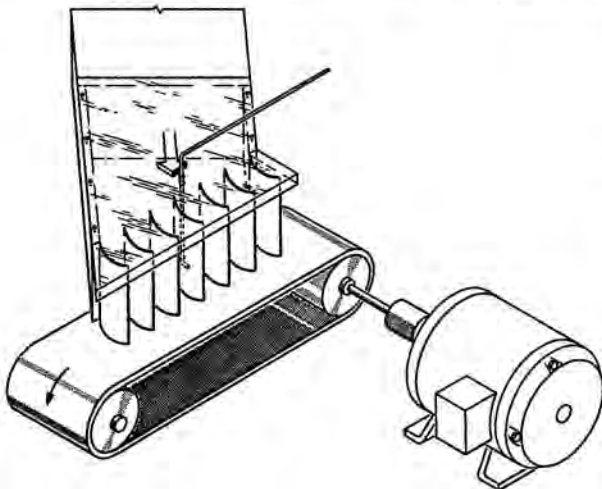

FIGURE 292.—Schematic diagram of apparatus used for studying tip-clearance effects with relative motion between wall and blades (ref. 318).


FIGURE 293.—Streamline pattern showing scraping effects at leading surfaces of blades with relative motion between blades and wall (ref. 318).

Another consequence of this scraping action in a compressor is that flow along the pressure surface that would normally have deflected under the blade tip with a stationary wall is deflected away from the wall when relative motion exists. This flow deflection is shown for a stationary wall in figure 294(a) and for a wall moving at moderate speed (approximately equal to airspeed) in figure 294(b). The second result of interest was that the motion of the wall exerted an "aspirating" effect on low-momentum air on the blade surface that was trailing relative to the wall motion and deflected this air toward the moving wall. Figure 295 depicts the significant increase in flow deflection toward the wall caused by aspiration on the suction surface.

For both the stationary and moving wall, smoke tests indicated that the flow over the blade surface at midspan showed no spanwise deflections on either the pressure or the suction surface. Therefore, if it is assumed that the midspan conditions have not changed much, the deflection off the pressure surface near the tip (fig. 294(a)) indicates the static pressure to be lower there than at midspan. Smoke tests on the blade suction surface showing a deflection of the blade tip surface flows toward midspan indicate an increased static pressure at the blade suction-surface tip region as compared with midspan. Thus, tip-clearance effects can result in a smaller pressure differential across the blade tip section

than at the midspan section—in effect, reduced blade tip loading. The scraping and aspirating effects of relative motion (figs. 294(b) and 295(b)),
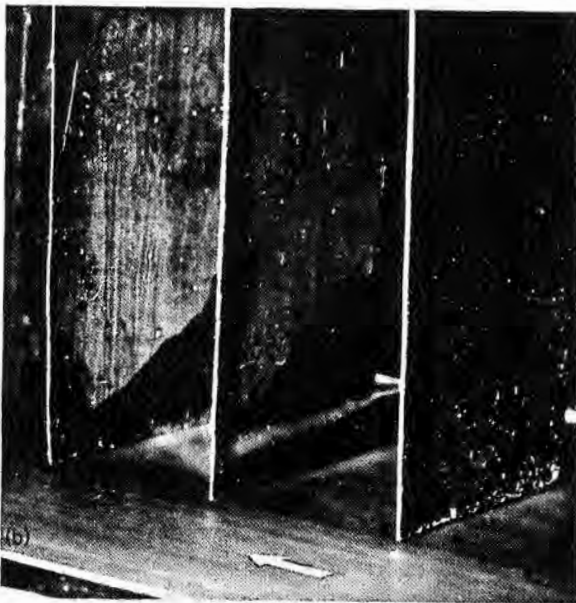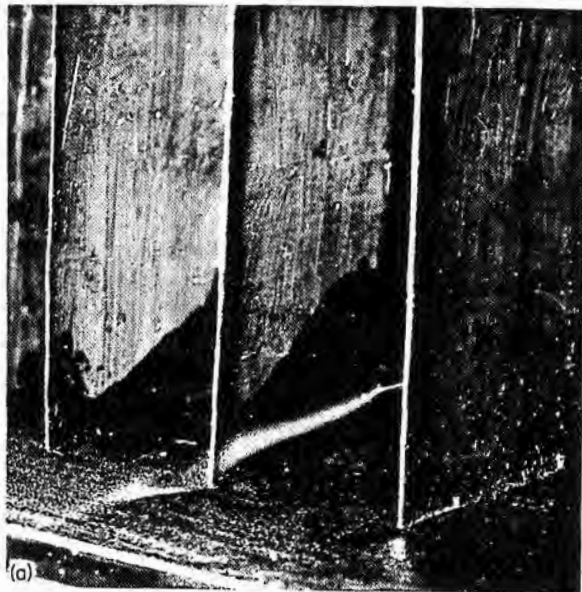
(a) Stationary wall.
(b) Moderate-speed wall.

FIGURE 294.—Effects of scraping action on streamline deflections on pressure surface of blade for "compressor configuration." Probe on nose of blade (ref. 318).
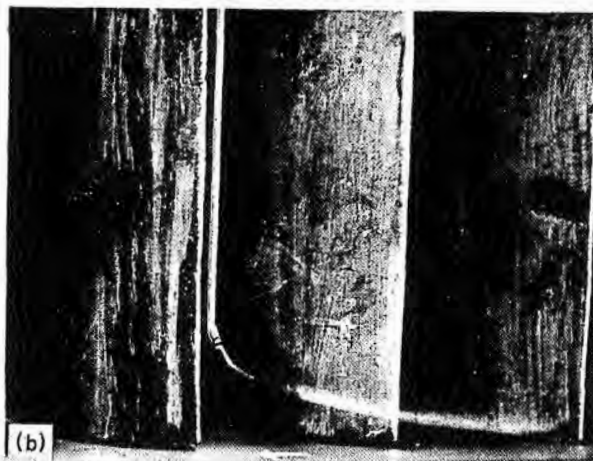

(a) Stationary wall.
(b) Moderate-speed wall.

FIGURE 295.—Aspirating effects on streamline deflections on suction surface of blades. Probe on nose of blade (ref. 318).

which show that these tip streamline deflections can be prevented or reversed, indicate that the relative-motion secondary-flow effects may even benefit a compressor by increasing the blade tip loading.

ROTOR-STATOR INTERACTION EFFECTS

The interference effects of a rotating blade row upon a stationary row upstream are shown by high-speed flash in figure 296. (While the blade rows depicted are more typical of a turbine configuration, the effects should be qualitatively the same for compressor blade rows.) Figure 296(a) shows that the pressure field associated

with the rotor blading at certain rotor positions causes thickening of the boundary layer on the suction surface and along the trailing edge of the upstream blades, and increased radial flow results. At the second rotor position (fig. 296(b)), this
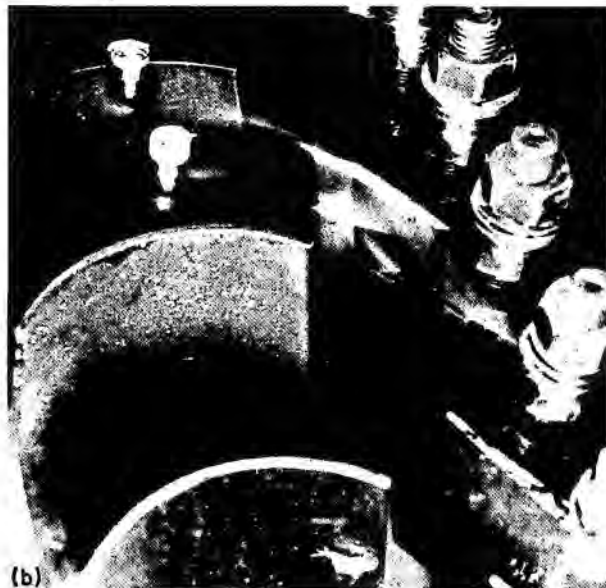
(a) First rotor position.
(b) Second rotor position.

FIGURE 296.—Effect of rotor blade position on radial flow (ref. 320).

thickening does not occur. Further tests indicate that these effects depend on the blade stagger angles, pressure distribution, rotor speed, and mainstream Mach number. The motion-picture supplement to reference 320 shows these effects very clearly, as well as blade boundary-layer development and shedding in annular-cascade configurations, radial boundary-layer flows, secondary-flow double-boundary-layer rollup, and others.

A MODEL OF SECONDARY FLOW IN COMPRESSOR BLADE ROWS

On the basis of the experimental results presented herein, it is possible to construct a model of secondary flow in compressor blade rows. However, two important factors are not accounted for in the experimental tests: (1) the effect of centrifugal forces on flow in a rotor, and (2) the effect of upstream stages on flow in either stators or rotors. Therefore, before such a secondary-flow model can be assumed realistic, further knowledge of these factors is required.

Insight into the influence of both of these factors can be obtained from tests conducted on a multistage compressor (ref. 247). The results presented give indications of outward radial flow of boundary-layer material in rotor blade passages and subsequent accumulation of this material in the blade tip region. In stators, inward radial flow is indicated. As boundary-layer air flows through the various stages, the comparatively large secondary-flow displacements produce a mixing of this boundary-layer air with the main stream. This mixing action prevents continuous boundary-layer buildup on flow surfaces and tends to make the mainstream velocity more uniform. It also makes possible more direct application of the secondary-flow studies in cascades to flow analyses of multistage compressors. If continuous boundary-layer growth took place on compressor annulus walls, a situation would occur in which flow conditions would be significantly different from those occurring in the cascade studies. Theories of compressor flow behavior based on cascade studies would then be of doubtful validity even in a qualitative sense.

The aforementioned factors, along with the experimental results previously presented, are used to predict the probable secondary-flow patterns in the various types of blade rows of axial-flow compressors.

Flow in shrouded stators.—Pressure gradients in inlet guide vanes or in a shrouded stator transport wall boundary layers toward the suction-surface side of blade passages and transport blade surface boundary layer and boundary layer that accumulates near blade tips radially inward. Radial transport of boundary layer takes place in regions where viscous shear forces are low; for example, in blade wakes. The paths by which the secondary-flow mechanism transports boundary layer are indicated in figure 297.
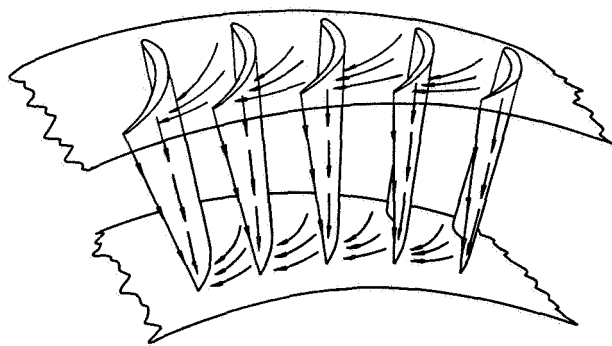

FIGURE 297.—Schematic sketch of secondary-flow paths in annular-nozzle cascade (ref. 311).

Boundary layer that accumulates near a blade suction surface at the hub generally rolls up into a pair of flow vortices rotating side by side in opposite directions. In physical extent, this vortex pair is dominated by the passage vortex. On the outer annulus walls, vortices may or may not form. As indicated by these experiments, a vortex is likely to form if the boundary layer on the suction surface is either separated or relatively thick—a condition associated with "poor" suction-surface velocity profiles. If suction-surface boundary layers are thin and unseparated, cross-channel boundary layers tend to flow radially inward in the wake region rather than to roll up at the blade tip.

Because of the pressure rise through a given stage, there may be flow leakage around a shroud ring causing local disturbances at the inlet to a stage. This would tend to qualify to some degree the secondary-flow model presented.

Flow in unshrouded stators.—In unshrouded stator passages, two secondary-flow components exist in addition to those noted previously: (1)

tip-clearance flow through the gap between the blade ends and the hub, and (2) flow caused by the relative motion between the blades and the rotating hub. The effect of this relative motion appears to be aspiration of boundary-layer material from the blade suction surface with attendant transport of this boundary-layer air in the direction of the rotating hub. As these two flow components oppose the motion of cross-channel secondary-flow components, the resultant flow pattern is a function of the respective magnitudes of the various components. As such, the resultant flow depends upon such factors as the size of the blade end-clearance space, blade end loading, magnitude of cross-channel pressure gradient, boundary-layer accumulation on blade surfaces, and speed of the rotor relative to the blades. Because of the motion of the hub, accumulations of boundary-layer material that would occur near a blade suction surface for a stationary hub will now occur nearer the pressure-surface side of a passage. As indicated in the tests of the two-dimensional cascade with a moving wall, boundary-layer material may be swept completely across a blade passage and roll up against the pressure-surface side.

Flow in rotors.—Experimental information concerning secondary flow in rotors indicates that radially outward flow of boundary-layer material will probably take place because of the predominance of centrifugal-force effects over radial pressure gradients. At present, details of flow behavior in the blade tip region must be inferred from knowledge of secondary flows in other types of configurations. On this basis, it is highly probable that flow behavior in the tip regions should not differ markedly from the behavior predicted in the hub region of unshrouded stators.

THEORETICAL INVESTIGATION OF SECONDARY FLOWS

The limitations inherent in the types of experimental analysis of secondary flows considered leave several important problems to be investigated. One of these problems is quantitative prediction of variations in thermodynamic properties of the fluid that result from the development of secondary flows. Another problem is the establishment of the physical basis or underlying causes for certain observed phenomena (e.g., vortex rollup near a blade suction surface). Problems of this nature are perhaps best attacked by means of theoretical investigations.

To date, theoretical research on secondary flows has been limited because of mathematical complexities. However, certain special aspects of secondary-flow behavior have been treated analytically by use of simplified theories. A fair amount of progress, for example, has been made on the calculation of boundary-layer crossflows and on the calculation of vorticity components associated with secondary flows in two-dimensional cascades and channels. While much of the work has been restricted in scope, important groundwork has been provided for more extended investigations.

In the following sections a review of representative analyses from the body of current theoretical research is presented and discussed. It is the purpose of this review to provide insight into methods of analytically attacking secondary-flow problems, to illustrate the nature of the mathematical theory involved, to indicate application of solutions to specific problems, and to point out possible bases for further research.

As will be noted, the analyses discussed are categorized on the basis of assumptions made in current secondary-flow theory regarding the nature of the fluid analyzed. The two major categories are (1) nonviscous-flow analysis and (2) boundary-layer-flow analysis. The analyses are discussed in this way because particular analyses in one of these categories are necessarily restricted to the consideration of specific types of physical flow phenomena. As a consequence, only certain special aspects of secondary flows observed experimentally can be treated within the framework of the theory. A division of the discussion into "analysis types" is therefore equivalent, in a sense, to a division into specific types of problems having certain common characteristics.

DISCUSSION OF METHODS

With only minor exceptions, the theoretical research on secondary flows has been concerned with steady, incompressible flows. Such flows are described in their most general form by the Navier-Stokes equations along with the equation of continuity. This system of four equations in rectangular coordinates is as follows:

$$u\frac{\partial u}{\partial x}+v\frac{\partial u}{\partial y}+w\frac{\partial u}{\partial z}=-\frac{1}{\rho}\frac{\partial p}{\partial x}+\nu\left(\frac{\partial^2 u}{\partial x^2}+\frac{\partial^2 u}{\partial y^2}+\frac{\partial^2 u}{\partial z^2}\right)$$

(387a)

$$u\frac{\partial v}{\partial x}+v\frac{\partial v}{\partial y}+w\frac{\partial v}{\partial z}=-\frac{1}{\rho}\frac{\partial p}{\partial y}+\nu\left(\frac{\partial^2 v}{\partial x^2}+\frac{\partial^2 v}{\partial y^2}+\frac{\partial^2 v}{\partial z^2}\right)$$

(387b)

$$u\frac{\partial w}{\partial x}+v\frac{\partial w}{\partial y}+w\frac{\partial w}{\partial z}=-\frac{1}{\rho}\frac{\partial p}{\partial z}+\nu\left(\frac{\partial^2 w}{\partial x^2}+\frac{\partial^2 w}{\partial y^2}+\frac{\partial^2 w}{\partial z^2}\right)$$

(387c)

$$\frac{\partial u}{\partial x}+\frac{\partial v}{\partial y}+\frac{\partial w}{\partial z}=0$$

(388)

where u, v, and w are components in the x, y, and z directions, ρ is the density, p the static pressure, and ν the kinematic viscosity.

Solutions to the complete set of equations are almost impossible to obtain for boundary conditions of the type usually occurring in aerodynamic problems. In general, it is necessary to make such simplifying assumptions concerning the nature of the flow problems that the corresponding simplifications in the equations make them mathematically tractable. Two typical simplifying assumptions occurring in secondary-flow research are now considered.

One of the ways to simplify the Navier-Stokes equations greatly is to assume a nonviscous flow, that is, $\nu=0$. Although secondary flows are almost always a result of viscous action in a fluid, the assumption of nonviscous fluid flow is considered reasonable in certain instances. One of the most common is the case where the flow paths under consideration are not large in extent (e.g., flow in cascade passage) and where viscous shear forces are not likely to be high. The flow crossing the boundary of this region is considered to have a velocity gradient, and hence vorticity, by virtue of viscous action upstream of the boundary. Within the region, however, the basic assumption is that the effects of viscosity over the short flow path are negligible compared with effects of the vorticity associated with the flow.

It should be noted at this point that, with the assumption $\nu=0$, the flow equations are reduced to first-order equations and it is no longer possible to satisfy the two boundary conditions for a real flow, that is, that the normal and tangential components of the flow at a surface be zero. The single boundary condition specified is that the flow normal to the surface is zero and hence the condition of "no-slip" at the surface is not assured. In actual application of nonviscous-flow analyses, this defect is generally of secondary importance.

In flow problems where viscous shear forces near bounding surfaces are likely to be high, it is desirable to retain the friction terms ($\nu \neq 0$) in the Navier-Stokes equations. One of the ways in which this is done, while still simplifying the general form of the equations, is by use of boundary-layer theory. The principal physical assumption made here is that the effects of viscosity are predominant only in a very thin region (the boundary layer) in the neighborhood of the fluid boundaries, while the rest of the flow is regarded as frictionless. Furthermore, the pressures associated with the frictionless region of the flow are assumed known and are superimposed on the boundary-layer flow. Mathematically, the governing equations for the boundary layer can be obtained in several ways, with the various derivations stressing either intuitive physical considerations or rigorous mathematical theory. [See ref. 152 (vol. I, ch. 4) for the physical approach, and ref. 321 (ch. 18) for the mathematical approach.] To illustrate the simplifications in the Navier-Stokes equations that result from boundary-layer hypotheses, the boundary-layer equations for flow on a nonrotating, flat (or slightly curved) surface are given:

$$u\frac{\partial u}{\partial x}+v\frac{\partial u}{\partial y}+w\frac{\partial u}{\partial z}=\nu\frac{\partial^2 u}{\partial y^2}+U\frac{\partial U}{\partial x}+V\frac{\partial U}{\partial y}+W\frac{\partial U}{\partial z}$$

$$(389a)$$

$$u\frac{\partial w}{\partial x}+v\frac{\partial w}{\partial y}+w\frac{\partial w}{\partial z}=\nu\frac{\partial^2 w}{\partial y^2}+U\frac{\partial W}{\partial x}+V\frac{\partial W}{\partial y}+W\frac{\partial W}{\partial z}$$

$$(389b)$$

where x, y, and z are rectangular coordinates with x and z parallel to the bounding surface and y normal to the surface; u, v, and w are boundary-layer velocity components in the x, y, and z directions, respectively; and U, V, and W are the velocity components of the nonviscous region of the flow in the x, y, and z directions, respectively. These velocity components of the nonviscous region are assumed known. The third equation necessary for solution (the continuity equation) has the same form as equation (388).

Although equations (389) indicate that the Navier-Stokes equations have been greatly simplified, solutions for the system of equations (388) and (389) are difficult to obtain for even relatively simple three-dimensional configurations. In fact,

almost all existing analyses require the application of numerical methods to obtain solutions.

The boundary-layer approach to secondary-flow behavior should be satisfactory for flow problems where frictional effects or energy gradients are confined to the neighborhood of the fluid boundaries and flow separation does not exist.

It might be noted that a few investigations of secondary flows have dealt directly with the Navier-Stokes equations without assuming any special properties for the flow. This approach is practical only if the aerodynamic configuration is simple in form. At the present time, analyses of completely viscous flow that might have had significance for secondary-flow research in turbomachines have been confined to the study of flows in pipes and channels (refs. 322 to 325). Unfortunately, the solutions presented in these references have been achieved only for very low Reynolds numbers and for the case of fully developed flow; that is, flow in which the effects of the centrifugal forces acting on the energy particles and the effects of viscous dissipation in the fluid are in balance. In turbomachine blade rows, this condition of equilibrium is generally not achieved, and hence the secondary flow is a function of the turning. Although theoretical studies of viscous flows of this type are of great interest in their own right, further discussion of these studies will not be undertaken in the present chapter.

NONVISCOUS-SECONDARY-FLOW THEORY

The study of secondary flows through application of incompressible nonviscous-flow theory has been principally restricted to investigations of flows in pipes or rectangular channels such as formed by airfoils in cascades. The fairly large number of reports dealing with this topic make a complete review of the theoretical literature prohibitive. Consequently, the review is restricted to four reports (refs. 326 to 329) that are closely associated with flow through cascades and that incorporate basic notions common to most nonviscous-flow analyses.

Flows in channels and two-dimensional cascades.—Two reports (refs. 326 and 327) have become classical references in nonviscous-secondary-flow research. Both papers consider, in general, secondary flow in a guiding passage (pipe, channel, blade row, etc.) that results from a nonuniform total-pressure distribution upstream of

the passage inlet. Mathematically, the analyses are based upon three governing equations for flow of a steady, incompressible, inviscid fluid. These equations are the equation of motion,

$$curl(V \times \Omega) = 0 \qquad (390)$$

the conservation of vorticity,

$$div \ \Omega = 0 \qquad (391)$$

and the continuity equation,

$$div \ V = 0 \qquad (392)$$

where V and Ω are, respectively, the velocity and vorticity vectors of the flow.

From equations (390) to (392), reference 326 derives an expression for the vorticity component in the through-flow direction downstream of a two-dimensional cascade. When the magnitude of this vorticity component is known, obtaining an approximation to the secondary-flow velocities is then possible. This derivation is based upon a perturbation analysis that considers the two-dimensional potential flow through the cascade as a first approximation to the actual flow. Consequently, the applicability of the analysis is restricted to a class of flows for which the perturbation assumptions are reasonable.

The expression for the vorticity component in the through-flow direction was actually evaluated for flow in a circular-arc channel in which the basic flow was given as that of a free vortex. Before the calculations were completed, however, a further assumption was made that is physically equivalent to assuming the channel to be very narrow. This leads to the following expression for the vorticity component:

$$\xi_1 = -2\epsilon \frac{\partial U}{\partial z}$$

where

ξ_1 magnitude of vorticity component in through-flow direction at cascade exit ($\xi = 0$ at inlet)

ϵ total turning of channel

U inlet flow velocity

z distance measured normal to base of channel

From the expression for ξ_1, the secondary-flow velocity components were obtained and a plot of secondary-flow streamlines calculated (ref. 326). These theoretical results were compared with experimental data taken in a circular-arc turning
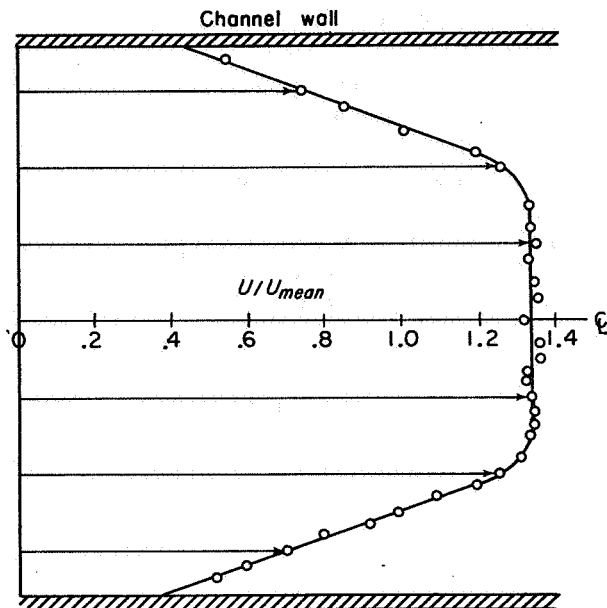

FIGURE 298.—Velocity variation at inlet to channel (ref. 326).

section. The flow in the experimental tests had an induced inlet velocity variation of the type required in the analysis—that is, small velocity gradient. For the velocity profile shown in figure 298, agreement between theory and experiment was fairly good.

Reference 327 differs from reference 326 in that the former analysis begins with equations (390) to (392) and develops a general expression for the change in "secondary circulation" along a streamline in a perfect, incompressible fluid. The secondary circulation is proportional to ξ/q, where ξ is the component of vorticity in the direction of fluid flow and q is the magnitude of the flow velocity vector.

The expression for the change in secondary circulation along a streamline is obtained from equations (390) to (392) by applying certain well known results from vector analysis and differential geometry. The final form of the expression is given by

$$\left(\frac{\xi}{q}\right)_2 - \left(\frac{\xi}{q}\right)_1 = -2\int_{s_1}^{s_2} \left| grad\left(\frac{p_0}{\rho}\right) \right| \frac{\sin \varphi}{R} \frac{ds}{q^2} \qquad (393)$$

where

s streamline arc length

p_0 total pressure

ρ density

φ angle between direction of principal normal to streamline and normal to Bernoulli surface (surface of constant total pressure) on which streamline lies

R radius of curvature of streamline

and the subscripts 1 and 2 indicate arbitrary points on the streamline. It follows at once that, if $\varphi=0(R\neq0)$, then $(\xi/q)_2=(\xi/q)_1$; that is, there is no change in secondary circulation along the streamline. Furthermore, from differential-geometric considerations, $1/R_g=\sin\varphi/R$, where $1/R_g$ is the geodesic curvature of the streamline on the Bernoulli surface. Therefore, $\varphi=0(R\neq0)$ implies that $1/R_g=0$. Reference 327 summarizes these results by stating, "Hence streamlines along which the secondary circulation remains unchanged are geodesics on the Bernoulli surface."

It is pointed out that the simplest examples to which the general theory may be applied are those in which the initial flow has a uniform static pressure and a velocity varying in one direction only. Such flows may exist in the boundary layer of a large straight duct or in an open channel whose width is large compared with its depth.

From a physical standpoint, when a stream enters a bend whose plane is parallel to the Bernoulli surfaces, a secondary circulation is created and the ensuing secondary flow will eventually distort the Bernoulli surfaces so that all semblance to the original velocity and total-pressure distribution may be lost. However, if the distortion of the Bernoulli surfaces is assumed small, $|grad\ (p_0/\rho)|$ and φ in equation (393) can be considered constant and a first-order solution obtained for the secondary circulation. As an illustration, the method (with these assumptions) is applied to the problem posed in reference 326. The resulting equation for change in the vorticity component in the through-flow direction is identical to that obtained in reference 326.

Even though nonviscous-flow analyses represent a simplified approach to secondary-flow problems, solutions of the governing equations still are difficult to obtain. A question always exists as to the meaningfulness of results obtained by introducing further simplifying assumptions in the flow model to obtain solutions. A partial answer to this question is found in reference 328,

which considers secondary flow in a 90° bend of rectangular cross section. The secondary flow is first calculated by means of a perturbation analysis and then compared with a "simplified solution." Theoretical results are finally compared with experimental data.

In carrying out the perturbation analysis in reference 328, the stagnation pressure is assumed to vary in a direction perpendicular to the plane of the bend, and the secondary-flow velocities are assumed small compared with the main-flow velocities. The basic flow is defined, as in reference 326, to be the flow in a free vortex. The perturbation velocities are then shown to be determinable from the solution of a Poisson equation. This solution is expressed as an infinite series involving Bessel functions. The series, however, converges slowly, and a great deal of calculation is required to obtain answers of reasonable accuracy.

The simplified analysis presented incorporates further assumptions than those made in the perturbation analysis, and the problem is finally made comparable to the one considered in reference 326. A particular solution to the problem is then calculated by assuming a linear variation in stagnation pressure at the entrance of a bend having the geometry of the author's test apparatus. The velocities obtained by the simplified method are compared with the more exact perturbation solution mentioned earlier, and the agreement is found to be good for this particular case.

The theoretical results are then compared with experimental results in a 90° bend (ref. 328). For a turning angle in the bend comparable to that found in compressor cascades, a comparison of the theoretical and experimental radial velocities falls within the limits of experimental accuracy. Therefore, for the types of nonviscous-flow analysis under consideration, the extra labor involved in improving the solutions to secondary flow in a channel by the more exact calculations would appear to be unwarranted so long as the secondary-flow velocities are assumed small.

A few attempts have been made to develop methods that are extensions of the type of analysis initiated in references 326 and 327 and that potentially are capable of yielding more exact solutions to secondary-flow problems. One such method is outlined in reference 329. In this report the secondary flow in channels and cascades of airfoils

is considered calculable by a successive-approximation technique. The flow is assumed to become asymptotically parallel and nonuniform at upstream infinity. A velocity field is postulated for the region to be investigated that has zero normal velocities on the flow boundaries and that assumes the given asymptotic values at upstream infinity. This velocity field is chosen to satisfy the continuity equation though not necessarily the momentum equations. From the prescribed velocities, a vortex field is calculated by means of the Cauchy vorticity equations. The vortex field is then integrated to give a new velocity field, and the process is repeated until discrepancies between successively calculated velocity fields are small.

Reference 329 points out, however, that the computational labor involved in the approximation scheme makes more than one step unlikely. A realistic choice of the initial velocity field is required, and usually enough is known about the desired solution to make this possible.

Evaluation and conclusions.—The various analyses discussed outline approximate methods for predicting secondary flows in channels and two-dimensional cascades. The principal restriction applying to these analyses is that they assume a variation in inlet velocity that extends well into the flow passage (see fig. 298). In most two-dimensional-cascade investigations, the variation is likely to be confined to a thin boundary layer. Tests in such cascades indicate a pronounced cross-channel flow and a concentration of vorticity near the suction-surface side of the passage. As would be expected, none of the examples worked out by nonviscous-flow methods predict such a phenomenon. There are indications, however, that this type of approach may be a first step in treating secondary flow in the final stages of a compressor where variations in velocity are of the type required and viscous effects on the primary flow pattern are of secondary importance. A complete analysis, of course, would have to include the effects of tip clearance and radial pressure gradients. It might also be possible to combine nonviscous-flow theory and boundary-layer theory in a manner that would allow for calculation of secondary flows in the inlet stages of a compressor.

Reference 327 is of particular interest, in that the equations derived are general in form. However, it should be noted that the formula for secondary circulation (eq. (393)) is not an explicit

relation for the change in secondary circulation. This follows from the fact that the velocity q is affected by ξ, and hence the integrand is in turn a function of ξ. Consequently, equation (393) is actually an integral equation for the secondary circulation or the vorticity component ξ. The cases where the formula for a change in secondary circulation can be readily simplified are those in which it is assumed that the Bernoulli surfaces remain flat. The formula then becomes

$$\left(\frac{\xi}{q}\right)_2-\left(\frac{\xi}{q}\right)_1=-2\left|grad\frac{p_0}{\rho}\right|\int_{s_1}^{s_2}\frac{ds}{q^2R}$$

Experimental studies have shown, however, that this assumption (without further modifications) will be invalid for many problems of practical interest (see experimental section of the present chapter). This fact is recognized by the author of reference 327 in a discussion of flow in bent circular pipes. In this case, simplification was achieved by considering only the path of a particle of maximum total pressure near the outside wall of the pipe and assuming that the velocity and $|grad(p_0/\rho)|$ remain constant on a streamline.

References 328 and 329 emphasize the mathematical difficulties involved when more exact methods are used in calculating secondary flows by use of nonviscous-flow theory. However, the reports also indicate that the simplified solutions give fairly adequate results for the type of problem under consideration.

THREE-DIMENSIONAL BOUNDARY-LAYER FLOWS

One of the early theoretical papers on three-dimensional boundary layers is reference 330, which points out two effects in three-dimensional boundary-layer flows that are not present in the two-dimensional case. The first effect is the result of lateral expansion or convergence of streamlines in the "potential-flow region" that are parallel to the bounding wall. This convergence causes changes in boundary-layer thickness and profile shape. The second effect is the displacement of the boundary layer toward the concave side of the potential stream as a result of lateral curvature of that stream. This results in boundary-layer crossflows such as shown in figure 277. As indicated in reference 330, theoretical calculation of such flows entails difficulties not present in two-dimensional boundary-layer studies.

The theoretical investigation of secondary flows in blade passages through application of boundary-layer theory has, in the past, been restricted in scope. Almost all analyses bearing on compressor secondary-flow problems have been confined to the study of boundary-layer cross-flows of the type noted in the experimental section. Because of the assumptions generally made in classical boundary-layer theory, investigation of such phenomena as vortex rollup and tip-clearance flows is, of necessity, severely limited.

In the following sections, reports dealing with basic boundary-layer theory and the application of this theory to secondary-flow problems are discussed. Although reports that employ momentum-integral concepts play an important part in the study of boundary layers in turbomachines, this class of reports is excluded from the discussion. This restriction is made because momentum-integral methods require *a priori* assumptions concerning the character of the velocity profiles in the boundary layer, and at present some important questions remain as to how to make these assumptions realistically for three-dimensional flows (ref. 331). Consequently, reports that evolve basic concepts and determine fundamental flow characteristics are considered principally.

All the reports that give solutions to specific secondary-flow problems assume that the boundary layer under investigation is laminar, as a result of general inability to apply current mathematical techniques to the vastly more complicated problems of turbulent viscous-flow phenomena. However, as boundary layers in turbomachines are not likely to be laminar but rather turbulent, the question may arise as to the significance of laminar-flow studies in relation to turbomachines. In this regard, past experience indicates that the factors having an important influence on laminar-boundary-layer flow behavior are qualitatively the same for turbulent flow.

Investigations of three-dimensional boundary-layer equations.—Because of the complexity of the boundary-layer equations, it has been profitable to examine the nature of the equations without actually carrying out solutions of specific problems. Several reports, for example, give derivations of the boundary-layer equations in various curvilinear coordinate systems followed by detailed examination of the equations in these systems to determine their important character-

istics. Some of the basic reports of this type that can be considered ultimately applicable to secondary-flow analysis in turbomachines are summarized briefly.

The equations in reference 332 are derived for incompressible boundary-layer flow in a general orthogonal curvilinear coordinate system, and the influence of curvature of the main flow on boundary-layer behavior is discussed. Compressible boundary-layer equations in orthogonal curvilinear coordinates are developed in reference 333, along with the energy equation. The results of reference 333 are therefore more widely applicable than those of reference 332. Following the general development, the boundary-layer equations are derived for various special cases and the nature of the equations is discussed. The special cases include flow over a body of revolution, cylindrical flow, and conical flow. For treatment of more general cases, the equations are derived for an orthogonal coordinate system determined by the external flow streamlines, the orthogonal trajectories of those streamlines, and a line mutually perpendicular to the streamlines and their trajectories.

In the discussion of the boundary-layer equations in the system designated, reference 333 shows that, in the absence of a lateral body force, external stream curvature is needed to produce crossflow. Therefore, if the curvature is small and the flow unseparated, the crossflow velocity will probably be small. This then suggests that it might be possible to simplify the boundary equations by considering a "small-crossflow" approximation. In such an approximation, the terms of higher order than unity in the crossflow velocity or lateral derivatives would be neglected. This approximation is carried out, and it is shown that the equations for the flow velocity in the streamline direction (the "principal velocity") can be put into the precise form of the two-dimensional boundary-layer equations and independently solved. Once such a solution has been achieved, it is possible to solve for the crossflow component. Solving for this component, however, is difficult, and it is suggested that the boundary layer be considered as divided into two parts. One part would consist of the outer region of the boundary layer where viscous forces are not large. By setting the viscous terms in the governing equation equal to zero, a

"stripwise" solution for this region can be obtained along a given external streamline. The other part of the boundary layer, termed the "boundary sublayer" would consist of the region adjacent to the surface where viscous forces are large. By assuming that the principal velocity component is linear in this region, an approximate solution for the crossflow component can be obtained that is valid in the region close to the wall. This sublayer solution can then be joined to the solution obtained for the upper region of the boundary layer to give a result valid for the entire boundary layer.

The equations for steady, compressible three-dimensional boundary-layer flow in Cartesian coordinates and in an "implicit" orthogonal coordinate system applicable to flow over bodies of revolution and conical bodies are derived in reference 334. A discussion of the energy equation, along with a simplification of the energy equation for a Prandtl number of 1, is then presented. By introducing a vector potential, the number of dependent variables in the boundary-layer equation can be reduced by one. This is accomplished by properly defining the boundary-layer velocity components in terms of the components of the vector potential. The boundary-layer equations and the energy equation are then transformed to a system of equations including the components of the vector potential as dependent variables. In incompressible flows, these components are the only two dependent variables.

Various applications of the equations to specific types of problems are also discussed in reference 334. Among the conclusions reached are the following: (1) For flow with plane or axisymmetric boundary conditions, the three-dimensional equations reduce to two-dimensional form by Mangler's transformation; and (2) for flow over flat plates at zero angle of attack, when the leading edge is some arbitrary curve, the flow viewed in planes parallel to the stream and perpendicular to the plate is given by the plane Blasius solution.

The effect of angular rotation of the coordinate system on the boundary-layer equations is considered in references 335 and 336. The boundary-layer equations are obtained in reference 335 for a Cartesian coordinate system rotating with a constant angular velocity about a fixed axis in space. In this report the additional forces caused by rotation of the system and the influence of

blade rows in a turbomachine on the boundary layer are qualitatively discussed. In reference 336 the boundary-layer equations are derived for an orthogonal coordinate system rotating with a constant angular velocity. Both the laminar and the turbulent forms are given. These equations are then used to develop generalized momentum-integral equations.

Boundary-layer crossflow over flat plate with leading edge.—Initial research on boundary-layer crossflow on flat or slightly curved surfaces was principally concerned with calculations of two special types of boundary-layer flow over an infinite flat plate. The first was the result of rotating the plate about an axis normal to its surface in a uniform stream (ref. 169). The second was the result of imposing a flow having circular streamline (e.g., a free-vortex type flow) on the plate surface (ref. 337). In neither of these cases, however, is there any variation of boundary-layer properties with mainstream turning, nor is there any concept that allows boundary-layer development in the direction of the mainstream flow relative to the plate. The results obtained, therefore, do not directly apply to the type of crossflow observed in two-dimensional cascades and channels (fig. 277). As a first approximation to the latter type of secondary flow, several investigators have calculated boundary-layer crossflows over flat plates having a leading edge. In this type of problem, both the variation of the boundary layer with mainstream turning and the development of the boundary layer in the mainstream direction can be studied.

One of the early papers dealing with this problem is reference 338. This analysis considers laminar-boundary-layer development over a semi-infinite flat plate placed in a flow with concentric circular streamlines. Both incompressible flow and a compressible flow with Prandtl number of 1 are investigated. The method of solution for the incompressible case is similar to that employed in two-dimensional boundary-layer theory. The boundary-layer equations are first expressed in a curvilinear system of the type outlined in reference 336. A "similarity parameter" η is then defined; and, with suitable definitions for the boundary-layer velocity components in terms of unknown functions $F(\eta)$ and $G(\eta)$, the boundary-layer equations are simplified to two simultaneous total differential equations for F and G. However,

certain terms in these equations have as a coefficient the square of the total turning of the main flow from the plate leading edge. The analysis is then restricted to apply to the region of the flow where the total turning is small, and all terms containing the square of the total turning are discarded. This approximation simplifies greatly the equations for the unknown functions F and G, and solutions are obtained for the special case of a mainstream flow of the free-vortex type. The results show that the velocity component u in the direction of the main flow and the component w normal to the main flow direction and parallel to the plate surface can be expressed by

$$u = U_1 F'(\eta)$$

and

$$w = \theta U_1 G'(\eta)$$

where U_1 is the mainstream velocity and θ is the total turning of the flow.

Typical velocity profiles are shown in figure 299. The analysis of reference 338 also discloses that there is a limiting deflection of the boundary layer at the plate surface, which for the particular case discussed is a function of the total mainstream turning. Limiting deflection has also been noted in visualization studies of crossflows.

Further progress in the investigation of crossflow phenomena is made in references 339 and 340. Both analyses treat a flow over a flat plate which is of a type that makes possible the exact solution of the boundary-layer equations. Their solutions, therefore, are not subject to the restrictions inherent in reference 338 because of the assumption of small mainstream turning made in that reference. The special two-dimensional mainstream flow considered in references 339 and 340 is defined by

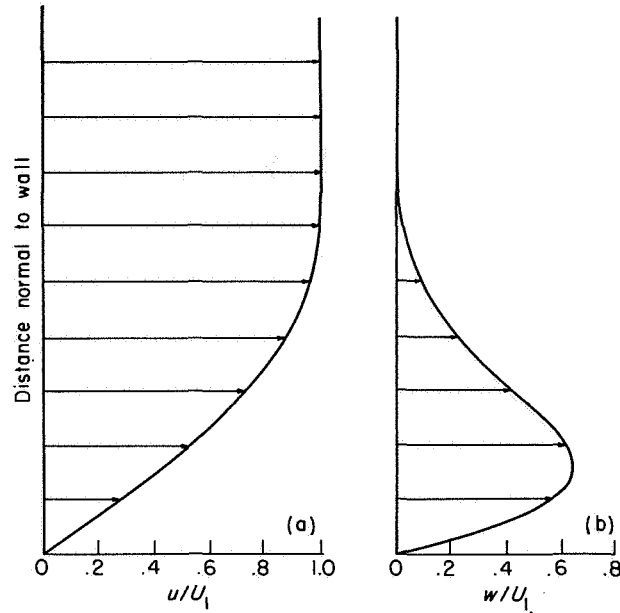$$U = \text{constant}$$

$$W = a + bx$$

where

U mainstream component normal to plate leading edge

W mainstream component parallel to leading edge

a, b constants

x distance from leading edge measured along plate surface

This rotational flow has streamlines that are parabolic in form. Furthermore, the entire streamline

(a) Mainstream direction.   (b) Cross-channel direction.

FIGURE 299.—Typical boundary-layer velocity profiles (ref. 338).

pattern can be obtained by simply translating a given streamline in a direction parallel to the plane leading edge (fig. 300).

The solutions of the boundary-layer equations in this problem are obtained in the usual way of defining a similarity variable and reducing the boundary-layer equations to ordinary differential equations. In both reference 169 and reference 340, solutions are obtained for the case where the mainstream flow has 0° inclination to a line perpendicular to the plate leading edge. Reference 339 also considers two other cases where the inclinations are 60° and −60°. The streamline patterns for these flows are obtained by merely shifting the parabolas in figure 300 to the left or to the right.

In the three cases discussed in reference 339, regions exist in the flow field for which the total pressure in the boundary layer exceeds that in the mainstream. The reason that particles in the boundary layer can have a larger total pressure than those in the mainstream follows the postulation of a total-pressure gradient for the main flow parallel to the leading edge of the plate. Consequently, boundary-layer streamlines (which curve more sharply than those in the main stream, fig. 300) may transport particles of high total
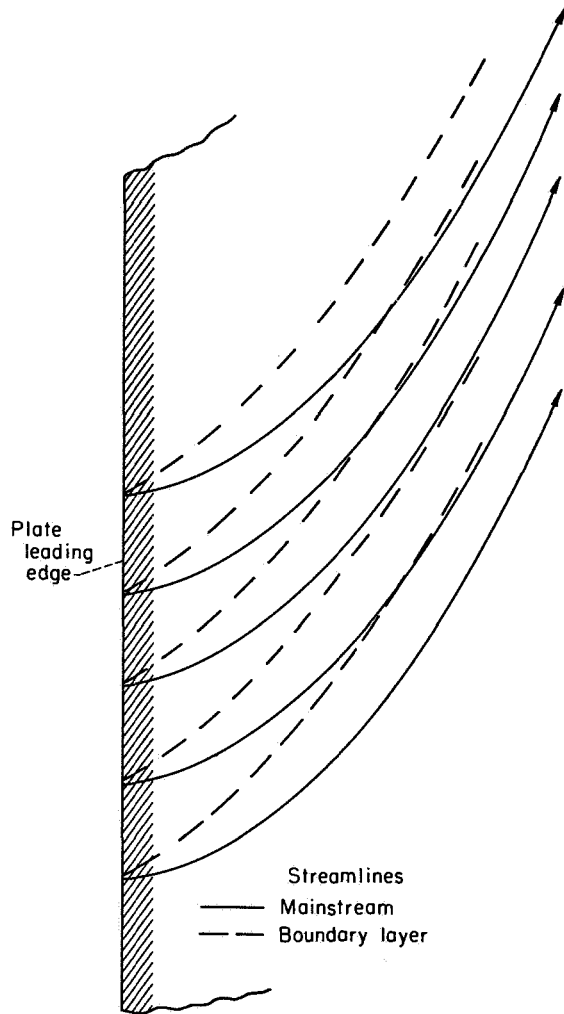
FIGURE 300.—Parabolic mainstream flow over flat plate with crossflow in boundary layer (refs. 339 and 340).

pressure underneath main-flow streamlines of lower total pressure.

Reference 339 also discusses the problem of "three-dimensional separation" (i.e., separation of the actual flow profile as distinguished from separation of a single velocity-component profile that may not indicate separation of the total flow) The reference shows that such three-dimensional separation does not occur, because the crossflow prevents separation (in the example presented) by transporting fluid with high energy to the "critical" regions.

In addition to the research mentioned, there is one other publication known to the authors that includes detailed treatment of crossflow over flat plates, namely, reference 331. In this report a group of problems for which the mainstream flow

has small curvature in the lateral direction are analyzed. The velocity components of the mainstream are characterized by

$$U = U_0 + U^*(x, z)$$

$$W = W^*(x, z)$$

where U is the velocity component in the direction normal to the leading edge of the plate (the x-direction), and W is the velocity component parallel to the leading edge of the plate (the z-direction, fig. 301). It is also assumed that

$$U_0 = \text{constant}$$

$$W^* << U_0$$

$$U^* << U_0$$

By a perturbation method, the velocity profiles of the crossflow in the x- and z-directions are calculated for a variety of incompressible mainstream flows for which U^* and W^* are expressible as

$$U^* = bx^m z^i$$

and

$$W^* = ax^n z^k$$

In this analysis, the boundary-layer velocities u, w, and v in the x-, z-, and y-directions, respectively, are then considered to be of the form

$$u = u_0 + u^*$$

$$w = w^*$$

$$v = v_0 + v^*$$

where u_0 and v_0 are the boundary-layer velocity components in the well-known Blasius solution for a uniform flow of velocity U_0 over a flat plate. The quantities u^*, w^*, and v^* are the perturbation velocities on this basic boundary-layer flow.

It can be seen that one of the flows considered in references 339 and 340 is a special case of the family of flows investigated here; for example, $U^* = 0$, $W^* = ax$. This special case is worked out with the use of the perturbation analysis; and, in this instance, the perturbation analysis is equivalent to the type of analysis employed in references 339 and 340.

By considering a range of values of the exponents m, i, n, and k, the effect of various flow patterns on velocity profiles and boundary-layer displace-
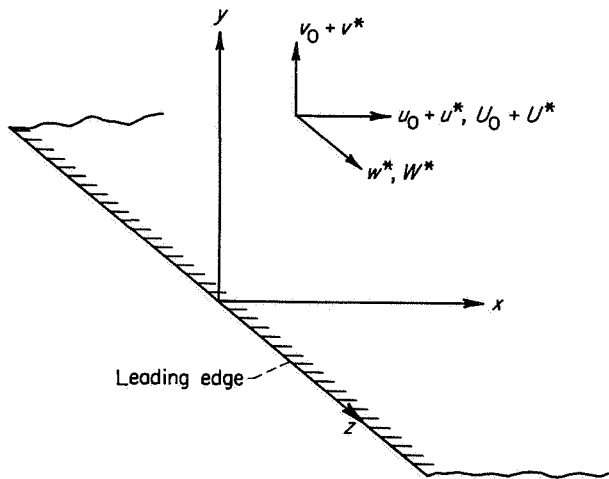
FIGURE 301.—Coordinate system for flow along semi-infinite flat plate (ref. 331).

ment thickness is investigated at some length. As in references 339 and 340, certain rotational flows give rise to boundary-layer velocities that exceed mainstream values. The effects of angular rotation of the coordinate system and compressibility on crossflow velocities are briefly analyzed. The results of the analysis of angular rotation are applied to flow on surfaces of compressor blades. It is concluded that, if the main flow deflects toward the blade tip near the suction-surface side and toward the hub near the pressure-surface side, then the effect of angular rotation is to increase the crossflow on the suction surface and decrease the crossflow on the pressure surface.

The effect of compressibility is discussed for the flow defined by $W^*=ax$ and $U^*=bx$. The conclusion reached is that compressibility has the over-all effect of increasing the boundary-layer perturbation velocities.

Flow over flat plate with thick boundary layer.— In the previous discussion of boundary-layer flow over a flat plate, the boundary layer developed from a definite leading edge and was immediately subjected to lateral pressure gradients that gave rise to secondary flows. For flow in turbomachine configurations, this is usually not the case. Generally, the boundary layer develops for a distance in the absence of lateral pressure gradients before secondary flows develop. This is true, for example, in flow through the inlet of a channel or cascade or along the casing of a compressor between blade rows. Reference 341 attempts to gain some insight into the effect of this boundary-

layer growth on secondary-flow behavior. The problem analyzed is that of a thick boundary-layer flow over a flat plate where the boundary layer is subjected to a sudden lateral perturbation caused either by a pressure gradient or a sudden movement of a part of the plate surface over which the flow develops.

The analysis presented is a small-crossflow perturbation analysis of the type employed in reference 331. In obtaining solutions for boundary-layer velocities, an approximate but rapid method of solution is employed. This method is based on the assumption that the flow can be considered to be composed of a nonviscous outer region and a viscous inner region adjacent to the wall. In view of this assumption, separate solutions are obtained for these two regions. These solutions are then joined at a distance from the wall that is determined from the analysis.

As most of the report is devoted to the development of methods, only two simple applications are given. In the first, a boundary layer flowing two-dimensionally from the leading edge of a plate encounters at some fixed distance from the edge a surface moving laterally with a constant velocity. At a given distance from the edge of the moving surface, the crossflow velocity is a function of the Blasius similarity variable η. Near the leading edge of the moving plate, these functions have a steep slope, which indicates rapid rise of velocity from the plate surface to the main stream. Farther downstream, they approach the well-known Blasius solution for flow over a flat plate with zero pressure gradient.

The second example given is the case of a thick boundary layer which, at a given reference line parallel to the leading edge, encounters a pressure field arising from a "parabolic" mainstream flow; for example, a flow having a lateral velocity component that varies as the nth power of the distance from the fixed reference line. Solutions are carried out for various values of these powers and for various distances from the reference line. Near the point where the pressure perturbation is first felt, the solutions indicate that the thick boundary layer develops greater crossflow velocities than in the case where the boundary develops from the leading edge. It is possible in this analysis to compare the solutions obtained for flow at a great distance from the reference line with the more exact solutions worked out in reference

331, for here the two theoretically must agree. Progressively better agreement results from taking larger values of the powers defining the mainstream lateral velocity.

Boundary-layer flow in corners.—One of the important problems mentioned earlier was that of analyzing secondary flows in the corner formed by the side of a channel or blade row and the end wall of the flow passage. As outlined in the experimental section of this report, a fair amount of information on boundary-layer behavior in corners has been obtained in visualization studies. Theoretically, however, the analysis of boundary-layer behavior in corner regions is still in a very preliminary stage of development.

Early analyses of flow in corner regions (e.g., refs. 342 and 343) are generally confined to special cases in which there is no pressure gradient in the main flow and the corner region is formed by the intersection of plane walls. Reference 331 considers flows over surfaces with very sharply varying lateral curvature (equivalent to a corner with a fillet). Perturbation assumptions of the type employed in the analysis of flow over a flat plate in the same reference are employed in this case. In particular, the mainstream velocity is considered to be the resultant of a constant "axial" velocity and superimposed perturbation velocities of very small magnitude in the axial and lateral directions.

The boundary-layer equations in reference 331 are solved numerically for two choices of mainstream flow in a corner having a hyperbolic cross section. For the first flow analyzed, the axial perturbation velocity is assumed zero and the lateral perturbation velocity is assumed constant. In the second case, the axial perturbation velocity is again assumed zero, but the lateral perturbation velocity is assumed to vary as the first power of the axial distance. Plots of velocity profiles and deflections of the crossflow from the mainstream direction are presented. The results indicate that, for the case of constant lateral perturbation velocity, the corner establishes a crosswise pressure gradient that causes boundary-layer air to flow from the upper part of the wall into the corner region. For the second example, the results indicate that the external flow possesses a crosswise pressure gradient before it reaches the corner and that this pressure gradient not only opposes the one established in the corner but

also causes a strong crossflow from the corner region up onto the side of the wall.

Evaluation and conclusions.—Application of boundary-layer theory to the analysis of secondary flow in turbomachines has the advantage of accounting for viscosity in the fluid and thereby allowing the computation of secondary flows that are principally the result of viscous action, for example, cross-channel flows. However, the application of the boundary-layer studies outlined in this chapter to compressor flows is severely limited. For example, the theories in general have assumed steady, incompressible, laminar-boundary-layer flow. In compressor blade rows, such flows will be primarily unsteady, compressible, and turbulent. (To date, of course, it has not been possible to give an adequate mathematical treatment of flows of this type.) Furthermore, the present state of boundary-layer theory does not allow the ready computation of flows in the presence of blade rows. Although some progress has been made in this direction (ref. 331), the computations of secondary flows arising from lateral pressure variations in the main stream are principally confined to flows over surfaces that are essentially flat.

In spite of these restrictions, several advantages can be gained from present boundary-layer analyses. As mentioned earlier, they can serve as the first step in a more comprehensive study of secondary flows and can possibly be combined with analyses treating other aspects of the flow. Secondly, they can be used in their present form to explain and interpret experimental findings in relatively simple flow configurations. (The "limiting crossflow" phenomenon found in both experimental and theoretical studies is an example.) Finally, calculations of velocity-profile shapes and basic parameters are useful in the application of more general theoretical treatments that presently exist (such as the momentum-integral methods). The determination of profile shapes, in fact, was one of the principal motivations for the analysis presented in reference 331.

CONCLUDING REMARKS

The survey of experimental and theoretical research on secondary flows and three-dimensional boundary-layer effects indicates in broad outline the present state of knowledge in this field. It is evident from the work discussed that, at best,

only an elementary understanding of the basic flow behavior has been achieved.

The experimental work indicates how such phenomena as flow disturbances caused by relative motion between blade ends and annulus walls, cross-channel and radial flows, and vortex formation in blade passages may occur in simple compressor configurations. In a multistage unit, however, the pattern of flow is greatly complicated by the interaction of these effects and the influence of other compressor phenomena (e.g., rotating stall) that have not been considered in conjunction with these studies. The experimental studies, therefore, are best used as a guide for interpreting experimental findings in multistage compressors and as a basis for constructing more comprehensive models of the actual flow behavior. With proper caution, however, the results can be used in their present form to guide certain design considerations.

In the past, for example, shrouding of blade rows has at times been advocated for the reduction of losses in blade end regions (ref. 344). The tests concerning relative motion between blade ends and annulus wall, however, indicate that smaller flow disturbances and better performance are likely to occur in unshrouded blade passages (with due regard for clearance, of course) than in shrouded passages.

Theoretical research on secondary flows and three-dimensional boundary-layer effects has been severely handicapped by the mathematical complexity associated with even the simplest types of problems. It is probably sufficient to hope that present theories can be used to predict "orders of magnitude" of various quantitative aspects of the flow and to provide a better physical understanding of the mechanisms that give rise to observable flow patterns.

CHAPTER XVI

EFFECTS OF DESIGN AND MEASUREMENT ERRORS ON COMPRESSOR PERFORMANCE

By Robert J. Jackson and Peggy L. Yohner

Effects of design errors on compressor performance parameters and of measurement errors on calculated values of performance parameters are analyzed. Formulas and charts are presented from which the changes in blade-element performance and calculated parameters due to the design and measurement errors can be determined.

The use of the design-error charts during the design calculations and in the analysis and interpretation of data is discussed. The charts can be used to evaluate the sensitivity of a given velocity diagram to design errors and to determine whether iterations of design calculations are warranted. To a limited extent, the uncertainty intervals in blade-element performance can be calculated from the charts.

The measurement-error charts can be employed along with the procedure devised at the Gas Turbine Laboratory of the Massachusetts Institute of Technology for the estimation of uncertainty intervals in calculated performance and can also be of assistance in the evaluation of data and in the planning of instrumentation for research or development.

INTRODUCTION

The attainment of design rotor pressure ratio for an axial-flow-compressor stage depends upon the correct prediction of blade-element turning angle and loss, upon an accurate design distribution radially of the local specific mass flow downstream of the rotor, and upon the agreement between the actual and design rotor-inlet flow distribution. Rotor blade-element design errors can result from the approximate nature of available design-data correlations, from blade manufacturing tolerances, and from the necessary simplifications in the design equations. Discrepancies between the actual and design rotor-inlet flow distribution can result from the foregoing types of design errors in preceding blade rows. (The design variables and their sources of error are identified and discussed in the section ANALYTICAL APPROACH.)

A means for estimating the error in a performance parameter due to an assumed error in a blade-element design variable or to an error in the inlet flow conditions is useful both to the compressor designer and to the research worker. Therefore, an analysis of this problem was made, the results of which are presented in this chapter. From the available equations relating blade-element performance parameters to the design variables, differential formulas were calculated that relate a small change in a design variable to the consequent change in the performance parameter. The formulas are presented in this chapter in the form of carpet plots, and the significant trends are discussed.

An analysis of this type may be expected to indicate the degree of design control required for a given velocity diagram as evidenced by its sensitivity to design errors. Among a group of suitable design velocity diagrams, the analysis may show that one diagram is relatively insensitive to design errors, thus indicating that it would be the best choice for the design. The charts can also be employed to determine, in certain cases, whether an iteration of the design calculations is warranted.

The interpretation of experimental data requires some consideration of measurement errors. This problem is particularly relevant to the work of the researcher and also to the compressor designer, since correlations of design variables are based on experimental data, and compressor development programs depend on the interpretation and application of experimental data. Differential formulas were calculated that give the error in a performance parameter caused by a measurement error in one of the flow properties. These formulas are presented in this chapter in the form of carpet plots. A method for combining the effects of several measurement errors is outlined.

413

Preceding page blank

SYMBOLS

The following symbols are used in this chapter:

a	speed of sound
D	diffusion factor
H	total or stagnation enthalpy
H_M	total enthalpy calculated from change of moment of momentum
h	static enthalpy
M	Mach number
P	total or stagnation pressure
p	static or stream pressure
R	gas constant
r	radius
T	total or stagnation temperature
U	rotor speed
V	air velocity
β	air angle, angle between air velocity and axial direction, deg
γ	ratio of specific heats
$\delta°$	deviation angle, angle between outlet-air direction and tangent to blade mean camber line at trailing edge, deg
η_{ad}	adiabatic efficiency
ρ	density
σ	solidity, ratio of chord to spacing
Ω	quantity $\dfrac{P'_{2,\,id}}{P'_2}-1$
$\bar{\omega}$	total-pressure-loss coefficient

Subscripts:

d	design value
h	hub
id	ideal
l	lower limit of uncertainty interval
sys	denotes systematic error
t	tip
u	upper limit of uncertainty interval
z	axial direction
0	station ahead of guide vanes or stators
1	station at rotor inlet or stator exit
2	station at rotor exit
$i \ldots viii$	denotes variable in error

Superscript:

$'$	indicates quantity relative to rotor

ANALYTICAL APPROACH

Consider a function of several variables $f(x_1, x_2, \ldots x_n)$. The change in f caused by a given set of small changes in $x_1, x_2, \ldots x_n$ is given approximately by the following formula (ref. 345, ch. IV):

$$\Delta f=\frac{\partial f}{\partial x_1}\Delta x_1+\frac{\partial f}{\partial x_2}\Delta x_2+\ldots+\frac{\partial f}{\partial x_n}\Delta x_n \quad (394)$$

The nth term of formula (394),

$$\Delta f_n=\frac{\partial f}{\partial x_n}\Delta x_n \quad (395)$$

can be directly calculated (for an assumed value of Δx_n) and plotted as a function of the parameters that fix the value of $\partial f/\partial x_n$. This procedure is used in the present chapter.

The degree of approximation of formula (395) depends upon the way f varies with x_n and upon the magnitude of Δx_n. The accuracy of the formulas presented in this chapter for reasonable magnitudes of design errors was spot-checked by means of sample calculations and plots. The results of these calculations are given in appendix A of this chapter. These checks do not constitute a general proof of the accuracy of the formulas, but do verify their applicability for certain conditions of flow and velocity diagram.

DESIGN ERRORS

A brief outline of the blade-element approach to single-stage-compressor design follows in order to clarify the application of formula (394) to the analysis of design errors.

For given design values of pressure ratio, mass flow, rotational speed, and tip diameter, the hub profile and the preliminary velocity diagrams are calculated by methods discussed in chapter VIII. These preliminary velocity diagrams determine approximate values of diffusion factor and other blade-loading and blade-configuration parameters. This information permits the estimation of the radial distribution of the relative total-pressure-loss coefficient $\bar{\omega}$ (or $\bar{\omega}'$) for each blade row as discussed in chapter VII. The velocity-diagram calculations (including the radial-equilibrium calculation) are then repeated in order to incorporate the effects of the loss estimation. Finally, the methods of chapter VII can be employed for the selection of blade-section cambers, incidence angles, and deviation angles.

The employment of blade elements in this design procedure (as discussed in ch. III) requires

the estimation or calculation of the radii to each blade element at the axial stations upstream and downstream of the rotor. Thus, since r_1 is assigned by the designer, r_2 is identified as a design variable. For a rotor, the design method outlined in the preceding paragraph requires predictions of relative stagnation-pressure loss (in terms of $\bar{\omega}'$) and of deviation angle. The radial-equilibrium calculation and the condition of continuity determine the values of axial velocity or local specific mass flow downstream of the rotor for each blade element. Therefore, three additional design variables are $\bar{\omega}$, β_2', and $(\rho V_z)_2$. (The local specific mass flow $(\rho V_z)_2$ was found to be more convenient to use in this analysis than the axial velocity $V_{z,2}$.)

Errors in the design rotor-inlet flow distribution can be caused by design or blade manufacturing tolerances or errors in any of the upstream blade rows. At the design mass flow, these errors can lead to off-design values of rotor-inlet stagnation pressure P_1, absolute air angle β_1, local specific mass flow $(\rho V_z)_1$, and stagnation enthalpy H_1.

In summary, then, the design variables for rotor blade elements are identified as P_1, β_1, $(\rho V_z)_1$, H_1, $\bar{\omega}'$, β_2', $(\rho V_z)_2$, and r_2. Instead of the general design variable P_1, the loss parameter $\bar{\omega}$ for the adjacent upstream stationary blade row can be used. The agreement between the actual and design values of a performance parameter (such as P_2) depends, within the limitations of the design system, on the agreement between the actual and design values of these design variables.

In the following discussion, the foregoing design variables are identified by the lower-case Roman numerals i to viii as follows:

P_1 or $\bar{\omega}$	β_1	$(\rho V_z)_1$	H_1	$\bar{\omega}'$	β_2'	$(\rho V_z)_2$	r_2
i or (i)	ii	iii	iv	v	vi	vii	viii

The symbol denoting the error in a performance parameter due to a design error in any one variable (assuming for the moment that all other variables are correct) is identified by the appropriate lower-case Roman numeral subscript. For instance, $(\Delta H_2/H_2)_i$ denotes the error in H_2 due to an error solely in P_1. The stator (or guide-vane) loss parameter $\bar{\omega}$ is not an independent design variable; an error in $\bar{\omega}$ is one of many sources of error in P_1,

and it is denoted by parentheses around its identifying number.

Some sources of errors in the variables are as follows:

Design variable	Some sources of error
$\bar{\omega}'$ ------------	(1) Accuracy of loss parameter and incidence-angle correlation system (ch. VII)
β_2' ------------	(2) Accuracy of deviation-angle correlation system (3) Blade-fabrication tolerances
$(\rho V_z)_2$ ------------	(4) Degree of simplification of radial-equilibrium equation (5) Effects of errors in $\bar{\omega}'$ and β_2' on radial-equilibrium calculation (6) Inaccurate allowance for wall boundary-layer development
r_2 ------------	(7) Same as (4), (5), and (6) if r_2 is calculated (8) If r_2 is assumed, error depends on degree of radial shift in flow as gas crosses rotor

The foregoing types of design errors in blade rows upstream of a given rotor contribute to discrepancies between actual and design values of P_1, β_1, $(\rho V_z)_1$, and H_1. For the inlet stage of a compressor, an additional source of such errors lies in the performance of the inlet diffuser section.

A basic source of disagreement between actual and design performance is contained in certain simplifications to the equations of motion as applied to the blade-element design method (e.g., the assumptions of axial symmetry and steady flow). This source of error is not amenable to analytical investigation and is not considered in this chapter.

The design variables P_1, β_1, $(\rho V_z)_1$, H_1, $\bar{\omega}'$, β_2', $(\rho V_z)_2$, and r_2, in conjunction with known inlet conditions, determine the value of a compressor blade-element performance parameter. For the purposes of this investigation, then, any of the blade-element performance parameters can be designated as a function of these eight design variables:

$$f = f[P_1, \beta_1, (\rho V_z)_1, H_1, \bar{\omega}', \beta_2', (\rho V_z)_2, r_2] \quad (396)$$

Formula (394) (the total differential of f) is particularized as follows for application to the analysis of design errors:

$$\Delta f = \frac{\partial f}{\partial P_1} \Delta P_1 + \frac{\partial f}{\partial \beta_1} \Delta \beta_1 + \frac{\partial f}{\partial (\rho V_z)_1} \Delta (\rho V_z)_1 + \frac{\partial f}{\partial H_1} \Delta H_1$$

$$+ \frac{\partial f}{\partial \bar{\omega}'} \Delta \bar{\omega}' + \frac{\partial f}{\partial \beta_2'} \Delta \beta_2' + \frac{\partial f}{\partial (\rho V_z)_2} \Delta (\rho V_z)_2 + \frac{\partial f}{\partial r_2} \Delta r_2$$

$$(394a)$$

The partial-derivative coefficients of formula (394a) can be calculated from the available blade-element performance equations. Each individual term $\left(\text{such as } \dfrac{\partial f}{\partial P_1}\Delta P_1\right)$ represents the contribution to the total error in f caused by a design error in one variable only (ΔP_1, e.g.), with all other design variables assumed correct.

For the calculations and the plotting of the results, it is convenient to make all terms of formula (394a) dimensionless in order to reduce the number of parameters determining the value of each error term. Formula (394a) is modified as follows:

$$\frac{\Delta f}{f}=\frac{P_1}{f}\frac{\partial f}{\partial P_1}\frac{\Delta P_1}{P_1}+\frac{1}{f}\frac{\partial f}{\partial \beta_1}\Delta\beta_1+\frac{(\rho V_z)_1}{f}\frac{\partial f}{\partial(\rho V_z)_1}\frac{\Delta(\rho V_z)_1}{(\rho V_z)_1}$$

$$+\frac{H_1}{f}\frac{\partial f}{\partial H_1}\frac{\Delta H_1}{H_1}+\frac{1}{f}\frac{\partial f}{\partial\bar\omega'}\Delta\bar\omega'+\frac{1}{f}\frac{\partial f}{\partial\beta_2'}\Delta\beta_2'$$

$$+\frac{(\rho V_z)_2}{f}\frac{\partial f}{\partial(\rho V_z)_2}\frac{\Delta(\rho V_z)_2}{(\rho V_z)_2}+\frac{r_2}{f}\frac{\partial f}{\partial r_2}\frac{\Delta r_2}{r_2} \quad (394b)$$

For cases where a performance parameter is associated with axial station 2 (f_2), any one of the first four terms might contain as many as eight design variables. A degree of further simplification in the plotting of some of these formulas is achieved by the use of certain performance-parameter error terms as intermediate variables. In certain cases the formula for one term of (394b) takes the following form:

$$\left(\frac{\Delta f_2}{f_2}\right)_1=Y[\bar\omega',\beta_2',(\rho V_z)_2,r_2]Z[P_1,\beta_1,(\rho V_z)_1,H_1]\frac{\Delta P_1}{P_1}$$
$$(397)$$

A formula for error in a performance parameter associated with axial station 1 might be

$$\left(\frac{\Delta f_1}{f_1}\right)_1=Z[P_1,\beta_1,(\rho V_z)_1,H_1]\frac{\Delta P_1}{P_1} \quad (398)$$

In this case, formula (397) can be expressed in terms of the intermediate variable f_1 as follows:

$$\left(\frac{\Delta f_2}{f_2}\right)_1=Y[\bar\omega',\beta_2',(\rho V_z)_2,r_2]\left(\frac{\Delta f_1}{f_1}\right)_1 \quad (397a)$$

Formula (394b) can be written as follows:

$$\frac{\Delta f}{f}=\left(\frac{\Delta f}{f}\right)_I+\left(\frac{\Delta f}{f}\right)_{II}+\cdots+\left(\frac{\Delta f}{f}\right)_{VIII} \quad (394c)$$

Each term of formula (394c) represents the contribution to the relative error in f of an error in the particular design variable identified by the subscript.

Formula (394c) gives a value of relative error in f caused by a given set of errors in the design variables. The only case for which a set of errors in design variables is known is the case of analysis of experimental data. For this case, formuld (394c) can be applied to determine, at least approximately, what design errors may have caused a measured discrepancy between the actual and design values of a performance parameter. This use of the design-error charts is outlined in a later section.

The estimation of a probable discrepancy between the actual and design values of a performance parameter requires that the design errors be identified as either random errors or as systematic errors. For the purposes of this investigation, random errors are defined as errors that are unpredictably positive or negative. Systematic errors are predictable in sign, and in some cases an approximate estimate of their magnitudes can be made. An example of a systematic design error is the error in local specific mass flow, (or axial velocity) caused by neglect of the entropy gradient during the radial-equilibrium calculation. This type of design error depends on the design flow distribution and the radial distribution of blade losses.

The approximate nature of the available correlations of design data (deviation angle and loss) leads to random design errors. The actual causes of such discrepancies are not known; their influence cannot, at present, be correlated with the various combinations of velocity-diagram parameters.

For the analysis of random errors, an uncertainty interval in a design variable can be estimated on the basis of past experience. An uncertainty interval in β_1, for instance, can be defined as a finite interval in β_1, such as $\beta_{1,u}-\beta_{1,l}$, for which a definite statistical probability exists that the value of β_1 will lie. For example, if, for a design

value of $\beta_1 = 30°$, 80 percent of the actual values of β_1 for different design cases fall in the interval from $\beta_1 = 29°$ to $\beta_1 = 31°$, then the uncertainty interval corresponding to odds of 4 to 1 is 2°.

The term $\frac{1}{f} \frac{\partial f}{\partial \beta_1} \Delta \beta_1 = \left(\frac{\Delta f}{f}\right)_{11}$ represents the corresponding uncertainty interval in f due to that in β_1 only. For the uncertainty interval in f due to the uncertainty intervals corresponding to the same odds in all the design variables, the second-power formula of reference 346 can be employed:

$$\left(\frac{\Delta f}{f}\right)^2 = \left(\frac{\Delta f}{f}\right)_1^2 + \ldots + \left(\frac{\Delta f}{f}\right)_{VIII}^2 \quad (399)$$

The uncertainty interval in f due to the uncertainty intervals in all of the design variables for a given probability can be calculated approximately for a mean-radius condition only. The reasons for this limitation are given in the section entitled USE OF DESIGN-ERROR CHARTS. As an example of the use of formula (399), uncertainty intervals in $\bar{\omega}'$ and β_2' would be combined as follows to give the corresponding interval in the performance parameter f:

$$\frac{\Delta f}{f} = \sqrt{\left(\frac{1}{f} \frac{\partial f}{\partial \bar{\omega}'} \Delta \bar{\omega}'\right)^2 + \left(\frac{1}{f} \frac{\partial f}{\partial \beta_2'} \Delta \beta_2'\right)^2}$$

If all the uncertainty intervals of the design variables are estimated on the basis of the best available information so that the same odds (say b to 1) can be quoted that the value of each variable will lie within its interval, then, according to reference 348, statistical analysis shows that the odds will be b to 1 that the actual value of the performance parameter f will fall within the uncertainty interval given by formula (399).

The errors in axial velocity caused by neglect of the entropy gradient in the radial-equilibrium calculation can be interpreted not as uncertainty intervals but as estimated corrections to the design values. An investigation of these errors (wherein the error is discussed in terms of axial velocity rather than the local specific mass flow) and a method of making the corrections are reported in reference 49. These estimated corrections and uncertainty intervals can be combined as follows:

$$f_{u,i} = f_d \left\{ 1 + \left[\left(\frac{\Delta f}{f}\right)_1 + \ldots + \left(\frac{\Delta f}{f}\right)_{VIII}\right]_{sys} \right.$$
$$\left. \pm \frac{1}{2} \sqrt{\left(\frac{\Delta f}{f}\right)_1^2 + \ldots + \left(\frac{\Delta f}{f}\right)_{VIII}^2} \right\} \quad (400)$$

The second term of formula (400) constitutes the estimated corrections to the design value of f for the systematic design errors, and the last term represents half the uncertainty interval in f due to the uncertainty intervals in each of the design variables.

The eight terms of formula (394b) were calculated (where applicable) for each of the following blade-element performance parameters: axial velocities $V_{z,1}$ and $V_{z,2}$, relative stagnation enthalpies H_1' and H_2', stagnation enthalpy H_2, stagnation pressures P_1 and P_2, relative air angle β_1', absolute air angle β_2, and diffusion factor D. The stagnation pressure P_1, which is one of the rotor design variables, is a performance parameter only in the specialized sense that is affected by design errors in stationary-blade-row loss parameter $\bar{\omega}$. The resulting formulas are presented in this report in the form of carpet and lattice plots. For the purpose of preparing the charts, unit errors were assigned to the design variables (1 percent, 0.01, or 1°, as applicable). The technique of preparing plots of two or more independent parameters (carpet and lattice plots) is discussed in reference 347.

The analysis was made for a rotor of any stage of a compressor. The results are given for blade-element performance parameters only; the estimation of uncertainty intervals in the radially averaged over-all performance of a stage is not discussed in this chapter. This problem involves considerations of statistical and probability theory that are beyond the scope of the present investigation.

MEASUREMENT ERRORS

For the analysis of measurement errors, formula (394) assumes the following form:

$$\Delta f = \frac{\partial f}{\partial P_1} \Delta P_1 + \frac{\partial f}{\partial p_1} \Delta p_1 + \frac{\partial f}{\partial \beta_1} \Delta \beta_1 + \frac{\partial f}{\partial T_1} \Delta T_1$$
$$+ \frac{\partial f}{\partial P_2} \Delta P_2 + \frac{\partial f}{\partial p_2} \Delta p_2 + \frac{\partial f}{\partial \beta_2} \Delta \beta_2 + \frac{\partial f}{\partial T_2} \Delta T_2 \quad (394d)$$

Formula (394d) can be applied directly only in cases where, for a specific experiment, each of the error terms is known. This situation, of course, is never realized. When the best methods of calibration are used, measurement errors are considered as random errors and can only be estimated; thus, the statistical approach outlined in the preceding section was applied also to the analysis of measurement errors. The terms of formula (394d) are interpreted as uncertainty intervals for the function f due to uncertainty intervals for the same prescribed odds in each variable. The uncertainty interval in f due to all the estimated errors can be calculated from the following formula (in dimensionless form):

$$\left(\frac{\Delta f}{f}\right)^2 = \left(\frac{P_1}{f}\frac{\partial f}{\partial P_1}\frac{\Delta P_1}{P_1}\right)^2 + \left(\frac{p_1}{f}\frac{\partial f}{\partial p_1}\frac{\Delta p_1}{p_1}\right)^2$$

$$+ \left(\frac{1}{f}\frac{\partial f}{\partial \beta_1}\Delta\beta_1\right)^2 + \left(\frac{T_1}{f}\frac{\partial f}{\partial T_1}\frac{\Delta T_1}{T_1}\right)^2$$

$$+ \left(\frac{P_2}{f}\frac{\partial f}{\partial P_2}\frac{\Delta P_2}{P_2}\right)^2 + \left(\frac{p_2}{f}\frac{\partial f}{\partial p_2}\frac{\Delta p_2}{p_2}\right)^2$$

$$+ \left(\frac{1}{f}\frac{\partial f}{\partial \beta_2}\Delta\beta_2\right)^2 + \left(\frac{T_2}{f}\frac{\partial f}{\partial T_2}\frac{\Delta T_2}{T_2}\right)^2 \quad (401)$$

Formula (401) is valid only for the estimation of uncertainty intervals due to random errors. That is, as the number of observations of each variable approaches infinity, the mean of all observations should approach the true value of the variable.

The error terms of formula (401) were calculated, and the results are presented in chart form for the following performance parameters: ρV_z, β', $\bar{\omega}$, $\bar{\omega}'$, η_{ad}, $H_{M,2}$, and D.

CALCULATION AND PRESENTATION OF FORMULAS

In the following presentation, all formulas are designated by a lower-case letter, a capital letter, and a lower-case Roman numeral. The letters d and m denote, respectively, the analysis of design and measurement errors. The capital letter identifies the performance parameter under analysis, and the lower-case Roman numeral identifies the variable in error. The following tables provide this identification:

Case d—Design-error performance parameters									
Performance parameter	P_1	$V_{z,1}$	H_1'	β_1'	H_1'	$V_{z,2}$	H_2	P_2	β_2	D
Formula symbol	A	B	C	D	E	F	G	H	J	K

Case d—Design variables							
Design variable	P_1 or $\bar{\omega}$	β_1	$(\rho V_z)_1$	H_1	$\bar{\omega}'$	β_2'	$(\rho V_z)_2$	r_2
Formula numeral	i or (I)	ii	iii	iv	v	vi	vii	viii

Case m—Measurement-error performance parameters						
Performance parameter	(ρV_z)	β'	$\bar{\omega}$	$\bar{\omega}'$	η_{ad}	$H_{M,2}$	D
Formula symbol	A	B	C	D	E	F	G

Case m—Flow variables							
Flow variable	p_1	P_1	T_1	β_1	p_2	P_2	T_2	β_2
Formula numeral	i	ii	iii	iv	v	vi	vii	viii

The symbol for the error in the performance parameter under consideration is given a subscript to identify the source of error. This subscript is the lower case Roman numeral of the appropriate table.

DESIGN-ERROR FORMULAS

The design-error differential formulas were calculated from the following equations:

$$P_1 = P_0\left\{1 - \bar{\omega}\left[1 - \left(\frac{h_0}{H_1}\right)^{\frac{\gamma}{\gamma-1}}\right]\right\} \quad (402)$$

$$V_{z,1} = \sqrt{2}\,(H_1 - h_1)^{1/2}\cos\beta_1 \qquad (403)$$

$$H_1' = H_1 + \tfrac{1}{2}U_1^2 - U_1 V_{z,1}\tan\beta_1 \qquad (404)$$

$$\tan\beta_1' = \frac{U_1}{V_{z,1}} - \tan\beta_1 \qquad (405)$$

$$H_2' = H_1' + \tfrac{1}{2}U_1^2\left[\left(\frac{r_2}{r_1}\right)^2 - 1\right] \qquad (406)$$

$$V_{z,2} = \sqrt{2}\,(H_2' - h_2)^{1/2}\cos\beta_2' \qquad (407)$$

$$H_2 = H_1 + U_1^2\left(\frac{r_2}{r_1}\right)^2 - U_1\frac{r_2}{r_1}V_{z,2}\tan\beta_2' - U_1 V_{z,1}\tan\beta_1 \qquad (408)$$

$$\frac{P_2}{P_1} = \left(\frac{H_2}{H_1}\right)^{\frac{\gamma}{\gamma-1}}\left\{1 - \bar{\omega}'\left(\frac{P_1'}{P_2'}\right)_{td}\left[1 - \left(\frac{h_1}{H_1'}\right)^{\frac{\gamma}{\gamma-1}}\right]\right\} \qquad (409)$$

$$\tan\beta_2 = \frac{r_2}{r_1}\frac{U_1}{V_{z,2}} - \tan\beta_2' \qquad (410)$$

$$D = 1 + \frac{\sin\beta_1'}{2\sigma} - \left(1 + \frac{\sin\beta_2'}{2\sigma}\right)\frac{V_{z,2}\cos\beta_1'}{V_{z,1}\cos\beta_2'} \qquad (411)$$

$$(\rho V_z)_1 = \frac{\sqrt{2}\gamma}{\gamma-1}\frac{P_1}{H_1}\left(\frac{h_1}{H_1}\right)^{\frac{1}{\gamma-1}}(H_1 - h_1)^{1/2}\cos\beta_1 \qquad (412)$$

$$(\rho V_z)_2 = \frac{\sqrt{2}\gamma}{\gamma-1}\frac{P_2'}{H_2'}\left(\frac{h_2}{H_2'}\right)^{\frac{1}{\gamma-1}}(H_2' - h_2)^{1/2}\cos\beta_2' \qquad (413)$$

$$\left(\frac{P_2'}{P_1'}\right)_{td} = \left(\frac{H_2'}{H_1'}\right)^{\frac{\gamma}{\gamma-1}} \qquad (414)$$

(Formula (411) was obtained from the form given in ref. 9 by rearranging terms.) Some of the resulting differential formulas included terms that were considered sufficiently small that they could be neglected. Two specific examples of the general procedure used in deriving the differential formulas are presented in appendix B of this chapter.

The design-error formulas contain certain parameters that are presented in the form of carpet and lattice plots. The formulas for these parameters are as follows:

$$\frac{H_2'}{H_1'} = \frac{1}{1 - \dfrac{\gamma-1}{2}\dfrac{(M_2')^2}{1 + \dfrac{\gamma-1}{2}(M_2')^2}\left[1 - \left(\dfrac{r_1}{r_2}\right)^2\right]\cos^2\beta_2'(\tan\beta_2 + \tan\beta_2')^2} \qquad \begin{array}{l}(415)\\ (\text{fig. 302})\end{array}$$

$$\Omega = \frac{P_{2,td}'}{P_2'} - 1 = \frac{\bar{\omega}'\left\{1 - \left[1 + \dfrac{\gamma-1}{2}(M_1')^2\right]^{-\frac{\gamma}{\gamma-1}}\right\}}{\left(\dfrac{H_2'}{H_1'}\right)^{\frac{\gamma}{\gamma-1}} - \bar{\omega}'\left\{1 - \left[1 + \dfrac{\gamma-1}{2}(M_1')^2\right]^{-\frac{\gamma}{\gamma-1}}\right\}} \qquad \begin{array}{l}(416)\\ (\text{fig. 303})\end{array}$$

The following differential formulas were obtained from the analysis of errors in design variables:

$$\left(\frac{\Delta P_1}{P_1}\right)_{(1)} = -\frac{1 - \left(1 + \dfrac{\gamma-1}{2}M_0^2\right)^{-\frac{\gamma}{\gamma-1}}}{1 - \bar{\omega}\left[1 - \left(1 + \dfrac{\gamma-1}{2}M_0^2\right)^{-\frac{\gamma}{\gamma-1}}\right]}\Delta\bar{\omega} \qquad \begin{array}{l}(\text{dA–(i)})\\ (\text{fig. 304})\end{array}$$

$$\left(\frac{\Delta V_{z,1}}{V_{z,1}}\right)_{\text{I}} = -\frac{1}{1 - M_1^2}\frac{\Delta P_1}{P_1} \qquad \begin{array}{l}(\text{dB–i})\\ (\text{fig. 305(a)})\end{array}$$

$$\left(\frac{\Delta V_{z,1}}{V_{z,1}}\right)_{\text{II}} = \frac{\pi M_1^2\tan\beta_1}{180(1 - M_1^2)}\Delta\beta_1 \qquad \begin{array}{l}(\text{dB–ii})\\ (\text{fig. 305(b)})\end{array}$$

$$\left(\frac{\Delta V_{z,1}}{V_{z,1}}\right)_{\text{III}} = \frac{1}{1 - M_1^2}\frac{\Delta(\rho V_z)_1}{(\rho V_z)_1} \qquad (\text{dB–iii})$$

(fig. 305(a), substitute ρV_z for P, multiply result by -1)

$$\left(\frac{\Delta V_{z,1}}{V_{z,1}}\right)_{\mathrm{iv}}=\frac{1-\frac{1}{2}M_1^2}{1-M_1^2}\frac{\Delta H_1}{H_1}$$

<div align="right">(dB–iv)
(fig. 305(c))</div>

$$\left(\frac{\Delta H_1'}{H_1'}\right)_{\mathrm{i,\,iii}}=-(\gamma-1)\frac{M_1^2\sin\beta_1\cos\beta_1(\tan\beta_1+\tan\beta_1')}{1+\frac{\gamma-1}{2}M_1^2\cos^2\beta_1\sec^2\beta_1'}\left(\frac{\Delta V_{z,1}}{V_{z,1}}\right)_{\mathrm{i,\,iii}}$$

<div align="right">(dC–i, iii)
(fig. 306(a))</div>

$$\left(\frac{\Delta H_1'}{H_1'}\right)_{\mathrm{ii}}=-\frac{\pi(\gamma-1)M_1^2(\sec^2\beta_1-M_1^2)\cos^2\beta_1(\tan\beta_1+\tan\beta_1')}{180(1-M_1^2)\left(1+\frac{\gamma-1}{2}M_1^2\cos^2\beta_1\sec^2\beta_1'\right)}\Delta\beta_1$$

<div align="right">(dC–ii)
(fig. 306(b))</div>

$$\left(\frac{\Delta H_1'}{H_1'}\right)_{\mathrm{iv}}=\frac{1+\frac{\gamma-1}{2}M_1^2}{\left(1+\frac{\gamma-1}{2}M_1^2\cos^2\beta_1\sec^2\beta_1'\right)(1-M_1^2)}$$

$$\times\left[1-M_1^2\cos^2\beta_1(1-\tan\beta_1\tan\beta_1')-\frac{\gamma M_1^2}{1+\frac{\gamma-1}{2}M_1^2}\sin\beta_1\cos\beta_1(\tan\beta_1+\tan\beta_1')\right]\frac{\Delta H_1}{H_1}$$

<div align="right">(dC–iv)</div>
<div align="right">(fig. 306(c))</div>

$$(\Delta\beta_1')_{\mathrm{i,\,iii,\,iv}}=-\frac{180}{\pi}\cos^2\beta_1'(\tan\beta_1+\tan\beta_1')\left(\frac{\Delta V_{z,1}}{V_{z,1}}\right)_{\mathrm{i,\,iii,\,iv}}$$

<div align="right">(dD–i, iii, iv)
(fig. 307(a))</div>

$$(\Delta\beta_1')_{\mathrm{ii}}=-\frac{\cos^2\beta_1'}{\cos^2\beta_1}\left[1+\frac{M_1^2}{1-M_1^2}\sin\beta_1\cos\beta_1(\tan\beta_1+\tan\beta_1')\right]\Delta\beta_1$$

<div align="right">(dD–ii)
(fig. 307(b))</div>

$$\left(\frac{\Delta H_2'}{H_2'}\right)_{\mathrm{i-iv}}=\frac{H_1'}{H_2'}\left(\frac{\Delta H_1'}{H_1'}\right)_{\mathrm{i-iv}}$$

<div align="right">(dE–i–iv)
(No fig. necessary)</div>

$$\left(\frac{\Delta H_2'}{H_2'}\right)_{\mathrm{viii}}=(\gamma-1)\frac{(M_2')^2}{1+\frac{\gamma-1}{2}(M_2')^2}\cos^2\beta_2'(\tan\beta_2+\tan\beta_2')^2\frac{\Delta r_2}{r_2}$$

<div align="right">(dE–viii)
(fig. 308)</div>

$$\left(\frac{\Delta V_{z,2}}{V_{z,2}}\right)_{\mathrm{i}}=-\frac{1}{\gamma-1}\frac{1+\frac{\gamma-1}{2}(M_2')^2}{1-(M_2')^2}\left(\frac{\Delta H_2'}{H_2'}\right)_{\mathrm{i}}-\frac{1}{1-(M_2')^2}\frac{\Delta P_1}{P_1}$$

<div align="right">(dF–i)
(fig. 309(a))</div>

$$\left(\frac{\Delta V_{z,2}}{V_{z,2}}\right)_{\mathrm{ii,\,iii}}=-\frac{1}{\gamma-1}\frac{1+\frac{\gamma-1}{2}(M_2')^2}{1-(M_2')^2}\left(\frac{\Delta H_2'}{H_2'}\right)_{\mathrm{ii,\,iii}}$$

<div align="right">(dF–ii, iii)
(fig. 309(b))</div>

$$\left(\frac{\Delta V_{z,2}}{V_{z,2}}\right)_{\mathrm{iv}}=\frac{\gamma}{(\gamma-1)[1-(M_2')^2]}\frac{\Delta H_1}{H_1}-\frac{1+\frac{\gamma-1}{2}(M_2')^2}{(\gamma-1)[1-(M_2')^2]}\left(\frac{\Delta H_2'}{H_2'}\right)_{\mathrm{iv}}$$

<div align="right">(dF–iv)
(fig. 309(c))</div>

$$\left(\frac{\Delta V_{z,2}}{V_{z,2}}\right)_{\mathrm{v}}=\frac{\Omega}{\bar{\omega}'[1-(M_2')^2]}\Delta\bar{\omega}'$$

<div align="right">(dF–v)
(fig. 309(d))</div>

$$\left(\frac{\Delta V_{z,2}}{V_{z,2}}\right)_{\mathrm{vi}}=\frac{\pi(M_2')^2}{180[1-(M_2')^2]}\tan\beta_2'\Delta\beta_2'$$

<div align="right">(dF–vi)</div>

<div align="center">(fig. 305(b), substitute M_2', β_2' for M_1, β_1, respectively)</div>

$$\left(\frac{\Delta V_{z,2}}{V_{z,2}}\right)_{vii}=\frac{1}{1-(M_2')^2}\frac{\Delta(\rho V_z)_2}{(\rho V_z)_2} \qquad \text{(dF–vii)}$$

(fig. 305(a), substitute M_2', $(\rho V_z)_2$ for M_1, P_1, respectively, multiply result by -1)

$$\left(\frac{\Delta V_{z,2}}{V_{z,2}}\right)_{viii}=\frac{1}{(\gamma-1)[1-(M_2')^2]}\left\{\gamma\Omega-\left[1+\frac{\gamma-1}{2}(M_2')^2\right]\right\}\left(\frac{\Delta H_2'}{H_2'}\right)_{viii} \qquad \begin{array}{l}\text{(dF–viii)}\\ \text{(fig. 309(e))}\end{array}$$

$$\left(\frac{\Delta H_2}{H_2}\right)_{i,iv}=\varphi\left(\frac{\Delta H_2'}{H_2'}\right)_{i,iv}+\psi\left(\frac{\Delta V_{z,2}}{V_{z,2}}\right)_{i,iv} \qquad \text{(dG–i, iv)}$$

where

$$\varphi=\frac{1+\frac{\gamma-1}{2}(M_2')^2}{1+\frac{\gamma-1}{2}(M_2')^2\cos^2\beta_2'\sec^2\beta_2} \qquad \begin{array}{l}\text{(417)}\\ \text{(fig. 310(a))}\end{array}$$

and

$$\psi=-\frac{(\gamma-1)(M_2')^2\sin\beta_2'\cos\beta_2'(\tan\beta_2+\tan\beta_2')}{1+\frac{\gamma-1}{2}(M_2')^2\cos^2\beta_2'\sec^2\beta_2} \qquad \begin{array}{l}\text{(418)}\\ \text{(fig. 310(b))}\end{array}$$

$$\left(\frac{\Delta H_2}{H_2}\right)_{ii,iii}=\frac{1+\frac{\gamma-1}{2}(M_2')^2}{1+\frac{\gamma-1}{2}(M_2')^2\cos^2\beta_2'\sec^2\beta_2}\times\left[1+\frac{(M_2')^2}{1-(M_2')^2}\sin\beta_2'\cos\beta_2'(\tan\beta_2+\tan\beta_2')\right]\left(\frac{\Delta H_2'}{H_2'}\right)_{ii,iii}$$

$$\begin{array}{l}\text{(dG–ii, iii)}\\ \text{(fig. 311)}\end{array}$$

$$\left(\frac{\Delta H_2}{H_2}\right)_{v,vii}=\psi\left(\frac{\Delta V_{z,2}}{V_{z,2}}\right)_{v,vii} \qquad \begin{array}{l}\text{(dG–v, vii)}\\ \text{(No fig. necessary)}\end{array}$$

$$\left(\frac{\Delta H_2}{H_2}\right)_{vi}=-\frac{\pi(\gamma-1)(M_2')^2[\sec^2\beta_2'-(M_2')^2]\cos^2\beta_2'(\tan\beta_2+\tan\beta_2')}{180[1-(M_2')^2]\left[1+\frac{\gamma-1}{2}(M_2')^2\cos^2\beta_2'\sec^2\beta_2\right]}\Delta\beta_2' \qquad \text{(dG–vi)}$$

(fig. 306(b), substitute M_2', β_2', β_2 for M_1, β_1, β_1', respectively)

$$\left(\frac{\Delta H_2}{H_2}\right)_{viii}=\xi\frac{\Delta r_2}{r_2}+\psi\left(\frac{\Delta V_{z,2}}{V_{z,2}}\right)_{viii} \qquad \text{(dG–viii)}$$

where

$$\xi=\frac{(\gamma-1)(M_2')^2\cos^2\beta_2'(\tan\beta_2+\tan\beta_2')(2\tan\beta_2+\tan\beta_2')}{1+\frac{\gamma-1}{2}(M_2')^2\cos^2\beta_2'\sec^2\beta_2} \qquad \begin{array}{l}\text{(419)}\\ \text{(fig. 310(c))}\end{array}$$

$$\left(\frac{\Delta P_2}{P_2}\right)_i=\frac{\Delta P_1}{P_1}+\frac{\gamma}{\gamma-1}\left(\frac{\Delta H_2}{H_2}\right)_i \qquad \begin{array}{l}\text{(dH–i)}\\ \text{(No fig. necessary)}\end{array}$$

$$\left(\frac{\Delta P_2}{P_2}\right)_{ii,iii,vi-viii}=\frac{\gamma}{\gamma-1}\left(\frac{\Delta H_2}{H_2}\right)_{ii,iii,vi-viii} \qquad \begin{array}{l}\text{(dH–ii, iii, vi–viii)}\\ \text{(No fig. necessary)}\end{array}$$

$$\left(\frac{\Delta P_2}{P_2}\right)_{iv}=\frac{\gamma}{\gamma-1}\left[\left(\frac{\Delta H_2}{H_2}\right)_{iv}-\frac{\Delta H_1}{H_1}\right] \qquad \begin{array}{l}\text{(dH–iv)}\\ \text{(No fig. necessary)}\end{array}$$

$$\left(\frac{\Delta P_2}{P_2}\right)_v = -\left\{[1-(M_2')^2]+\frac{\gamma(M_2')^2 \sin \beta_2' \cos \beta_2'(\tan \beta_2+\tan \beta_2')}{1+\frac{\gamma-1}{2}(M_2')^2 \cos^2 \beta_2' \sec^2 \beta_2}\right\}\left(\frac{\Delta V_{z,2}}{V_{z,2}}\right)_v$$

(dH–v)
(fig. 312)

$$(\Delta\beta_2)_{\text{i–v, vii}} = -\frac{180}{\pi}\cos^2 \beta_2(\tan \beta_2+\tan \beta_2')\left(\frac{\Delta V_{z,2}}{V_{z,2}}\right)_{\text{i–v, vii}}$$

(dJ–i–v, vii)

(fig. 307(a), substitute $\beta_2, \beta_2', V_{z,2}$ for $\beta_1', \beta_1, V_{z,1}$, respectively)

$$(\Delta\beta_2)_{\text{vi}} = -\frac{\cos^2 \beta_2}{\cos^2 \beta_2'}\left[1+\frac{(M_2')^2}{1-(M_2')^2}\sin \beta_2' \cos \beta_2'(\tan \beta_2+\tan \beta_2')\right]\Delta\beta_2'$$

(dJ–vi)

(fig. 307(b), substitute M_2', β_2', β_2 for M_1, β_1, β_1', respectively)

$$(\Delta\beta_2)_{\text{viii}} = \frac{180}{\pi}\cos^2 \beta_2(\tan \beta_2+\tan \beta_2')\left[1+\frac{(M_2')^2}{1-(M_2')^2}\cos^2 \beta_2'(\tan \beta_2+\tan \beta_2')^2\right]\frac{\Delta r_2}{r_2}$$

(dJ–viii)
(fig. 313)

$$(\Delta D)_{\text{i–iv}} = \Lambda(\Delta\beta_1')_{\text{i–iv}}+\Gamma\left(\frac{\Delta V_{z,2}}{V_{z,2}}-\frac{\Delta V_{z,1}}{V_{z,1}}\right)_{\text{i–iv}}$$

(dK–i–iv)

where

$$\Lambda = \frac{1}{2\sigma \cos \beta_1'}+(1-D)\tan \beta_1'$$

(420)
(fig. 314(a))

and

$$\Gamma = -\left[\frac{\sin \beta_1'}{2\sigma}+(1-D)\right]$$

(421)
(fig. 314(b))

$$(\Delta D)_{\text{v, vii, viii}} = \Gamma\left(\frac{\Delta V_{z,2}}{V_{z,2}}\right)_{\text{v, vii, viii}}$$

(dK–v, vii, viii)
(No fig. necessary)

$$\frac{V_1'}{V_2'}(\Delta D)_{\text{vi}} = -\frac{\pi}{180}\left[\left(1+\frac{\sin \beta_2'}{2\sigma}\right)\frac{\tan \beta_2'}{1-(M_2')^2}+\frac{\cos \beta_2'}{2\sigma}\right]\Delta\beta_2'$$

(dK–vi)
(fig. 315)

MEASUREMENT-ERROR FORMULAS

Measured quantities include the rotational speed, the inlet pressure and temperature, and the following flow properties: static pressure p, stagnation pressure P, absolute air angle β, and stagnation temperature T. In the following table, the calculated performance parameters are listed in the left column, and the flow properties of which they are explicit functions are listed in the right column:

ρV_z	p, P, T, β
β'	p, P, T, β
$\bar{\omega}$	p_0, P_0, P_1
$\bar{\omega}'$	$p_1, P_1, T_1, \beta_1, P_2, T_2$
η_{ad}	P_1, T_1, P_2, T_2
H_M	$p_1, P_1, T_1, \beta_1, p_2, P_2, T_2, \beta_2$
D	$p_1, P_1, T_1, \beta_1, p_2, P_2, T_2, \beta_2$

The equations for the performance parameters in the foregoing table, as explicit functions of the measured flow properties, are as follows (for

convenience in writing, some of the functions are given in terms of absolute velocity V):

$$\rho V_z = \left[\frac{2\gamma}{(\gamma-1)RT}\right]^{\frac{1}{2}} P\left(\frac{p}{P}\right)^{\frac{1}{\gamma}}\left[1-\left(\frac{p}{P}\right)^{\frac{\gamma-1}{\gamma}}\right]^{\frac{1}{2}}\cos \beta$$

(412a)

$$\tan \beta' = \left(\frac{\gamma-1}{2\gamma RT}\right)^{\frac{1}{2}}\frac{U}{\left[1-\left(\frac{p}{P}\right)^{\frac{\gamma-1}{\gamma}}\right]^{\frac{1}{2}}\cos \beta}-\tan \beta$$

(405a)

$$\bar{\omega} = \frac{P_0-P_1}{P_0-p_0}$$

(402a)

$$\bar{\omega}' = \left(\frac{P_2'}{P_1'}\right)_{id}\frac{1-\dfrac{\dfrac{P_2}{P_1}}{\left(\dfrac{T_2}{T_1}\right)^{\frac{\gamma}{\gamma-1}}}}{1-\dfrac{p_1}{P_1}\left(\dfrac{H_1}{H_1+\frac{1}{2}U_1^2-U_1V_1 \sin \beta_1}\right)^{\frac{\gamma}{\gamma-1}}}$$

(409a)

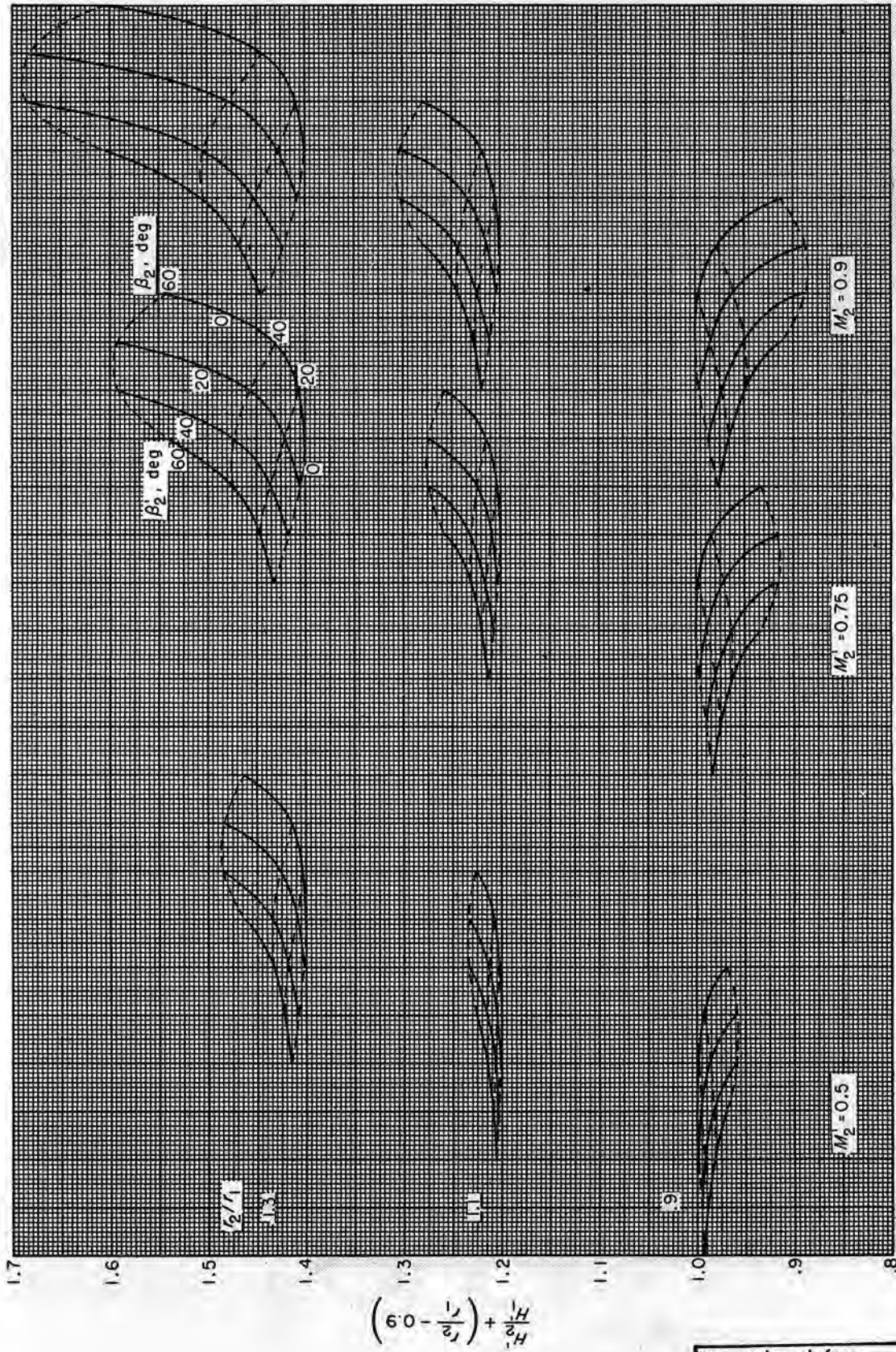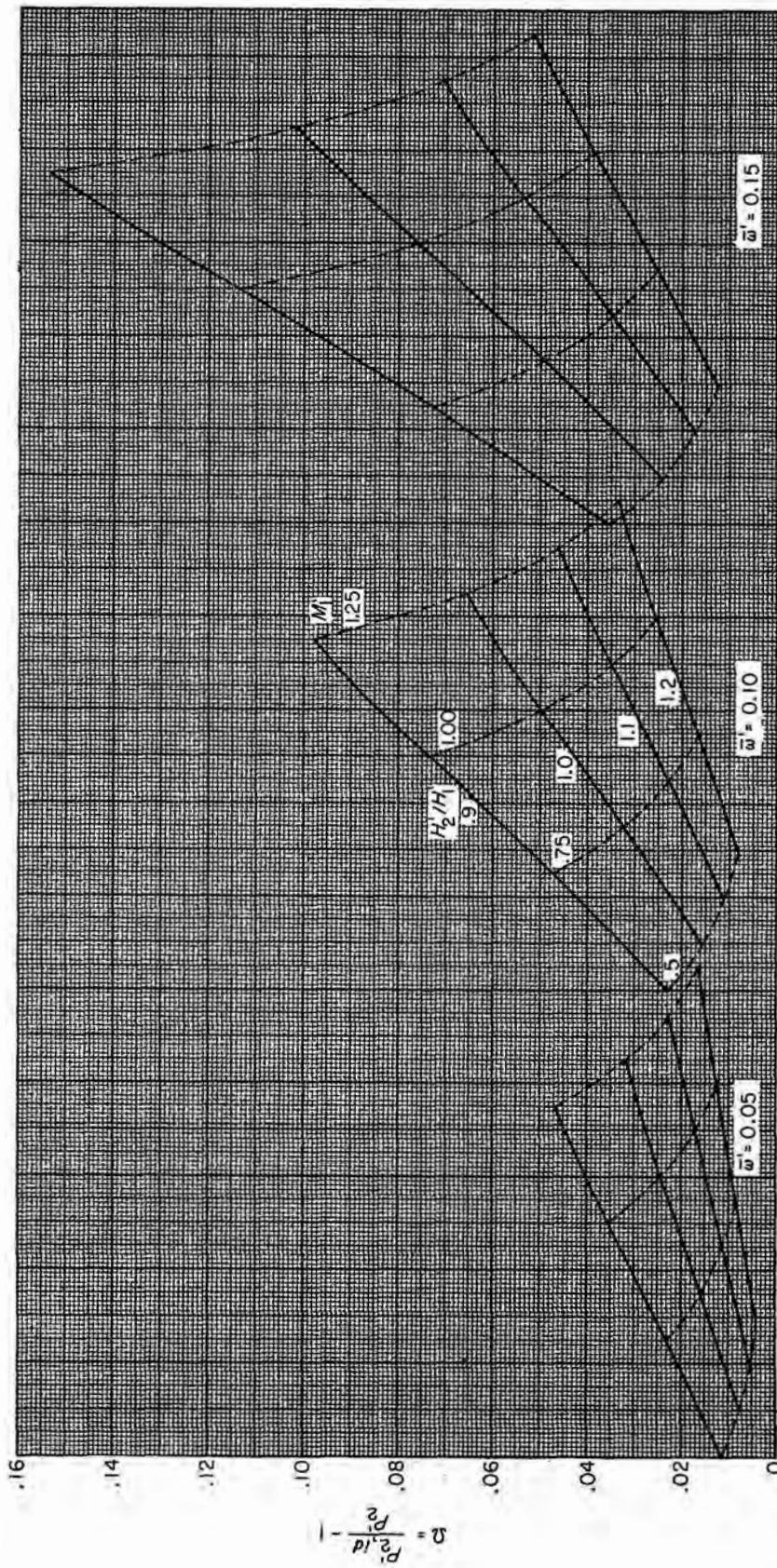FIGURE 302.—Relative stagnation-enthalpy ratio as function of velocity-diagram parameters (eq. (415)).

FIGURE 303.—Relative stagnation-pressure-ratio term Ω (eq. (416)) as function of relative stagnation-pressure-loss parameter, relative stagnation-enthalpy ratio, and relative Mach number.
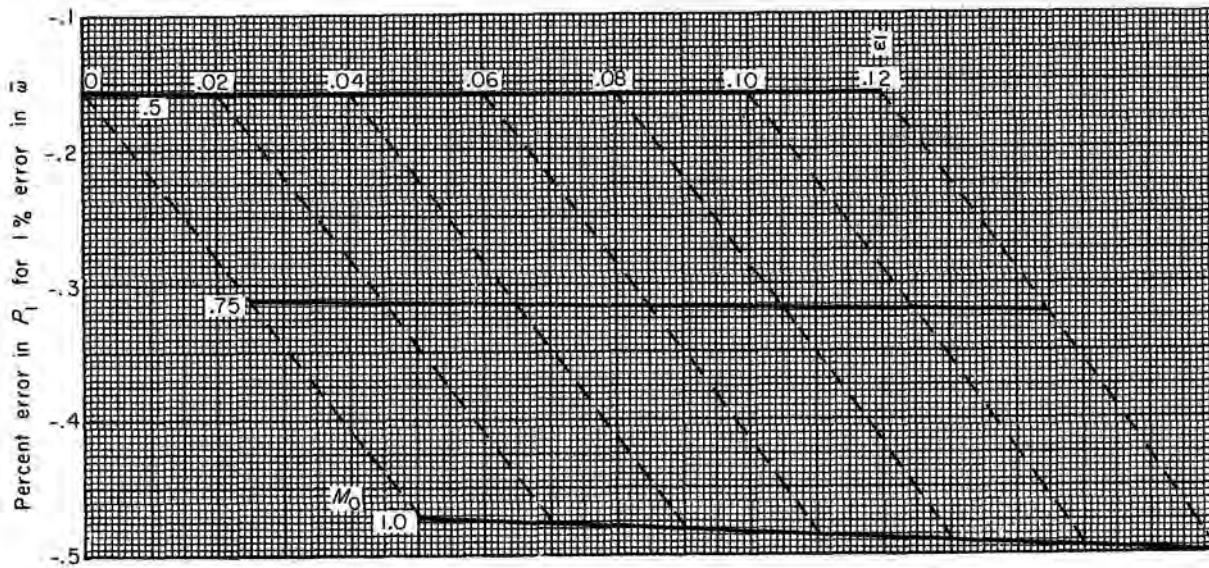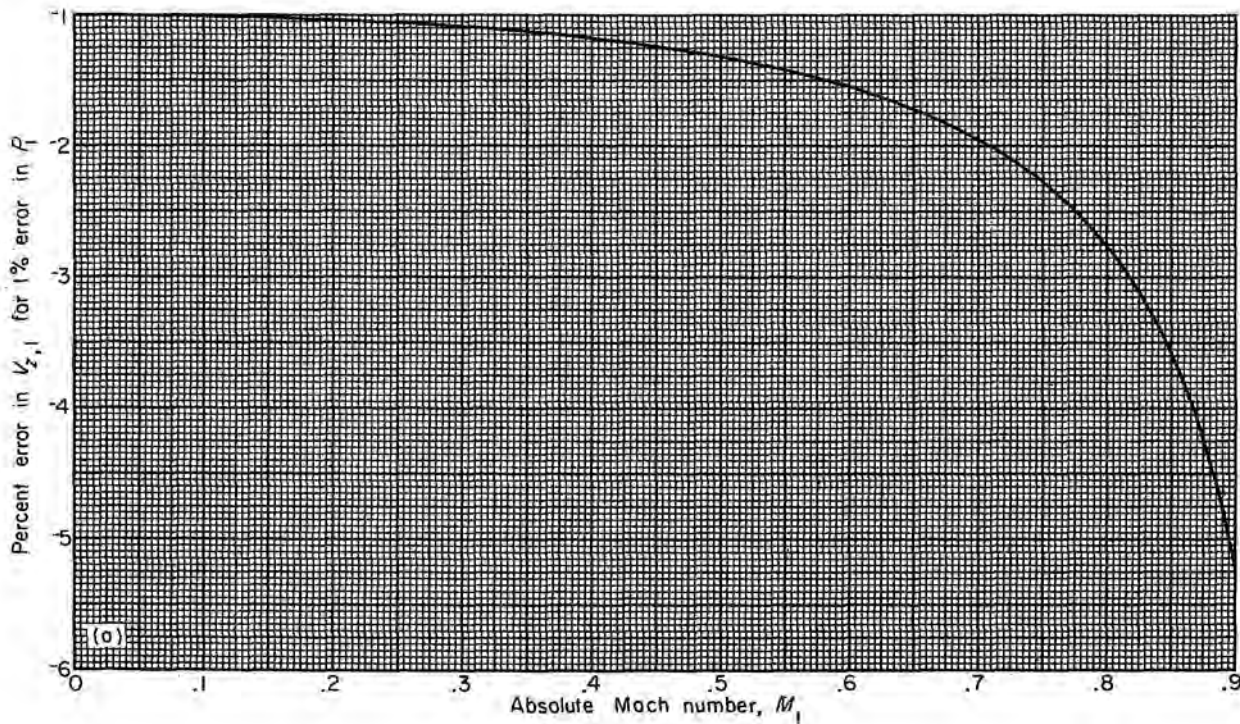
FIGURE 304.—Effect of design error in stagnation-pressure-loss parameter on stagnation pressure [eq. (dA–(i))].
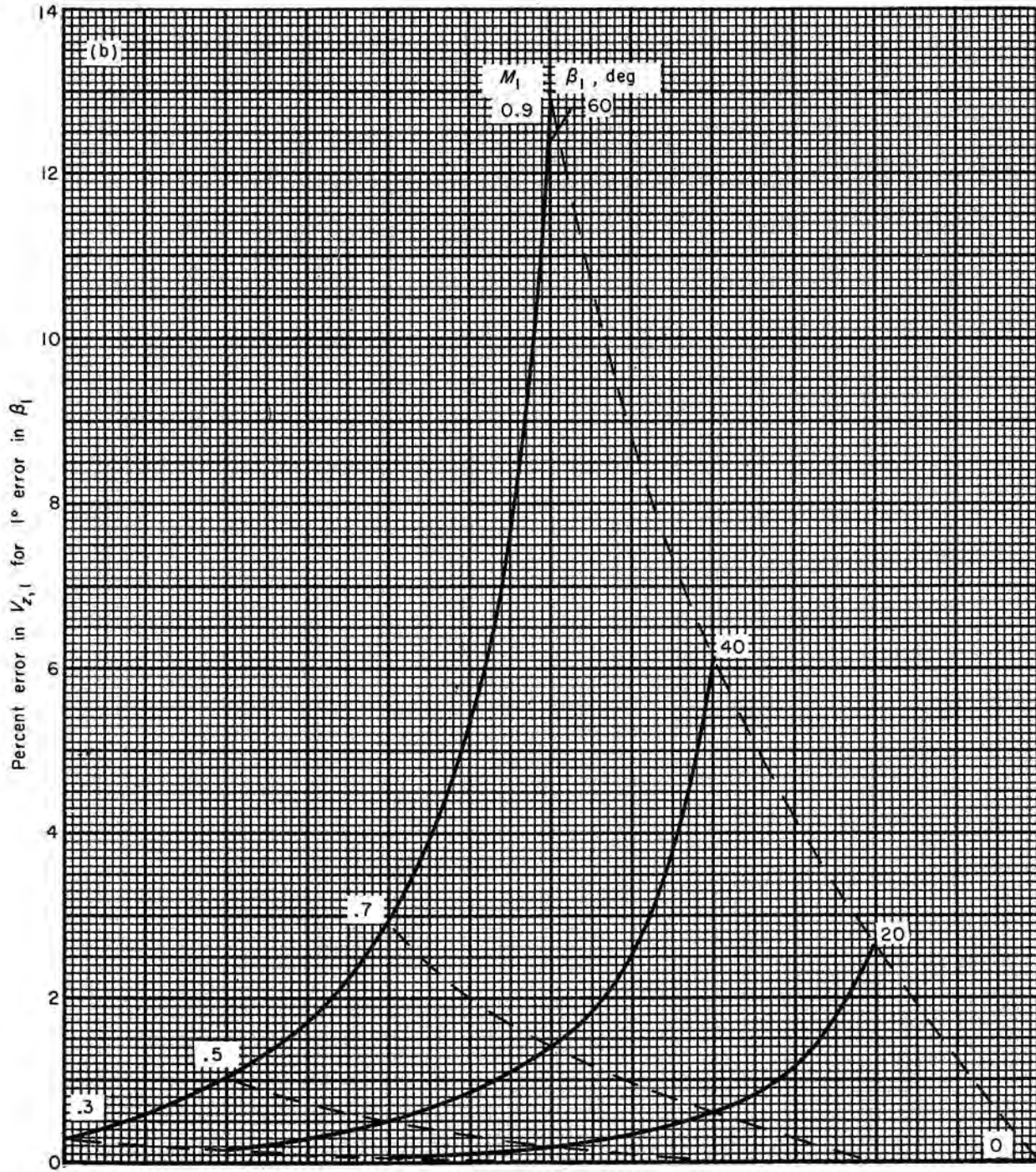

(a) Stagnation pressure (eq. (dB–i)).

FIGURE 305.—Effect of design errors on axial velocity upstream of rotor.

(b) Absolute air angle (eq. (dB–ii)).

FIGURE 305.—Continued.   Effect of design errors on axial velocity upstream of rotor.
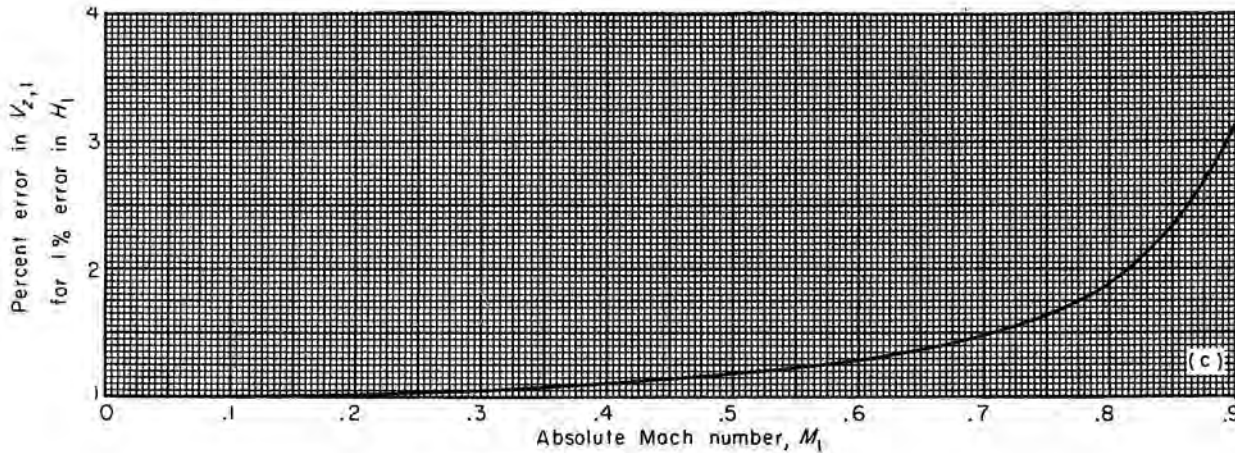
(c) Stagnation enthalpy (eq. (dB–iv)).

FIGURE 305.—Concluded.   Effect of design errors on axial velocity upstream of rotor.

$$\eta_{ad} = \frac{\left(\dfrac{P_2}{P_1}\right)^{\frac{\gamma-1}{\gamma}} - 1}{\dfrac{T_2}{T_1} - 1} \qquad (317)$$

$$H_{M,2} = H_1 + U_2 V_2 \sin \beta_2 - U_1 V_1 \sin \beta_1 \quad (408a)$$

$$D = 1 - \left(\frac{U_2^2 + V_2^2 - 2U_2 V_2 \sin \beta_2}{U_1^2 + V_1^2 - 2U_1 V_1 \sin \beta_1}\right)^{1/2} + \frac{U_1 - U_2 + V_2 \sin \beta_2 - V_1 \sin \beta_1}{2\sigma(U_1^2 + V_1^2 - 2U_1 V_1 \sin \beta_1)^{1/2}} \qquad (411a)$$

The analysis of measurement errors yielded the following formulas, which give the relative uncertainty interval in a performance parameter due to the corresponding uncertainty interval in the measurement of one flow property:

$$\left[\frac{\Delta(\rho V_z)}{\rho V_z}\right]_{\text{i, v}} = \frac{1}{\gamma}\left(1 - \frac{1}{M^2}\right)\frac{\Delta p}{p} \qquad \begin{array}{l}\text{(mA–i, v)}\\ \text{(fig. 316(a))}\end{array}$$

$$\left[\frac{\Delta(\rho V_z)}{\rho V_z}\right]_{\text{ii, vi}} = \frac{1}{\gamma}\left(\frac{1}{M^2} + \gamma - 1\right)\frac{\Delta P}{P} \qquad \begin{array}{l}\text{(mA–ii, vi)}\\ \text{(fig. 316(b))}\end{array}$$

$$\left[\frac{\Delta(\rho V_z)}{\rho V_z}\right]_{\text{iii, vii}} = -\frac{1}{2}\frac{\Delta T}{T} \qquad \begin{array}{l}\text{(mA–iii, vii)}\\ \text{(No fig. necessary)}\end{array}$$

$$\left[\frac{\Delta(\rho V_z)}{\rho V_z}\right]_{\text{iv, viii}} = -\frac{\pi}{180}\tan\beta\,\Delta\beta \qquad \begin{array}{l}\text{(mA–iv, viii)}\\ \text{(fig. 316(c))}\end{array}$$

$$(\Delta\beta')_{\text{i, v}} = \frac{180}{\pi}\frac{\cos^2\beta'(\tan\beta + \tan\beta')}{\gamma M^2}\frac{\Delta p}{p} \qquad \begin{array}{l}\text{(mB–i, v)}\\ \text{(fig. 317(a))}\end{array}$$

$$(\Delta\beta')_{\text{ii, vi}} = -\frac{180}{\pi}\frac{\cos^2\beta'(\tan\beta + \tan\beta')}{\gamma M^2}\frac{\Delta P}{P} \qquad \text{(mB–ii, vi)}$$
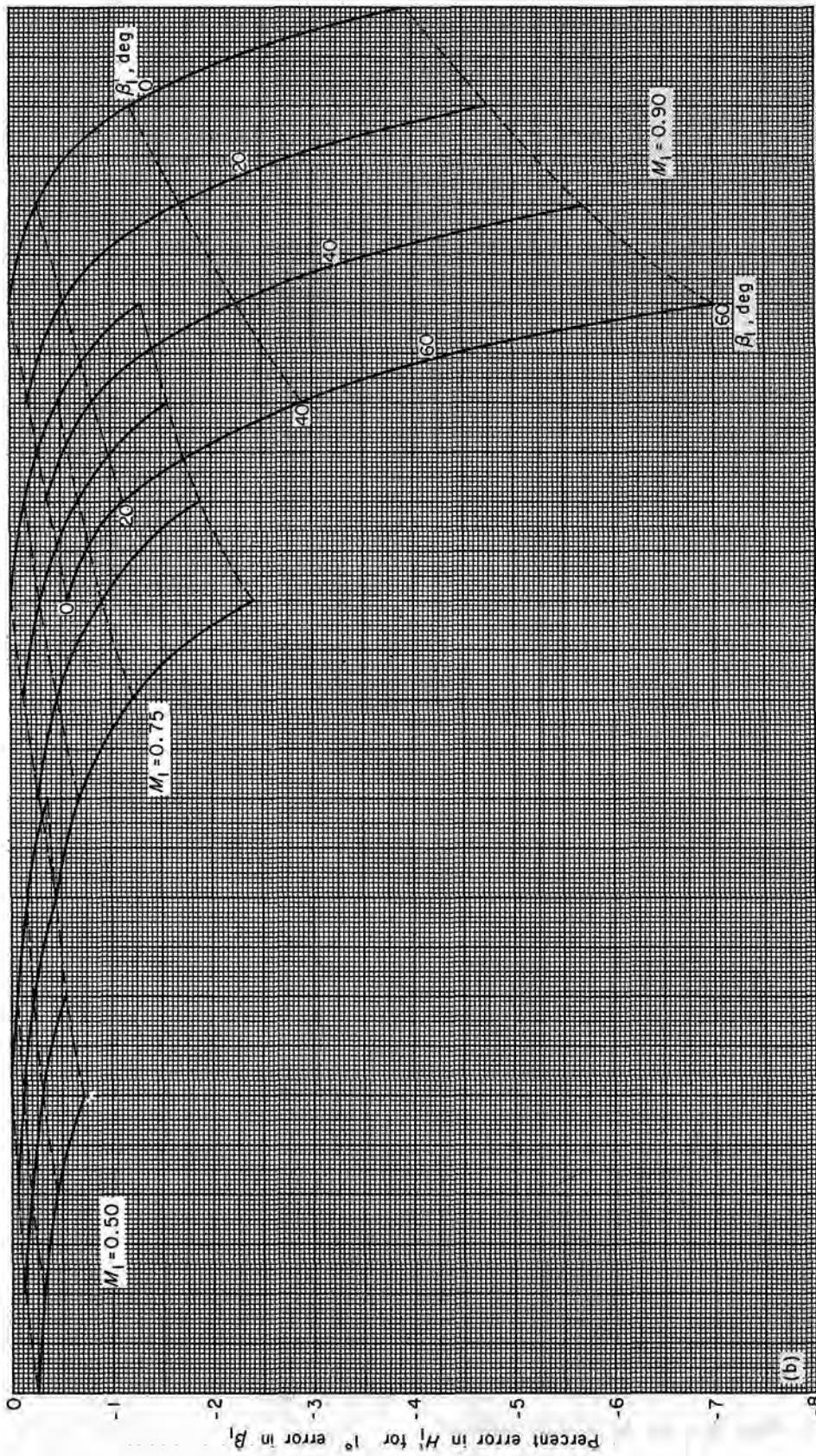
(fig. 317(a), prefix minus sign to result, substitute P for p)

$$(\Delta\beta')_{\text{iii, vii}} = -\frac{90}{\pi}\cos^2\beta'(\tan\beta + \tan\beta')\frac{\Delta T}{T} \qquad \begin{array}{l}\text{(mB–iii, vii)}\\ \text{(fig. 317(b))}\end{array}$$
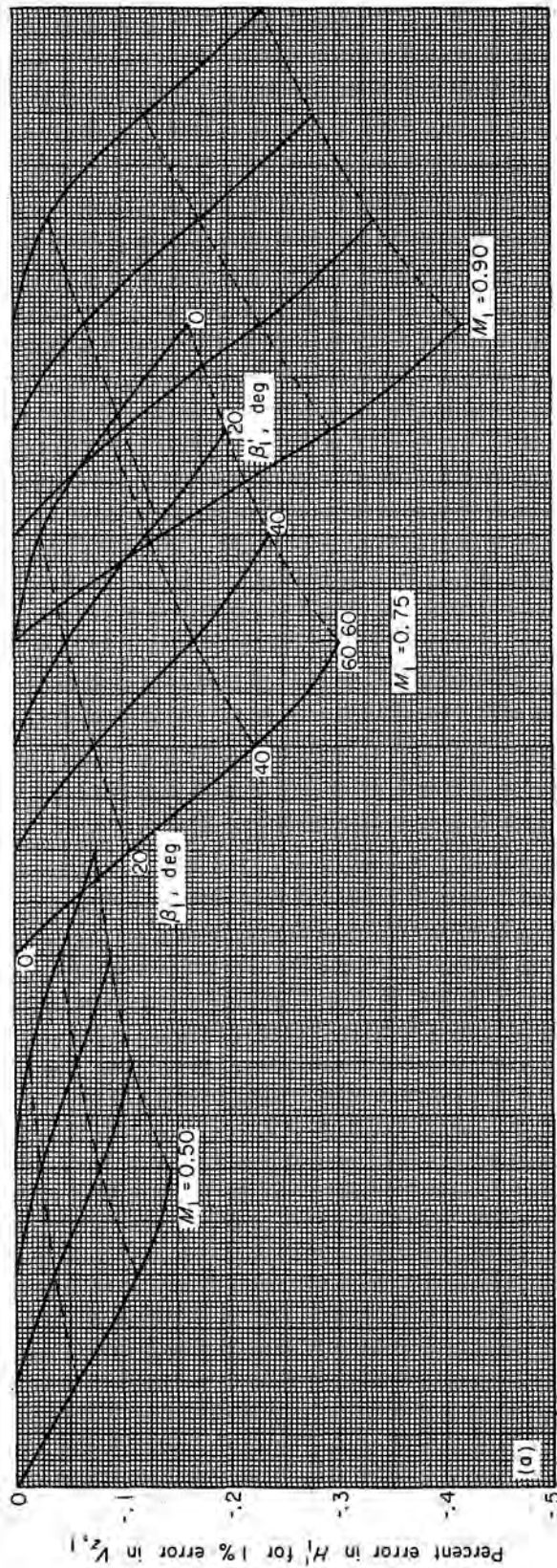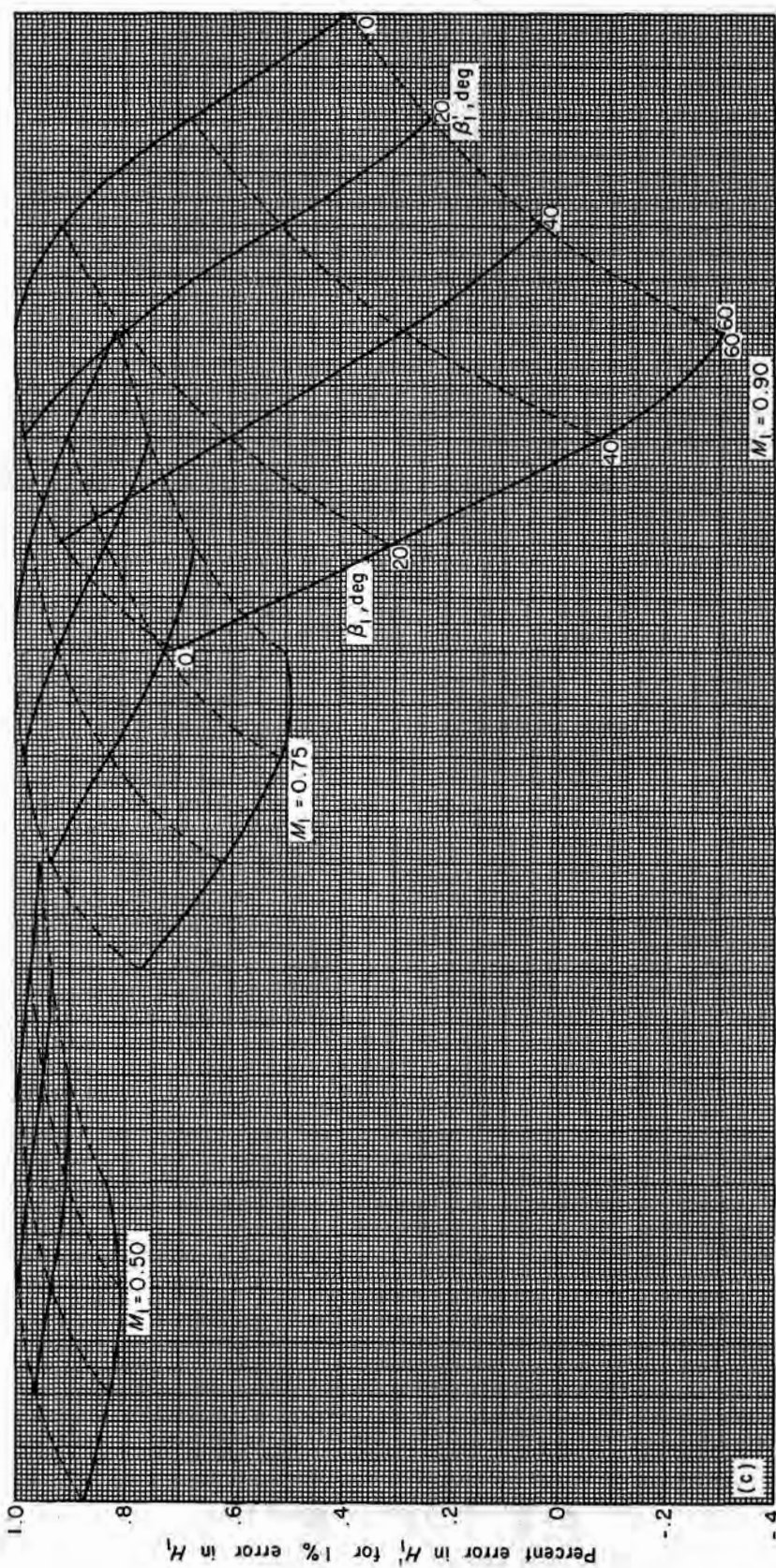
(a) Stagnation pressure or local specific mass flow (eq. (dC-i, iii)).

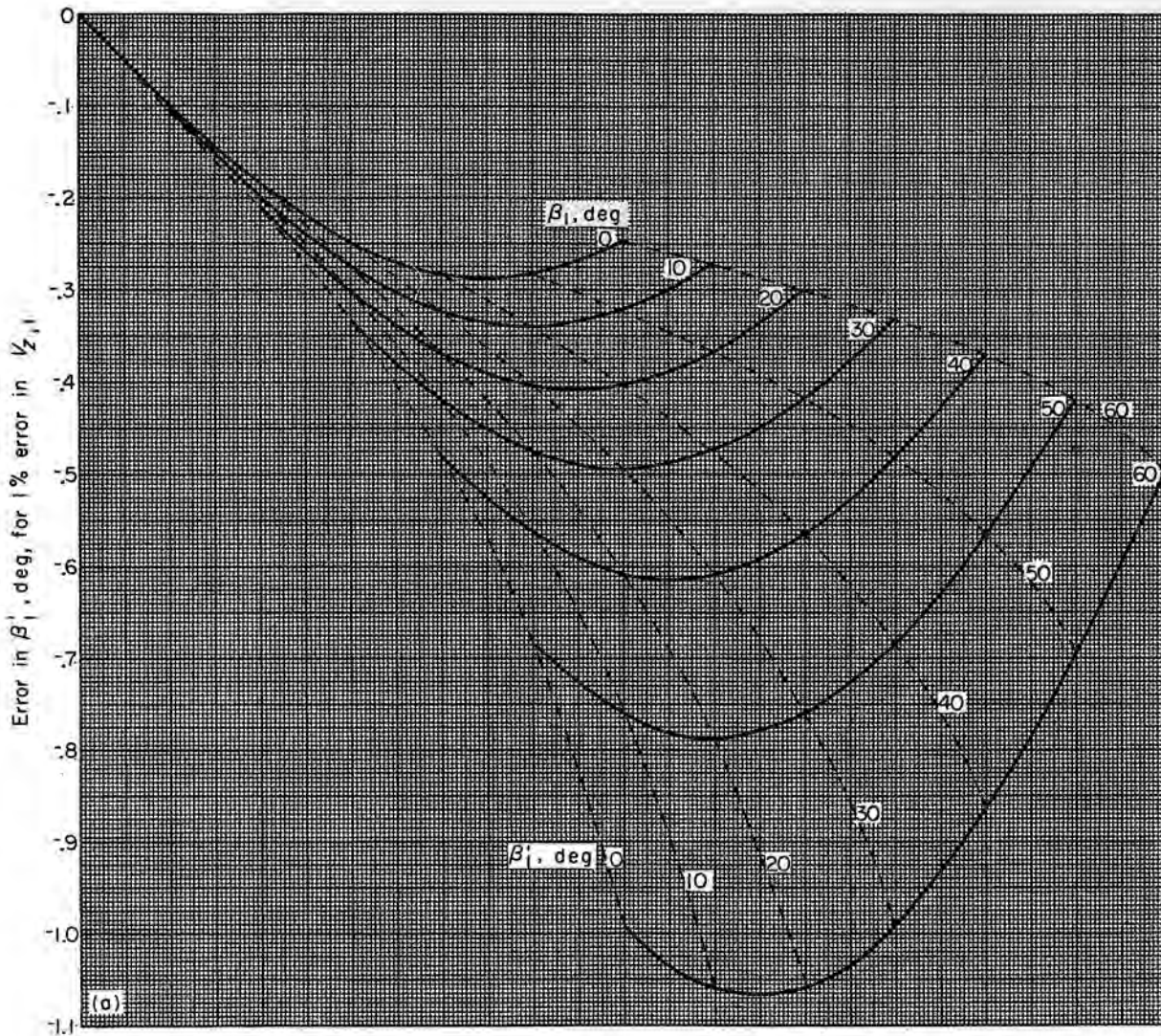FIGURE 306.—Effect of design errors on relative stagnation enthalpy.

(b) Absolute air angle (eq. (dC-ii)).

FIGURE 306.—Continued. Effect of design errors on relative stagnation enthalpy.

(c) Stagnation enthalpy (eq. (dC-iv)).

FIGURE 306.—Concluded.   Effect of design errors on relative stagnation enthalpy.

(a) Stagnation pressure, local specific mass flow, or stagnation enthalpy (eq. (dD–i,iii,iv))

FIGURE 307.—Effect of design errors on relative air angle.

$$(\Delta\beta')_{\text{iv, viii}} = -\cos^2\beta'(1-\tan\beta\tan\beta')\Delta\beta \qquad \text{(mB–iv, viii)}$$
$$\text{(fig. 317(c))}$$

$$(\Delta\bar{\omega})_{\text{ii}} = -\left[\frac{1}{1-\left(1+\dfrac{\gamma-1}{2}M_0^2\right)^{-\frac{\gamma}{\gamma-1}}} - \bar{\omega}\right]\frac{\Delta P_1}{P_1} \qquad \text{(mC–ii)}$$
$$\text{(fig. 318)}$$

$$(\Delta\bar{\omega}')_{\text{ii}} = \frac{\bar{\omega}'}{\Omega}\frac{\Delta P_1}{P_1} \qquad \text{(mD–ii)}$$
$$\text{(fig. 319)}$$

$$(\Delta\bar{\omega}')_{\text{iii}} = -\frac{\gamma}{\gamma-1}\frac{\bar{\omega}'}{\Omega}\frac{\Delta T_1}{T_1} \qquad \text{(mD–iii)}$$

$$\left(\text{fig. 319, multiply result by } -\frac{\gamma}{\gamma-1}, \text{ substitute } T_1 \text{ for } P_1\right)$$
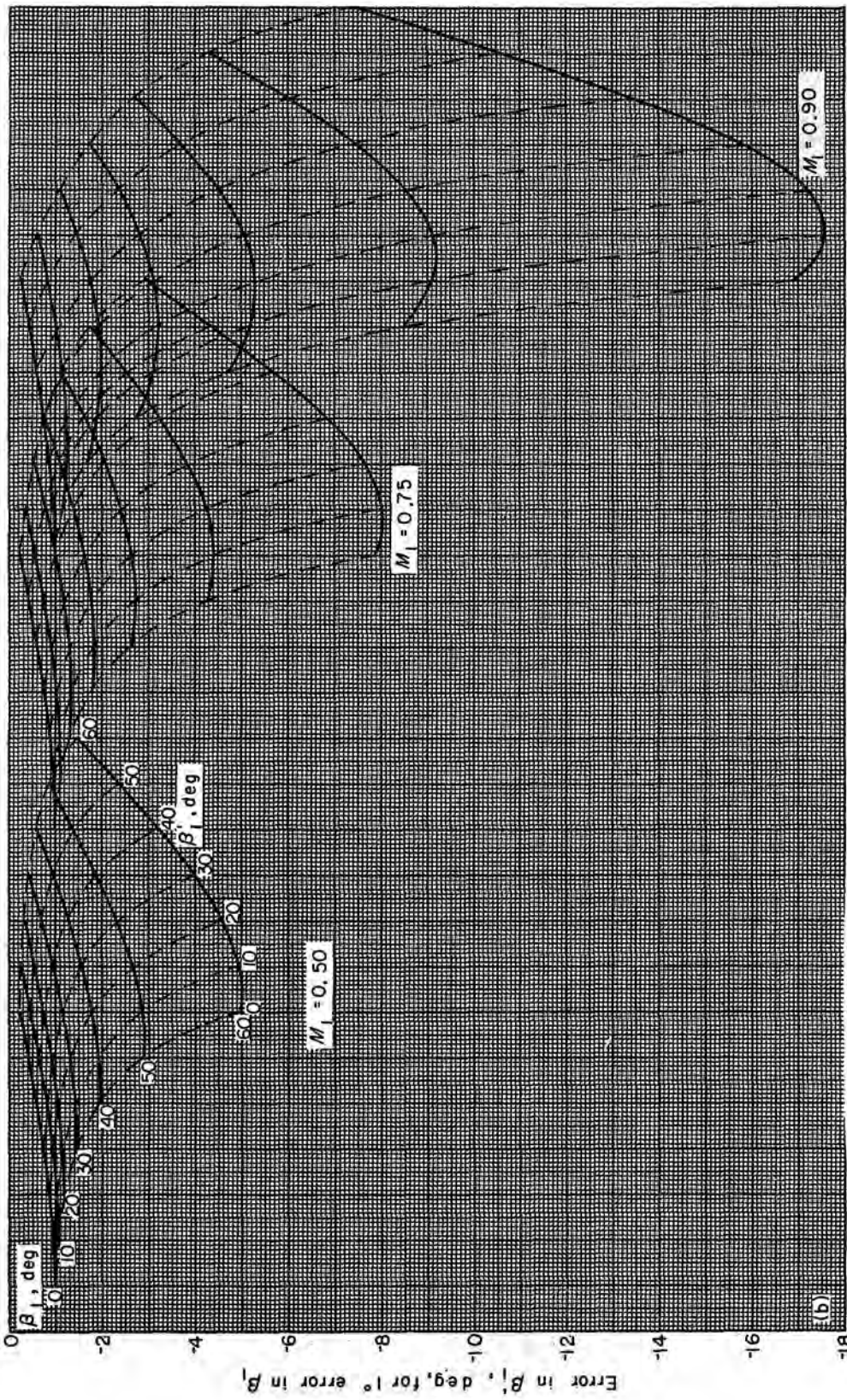
(b) Absolute air angle (eq. (dD–ii)).

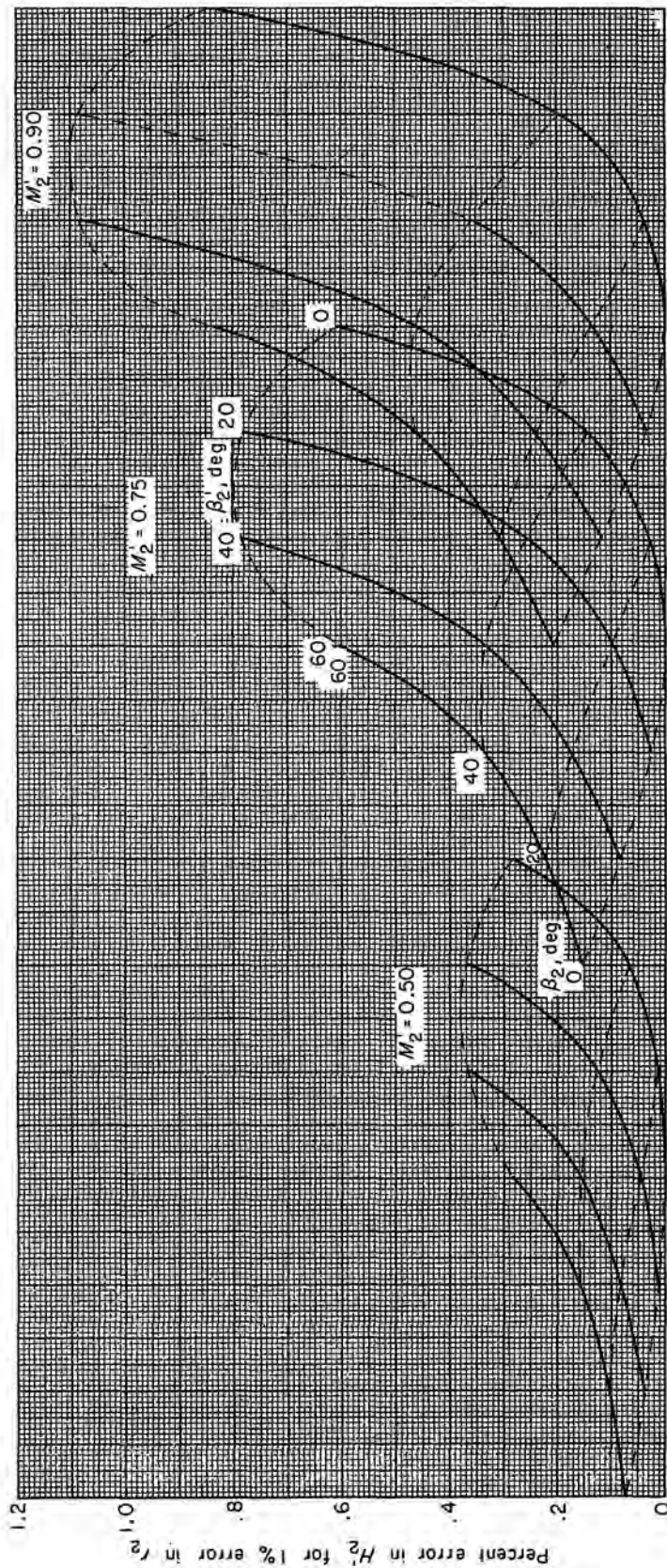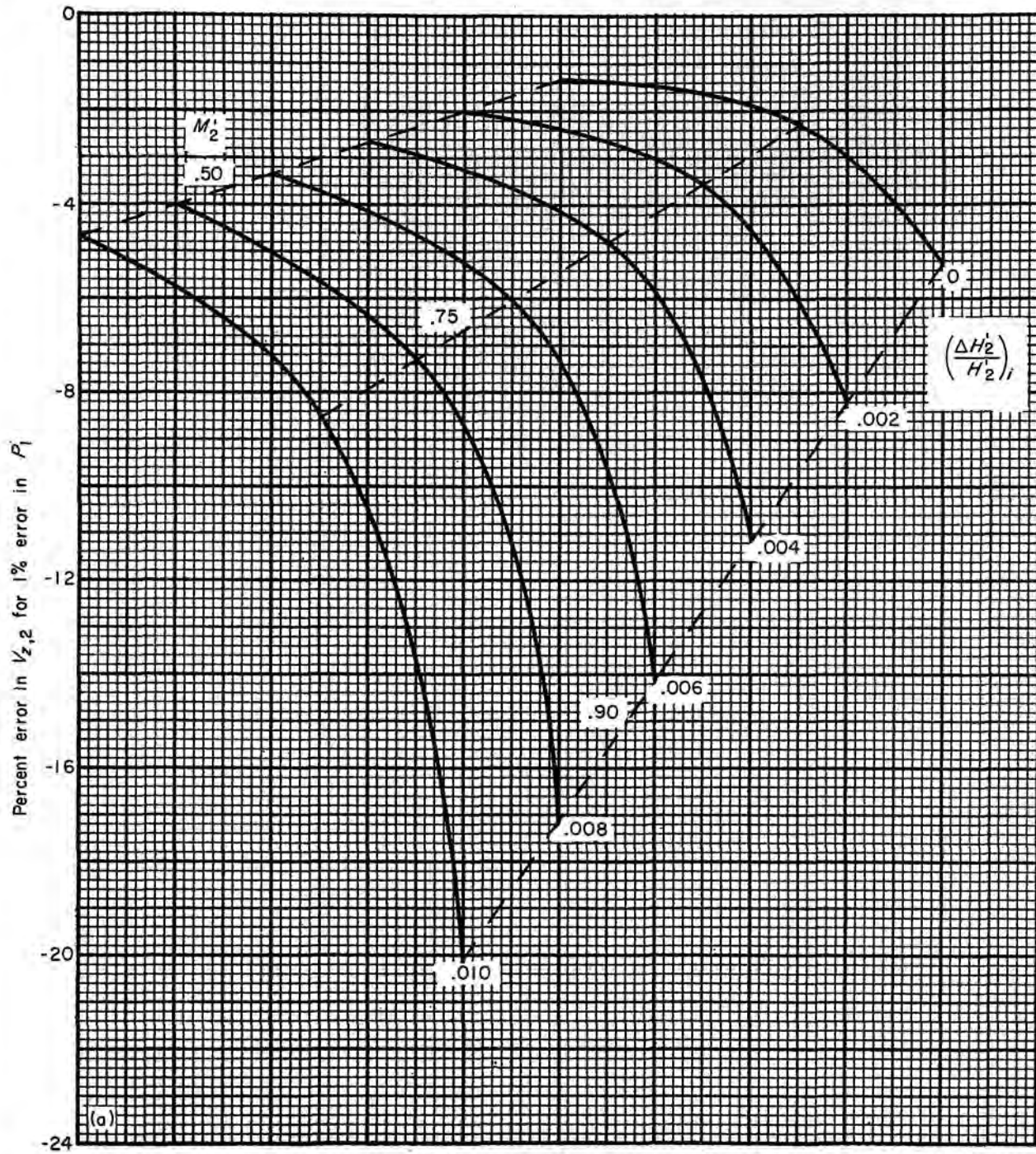FIGURE 307.—Concluded.   Effect of design errors on relative air angle.

FIGURE 308.—Effect of design error in radius to blade element on relative stagnation enthalpy (eq. (dE–viii)).
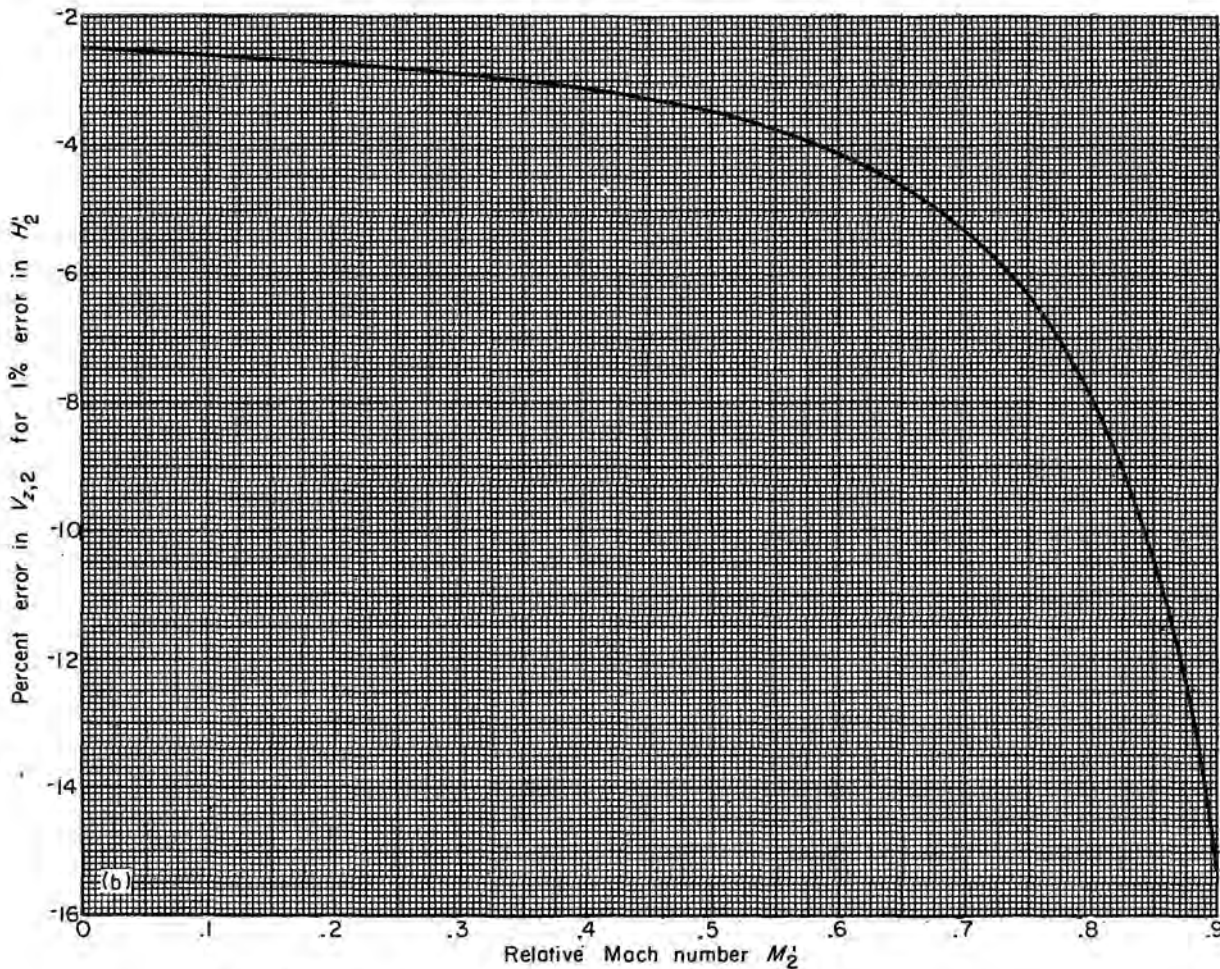
(a) Stagnation pressure (eq. (dF-i)).

FIGURE 309.—Effect of design errors on axial velocity downstream of rotor.

(b) Absolute air angle or local specific mass flow (eq. (dF–ii, iii)).

FIGURE 309.—Continued.   Effect of design errors on axial velocity downstream of rotor.

$$(\Delta\overline{\omega}')_{vi} = -\frac{\overline{\omega}'}{\Omega}\frac{\Delta P_2}{P_2} \qquad\qquad\qquad (mD–vi)$$

(fig. 319, prefix minus sign to result, substitute P_2 for P_1)

$$(\Delta\overline{\omega}')_{vii} = \frac{\gamma}{\gamma-1}\frac{\overline{\omega}'}{\Omega}\frac{\Delta T_2}{T_2} \qquad\qquad\qquad (mD–vii)$$

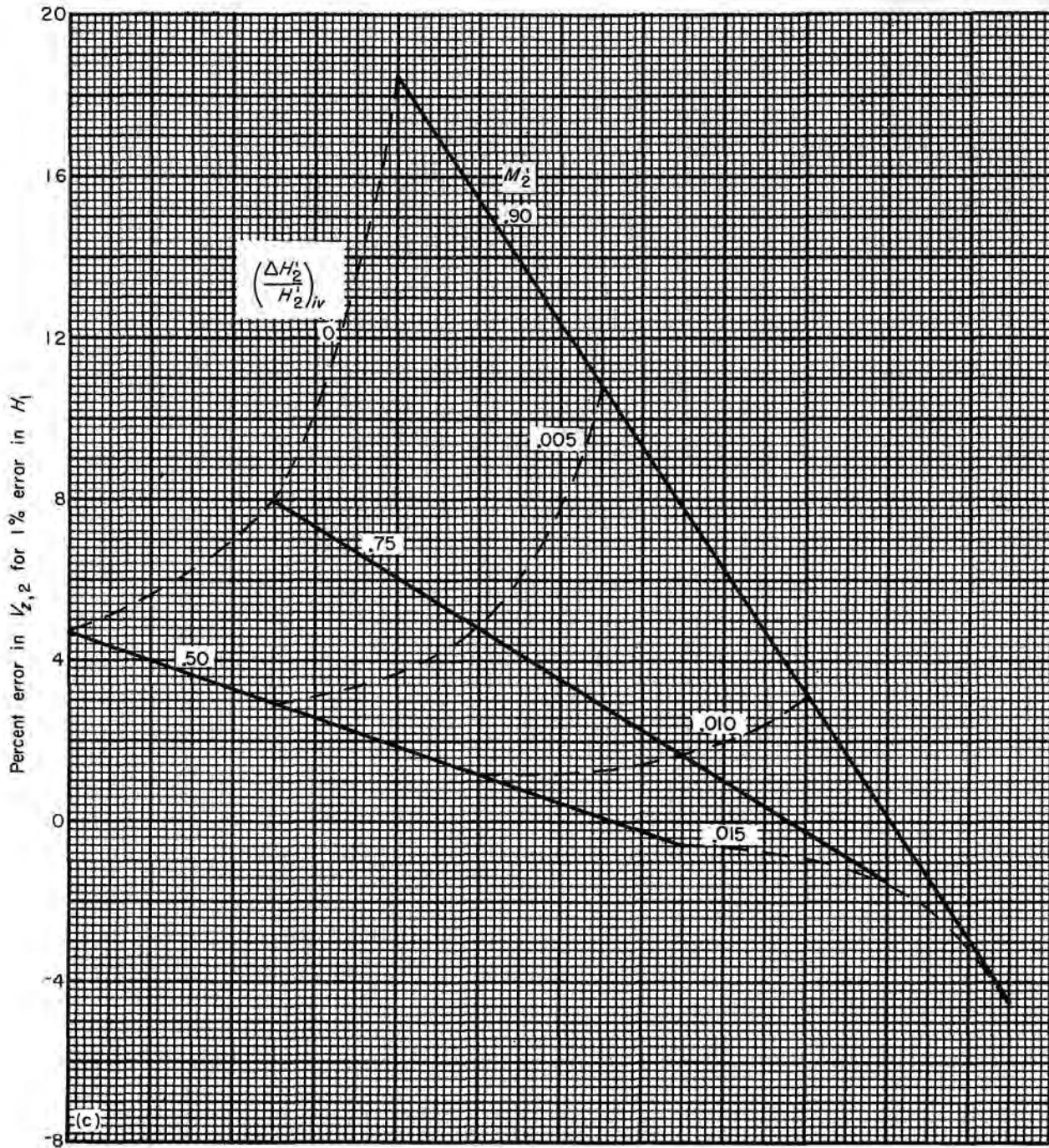(fig. 319, multiply result by $\frac{\gamma}{\gamma-1}$, substitute T_2 for P_1)

$$(\Delta\eta_{ad})_{ii} = -\frac{\gamma-1}{\gamma}\frac{\eta_{ad}\left(\frac{P_2}{P_1}\right)^{\frac{\gamma-1}{\gamma}}}{\left(\frac{P_2}{P_1}\right)^{\frac{\gamma-1}{\gamma}}-1}\frac{\Delta P_1}{P_1} \qquad (mE–ii)$$
$$\text{(fig. 320(a))}$$

$$(\Delta\eta_{ad})_{iii} = \frac{\eta_{ad}\dfrac{T_2}{T_1}}{\dfrac{T_2}{T_1}-1}\frac{\Delta T_1}{T_1} \qquad\qquad (mE–iii)$$
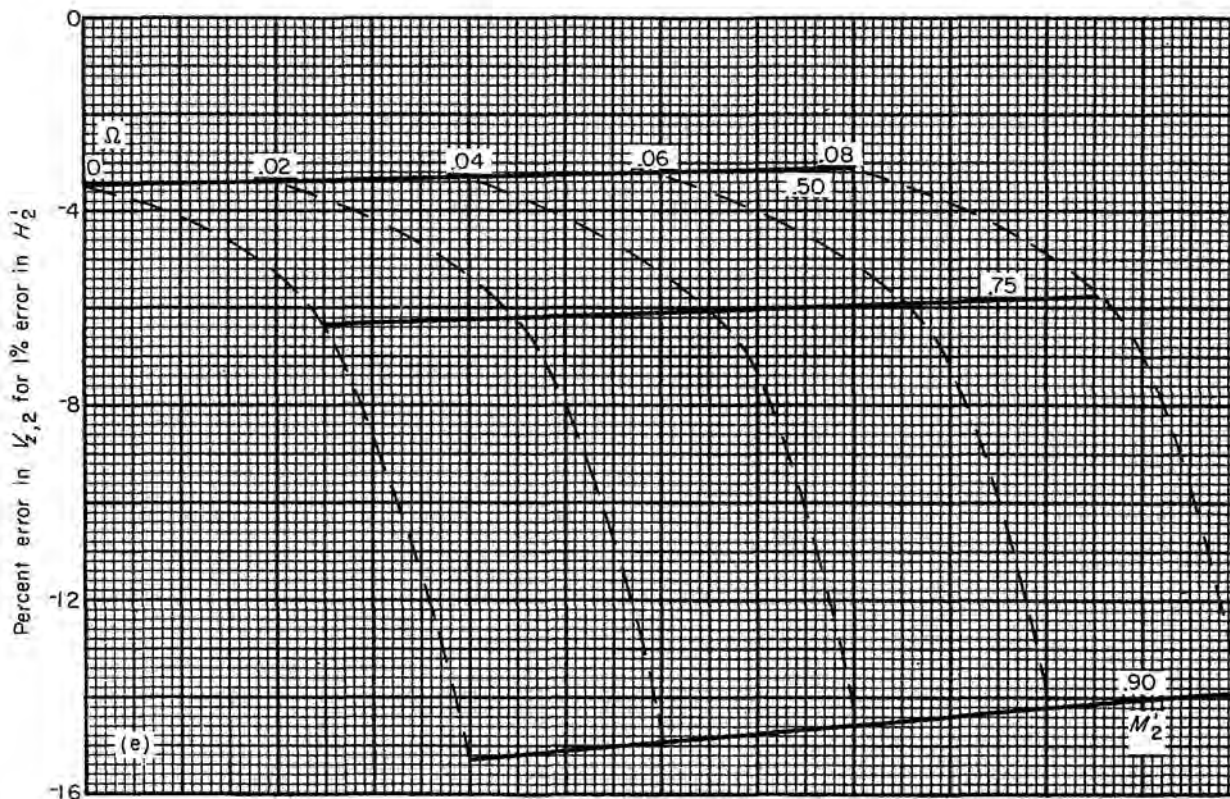$$\text{(fig. 320(b))}$$

(c) Stagnation enthalpy (eq. (dF–iv)).

FIGURE 309.—Continued. Effect of design errors on axial velocity downstream of rotor.
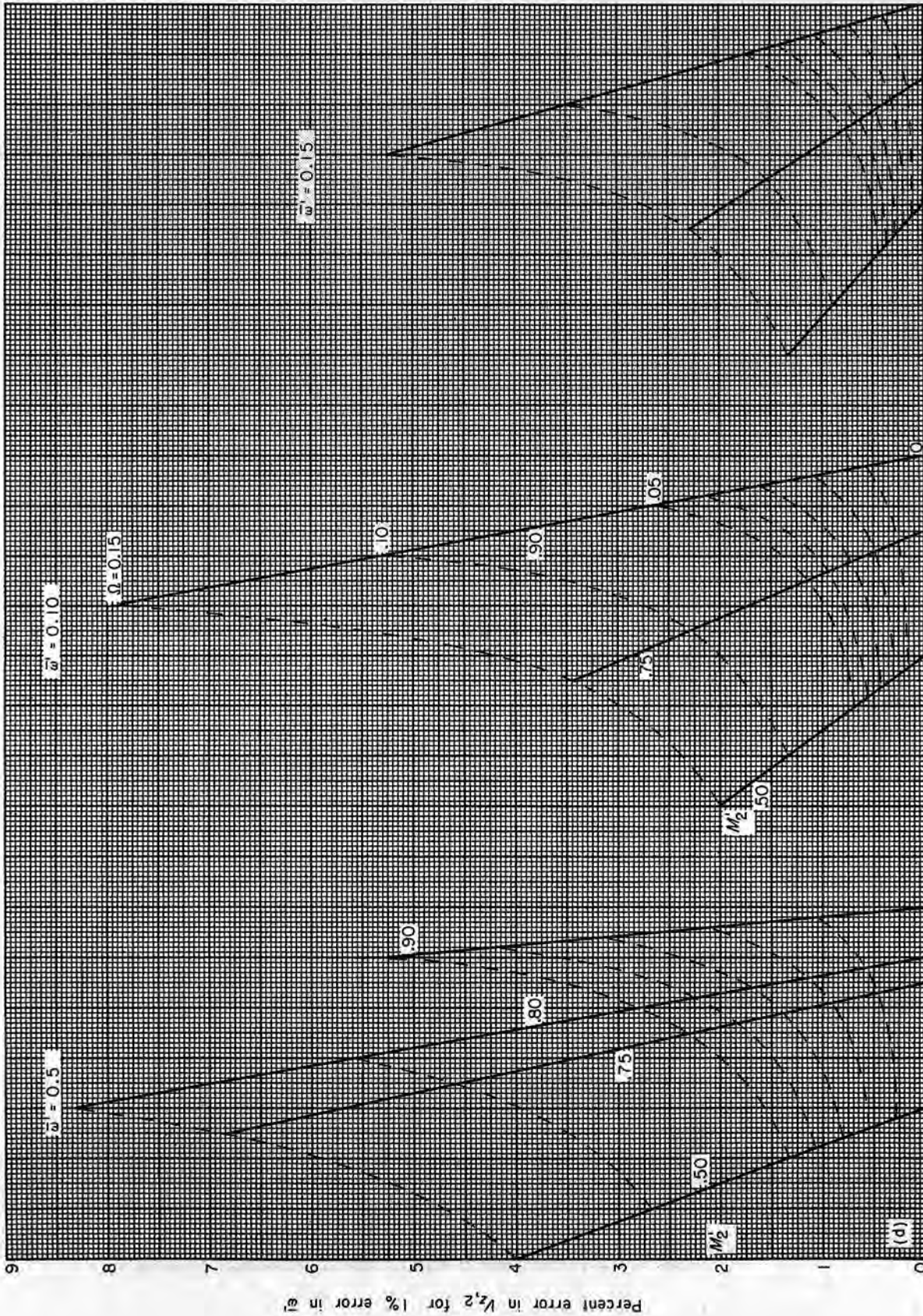
(d) Relative stagnation-pressure-loss parameter (eq. (dF–v)).

FIGURE 309.—Continued.   Effect of design errors on axial velocity downstream of rotor.

(e) Radius to blade element (eq. (dF–viii)).

FIGURE 309.—Concluded.   Effect of design errors on axial velocity downstream of rotor.

$$(\Delta\eta_{ad})_{vi}=\frac{\gamma-1}{\gamma}\frac{\eta_{ad}\left(\frac{P_2}{P_1}\right)^{\frac{\gamma-1}{\gamma}}}{\left(\frac{P_2}{P_1}\right)^{\frac{\gamma-1}{\gamma}}-1}\frac{\Delta P_2}{P_2} \qquad\qquad (\text{mE–vi})$$

(fig. 320(a), multiply result by -1, substitute $\Delta P_2/P_2$ for $\Delta P_1/P_1$)

$$(\Delta\eta_{ad})_{vii}=-\frac{\eta_{ad}\frac{T_2}{T_1}}{\frac{T_2}{T_1}-1}\frac{\Delta T_2}{T_2} \qquad\qquad (\text{mE–vii})$$
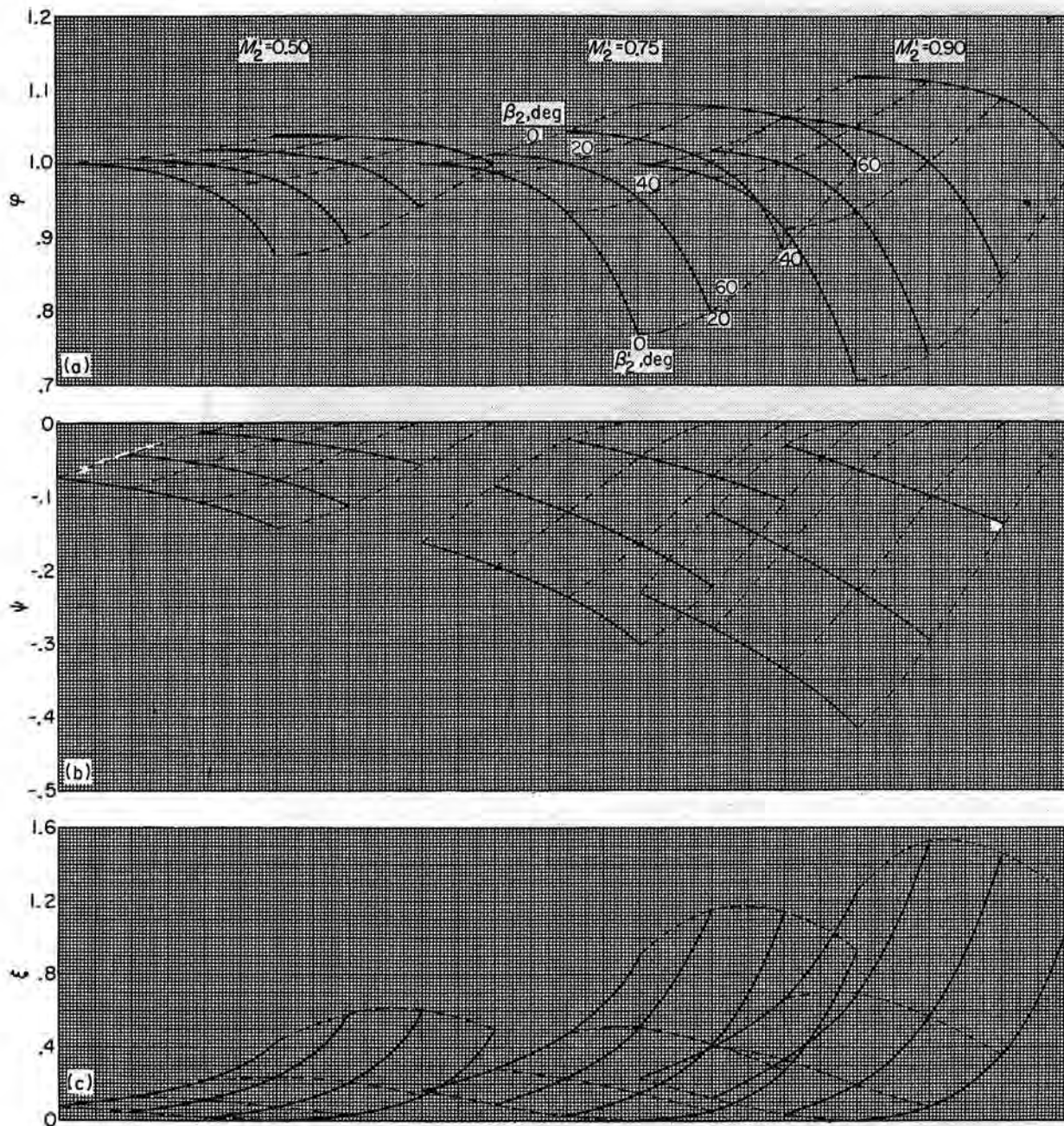
(fig. 320(b), prefix minus sign to result, substitute $\Delta T_2/T_2$ for $\Delta T_1/T_1$)

$$\left(\frac{\Delta H_{M,2}}{H_1}\right)_{i}=\frac{\gamma-1}{\gamma}\frac{\sin\beta_1\cos\beta_1(\tan\beta_1+\tan\beta_1')}{1+\frac{\gamma-1}{2}M_1^2}\frac{\Delta p_1}{p_1} \qquad (\text{mF–i})$$
$$ (\text{fig. 321(a)})$$

$$\left(\frac{\Delta H_{M,2}}{H_1}\right)_{ii}=-\frac{\gamma-1}{\gamma}\frac{\sin\beta_1\cos\beta_1(\tan\beta_1+\tan\beta_1')}{1+\frac{\gamma-1}{2}M_1^2}\frac{\Delta P_1}{P_1} \qquad (\text{mF–ii})$$

(fig. 321(a), prefix minus sign to result, substitute P_1 for p_1)

(a) Factor ϕ (eqs. (dG–i, iv) and (417)).

(b) Factor ψ (eqs. (dG–i, iv) and (418)).

(c) Factor ξ (eqs. (dG–viii) and (419)).

FIGURE 310.—Factors ϕ, ψ, and ξ as functions of relative Mach number, relative air angle, and absolute air angle.
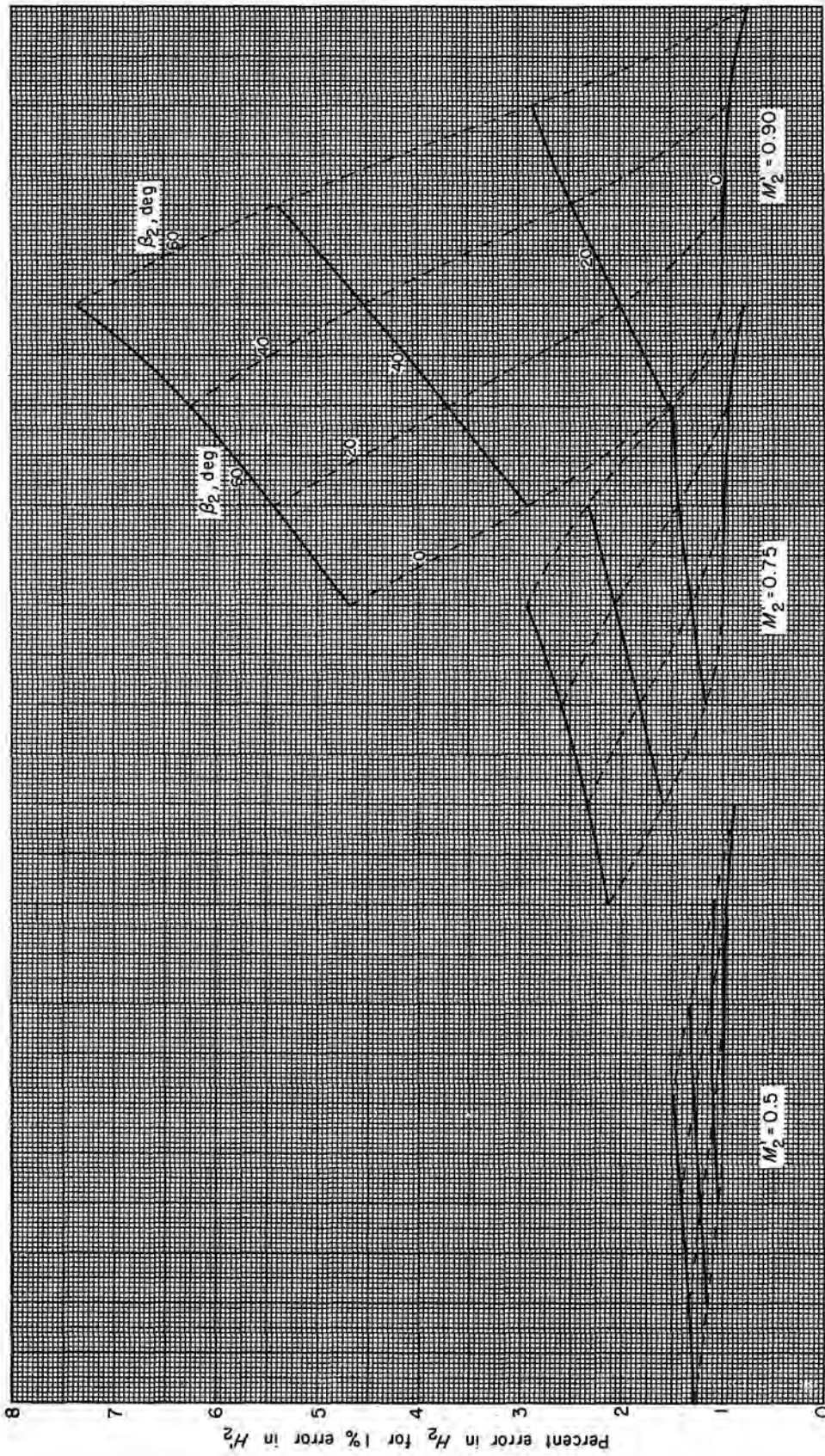
FIGURE 311.—Effect of design error in absolute air angle or local specific mass flow on stagnation enthalpy (eq. (dG–ii, iii)).
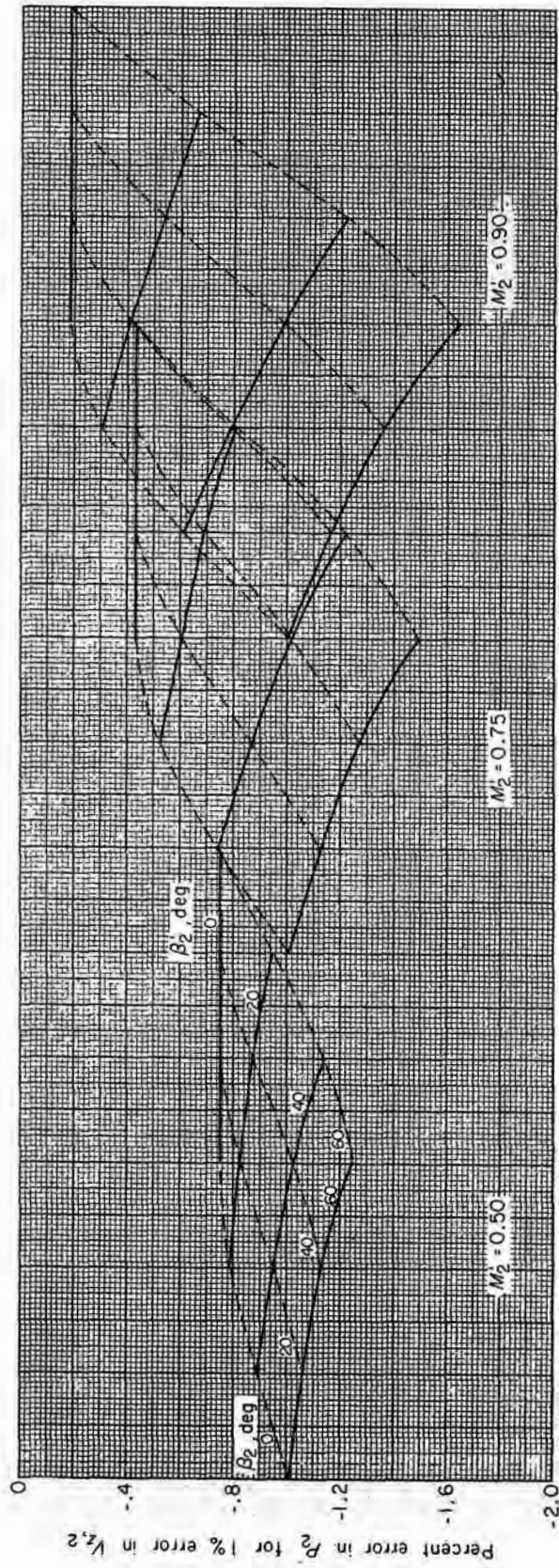
FIGURE 312.—Effect of design error in relative stagnation-pressure-loss parameter on stagnation pressure (eq. (dH–v)).
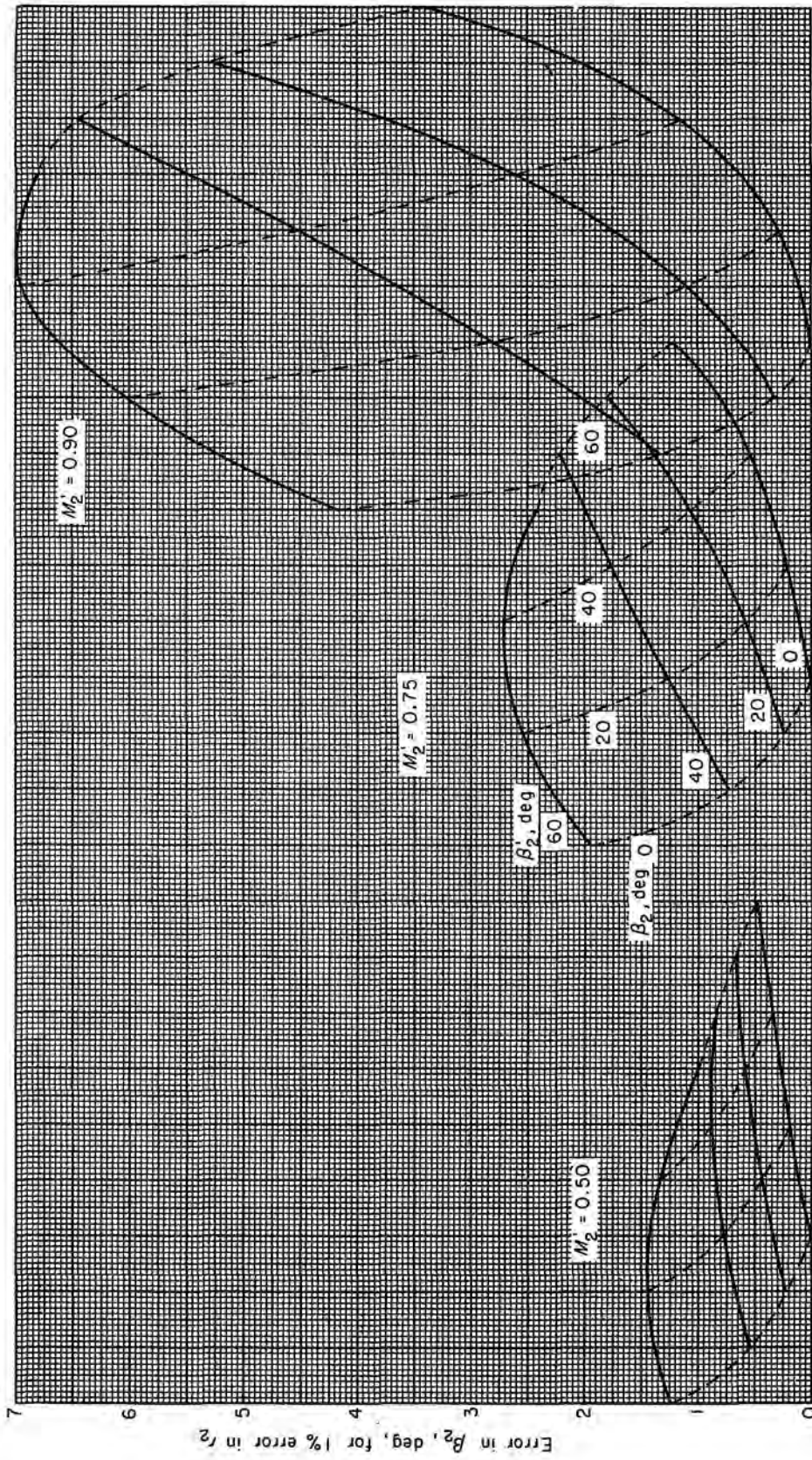
FIGURE 313.—Effect of design error in radius to blade element on absolute air angle (eq. (dJ–viii)).
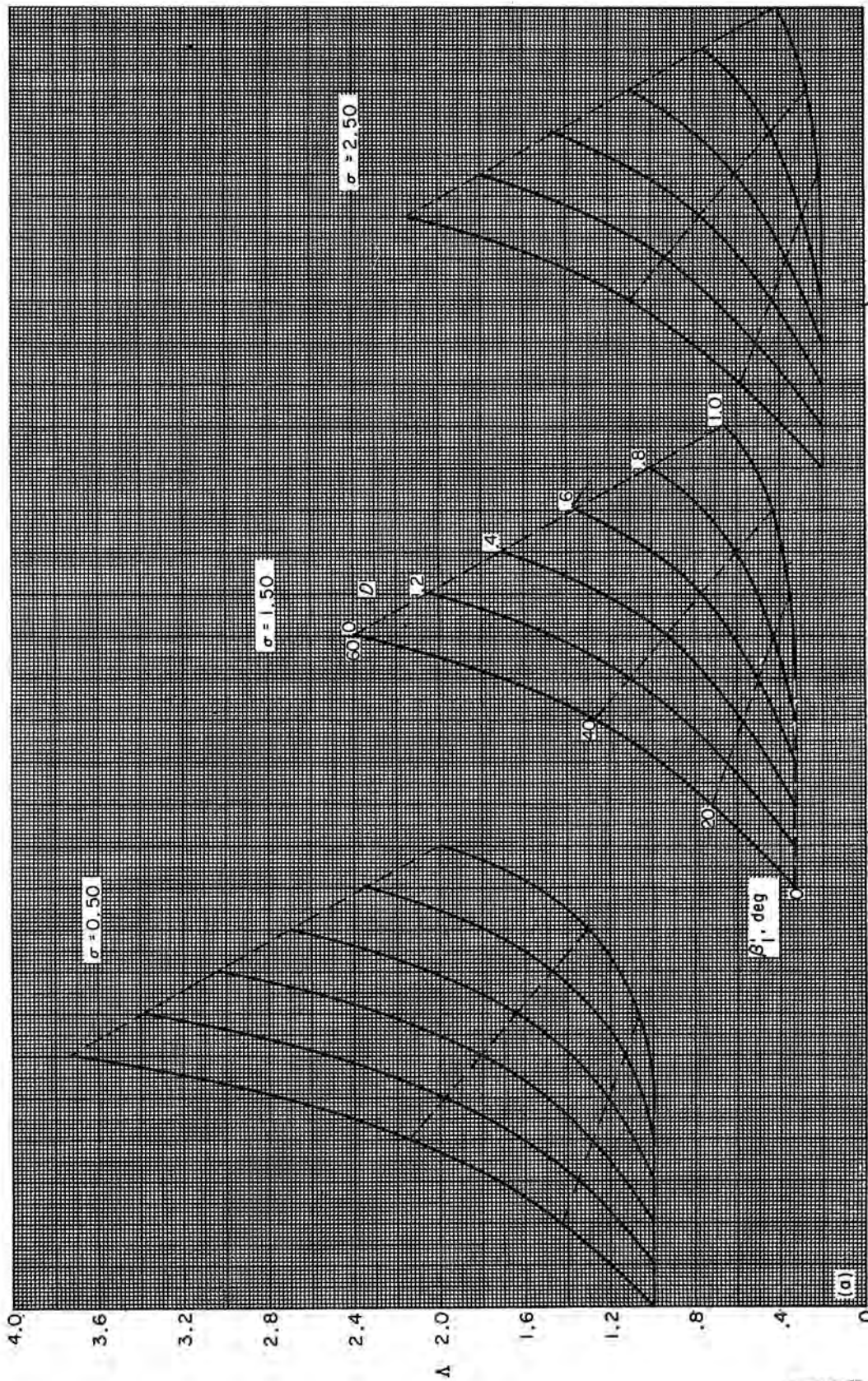
(a) Factor Λ (eqs. (dK–i–iv) and (420)).

FIGURE 314.—Factors Λ and Γ as functions of relative air angle, solidity, and diffusion factor.
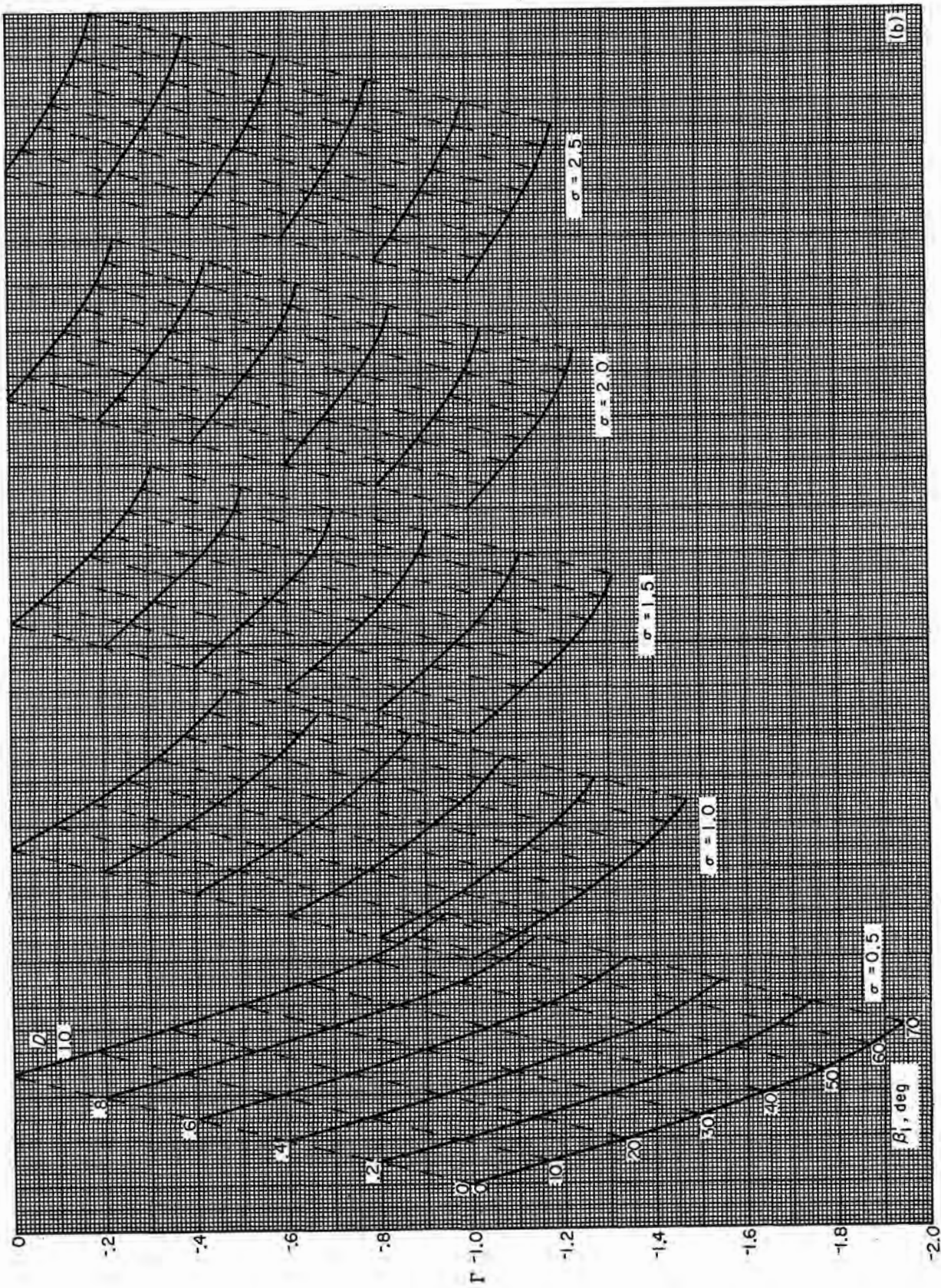
(b) Factor Γ (eqs. (dK-i-iv) and (421)).

FIGURE 314.—Concluded. Factors Λ and Γ as functions of relative air angle, solidity, and diffusion factor.

FIGURE 315.—Effect of design error in relative air angle on diffusion factor (eq. (dK–vi)).

$$\left(\frac{\Delta H_{M,2}}{H_1}\right)_{\text{iii}}=\left[1-\frac{\frac{\gamma-1}{2}M_1^2\sin\beta_1\cos\beta_1(\tan\beta_1+\tan\beta_1')}{1+\frac{\gamma-1}{2}M_1^2}\right]\frac{\Delta T_1}{T_1} \qquad (\text{mF–iii})$$

(fig. 321(c), substitute subscript 1 for 2 and subtract from 1)

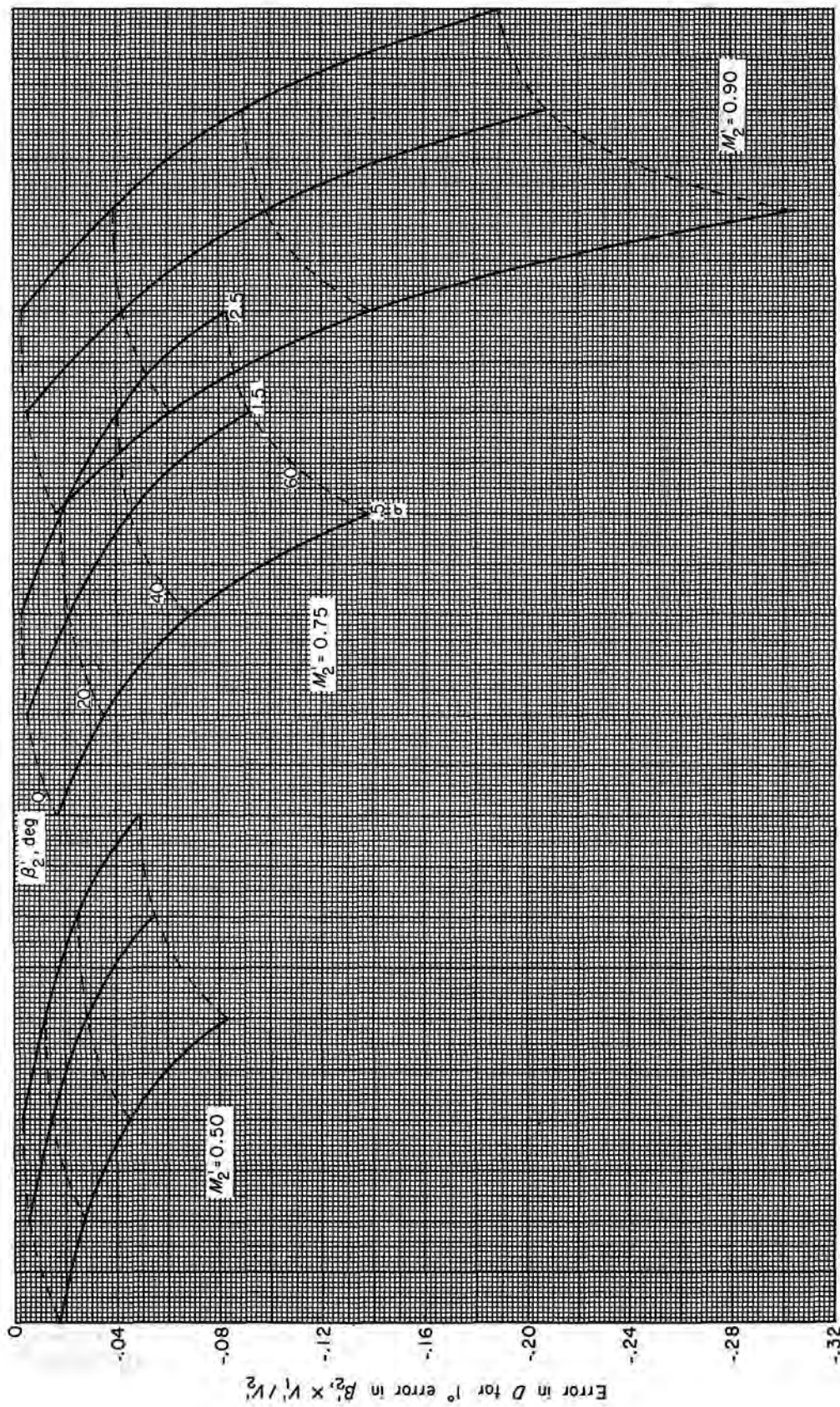$$\left(\frac{\Delta H_{M,2}}{H_1}\right)_{\text{iv}}=-\frac{\pi(\gamma-1)M_1^2\cos^2\beta_1(\tan\beta_1+\tan\beta_1')}{180\left(1+\frac{\gamma-1}{2}M_1^2\right)}\Delta\beta_1 \qquad \begin{array}{l}(\text{mF–iv})\\(\text{fig. 321(b)})\end{array}$$

$$\left(\frac{\Delta H_{M,2}}{H_{M,2}}\right)_{\text{v}}=-\frac{\gamma-1}{\gamma}\frac{\sin\beta_2\cos\beta_2(\tan\beta_2+\tan\beta_2')}{1+\frac{\gamma-1}{2}M_2^2}\frac{\Delta p_2}{p_2} \qquad (\text{mF–v})$$

(fig. 321(a), substitute subscript 2 for 1 and prefix minus sign)

$$\left(\frac{\Delta H_{M,2}}{H_{M,2}}\right)_{\text{vi}}=\frac{\gamma-1}{\gamma}\frac{\sin\beta_2\cos\beta_2(\tan\beta_2+\tan\beta_2')}{1+\frac{\gamma-1}{2}M_2^2}\frac{\Delta P_2}{P_2} \qquad (\text{mF–vi})$$

(fig. 321(a), substitute subscript 2 for 1, and P_2 for p_1)

$$\left(\frac{\Delta H_{M,2}}{H_{M,2}}\right)_{\text{vii}}=\frac{\gamma-1}{2}\frac{M_2^2\sin\beta_2\cos\beta_2(\tan\beta_2+\tan\beta_2')}{1+\frac{\gamma-1}{2}M_2^2}\frac{\Delta T_2}{T_2} \qquad \begin{array}{l}(\text{mF–vii})\\(\text{fig. 321(c)})\end{array}$$

$$\left(\frac{\Delta H_{M,2}}{H_{M,2}}\right)_{\text{viii}}=\frac{\pi(\gamma-1)M_2^2\cos^2\beta_2(\tan\beta_2+\tan\beta_2')}{180\left(1+\frac{\gamma-1}{2}M_2^2\right)}\Delta\beta_2 \qquad (\text{mF–viii})$$

(fig. 321(b), substitute subscript 2 for 1 and multiply result by -1)

$$M_1^2(\Delta D)_{\text{i}}=\frac{\cos^2\beta_1'}{\gamma}\left[\frac{\cos\beta_1'(\tan\beta_1+\tan\beta_1')}{2\sigma}-\left(\frac{\sin\beta_1'}{2\sigma}+1-D\right)(1-\tan\beta_1\tan\beta_1')\right]\frac{\Delta p_1}{p_1} \qquad \begin{array}{l}(\text{mG–i})\\(\text{fig. 322(a)})\end{array}$$

$$M_1^2(\Delta D)_{\text{ii}}=-\frac{\cos^2\beta_1'}{\gamma}\left[\frac{\cos\beta_1'(\tan\beta_1+\tan\beta_1')}{2\sigma}-\left(\frac{\sin\beta_1'}{2\sigma}+1-D\right)(1-\tan\beta_1\tan\beta_1')\right]\frac{\Delta P_1}{P_1} \qquad (\text{mG–ii})$$

(fig. 322(a), prefix minus sign to result, substitute P_1 for p_1)

$$(\Delta D)_{\text{iii}}=-\frac{\cos^2\beta_1'}{2}\left[\frac{\cos\beta_1(\tan\beta_1+\tan\beta_1')}{2\sigma}-\left(\frac{\sin\beta_1'}{2\sigma}+1-D\right)(1-\tan\beta_1\tan\beta_1')\right]\frac{\Delta T_1}{T_1} \qquad (\text{mG–iii})$$

(fig. 322(a), multiply result by $-\gamma/2$, substitute T_1 for p_1)

$$(\Delta D)_{\text{iv}}=-\frac{\pi}{180}\cos^2\beta_1'\left[\frac{\cos\beta_1'(1-\tan\beta_1\tan\beta_1')}{2\sigma}+\left(\frac{\sin\beta_1'}{2\sigma}+1-D\right)(\tan\beta_1+\tan\beta_1')\right]\Delta\beta_1 \qquad \begin{array}{l}(\text{mG–iv})\\(\text{fig. 322(b)})\end{array}$$

$$M_2^2\frac{V_1'}{V_2'}(\Delta D)_{\text{v}}=\frac{\cos^2\beta_2'}{\gamma}\left[\left(1+\frac{\sin\beta_2'}{2\sigma}\right)(1-\tan\beta_2\tan\beta_2')-\frac{\cos\beta_2'}{2\sigma}(\tan\beta_2+\tan\beta_2')\right]\frac{\Delta p_2}{p_2} \qquad \begin{array}{l}(\text{mG–v})\\(\text{fig. 322(c)})\end{array}$$
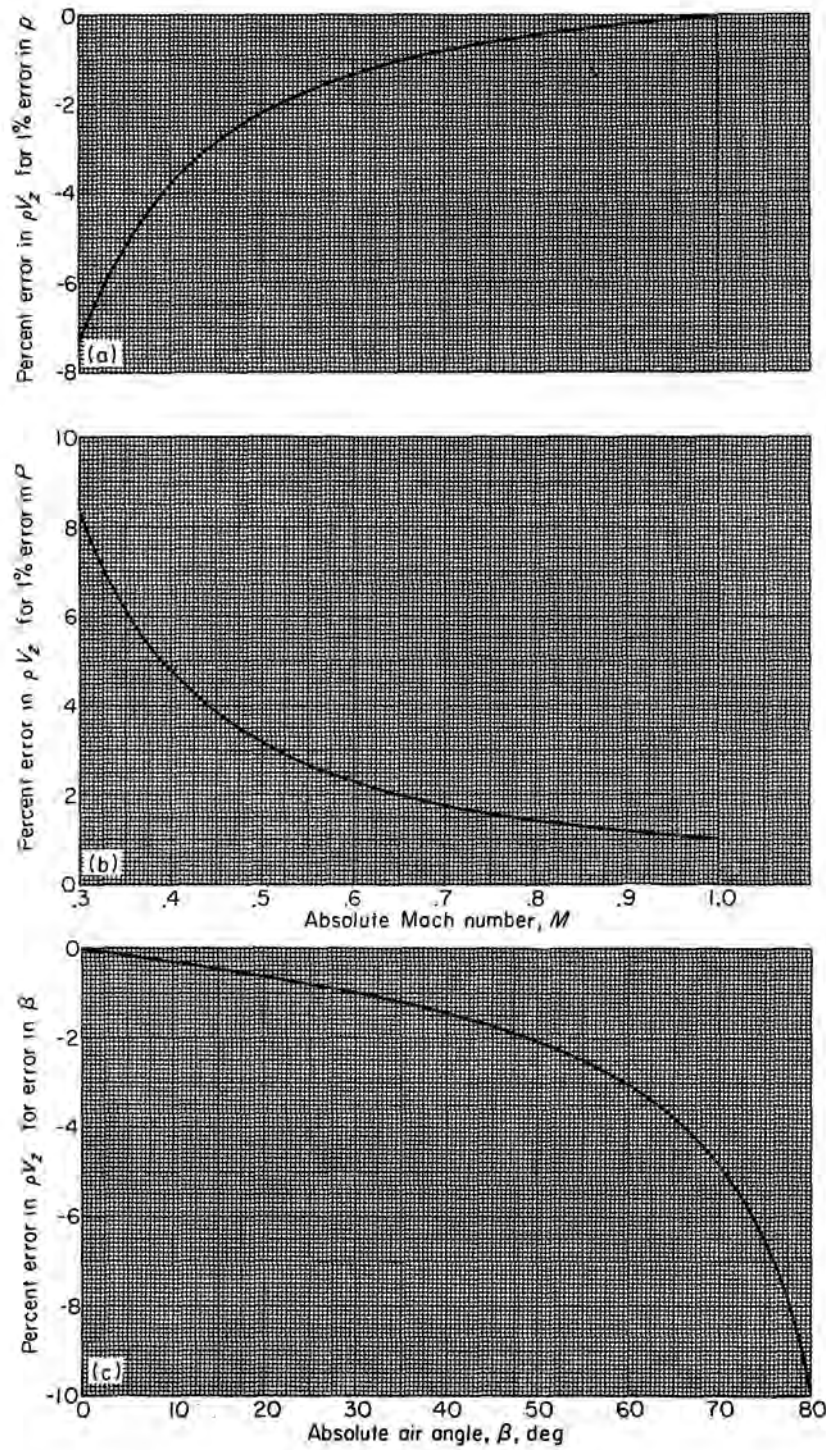
(a) Static pressure (eq. (mA–i, v)).

(b) Stagnation pressure (eq. (mA–ii, vi)).

(c) Absolute air angle (eq. (mA–iv, viii)).

FIGURE 316.—Effect of measurement errors on calculated value of local specific mass flow.
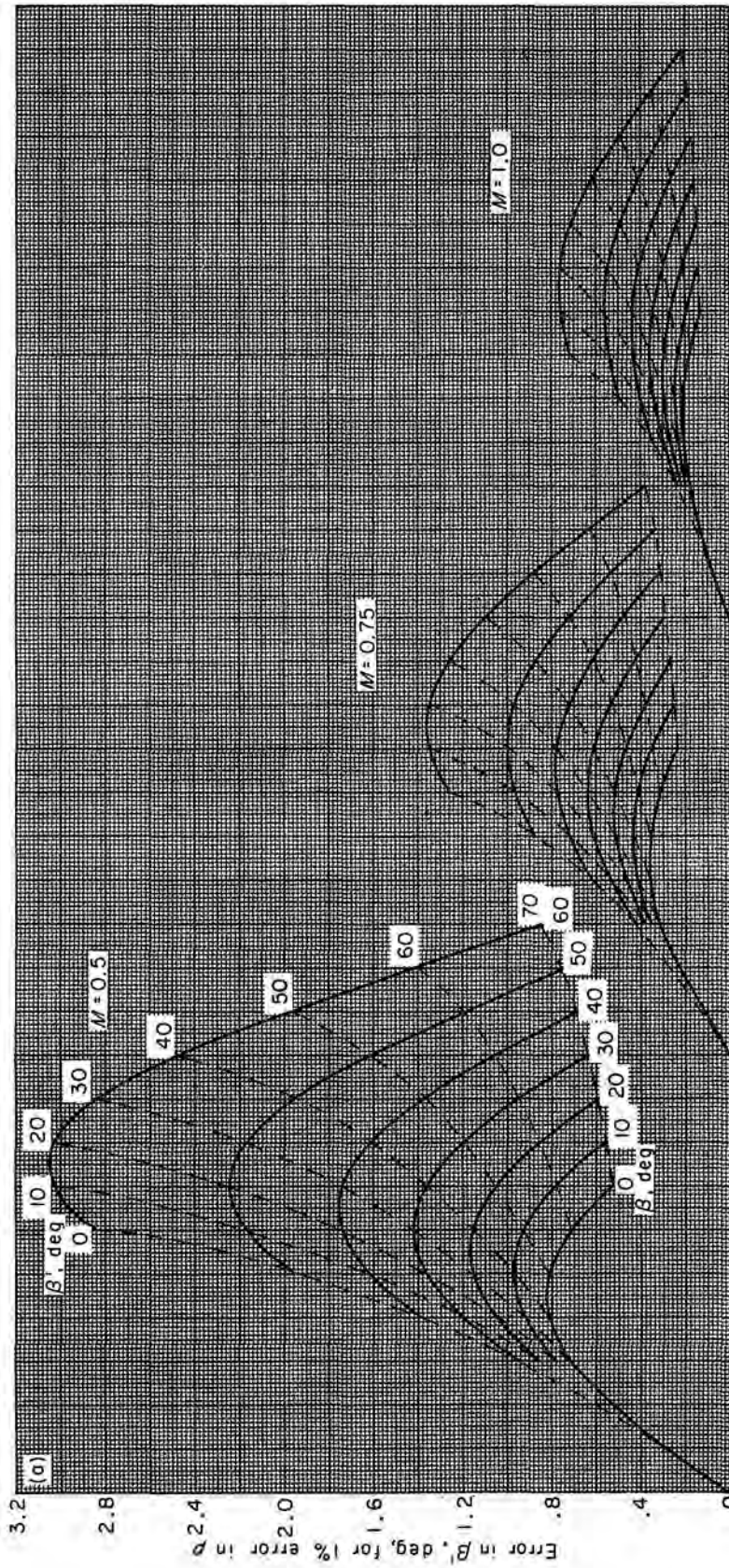
(a) Static pressure (eq. (mB−i, v)).

FIGURE 317.—Effect of measurement errors on calculated value of relative air angle.
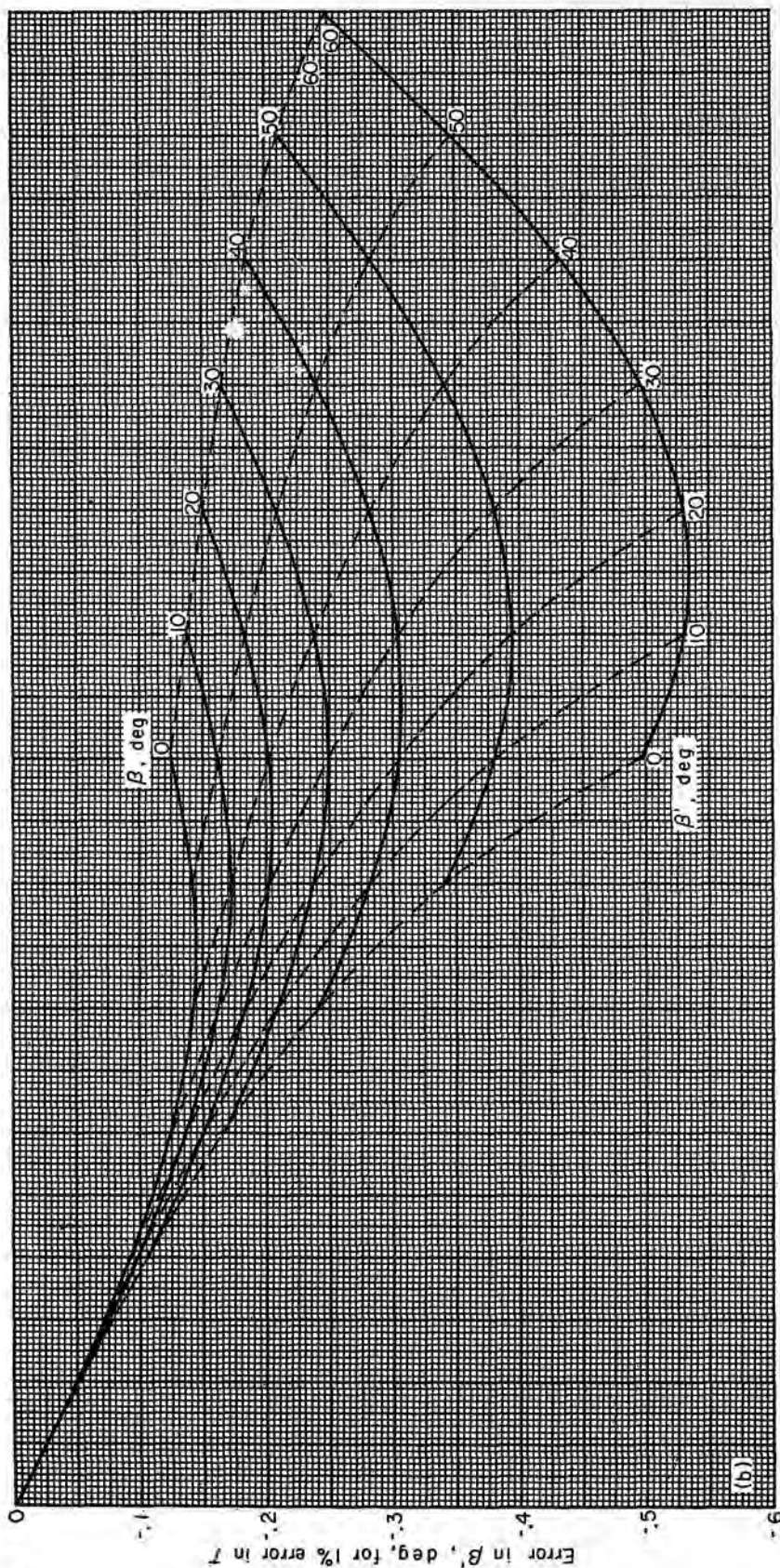
(b) Stagnation temperature (eq. (mB-iii, vii)).

FIGURE 317.—Continued.   Effect of measurement errors on calculated value of relative air angle.
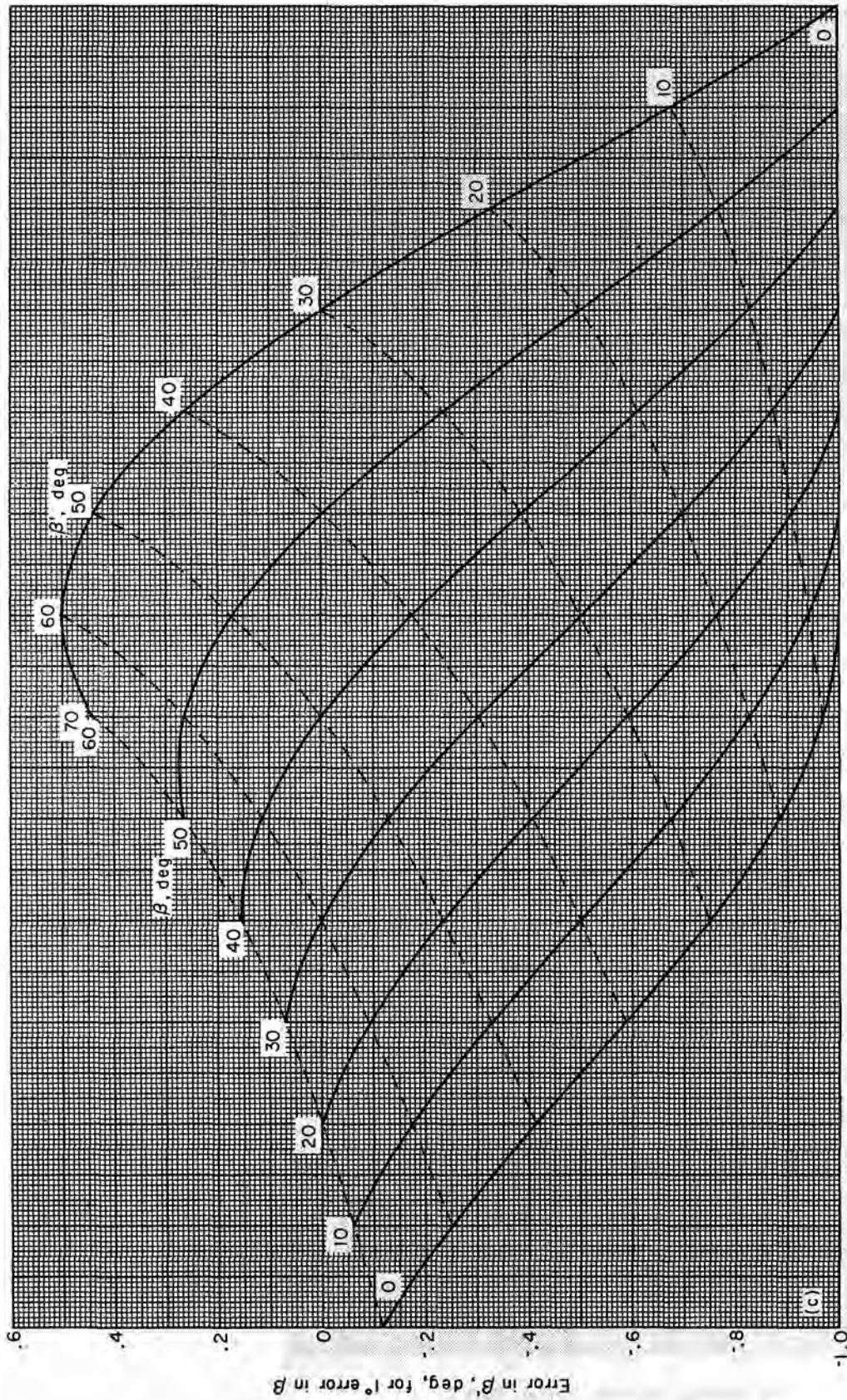
(c)　Absolute air angle (eq. (mB–iv, viii)).

FIGURE 317.—Concluded.　Effect of measurement errors on calculated value of relative air angle.

FIGURE 318.—Effect of measurement error in stagnation pressure on calculated value of absolute stagnation-pressure-loss parameter (eq. (mC–ii)).

$$M_2^2 \frac{V_1'}{V_2'} (\Delta D)_{vi} = -\frac{\cos^2 \beta_2'}{\gamma} \left[\left(1 + \frac{\sin \beta_2'}{2\sigma}\right) (1 - \tan \beta_2 \tan \beta_2') - \frac{\cos \beta_2'}{2\sigma} (\tan \beta_2 + \tan \beta_2') \right] \frac{\Delta P_2}{P_2} \quad \text{(mG–vi)}$$

(fig. 322(c), prefix minus sign to result, substitute P_2 for p_2)

$$\frac{V_1'}{V_2'} (\Delta D)_{vii} = -\frac{\cos^2 \beta_2'}{2} \left[\left(1 + \frac{\sin \beta_2'}{2\sigma}\right) (1 - \tan \beta_2 \tan \beta_2') - \frac{\cos \beta_2'}{2\sigma} (\tan \beta_2 + \tan \beta_2') \right] \frac{\Delta T_2}{T_2} \quad \text{(mG–vii)}$$
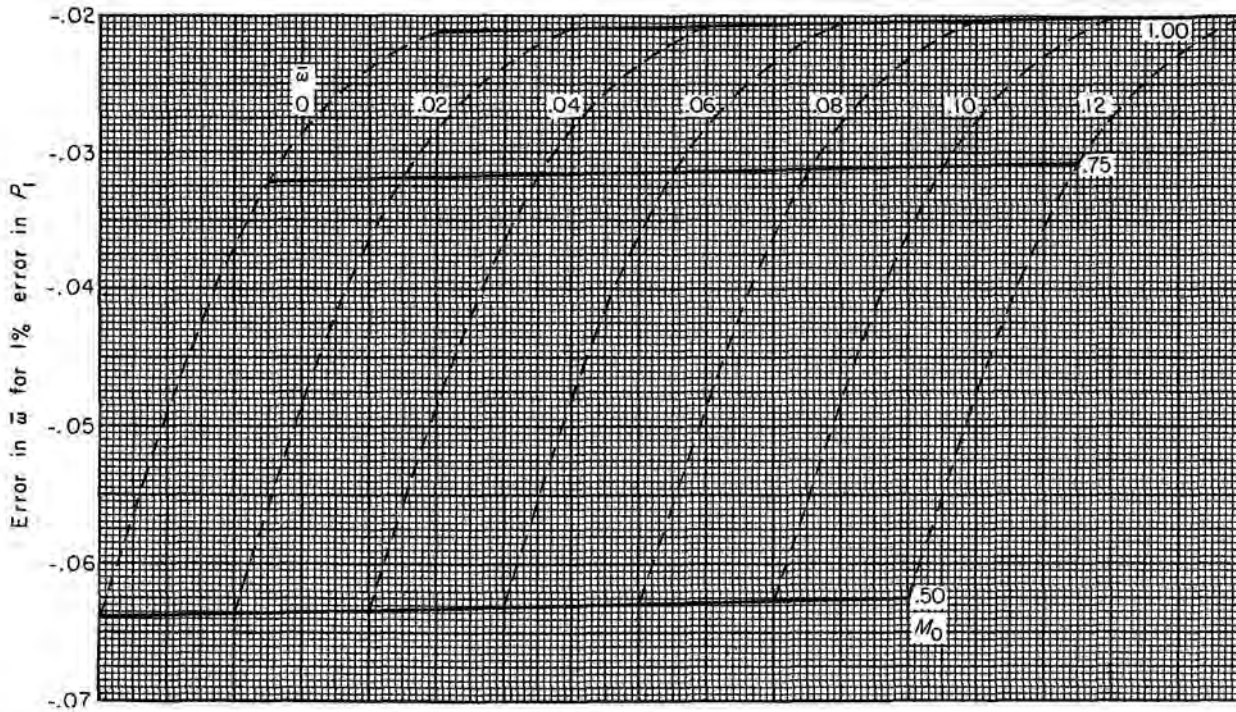
(fig. 322(c), multiply result by $-\gamma/2$, substitute T_2 for p_2)

$$\frac{V_1'}{V_2'} (\Delta D)_{viii} = \frac{\pi}{180} \cos^2 \beta_2' \left[\left(1 + \frac{\sin \beta_2'}{2\sigma}\right) (\tan \beta_2 + \tan \beta_2') + \frac{\cos \beta_2'}{2\sigma} (1 - \tan \beta_2 \tan \beta_2') \right] \Delta \beta_2 \quad \text{(mG–viii)}$$

(fig. 322(d)

The measurement-error formulas give the effects of independent measurement errors. For instance, formula (mE–ii) gives the error in calculated value of blade-element efficiency due to a measurement error solely in P_1. However, in many experimental compressors, the measured value of P_2 depends on the measured value of P_1, such as when P_2 is obtained by adding a measured pressure rise to the value of P_1. For such cases $\Delta P_2 = \Delta P_1$, and the effects of ΔP_1 on $\bar{\omega}'$ and η_{ad} become quite small because of the similarity, except for sign, of the –ii and –vi formulas. The

same situation prevails for measurements of T_2 that depend upon T_1.

READING OF CARPET PLOTS

As discussed in reference 347, carpet and lattice plots permit the charting of two or three independent variables and provide a means for interpolation among these variables. A fourth variable can also be charted by the use of an ordinate scale that is a function of the dependent variable and the fourth independent variable. An example of a four-variable chart is figure 302, the plot of the
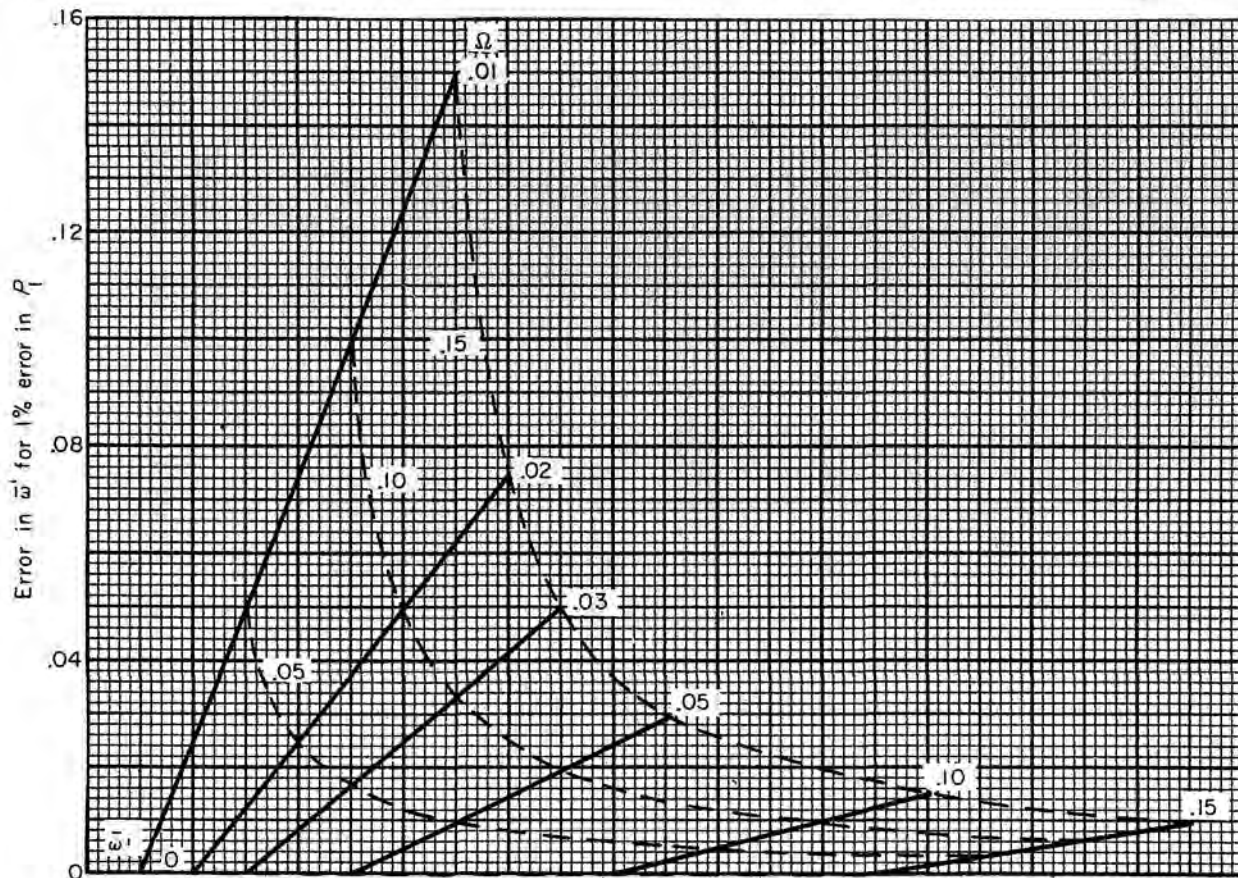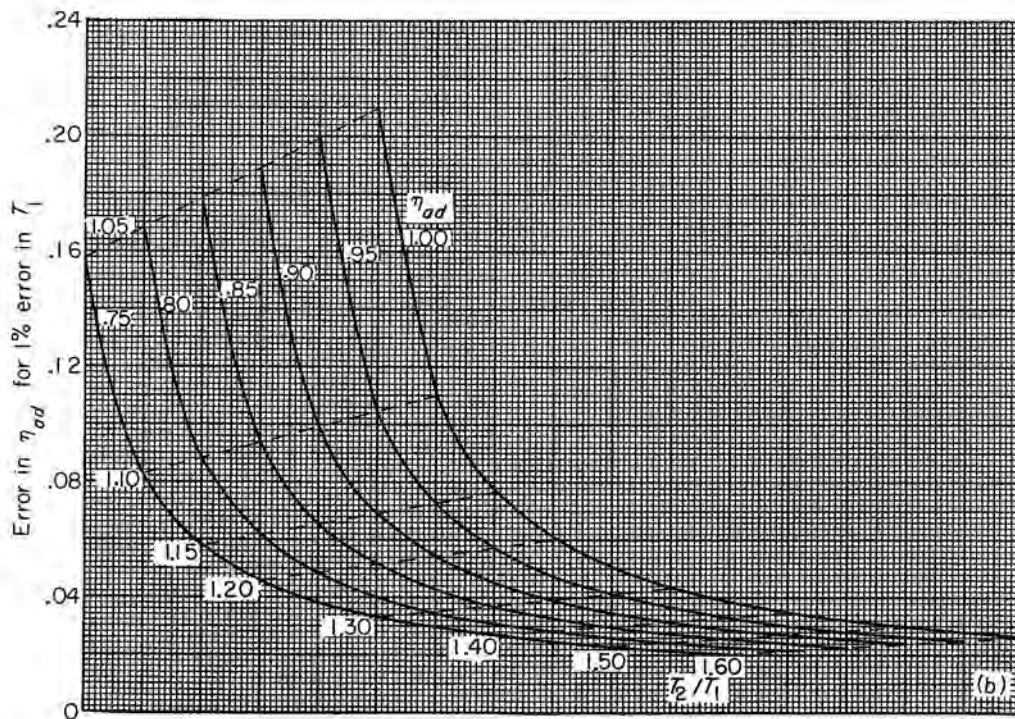
FIGURE 319.—Effect of measurement error in stagnation pressure on calculated value of relative stagnation-pressure-loss parameter (eq. (mD–ii)).

formula for relative stagnation enthalpy ratio (formula (415)), for which the independent variables are β_2, β_2', M_2', and r_2/r_1. The chart consists of nine carpets in β_2 and β_2', each of which corresponds to a given value of M_2' and r_2/r_1. The carpets for different values of M_2' are displaced horizontally by distances proportional to the changes in M_2', thus forming three lattices for three values of r_2/r_1. In order to provide a means for interpolation of r_2/r_1, these lattices are displaced horizontally by distances proportional to the changes in r_2/r_1. It is then necessary, for clear reading of the charts, to displace the lattices vertically and to incorporate r_2/r_1 into the ordinate function. A value of H_2'/H_1' for given values of β_2, β_2', M_2', and r_2/r_1 is obtained in principle from the chart as follows (in practice, many of the steps illustrated here can be omitted):

The first step is to locate on each of the nine carpets a point corresponding to the given values

of β_2 and β_2' as follows: It will be observed that each curve, in effect, has its own abscissa scale. On each of the curves for constant β_2', the given value of β_2 can be located; a curve sketched through these points will yield a curve for varying β_2' at the given value of β_2, whereupon the desired point on each carpet can be located. Appropriate points on the nine carpets are then connected by curves so as to form three curves of varying M_2', each having its own constant value of r_2/r_1. The three points corresponding to the given M_2' are then located. This is done by marking off a proportional horizontal distance along each curve from a known reference point. The three points thus obtained determine a curve of given β_2, β_2', M_2', and varying r_2/r_1. It will be noted that the carpets are staggered horizontally two major grid divisions for a change of 0.2 in r_2/r_1; therefore, the point corresponding to the given r_2/r_1 can be located and the value of the ordinate scale
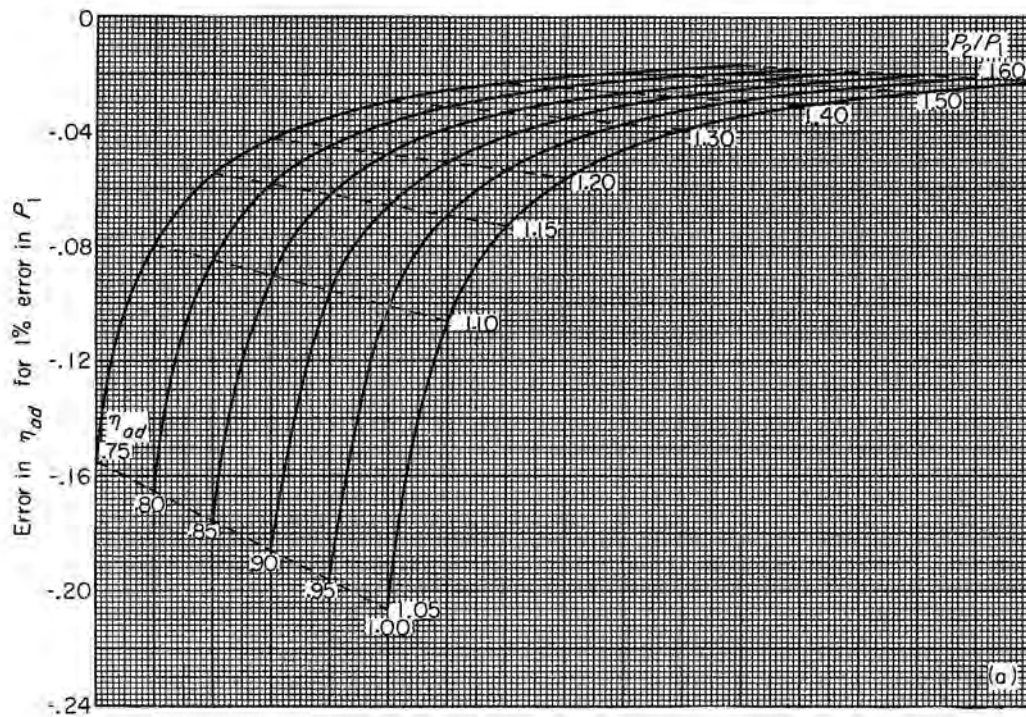
(a) Stagnation pressure (eq. (mE–ii)).

(b) Stagnation temperature (eq. (mE–iii)).

FIGURE 320.—Effect of measurement errors on calculated value of blade-element efficiency.
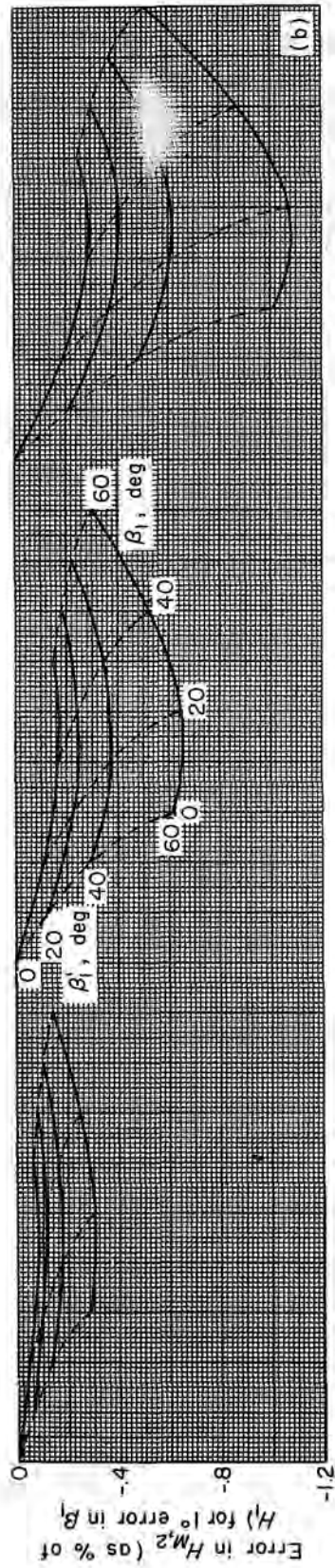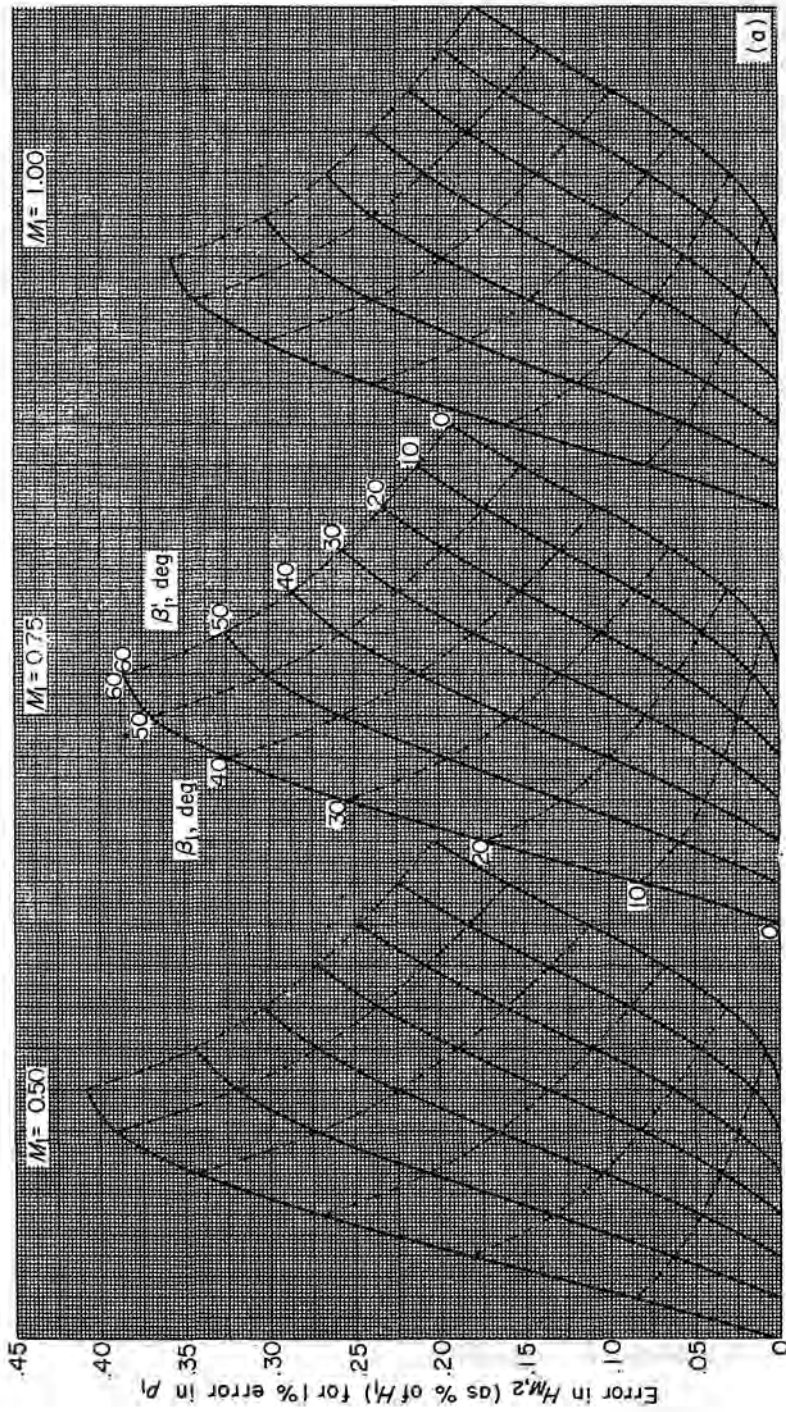
(a) Static pressure (eq. (mF-l)).
(b) Absolute air angle (eq. (mF-iv)).

FIGURE 321.—Effect of measurement errors on stagnation enthalpy calculated from change of moment of momentum.
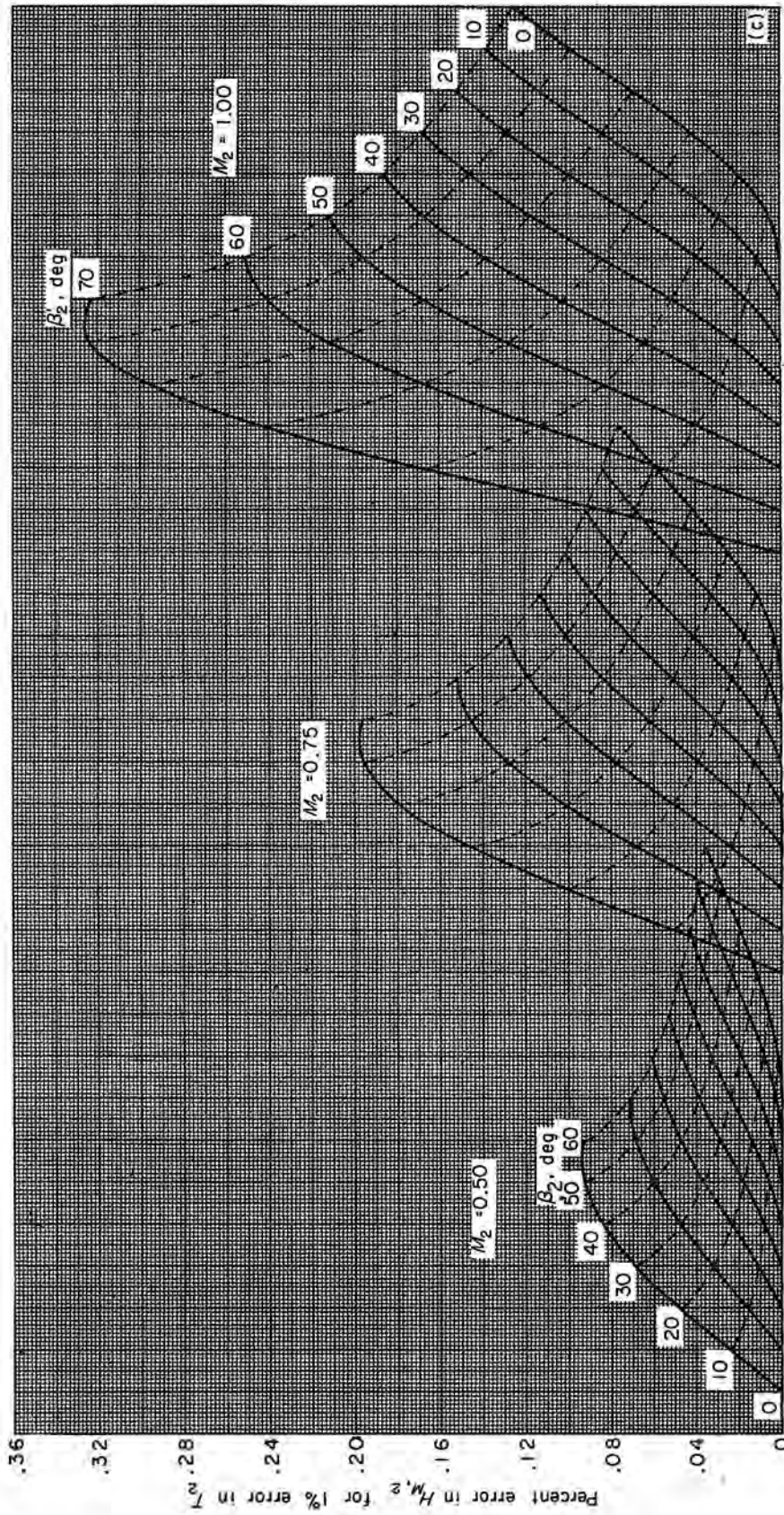
(c) Stagnation temperature (eq. (rnf-vii)).

FIGURE 321.—Concluded.   Effect of measurement errors on stagnation enthalpy calculated from change of moment of momentum.
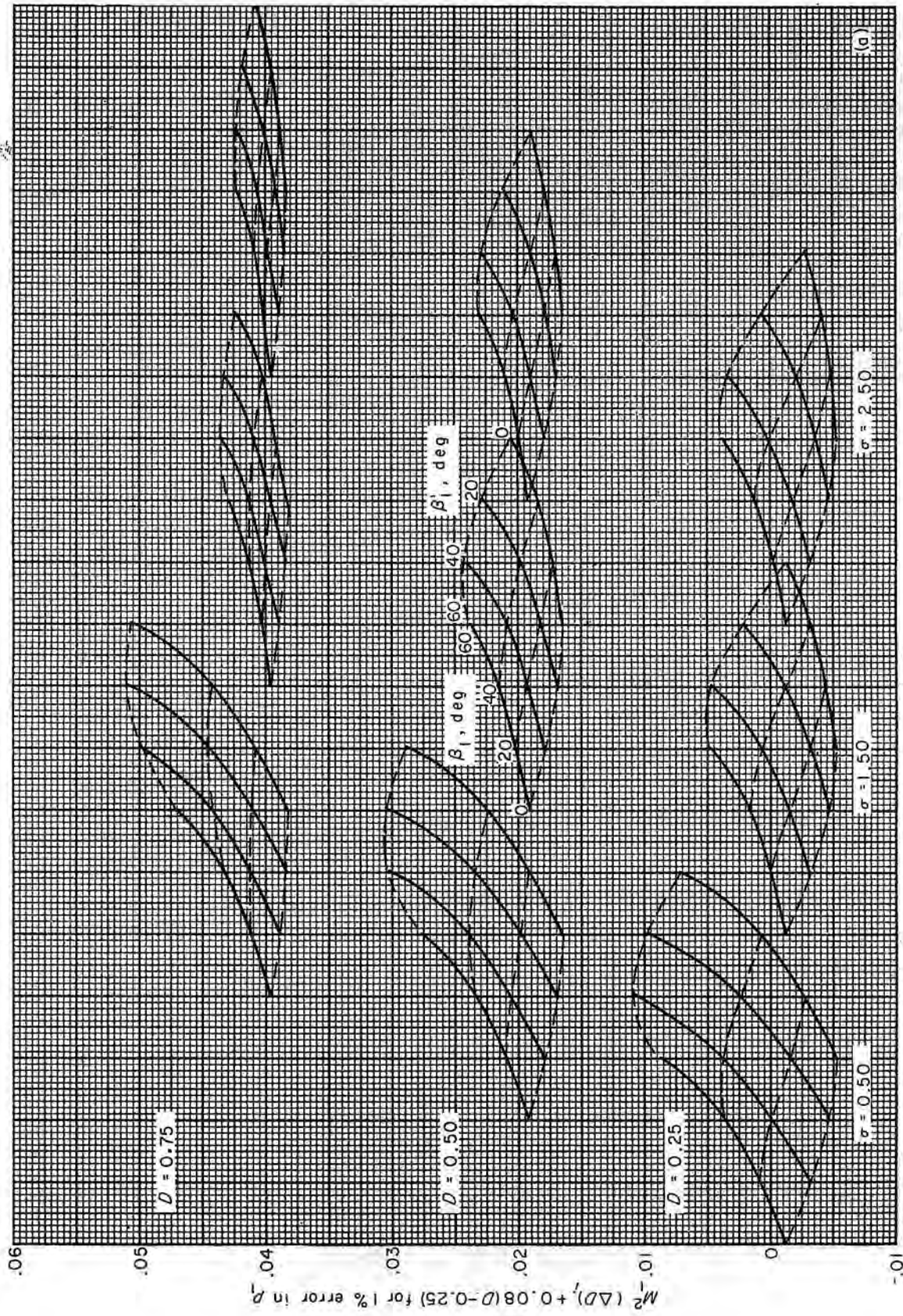
(a) Static pressure upstream of rotor (eq. (mG-1)).

FIGURE 322.—Effect of measurement errors on calculated value of diffusion factor.
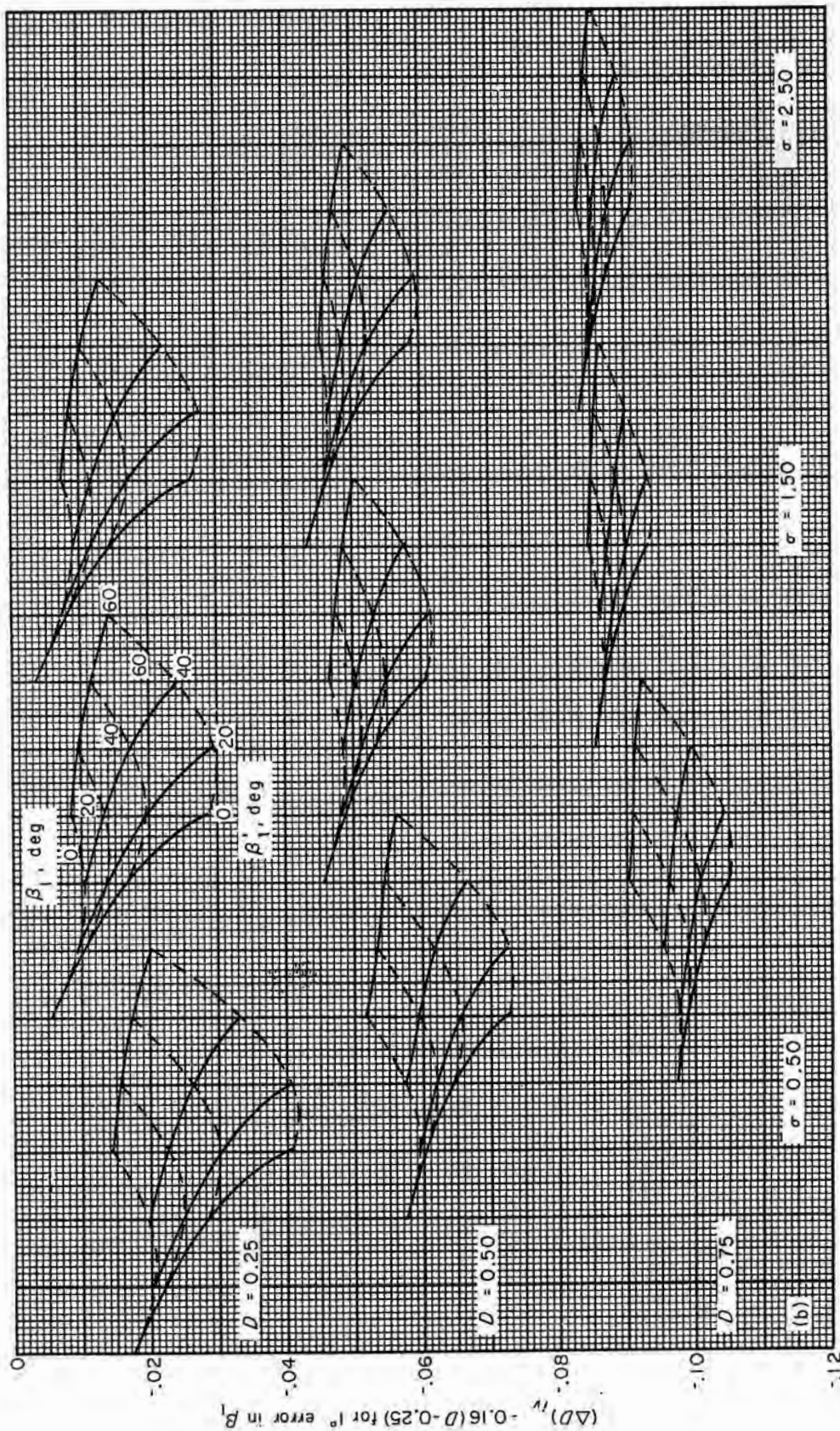
(b) Absolute air angle upstream of rotor (eq. (mG-iv)).

FIGURE 322.—Continued. Effect of measurement errors on calculated value of diffusion factor.
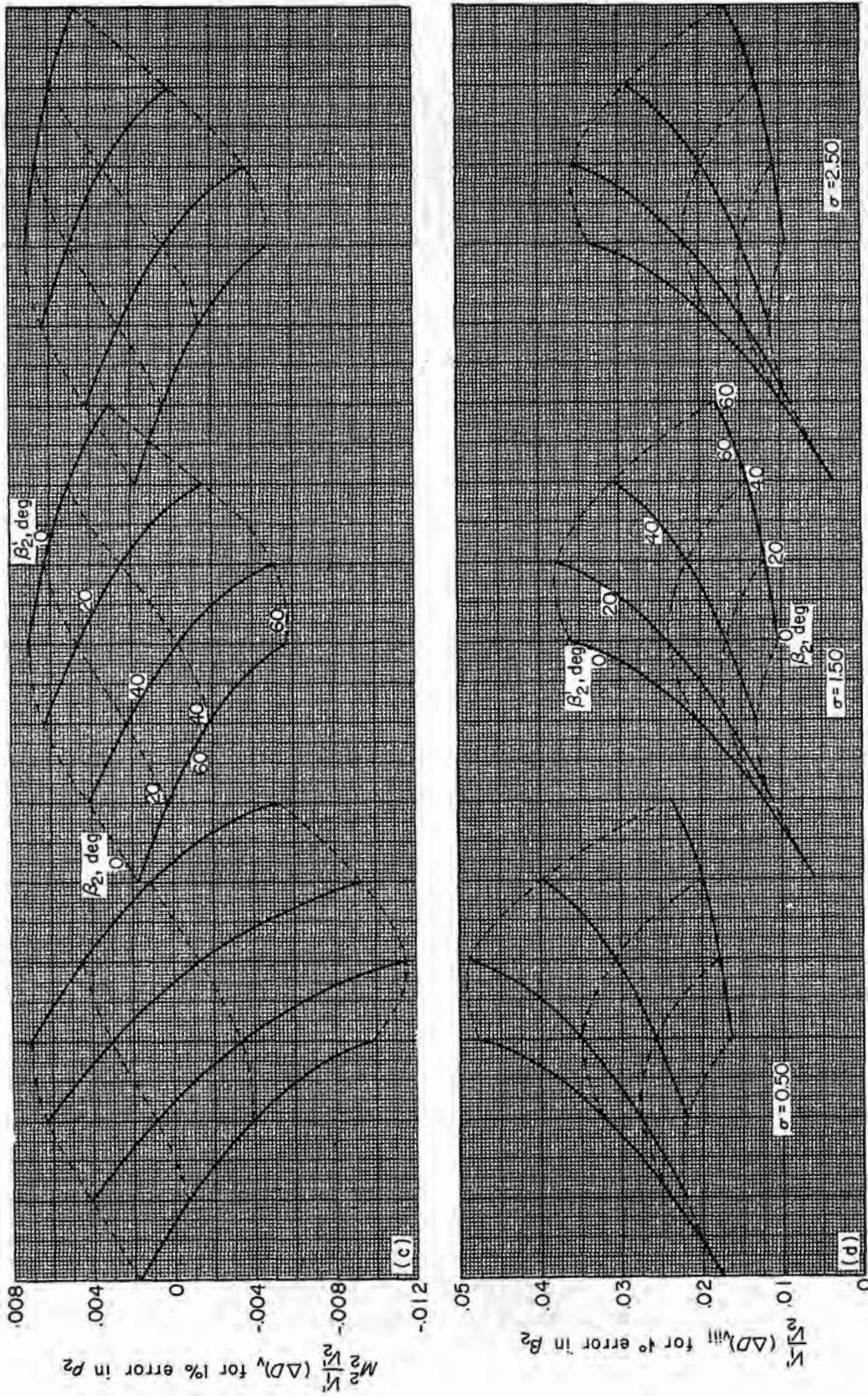
(c) Static pressure downstream of rotor (eq. (mG-v)).
(d) Absolute air angle downstream of rotor (eq. (mG-viii)).

FIGURE 322.—Concluded. Effect of measurement errors on calculated value on diffusion factor.

obtained. The final step is to equate this value to the ordinate function $(H_2'/H_1')+[(r_2/r_1)-0.9]$ and solve for H_2'/H_1'.

The foregoing procedure appears to be laborious, but in practice not all the various points need actually to be joined by curves; the interpolations can be made by an appropriate placing of French curves or splines on the charts and the desired points located directly. The work involved is, of course, much greater for the four-variable charts than for the three- or two-variable charts. For some formulas (formula (dG-i, iv), e.g.), two charts are employed, and the values obtained from each chart are combined to obtain the desired value of the dependent variable.

DISCUSSION OF FORMULAS AND CHARTS

In order to facilitate discussion of the formulas and charts, values of design and measurement errors were obtained from the charts for four velocity diagrams. These velocity diagrams are representative of inlet-stage rotor tip and hub operation at two Mach number levels. The velocity diagram specifications are as follows:

	Case 1 (tip condition)		Case 2 (hub condition)	
	Design (a)	Design (b)	Design (a)	Design (b)
M_1'	1.15	1.00	0.81	0.70
M_1	.58	.50	.58	.50
β_1'	60°	60°	45°	45°
β_1	0°	0°	0°	0°
M_2'	.90	.75	.60	.50
M_2	.64	.55	.73	.63
β_2'	50°	50°	15°	15°
β_2	24.6°	28.2°	38.3°	40.1°
ω'	.080	.080	.050	.050
σ	.80	.80	1.5	1.5
D	.34	.43	.41	.44
r_2/r_1	1.00	1.00	1.1	1.1
P_2/P_1	1.35	1.30	1.42	1.32
T_2/T_1	1.10	1.09	1.11	1.09
η_{ad}	.86	.87	.95	.95

SAMPLE DESIGN AND MEASUREMENT ERRORS

Values of design errors and measurement errors for the foregoing velocity-diagram cases were

read from the charts. For each case, an arbitrary assumption of 1-percent error in independent variable was made (except that the assumed error in flow angle was 1° and that in $\bar{\omega}$ or $\bar{\omega}'$ was 0.01). Design errors in $V_{z,1}$, β_1', $V_{z,2}$, H_2, P_2, β_2, and D, and measurement errors in ρV_z, β', $\bar{\omega}'$, η_{ad}, H_M, and D were obtained as follows:

Error term	Design errors, case number			
	1(a)	1(b)	2(a)	2(b)
$(\Delta V_{z,1}/V_{z,1})$i	−0.0150	−0.0133	−0.0150	−0.0133
ii	0	0	0	0
iii	.0150	.0133	.0150	.0133
iv	.0125	.0118	.0125	.0118
$(\Delta\beta_1')$i	0.38	0.33	0.44	0.39
ii	.25	.25	.60	.60
iii	−.38	−.33	−.44	−.39
iv	−.31	−.30	−.36	−.34
$(\Delta V_{z,2}/V_{z,2})$i	−0.0520	−0.0220	−0.0150	−0.0140
ii	.0460	.0166	.0079	.0052
iii	0	0	0	0
iv	.0550	.0240	.0150	.0140
v	.0310	.0110	.0050	.0037
vi	.0885	.0270	.0028	.0015
vii	.0525	.0230	.0155	.0133
viii	−.0447	−.0140	−.0049	−.0037
$(\Delta H_2/H_2)$i	0.0124	0.0038	0.0006	0.0004
ii	−.0143	−.0056	−.0021	−.0016
iii	0	0	0	0
iv	−.0041	.0051	.0085	.0088
v	−.0074	−.0019	−.0002	−.0001
vi	−.0303	−.0112	−.0025	−.0018
vii	−.0125	−.0040	−.0006	−.0004
viii	.0150	.0059	.0026	.0020
$(\Delta P_2/P_2)$i	0.0534	0.0233	0.0119	0.0113
ii	−.0500	−.0196	−.0074	−.0056
iii	0	0	0	0
iv	−.0494	−.0171	−.0058	−.0039
v	−.0326	−.0117	−.0039	−.0031
vi	−.1060	−.0392	−.0088	−.0063
vii	−.0437	−.0140	−.0020	−.0013
viii	.0525	.0206	.0091	.0070
$(\Delta\beta_2)$i	4.05	1.69	0.56	0.52
ii	−3.59	−1.26	−.29	−.19
iii	0	0	0	0
iv	−4.29	−1.84	−.56	−.52
v	−3.42	−.84	−.20	−.14
vi	−8.90	−3.90	−.70	−.70
vii	−4.10	−1.76	−.57	−.49
viii	4.60	2.00	.63	.52
(ΔD)i	0.0583	0.0244	0.0078	0.0045
ii	−.0410	−.0078	.0045	.0067
iii	.0005	.0004	.0042	.0028
iv	−.0618	−.0268	−.0085	−.0079
v	−.0350	−.0124	−.0040	−.0030
$(V_1'/V_1')(\Delta D)$vi	−.1790	−.0815	−.0130	−.0120
(ΔD)vii	−.0594	−.0260	−.0124	−.0106
viii	.0505	.0158	.0049	.0030

Error term	Measurement errors, case number			
	1(a)	1(b)	2(a)	2(b)
$\left[\dfrac{\Delta(\rho V_z)}{\rho V_z}\right]$ i	−0.0150	−0.0220	−0.0150	−0.0220
ii	−.0250	−.0310	.0250	.0310
iii	−.0050	−.0050	−.0050	−.0050
iv	0	0	0	0
v	−.0110	−.0170	−.0070	−.0115
vi	.0210	.0270	.0160	.0210
vii	−.0050	−.0050	−.0050	−.0050
viii	−.0080	−.0090	−.0130	−.0140
$(\Delta\beta')$i	0.58	0.71	0.67	0.82
ii	−.58	−.71	−.67	−.82
iii	−.13	−.13	−.15	−.15
iv	−.25	−.25	−.50	−.50
v	.73	1.16	.74	1.13
vi	−.73	−1.16	−.74	−1.13
vii	−.20	−.20	−.30	−.30
viii	−.19	−.15	−.76	−.72
$(\Delta\bar\omega')$ii	0.0170	0.0205	0.030	0.036
iii	−.0595	−.0717	−.105	−.126
vi	−0.0170	−.0205	−.030	−.036
vii	.0595	.0717	−.105	−.126
$(\Delta\eta_{ad})$ii	−0.030	−0.034	−0.028	−0.038
iii	.094	.106	.096	.118
vi	.030	.034	.028	.038
vii	−.094	−.106	−.096	−.118
$(\Delta H_{M,2}/H_1)$i	0	0	0	0
ii	0	0	0	0
iii	.0100	.0100	.0100	.0100
iv	−.0038	−.0029	−.0020	−.0016
v	−.0016	−.0019	−.0014	−.0015
vi	.0016	.0019	.0014	.0015
vii	.0007	.0005	.0005	.0005
viii	.0038	.0028	.0037	.0016
$M_1^2\,(\Delta D)$i	−0.0010	−0.0010	−0.0017	−0.0017
ii	.0010	.0010	.0017	.0017
(ΔD)iii	.0007	.0007	.0012	.0012
iv	−.0105	−.0105	−.0136	−.0136
$M_2^2\dfrac{V_1'}{V_2'}(\Delta D)$v	.0017	.0017	.0039	.0039
vi	−.0017	−.0017	−.0039	−.0039
$\dfrac{V_1'}{V_2'}(\Delta D)$vii	−.0012	−.0012	−.0027	−.0027
viii	.0138	.0138	.0127	.0127

The foregoing sample values of error terms provide data for the discussions of the following sections.

Interpretation of numerical values.—The numerical values of error terms obtained from the design-error charts must be carefully interpreted. Their main utility is in an evaluation of the sensitivity to design errors of one velocity diagram as compared with another. Secondarily, for a mean-radius condition where the local specific mass flow $(\rho V_z)_2$ can reasonably be assumed constant at a given annular mass flow, the values obtained from the charts can be combined to yield uncertainty intervals in blade-element performance.

The precautions concerning the interpretation of numerical values of error terms, such as those listed in the table, are partly involved with the fact that some of the design variables can be considered independent only for blade-element

flow. In actual compressor operation, the conditions of radial equilibrium and continuity impose a dependence between local specific mass flow and deviation angle and loss. Therefore, sweeping conclusions cannot be drawn from any one chart (one chart represents only one term of formula (400)).

An example of the dependence of local specific mass flow on deviation angle occurs for $M_2'=0.90$. At this Mach number, the local specific mass flow is very near its maximum value. A quite small increase in β_2' can cause a choking-flow condition, and any additional increase in β_2' will necessarily be accompanied by a decrease in the value of $(\rho V_z)_2$. The tabulated values of error terms show that the effects of an increase in β_2' and decrease in $(\rho V_z)_2$ are opposite in sign and therefore tend to nullify each other to some extent.

If the value of β_2' is smaller than expected, the choking-flow condition will not arise, but even in this case the value of $(\rho V_z)_2$ will probably change because of the effect of the error in β_2' on the radial-equilibrium condition. No method is available for estimating this effect without recomputing the entire flow field for a specified set of errors at all radii.

The foregoing discussion indicates that, to ensure the achievement of design mass flow, deviation angles near the upper limit of their uncertainty intervals should be employed for high Mach number designs.

Trends exhibited by sample design errors.— The trend most apparent from an examination of the tabulated values of design error is that, for case 1 (the tip operating condition), a Mach number level of $M_2'=0.90$ is accompanied by error terms much greater in magnitude than those for $M_2'=0.75$. This difference in magnitude is a consequence of the term $1/[1-(M_2')^2]$, which appears in many formulas. It is possible that the various errors would tend to cancel out; but it would apparently be advantageous, in the design of transonic rotors, to hold the value of M_2' as low as is consistent with reasonable values of diffusion factor D and, of course, to employ the highest possible degree of design control in the choice of the design variables. It would probably be warranted to employ the continuity condition in the design calculations for the choice of r_2 because of the large effects indicated in the table for an assumed error in r_2 of 1 percent. The results also

indicate no error in performance parameters at station 2 due to error in inlet local specific mass flow $(\rho V_z)_1$ for $\beta_1=0$, except for a very small effect on diffusion factor D. However, errors in $(\rho V_z)_1$ do cause errors in β_1' and hence in incidence angle. For high Mach numbers where the low-loss range of incidence angle might be narrow, this effect can lead to design errors in $\bar{\omega}'$ and deviation angle.

Trends exhibited by sample measurement errors.—For many of the parameters, the effects of measurement errors are greatest at low Mach numbers. This trend is especially evident for the loss parameter $\bar{\omega}'$ and is caused by terms like $1/M^2$

and $\dfrac{1}{1-\dfrac{p_1}{P_1'}}$ in the measurement-error formulas.

Case 2(b), for an inlet Mach number M_1' of 0.70, shows an error in $\bar{\omega}'$ of -0.036 due to an assumed error of 1 percent in the measurement of stagnation pressure P_2. This trend shows that the accurate determination of $\bar{\omega}'$ from low-speed data requires very precise measurement of stagnation pressure (and temperature).

USE OF DESIGN-ERROR CHARTS

Suggested uses of the formulas and charts that were obtained from the analyses of design and measurement errors are outlined in this section.

For the preliminary velocity-diagram calculations, a common practice is to assign r_2 at the same proportion of the passage depth as the corresponding r_1; or perhaps r_2 is located so that the same proportion of flow area is contained between r_2 and the hub as between the corresponding r_1 and the hub. After the calculations are made, r_2 can easily be determined as a function of r_1 by application of the continuity condition. The charts of the formulas for design errors in r_2 can then be employed to determine whether an iteration with the new values of r_2 is warranted.

Similarly, the preliminary radial-equilibrium calculations may neglect the effects of entropy gradient on the radial distribution of axial velocity. The order of magnitude of the consequent design errors in axial velocity can be estimated from the results of the investigation reported in reference 49. The design-error charts can then be consulted to determine whether the blade-element losses should be included in the radial-equilibrium calculation.

Certain refinements in the design calculations (such as the inclusion of blade-element losses in the radial-equilibrium calculation) may appreciably change the values of D. These new diffusion factors will lead to changes in the design values of $\bar{\omega}'$, and again the charts can be consulted to determine whether an iteration is warranted with the new values of $\bar{\omega}'$.

For any general blade element, the formulas and charts can be employed as a test of the sensitivity of a particular velocity diagram to design errors and manufacturing tolerances. Thus, the appropriate degree of design control can be applied to the problem, and in some cases, the sensitivity to design errors and manufacturing tolerances can be employed as one of the criteria by which choice among several otherwise suitable velocity diagrams can be made.

The charts can be employed by the research worker in the analysis of data. Discrepancies between actual and design performance of an experimental compressor that cannot reasonably be accounted for by measurement errors are caused mainly by design errors of the type herein analyzed. (Some of these discrepancies are undoubtedly caused by simplifications introduced into the equations of motion on which the design system is based, such as the assumption of axial symmetry.) The approximate contribution of the design error in each design variable to the measured discrepancy in a performance parameter can be obtained from the charts. The sum of these terms (formula (394b)) can be compared with the measured discrepancy between actual and design values of a performance parameter.

Such comparisons may serve as an additional means of evaluating measurement errors and may indicate just which phase of the design problem requires the highest degree of design control.

Within certain limitations, the design-error charts can be employed by the compressor designer to estimate an interval about the design point within which the performace of a given blade element should lie. The limitations on this procedure are involved with the estimation of uncertainty intervals in local specific mass flow.

Estimation of uncertainty intervals.—Local specific mass flow: The uncertainty intervals in local specific mass flow are caused by blade-element design errors. As evidenced by the radial-equilibrium equation, the radial distribution of flow is a function of flow angles and blade
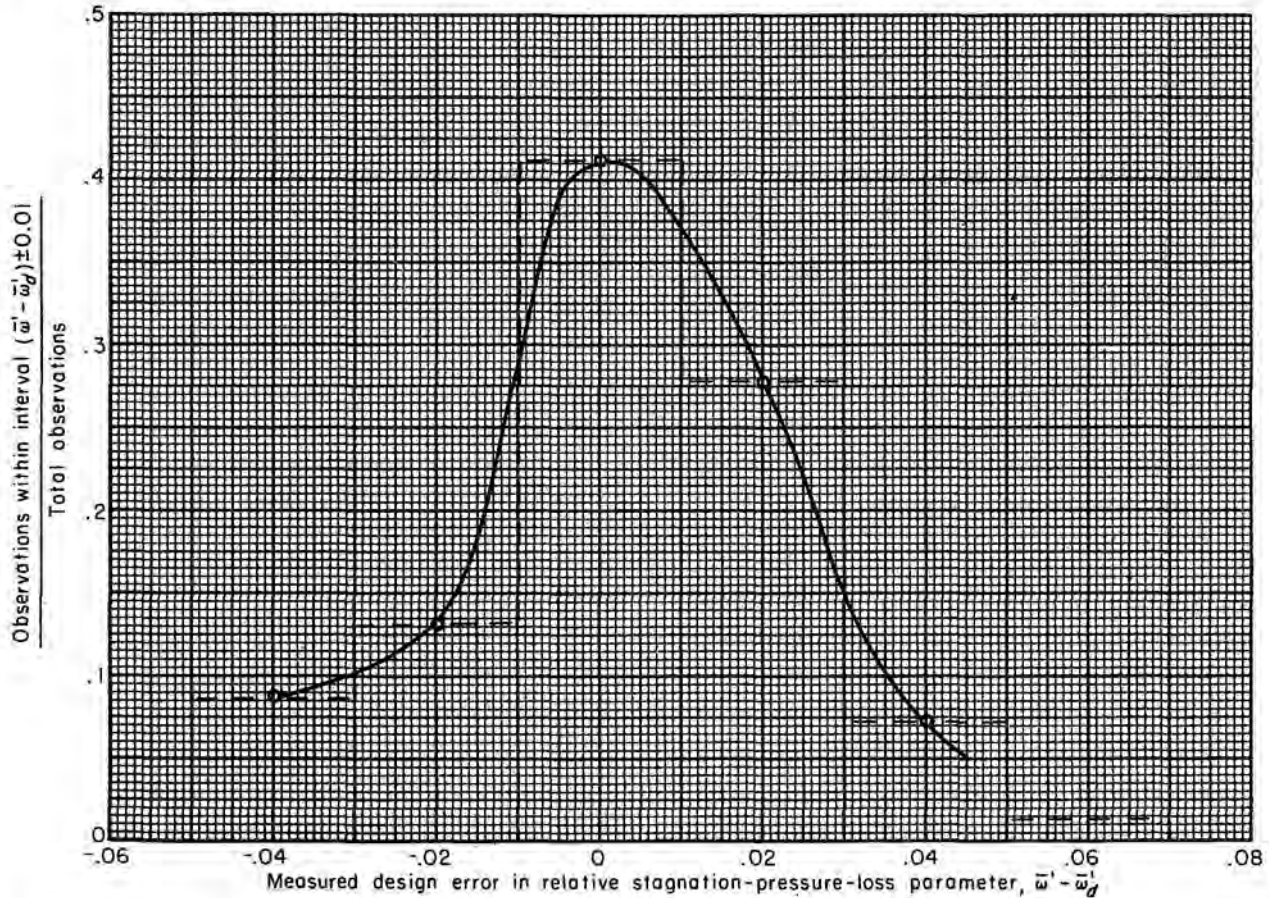
FIGURE 323.—Approximate frequency distribution for set of measured design errors in relative stagnation-pressure-loss parameter.

losses at all blade elements. Therefore, discrepancies between actual and design values of these quantities lead to discrepancies between actual and design values of local specific mass flow.

Unfortunately, no method is known for relating uncertainty intervals in local specific mass flow to uncertainty intervals in blade-element design data. This fact restricts the applicability of formula (400). However, at the design mass flow, the actual and design values of local specific mass flow must necessarily agree for at least one blade element. It would appear reasonable to assume that this blade element would be near the mean radius.

Loss parameter: A set of mean-radius loss data reported in chapter VII was employed in an investigation of the uncertainty intervals in loss parameter $\bar{\omega}'$. The design values of loss parameter $\bar{\omega}'_d$ for each observation were obtained by the use of the loss-correlation method of chapter VII,

and the quantities $(\bar{\omega}'-\bar{\omega}'_d)$ were calculated. Frequency ratios for increments in $(\bar{\omega}'-\bar{\omega}'_d)$ of 0.02 were calculated and are plotted in figure 323 as an approximate frequency-distribution curve. The frequency ratio plotted in figure 323 is the ratio of the number of observations within an increment in $(\bar{\omega}'-\bar{\omega}'_d)$ of 0.02 to the total number of observations. For instance, the value of 0.132 plotted at $(\bar{\omega}'-\bar{\omega}'_d)$ equal to −0.02 denotes that 13.2 percent of the values of $(\bar{\omega}'-\bar{\omega}'_d)$ fall within limits of from −0.03 to −0.01. The total number of observations for this set of mean-radius loss data was 68.

The curve of figure 323 indicates that the discrepancies between the design and measured values of $\bar{\omega}'$ plot in a rough approximation of a random distribution, although there is some bias in the direction of positive errors. These mean-radius data indicate that an interval of from −0.03 to 0.03 in $(\bar{\omega}'-\bar{\omega}'_d)$ (an uncertainty interval
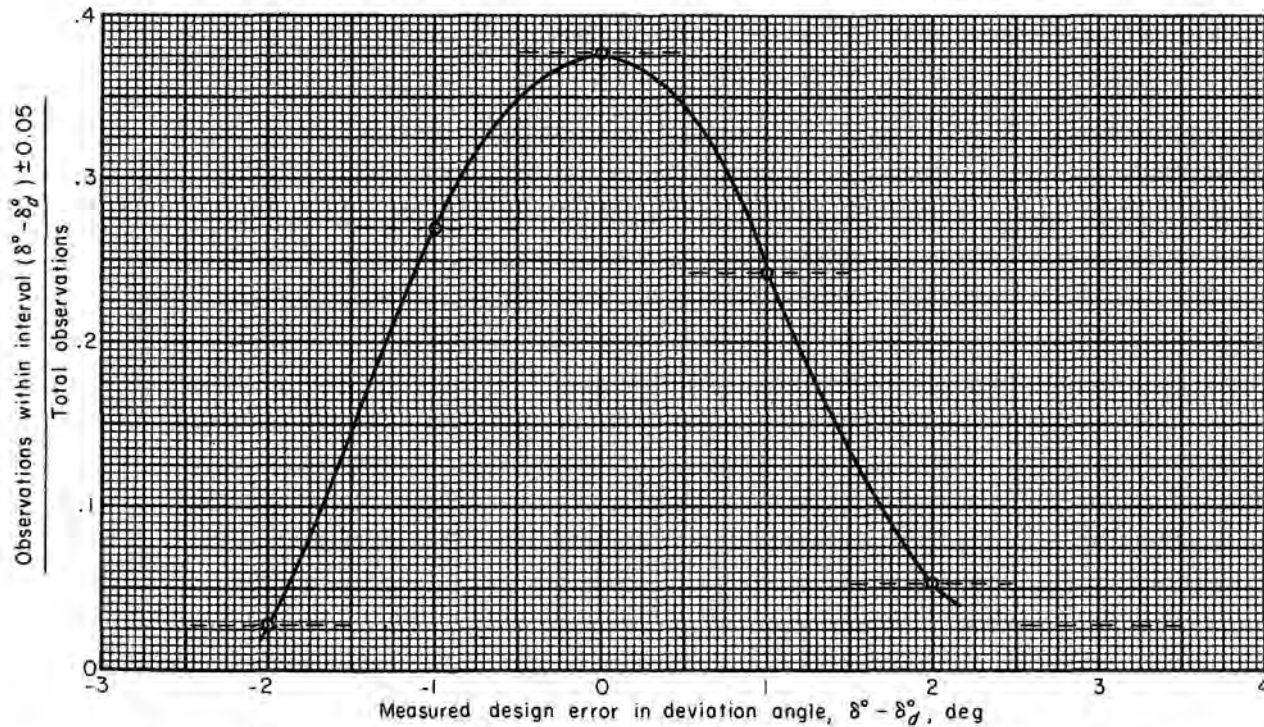
FIGURE 324.—Approximate frequency distribution for set of measured design errors in deviation angle.

of 0.06) contains 82.4 percent of the observations; the corresponding odds for this interval are 4.7 to 1.0.

The data of figure 323 represent a combination of measurement errors and design errors; thus, the uncertainty interval for design errors only corresponding to odds of 4.7 to 1.0 would be less than the value of 0.06 obtained from these data.

Deviation angle: An approximate frequency-distribution curve for mean-radius design errors in deviation angle was prepared in the same way as the corresponding curve for loss parameter. The resulting curve, which was prepared for intervals of 1°, is plotted in figure 324. For these data, 89.1 percent of the observations were within an interval in $(\delta° - \delta_d°)$ of 3° (−1.5° to 1.5°), which corresponds to odds of 8.2 to 1.0. As was the case for design error in loss parameter, this interval for the quoted odds in design error only would be smaller than 3°.

Radius to blade element: Design errors in the choice of r_2 as a function of r_1 are involved with the radial-equilibrium condition and are mainly systematic errors that depend on the design flow distribution and the compressor configuration. It can probably be assumed, therefore, that the

uncertainty interval for random errors in r_2 is negligible compared with the other errors introduced.

Calculation of uncertainty intervals in performance.—For the estimation of the limits in blade-element performance near the mean radius, formula (400) is employed.

USE OF MEASUREMENT-ERROR CHARTS

The charts for the analysis of measurement errors can be employed in several ways: (1) for the calculation of uncertainty intervals in performance parameters corresponding to estimated uncertainty intervals in the measured data, (2) for the evaluation of measured data based on the consistency evidenced by plots of performance parameters, and (3) as an aid in planning instrumentation.

Uncertainty intervals in performance.—For measurement errors of the random type, the procedure outlined in reference 346 can be followed. Intervals are estimated for each measured datum within which the same odds (b) can be quoted that the true value will lie. The uncertainty intervals in a performance parameter due to errors in each measured variable are then obtained from the charts and are com-

bined by means of formula (399). The final result will be an interval in the performance parameter for which the odds are b that the value of the performance parameter will lie.

Evaluation of data.—Plots of performance parameters against mass flow or incidence angle can sometimes be employed, along with the charts, to evaluate the accuracy of measured data. For instance, figure 319 shows that the calculated values of $\bar{\omega}'$ are very sensitive to errors in P and T. Therefore, if a plot of rotor $\bar{\omega}'$ against incidence angle shows only a slight scatter from a smooth curve, the measured values of P and T can be considered very consistent. Also, figure 321(b) shows that the calculated values of stagnation enthalpy (or stagnation temperature) by change of moment of momentum are sensitive at high Mach numbers to measurement errors in flow angle β. Even if a discrepancy of 2° F were observed between the measured stagnation temperature and the value obtained by change of moment of momentum, this could be accounted for by a measurement error of less than 1° in flow angle (for the conditions $M_2=0.64$, $\beta_2=25°$, $\beta_2'=50°$). This example illustrates the difficulty of checking the measurement of temperature at high Mach numbers by the temperature calculated from the change of moment of momentum across a rotor. At a Mach number of 0.5, the effects of errors in flow angle and static pressure on change of moment of momentum would be approximately the same; at lower Mach numbers, the static-pressure errors would have the greater effect (figs. 321(a) and (b)). For many conditions of velocity diagram, an error of 1 percent in static pressure would cause an error in change of moment of momentum equivalent to approximately 1° F in temperature rise. Since 1° F is also a reasonable error to be expected in the direct measurement of temperature, no advantage in accuracy is indicated either for the direct measurement of temperature or for the calculation of change of moment of momentum at low Mach numbers.

Instrumentation.—The charts can be used as a guide in choosing instrumentation of sufficient accuracy for the expected test conditions and combinations of flow parameters. The relative air angle β_1' or β_2' is an important parameter in the correlation of data, since these flow angles determine incidence, deviation, and turning angles. Figures 317(a) and (c) show that measurement errors in static pressure (or stagnation pressure) can cause greater error in the calculated value of β' than would a reasonable error in the measurement of absolute air angle β, especially at low Mach numbers. Thus, the necessity for careful design and calibration of static-pressure probes is emphasized.

CONCLUDING REMARKS

The effects of design errors on compressor performance parameters and of measurement errors on calculated values of performance parameters were analyzed. The following results were obtained:

1. Formulas and charts were prepared and presented from which the changes in blade-element performance parameters caused by design errors and the errors in calculated performance parameters due to measurement errors can be determined.

2. The use of the design-error charts during the design calculations and in the analysis and interpretation of data was discussed. The charts can be used to evaluate the sensitivity of a given velocity diagram to design errors, to determine whether iterations of design calculations are warranted, and, to a limited extent, to calculate the uncertainty intervals in blade-element performance.

3. The measurement-error charts can be employed along with the procedure devised at the Gas Turbine Laboratory of the Massachusetts Institute of Technology for the estimation of uncertainty intervals in calculated performance and can also be of assistance in the evaluation of data and in the planning of instrumentation.

APPENDIX A

ACCURACY OF FORMULAS

The accuracy of the design-error and measurement-error formulas for reasonable magnitudes of errors was spot-checked by means of sample calculations for various combinations of Mach number and absolute and relative flow angles.

DESIGN-ERROR FORMULAS

A sample calculation of the actual effects (within the limitations of the design system) of certain assumed design errors was made as follows: A transonic-inlet-stage rotor design was calculated. The rotor-outlet air angles β_2' were then increased $1°$ and a direct-problem calculation of the rotor performance was made. The consequent changes in various performance parameters were then compared with the corresponding results obtained from the charts. Similarly, the design values of rotor $\bar{\omega}'$ were increased 25 percent, the rotor performance was again calculated, and appropriate comparisons were made between the changes in performance and the predictions of the charts.

It should be pointed out that, in a direct-problem calculation of this type, the specified error in β_2' is propagated through the radial-equilibrium calculation and causes changes in local specific mass flow. Thus, the calculation yields the combined effects of errors in β_2' and $(\rho V_z)_2$ on the performance parameters. These combined effects cannot be obtained from the charts alone; the charts provide no means for obtaining $\Delta(\rho V_z)_2$ as a function of $\Delta\beta_2'$, because in blade-element flow β_2' and $(\rho V_z)_2$ are treated as if they were independent. The values of $\Delta(\rho V_z)_2$ obtained from the calculation were therefore employed along with the specified error of $1°$ in β_2' to obtain the chart predictions of changes in performance. The values obtained from the charts for effects of errors in β_2' and from the charts for effects of errors in $(\rho V_z)_2$ were added algebraically, as specified by formula (394c).

The design assumptions were as follows:

(1) $M_1'=1.10$ at rotor tip.

(2) $\beta_1'=60°$ at rotor tip, $\beta_1=0°$ at all radii.

(3) $(r_1/r_t)_h=0.5$.

(4) H_2-H_1 varied linearly from 300,000 ft-lb/slug at hub to 400,000 ft-lb/slug at tip.

An approximate calculation of density ratio was made to determine the annular-area ratio for no change in average axial velocity. This calculation yielded a value for $(r_2/r_t)_h$ of 0.6.

The radial-equilibrium calculation was based on simplified radial equilibrium including entropy gradient (ref. 49). An arbitrary assumption of $\bar{\omega}'$ was made, varying from 0.040 at the hub to 0.100 at the tip (nonlinearly).

The following table lists values of performance parameters obtained; the range given is the variation from hub to tip:

β_2'	$13.61°$–$48.52°$
β_2	$40.94°$–$34.19°$
M_2'	0.512–0.752
M_2	0.659–0.603
H_2/H_1	1.096–1.128
P_2/P_1	1.363–1.445

The direct-problem calculation, employing values of β_2' increased $1°$ at all radii, resulted in small changes in the local specific mass flow at the different radii of from -1.2 to 0.8 percent because of the propagation of the assumed error in β_2' through the radial-equilibrium calculation.

The changes in blade-element stagnation-pressure ratio were analyzed. The pressure ratio was reduced by the assumed decrease in turning angle, together with the consequent changes in $(\rho V_z)_2$, and the net decrement in pressure ratio obtained from the charts agreed very closely with the calculated values, as follows:

Radius ratio, r_1/r_t	Net $\Delta(P_2/P_1)$ due to $\Delta\beta_2'=1°$ and to consequent $\Delta(\rho V_z)_2$	
	Calculated	From charts
0.5	-0.0104	-0.0103
.6	$-.0145$	$-.0141$
.7	$-.0186$	$-.0185$
.8	$-.0236$	$-.0233$
.9	$-.0278$	$-.0278$
1.0	$-.0316$	$-.0318$

The assumed increase in $\bar{\omega}'$ for the second phase of the check calculation also caused small changes

465

in local values of $(\rho V_z)_2$ of from -1.6 to 1.2 percent. The net effect of these changes was a general decrease in pressure ratio, and good agreement between the calculated values and those obtained from the charts was observed:

Radius ratio, r_1/r_t	Net $\Delta(P_2/P_1)$ due to $\Delta\bar{\omega}'/\bar{\omega}'=0.25$ and to consequent $\Delta(\rho V_z)_2$	
	Calculated	From charts
0.5	−0.0061	−0.0065
.6	− .0093	− .0096
.7	− .0118	− .0125
.8	− .0146	− .0137
.9	− .0168	− .0159
1.0	− .0181	− .0189

It is believed that the foregoing calculation verifies the applicability of the design-error formulas, for the given range of Mach numbers and flow angles, to the uses suggested in the text.

A limitation of the design-error formulas containing the term $1-M^2$ in their denominators is that they are inaccurate for Mach numbers in the neighborhood of 1.0. Sample calculations indicate that the accuracy of such formulas is good for Mach numbers up to at least 0.75.

MEASUREMENT-ERROR FORMULAS

The measurement-error formulas were checked by means of sample calculations and in a few cases by comparison with the exact formula.

Local specific mass flow.—Calculations were made to compare the actual and chart values of $\Delta(\rho V_z)$ caused by changes in static or stagnation pressure of 1 percent. The following values were obtained:

M	Percent change in ρV_z for $\Delta p/p=0.01$	
	Calculated	From charts
0.5	−2.63	−2.14
.7	− .83	− .74

M	Percent change in ρV_z for $\Delta P/P=0.01$	
	Calculated	From charts
0.5	2.88	3.15
.7	1.67	1.74

Formula (mA–iii, vii), which gives the effect on ρV_z of a measurement error in T, contains the approximation that

$$\frac{1}{\left(1+\dfrac{\Delta T}{T}\right)^{1/2}}-1\cong-\frac{1}{2}\frac{\Delta T}{T}$$

Substitution of $\Delta T/T=0.01$ into the left side yields a value of -0.00496. Thus, for $\Delta T/T=0.01$, formula (mA–iii, vii) yields a result only 1.009 times the correct value.

Similarly, formula (mA–iv, viii), which gives the error in ρV_z due to a measurement error in β, contains the following approximation:

$$(\tan \beta)\Delta\beta\cong\frac{\cos \beta-\cos (\beta+\Delta\beta)}{\cos \beta}$$

For the range $0°\leq\beta\leq60°$, the degree of approximation decreases as β increases. For the worst case $(\beta=0°)$, where formula (mA–iv, viii) indicates no error in ρV_z, a measurement error of $\Delta\beta=1°$ would actually cause an error of 0.015 percent in ρV_z. This discrepancy is clearly negligible. For $\beta=60°$, the discrepancy between the values of $\Delta(\rho V_z)$ obtained from formula (mA–iv, viii) and from the exact calculation is only 0.0013 percent of ρV_z.

Relative air angle.—The following table presents a sample comparison of calculated magnitudes of changes in β' with the corresponding values obtained from the charts (formulas (mB–i, v) to (mB–iv, viii)) for the specified assumed measurement errors:

M ($\beta=30°$, $\beta'=40°$)	$|\Delta\beta'|$, deg					
	$\dfrac{\Delta p}{p}$ or $\dfrac{\Delta P}{P}=0.01$		$\dfrac{\Delta T}{T}=0.002$		$\Delta\beta=1°$	
	Actual	From charts	Actual	From charts	Actual	From charts
0.5	1.33	1.36	} 0.05	0.06	0.32	0.31
.7	.69	.71				

APPENDIX B

DERIVATION OF FORMULAS

DESIGN-ERROR FORMULAS

The derivation of formula (dF–v) is presented here as an example of the general procedure. The error in axial velocity $V_{z,2}$ due to an error in the rotor loss parameter must be found for the condition of unchanging local specific mass flow. A formula for $V_{z,2}$ is as follows:

$$V_{z,2} = \sqrt{2}\,(H_2' - h_2)^{1/2}\cos\beta_2' \qquad (407)$$

The relative stagnation enthalpy H_2' is not affected by an error in $\bar{\omega}'$; and, for this derivation, β_2' is held constant:

$$\frac{\partial V_{z,2}}{\partial \bar{\omega}'} = \frac{\sqrt{2}}{2}(H_2'-h_2)^{-1/2}\cos\beta_2'\left(-\frac{\partial h_2}{\partial\bar{\omega}'}\right) \quad (B1)$$

The condition of constant $(\rho V_z)_2$ provides a means for evaluation of $(\partial h_2/\partial\bar{\omega}')$:

$$(\rho V_z)_2 = \frac{\gamma}{\gamma-1}\frac{P_2'}{H_2'}\left(\frac{h_2}{H_2'}\right)^{\frac{1}{\gamma-1}}\sqrt{2}(H_2'-h_2)^{1/2}\cos\beta_2' \quad (413)$$

Differentiation of formula (413) with respect to $\bar{\omega}'$ yields the following:

$$0 = \frac{\gamma}{\gamma-1}\frac{1}{H_2'}\frac{\partial P_2'}{\partial\bar{\omega}'}\left(\frac{h_2}{H_2'}\right)^{\frac{1}{\gamma-1}}\sqrt{2}\,(H_2'-h_2)^{1/2}\cos\beta_2'$$

$$+\frac{\gamma}{\gamma-1}\frac{P_2'}{H_2'}\frac{1}{\gamma-1}\left(\frac{h_2}{H_2'}\right)^{\frac{1}{\gamma-1}-1}\frac{1}{H_2'}\frac{\partial h_2}{\partial\bar{\omega}'}$$

$$\times\sqrt{2}\,(H_2'-h_2)^{1/2}\cos\beta_2'$$

$$+\frac{\gamma}{\gamma-1}\frac{P_2'}{H_2'}\left(\frac{h_2}{H_2'}\right)^{\frac{1}{\gamma-1}}\frac{\sqrt{2}}{2}(H_2'-h_2)^{-1/2}\left(-\frac{\partial h_2}{\partial\bar{\omega}'}\right)$$

$$\times\cos\beta_2' \quad (B2)$$

Rearrangement of (B2) yields

$$0 = (\rho V_z)_2\frac{1}{P_2'}\frac{\partial P_2'}{\partial\bar{\omega}'}+\frac{1}{\gamma-1}(\rho V_z)_2\frac{1}{h_2}\frac{\partial h_2}{\partial\bar{\omega}'}-\frac{(\rho V_z)_2}{(V')^2}\frac{\partial h_2}{\partial\bar{\omega}'}$$

$$=\frac{1}{P_2'}\frac{\partial P_2'}{\partial\bar{\omega}'}+\left[\frac{1}{a_2^2}-\frac{1}{(V')^2}\right]\frac{\partial h_2}{\partial\bar{\omega}'} \quad (B3)$$

The relative stagnation pressure P_2' is a function of P_1', $\bar{\omega}'$, the relative enthalpy ratio H_2'/H_1', and p_1/P_1' (or M_1'):

$$P_2'=P_1'\left(\frac{H_2'}{H_1'}\right)^{\frac{\gamma}{\gamma-1}}\left[1-\bar{\omega}'\left(\frac{H_1'}{H_2'}\right)^{\frac{\gamma}{\gamma-1}}\left(1-\frac{p_1}{P_1'}\right)\right] \quad (B4)$$

$$\frac{\partial P_2'}{\partial\bar{\omega}'}=-P_1'\left(1-\frac{p_1}{P_1'}\right) \quad (B5)$$

Substitution of (B5) into (B3) and rearrangement yield

$$\frac{\partial h_2}{\partial\bar{\omega}'}=-(V_2')^2\frac{\dfrac{P_1'}{P_2'}\left(1-\dfrac{p_1}{P_1'}\right)}{1-(M_2')^2} \quad (B6)$$

Finally, (B6), (B4), and (B1) yield the following:

$$\frac{\partial V_{z,2}}{\partial\bar{\omega}'}=\frac{\cos\beta_2'}{V_2'}(V_2')^2\frac{1-\dfrac{p_1}{P_1'}}{\left[\left(\dfrac{H_2'}{H_1'}\right)^{\frac{\gamma}{\gamma-1}}-\bar{\omega}'\left(1-\dfrac{p_1}{P_1'}\right)\right][1-(M_2')^2]}$$

$$=\frac{V_{z,2}\left\{1-\left[1+\dfrac{\gamma-1}{2}(M_1')^2\right]^{-\frac{\gamma}{\gamma-1}}\right\}}{\left(\left(\dfrac{H_2'}{H_1'}\right)^{\frac{\gamma}{\gamma-1}}-\bar{\omega}'\left\{1-\left[1+\dfrac{\gamma-1}{2}(M_1')^2\right]^{-\frac{\gamma}{\gamma-1}}\right\}\right)[1-(M_2')^2]}$$

Therefore,

$$\left(\frac{\Delta V_{z,2}}{V_{z,2}}\right)_v=\frac{\Omega}{\bar{\omega}'[1-(M_2')^2]}\Delta\bar{\omega}' \qquad (dF\text{–}v)$$

467

where

$$\Omega=\frac{P'_{2,td}}{P'_2}-1=\frac{\bar{\omega}'\left\{1-\left[1+\frac{\gamma-1}{2}(M'_1)^2\right]^{-\frac{\gamma}{\gamma-1}}\right\}}{\left(\frac{H'_2}{H'_1}\right)^{\frac{\gamma}{\gamma-1}}-\bar{\omega}'\left\{1-\left[1+\frac{\gamma-1}{2}(M'_1)^2\right]^{-\frac{\gamma}{\gamma-1}}\right\}} \tag{416}$$

For some of the subsequent formulas of series d, $V_{z,2}$ was used as an intermediate variable. The derivation of the formula for error in P_2 is presented as an example:

$$P_2=P_1\left(\frac{H_2}{H_1}\right)^{\frac{\gamma}{\gamma-1}}\left[1-\bar{\omega}'\left(\frac{P'_1}{P'_2}\right)_{td}\left(1-\frac{p_1}{P'_1}\right)\right] \tag{B7}$$

$$\frac{\partial P_2}{\partial\bar{\omega}'}=P_1\frac{\gamma}{\gamma-1}\left(\frac{H_2}{H_1}\right)^{\frac{\gamma-1}{\gamma}-1}\frac{1}{H_1}\frac{\partial H_2}{\partial\bar{\omega}'}$$

$$\times\left[1-\bar{\omega}'\left(\frac{P'_1}{P'_2}\right)_{td}\left(1-\frac{p_1}{P'_1}\right)\right]+P_1\left(\frac{H_2}{H_1}\right)^{\frac{\gamma}{\gamma-1}}$$

$$\times\left[-\left(\frac{P'_1}{P'_2}\right)_{td}\left(1-\frac{p_1}{P'_1}\right)\right]$$

$$=\frac{\gamma}{\gamma-1}P_2\frac{1}{H_2}\frac{\partial H_2}{\partial\bar{\omega}'}-P_2\frac{\left(\frac{P'_2}{P'_1}\right)_{td}}{\frac{P'_2}{P'_1}}\left[\left(\frac{P'_1}{P'_2}\right)_{td}\left(1-\frac{p_1}{P'_1}\right)\right]$$

MEASUREMENT-ERROR FORMULAS

The derivation of formula (mA-i) is presented to illustrate the calculation of the series m formulas. Formula (mA-i) gives the error in ρV_z caused by a measurement error in p_1:

$$\rho V_z=\frac{\sqrt{2\gamma}}{\gamma-1}\frac{P}{H^{1/2}}\left(\frac{p}{P}\right)^{\frac{1}{\gamma}}\left[1-\left(\frac{p}{P}\right)^{\frac{\gamma-1}{\gamma}}\right]^{1/2}\cos\beta \tag{B11}$$

$$\frac{\partial(\rho V_z)}{\partial p}=\frac{\sqrt{2\gamma}}{\gamma-1}\frac{P\cos\beta}{H^{1/2}}\left\{\frac{1}{\gamma}\left(\frac{p}{P}\right)^{\frac{1}{\gamma}-1}\frac{1}{P}\right.$$

Therefore,

$$\left(\frac{\Delta P_2}{P_2}\right)_v=\frac{\gamma}{\gamma-1}\left(\frac{\Delta H_2}{H_2}\right)_v-\frac{1-\frac{p_1}{P'_1}}{\left(\frac{P'_2}{P'_1}\right)_{td}-\bar{\omega}'\left(1-\frac{p_1}{P'_1}\right)}\Delta\bar{\omega}' \tag{B8}$$

The term $(\Delta H_2/H_2)_v$ is obtained as follows:

$$H_2=H_1+U_2^2-U_2V_{z,2}\tan\beta'_2-U_1V_{z,1}\tan\beta_1 \tag{B9}$$

$$\frac{\partial H_2}{\partial\bar{\omega}'}=-U_2\tan\beta'_2\frac{\partial V_{z,2}}{\partial\bar{\omega}'}$$

Therefore,

$$\left(\frac{\Delta H_2}{H_2}\right)_v=-\frac{U_2V_{z,2}}{H_2}\tan\beta'_2\left(\frac{\Delta V_{z,2}}{V_{z,2}}\right) \tag{B10}$$

Combination of (B10), (B8), and (dF-v) yields the following:

$$\left(\frac{\Delta P_2}{P_2}\right)_v=-\frac{\gamma}{\gamma-1}\frac{U_2V'_2\sin\beta'_2}{H_2}\left(\frac{\Delta V_{z,2}}{V_{z,2}}\right)_v-[1-(M'_2)^2]\left(\frac{\Delta V_{z,2}}{V_{z,2}}\right)_v$$

$$=-\gamma\frac{M'_2\sin\beta'_2\cos\beta'_2(\tan\beta_2+\tan\beta'_2)}{1+\frac{\gamma-1}{2}M_2^2}\left(\frac{\Delta V_{z,2}}{V_{z,2}}\right)_v-[1-(M'_2)^2]\left(\frac{\Delta V_{z,2}}{V_{z,2}}\right)_v$$

$$=-\left\{[1-(M'_2)^2]+\frac{\gamma(M'_2)^2\sin\beta'_2\cos\beta'_2(\tan\beta_2+\tan\beta'_2)}{1+\frac{\gamma-1}{2}(M'_2)^2\cos^2\beta'_2\sec^2\beta_2}\right\}\left(\frac{\Delta V_{z,2}}{V_{z,2}}\right)_v \tag{dH-v}$$

$$\times\left[1-\left(\frac{p}{P}\right)^{\frac{\gamma-1}{\gamma}}\right]^{1/2}+\left(\frac{p}{P}\right)^{\frac{1}{\gamma}}\frac{1}{2}\left[1-\left(\frac{p}{P}\right)^{\frac{\gamma-1}{\gamma}}\right]^{-1/2}$$

$$\times\left[-\frac{\gamma-1}{\gamma}\left(\frac{p}{P}\right)^{\frac{\gamma-1}{\gamma}-1}\frac{1}{P}\right]\right\}$$

$$=\frac{1}{\gamma p}(\rho V_z)-\frac{1}{\gamma p}\frac{\rho V_z}{\frac{2}{\gamma-1}\left[\left(\frac{p}{P}\right)^{-\frac{\gamma-1}{\gamma}}-1\right]}$$

$$\left[\frac{\Delta(\rho V_z)}{\rho V_z}\right]_1=\frac{1}{\gamma}\left(1-\frac{1}{M^2}\right)\frac{\Delta p_1}{p_1} \tag{mA-i}$$

COMPRESSOR AND TURBINE MATCHING

By James F. Dugan, Jr.

In order that compressor operation can be found for specified flight conditions and a mode of engine operation, methods are presented for relating the compressor to the other components of four types of gas-turbine engines—the simple turbojet, the afterburning turbojet, the turboprop with coupled power turbine, and the turboprop with free-wheeling power turbine.

The method of superposing component matching maps to obtain one- and two-spool gas-generator performance is discussed, as well as simplified methods for obtaining gas-generator performance. The simplification results from assuming constant turbine-inlet equivalent weight flow and an approximate relation for turbine efficiency. Compressor operation can be found from the gas-generator performance alone for a range of flight conditions when the mode of engine operation is specified by assigning values of mechanical speed and turbine-inlet temperature.

Procedures are also discussed for (1) combining the gas generator with the other components of gas-turbine engines so that compressor operation can be found for a range of flight conditions when the operating mode is specified by assigning values of mechanical speed and exhaust-nozzle area; (2) locating a constant-exhaust-nozzle-area equilibrium operating line on the compressor performance map of a one-spool nonafterburning turbojet engine operated at static sea-level conditions; (3) matching the components of a one-spool simple turbojet engine during transient operation for a specified flight condition, a specified transient path on the compressor map, and a fixed exhaust-nozzle area; (4) finding the compressor paths during a transient for a nonafterburning two-spool turbojet for which the exhaust-nozzle area and inner-turbine-inlet temperature are maintained constant; and (5) calculating the time required to accelerate to a higher engine speed for both one- and two-spool turbojet engines.

INTRODUCTION

An axial-flow compressor is designed so that at a specific rotative speed and weight flow the desired value of total-pressure ratio is achieved at a high level of efficiency. As a component of a gas-turbine engine, the compressor is required to operate over a range of pressure ratios, weight flows, and rotational speeds during steady-state and transient engine operation. To illustrate this point, engine operation is related to the compressor performance map of pressure ratio plotted against equivalent weight flow with equivalent rotational speed as a parameter. During engine acceleration prior to takeoff when the compressor speed increases from zero to the takeoff value, the compressor may operate in a region characterized by severe blade vibrations caused by rotating stall. Acceleration may even be prevented by compressor operation outside the stable operating region bounded by the compressor surge- or stall-limit line. For subsonic flight in the stratosphere, the compressor may operate in a low-efficiency region at high values of compressor equivalent speed. At supersonic flight speeds, the compressor surge- or stall-limit line may be encountered or operation may be required in a region characterized by low compressor efficiency or dangerous blade vibrations.

The purpose of this chapter is to present matching procedures so that compressor operation can be found for specified flight conditions and a mode of engine operation. (The matching procedures also yield the operating points of all the other engine components and data from which engine performance can be calculated.) Such methods are useful in selecting engine design values for compressor pressure ratio and weight flow. After the compressor performance map is estimated (see ch. X), it may be evaluated by employing matching procedures to find the region over which the compressor will be required to operate

469

for the desired mode of operation and range of flight conditions. Besides permitting an evaluation of compressor performance maps, the matching methods presented herein permit calculation of the effects of compressor changes on engine performance. The methods of chapter X may be used to estimate the effect on compressor performance of changes involving interstage bleed, passage flow area, or blade-setting angles. With the new compressor performance map and the matching procedures, the effect of the compressor change on engine performance may be found.

In order to find where on its performance map a compressor will operate as part of an engine for a specified flight condition and mode of engine operation, the engine components must be matched. The following three approaches may be used to accomplish component matching. Regardless of the approach, four relations involving continuity of flow, power balance, speed of rotation, and pressure ratio are available.

In one approach, the conventional compressor and turbine performance maps are employed. For an operating point assigned to one of the component maps, the corresponding points on the other component maps are found by satisfying the four matching relations. Such an approach is discussed in reference 12 for the turbojet engine and in reference 13 for the turboprop engine.

In a second approach, the performances of the turbine, tailpipe, and exhaust nozzle are combined. The conventional compressor performance map is retained; and, for an operating point on this map, the corresponding operating points of the other components are found through the use of the combined performance of the turbine, tailpipe, and exhaust nozzle. This approach is used in reference 348 for the one-spool turboprop with coupled power turbine and in reference 349 for the one-spool turbojet without afterburning.

In a third approach, the combined performance of the compressor, combustor, and turbine is found. In place of the conventional compressor and turbine performance maps, matching maps are used. All possible match points are determined by the superposition of these matching maps. When the operating mode is such that the mechanical speed and turbine-inlet temperature are specified, this approach is especially useful. For this type of problem, the compressor operation

can be found from the combined performance of the compressor, combustor, and turbine, independent of the inlet, tailpipe, or exhaust-nozzle performance. The idea of superposition of component maps to achieve matching is used in references 350 to 352 for one-spool gas-turbine engines and in references 25 and 353 for two-spool gas-turbine engines.

Procedures for matching the components of one- and two-spool turbojet engines during transients are presented in references 22 and 27, respectively. The equations and procedures in reference 354 facilitate the computation of part-load and off-design-point internal performance by the use of automatic computing machinery.

Much of the material in this chapter is derived from references 22, 25, 27, 349, and 352. General and simplified methods are given for matching compressor and turbine components of one- and two-spool jet engines for equilibrium operation (refs. 25 and 352). Procedures for combining the performances of the compressor, combustor, and turbine components to yield gas-generator performance are explained, as well as the way compressor operation can be found from the gas-generator performance for a range of flight conditions when the mode of engine operation is specified by assigning values of mechanical speed and turbine temperature. In order that compressor operation can be found when the exhaust-nozzle area is specified, procedures are discussed for combining the gas-generator performance with that of other components such as an inlet, a propeller, an afterburner, a free-wheeling power turbine, and an exhaust nozzle. A simplified method for locating a constant-exhaust-nozzle-area equilibrium operating line on the compressor performance map of a one-spool turbojet engine operated at static sea-level conditions is discussed (ref. 349). The combined performance of the turbine, tailpipe, and exhaust nozzle is related to compressor pressure ratio and weight flow in several charts. Desired operating lines can be located on specific compressor performance maps through the use of the charts. A method is discussed whereby the compressor and turbine of a one-spool turbojet engine may be matched for a specified flight condition, a specified transient path on the compressor map, and a fixed exhaust-nozzle area (ref. 22). For a two-spool turbojet engine (ref. 27), procedures are

discussed for finding the compressor paths during a transient for which the exhaust-nozzle area and inner-turbine-inlet temperature are held constant.

SYMBOLS

The following symbols are used in this chapter:

A area, sq ft

$\bar{A}$ area parameter equal to $\dfrac{A_8}{A_4}\left(\dfrac{w^*}{w}\right)_4\dfrac{w_4}{w_8}$

B ratio of bleed weight flow to weight flow at compressor inlet

c_p specific heat at constant pressure, Btu/(lb)(°R)

F_j jet thrust, lb

f fuel-air ratio at combustor inlet

g acceleration due to gravity, 32.17 ft/sec^2

H total or stagnation enthalpy, Btu/lb

I moment of inertia, (lb)(ft)(sec^2)

J mechanical equivalent of heat, 778.2 ft-lb/Btu

K constant

M Mach number

N rotational speed, rps

P total or stagnation pressure, lb/sq ft

$\bar{P}$ pressure-ratio parameter equal to $\dfrac{P_3}{P_1}\dfrac{P_4}{P_3}\dfrac{P_1}{p_0}\dfrac{p_0}{p_8}$

$\mathscr{P}$ power for propeller and/or accessories, Btu/sec

p static or stream pressure, lb/sq ft

Q_{xs} excess torque, lb-ft

R gas constant, 53.35 ft-lb/(lb)(°R)

T total or stagnation temperature, °R

$\bar{T}$ temperature parameter equal to $(1-B_3)$

$(1+f)\dfrac{T_4}{T_1}\eta_{ad,C}\eta_{ad,T}$

U rotor speed, ft/sec

V air velocity, ft/sec

w weight flow, lb/sec

$\bar{w}$ weight-flow parameter equal to

$\sqrt{\dfrac{(1-B_3)(1+f)}{\eta_{ad,C}\eta_{ad,T}}}\,\dfrac{w_8}{w_4}\dfrac{A_1}{A_8}\dfrac{w_1\sqrt{\theta_1}}{\delta_1 A_1}$

β air angle, angle between air velocity and axial direction, deg

γ ratio of specific heats

δ ratio of total pressure to NASA standard sea-level pressure of 2116 lb/sq ft

η_{ad} adiabatic efficiency

θ ratio of total temperature to NASA standard sea-level temperature of 518.7° R

ρ density, lb/cu ft

τ time, sec

ψ turbine pressure coefficient, $(V \sin \beta)/U$

Subscripts:

C compressor

i inner spool

o outer spool

PT power turbine

T turbine

Station numbers shown in figs. 325 and 326:

	Two-spool notation	One-spool notation
0	ambient conditions	
1	outer-compressor inlet	compressor inlet
2	outer-compressor exit, inner-compressor inlet	
3	inner-compressor exit, combustor inlet	compressor exit, combustor inlet
4	combustor exit, inner-turbine inlet	combustor exit, turbine inlet
5	inner-turbine exit, outer-turbine inlet	
6	outer-turbine exit	turbine exit
6a	uncoupled power-turbine exit	
7	exhaust-nozzle inlet	
8	exhaust-nozzle exit	exhaust-nozzle exit

Superscript:

*   critical flow conditions

GENERAL DISCUSSION

The four types of gas-turbine engines discussed in this report are the simple turbojet, the afterburning turbojet, the turboprop with coupled power turbine, and the turboprop with freewheeling power turbine (fig. 325). Common to all four engines is the gas generator, which may be either the one- or two-spool type (fig. 326). This chapter is chiefly concerned with the compressor of a one-spool gas generator and the outer and inner compressors of a two-spool gas generator when operated as components of any of the four gas-turbine engines.

In the section GENERAL METHODS FOR EQUILIBRIUM OPERATION, a matching technique for the superposition of component maps is employed.

(a) Simple turbojet
(b) Afterburning turbojet
(c) Turboprop with coupled power turbine.
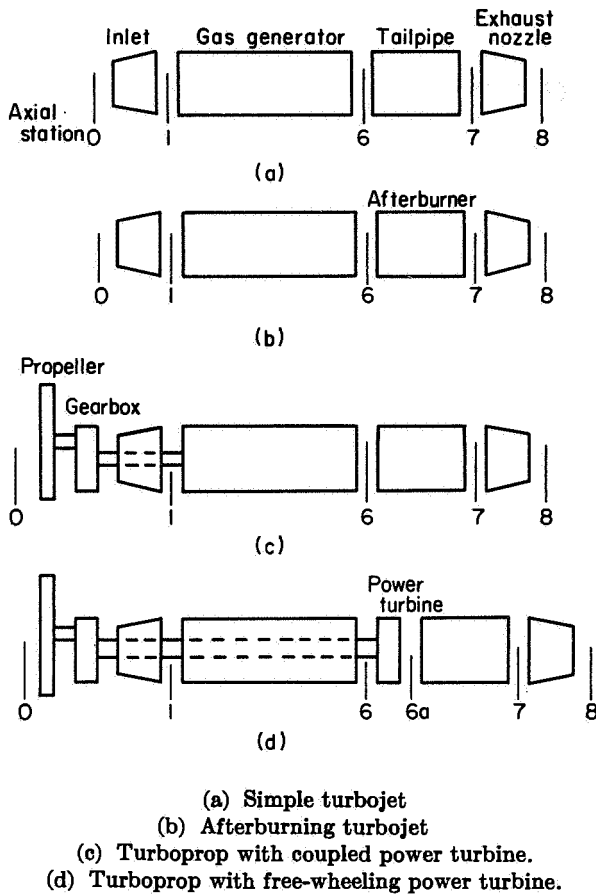(d) Turboprop with free-wheeling power turbine.

FIGURE 325.—Gas-turbine engines.

A procedure for obtaining the performance of a one-spool gas generator is followed by an explanation of the way compressor operating points for various flight conditions may be found from the gas-generator performance alone when engine operation is defined by setting values of mechanical speed and turbine-inlet temperature. The discussion of the two-spool gas generator parallels that for the one-spool. In order that compressor operation may be determined when engine operation is defined by setting values of exhaust-nozzle area and rotative speed, methods are discussed for matching the gas generator with the other components for each of the four engine types shown in figure 325.

In the SIMPLIFIED METHODS FOR EQUILIBRIUM OPERATION, turbine-inlet equivalent weight flow is assumed to be constant for all operating conditions and turbine efficiency is assumed to be a function only of the ratio of the rotative speed to the square root of the enthalpy drop. Methods

for obtaining the performance of one- and two-spool gas generators are discussed.

A matching technique involving the use of the combined performance of the turbine, tailpipe, and exhaust nozzle is used in the section EQUILIBRIUM OPERATING LINE OF ONE-SPOOL TURBOJET. An approximate method is discussed for locating a constant-exhaust-nozzle-area equilibrium operating line on the performance map of a compressor that is part of a one-spool turbojet engine operated at static sea-level conditions. The charts of reference 349, which are needed to accomplish this, are included.

In the section METHODS FOR TRANSIENT OPERATION, conventional compressor and turbine maps are used, and matching is achieved by satisfying the thermodynamic relations and the imposed conditions. A method is discussed whereby the compressor and turbine of a one-spool turbojet engine may be matched for a specified flight condition, a specified transient path on the compressor map, and a fixed exhaust-nozzle area. For a two-spool turbojet engine, procedures are discussed for finding the compressor paths during a transient for which the exhaust-nozzle area and inner-turbine-inlet temperature are held constant.

GENERAL METHODS FOR EQUILIBRIUM OPERATION

In this and the following main section, which discusses simplified methods for equilibrium operation, it is convenient to think of a gas-turbine engine as composed of a gas generator and other components. Sketches of one- and two-spool gas generators are shown in figure 326. The addition of other components such as an inlet, a propeller, an afterburner, a free-wheeling power turbine, and an exhaust nozzle results in either a turboprop or a turbojet engine (fig. 325).

In the discussion of the one-spool gas generator, the component performances are plotted in such a way that the maps may be superposed to satisfy the matching relations of continuity, power balance, and rotational speed. A similar discussion appears in references 350 to 352. In the discussion of the two-spool gas generator, two procedures are presented for matching the inner spool with the outer compressor and turbine, the inner-spool performance having been found by the procedures for the one-spool gas generator. Two-spool matching methods are discussed in references 25
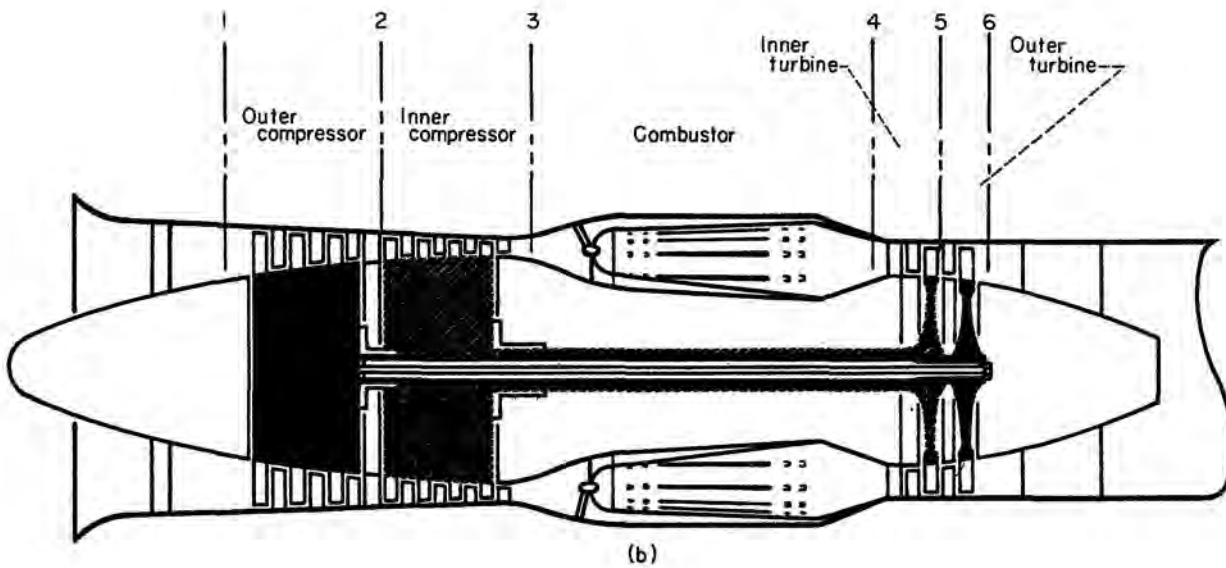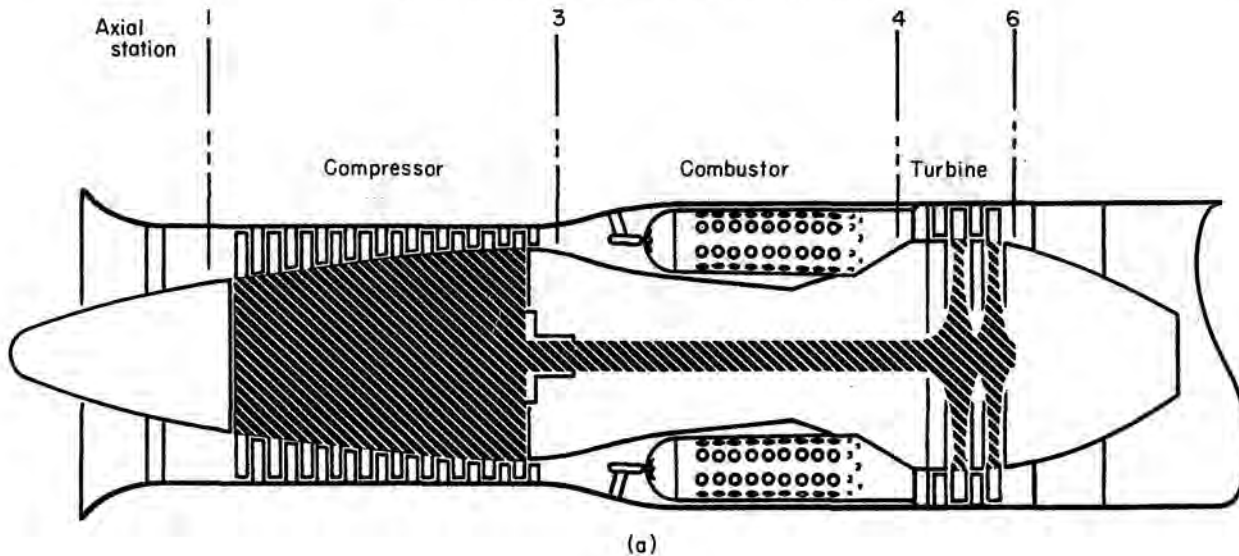
(a) One-spool.
(b) Two-spool.

FIGURE 326.—Schematic diagrams of gas generators.

and 353. The sections on compressor operation from gas-generator performance discuss the procedure for finding compressor operating points when engine operation is specified by assigning values of mechanical speed and turbine-inlet temperature. When exhaust-nozzle area and mechanical speed are assigned, compressor operation can be found for turbojet and turboprop engines as discussed in the section Matching Gas Generator with Other Engine Components.

ONE-SPOOL GAS GENERATOR

In order to match the compressor and turbine of a particular gas generator, the performance of the compressor, combustor, and turbine must be known. Typical compressor and turbine per-
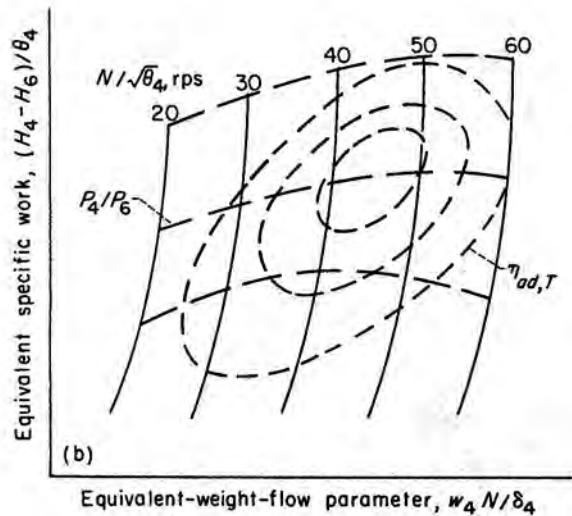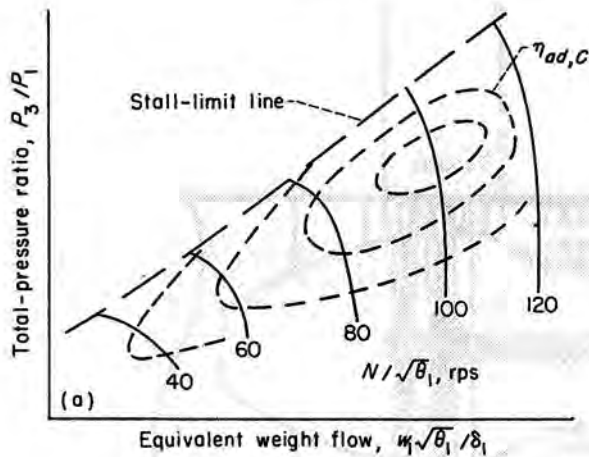
(a) Compressor performance map.

(b) Turbine performance map.

FIGURE 327.—Performance maps.

formance maps are shown in figures 327 (a) and (b), respectively. In figure 327(a), compressor total-pressure ratio is plotted against equivalent weight flow with equivalent speed and adiabatic efficiency as parameters. In figure 327(b), turbine equivalent specific work is plotted against a flow parameter with equivalent speed, total-pressure ratio, and adiabatic efficiency as parameters. The performance of a typical combustor is nearly constant for a wide range of operation. In this chapter the combustor total-pressure ratio P_4/P_3 is taken equal to a constant. When fuel-air

ratios are calculated, combustor efficiency is also taken to be a constant.

Matching relations.—In matching the compressor and turbine, three of the four matching relations are available.

(1) The air weight flow into the compressor minus the air weight flow bled from the compressor exit plus the fuel weight flow added in the combustor equal the gas weight flow into the turbine.

(2) The power output of the turbine is absorbed by the compressor and the accessories.

(3) The mechanical speeds of the compressor and its driving turbine are the same.

For simplicity, the three matching relations are expressed in terms of equivalent performance parameters as follows:

Continuity:

$$\frac{(1-B_3)(1+f)w_1N}{\frac{P_3}{P_1}\frac{P_4}{P_3}\delta_1}=\frac{w_4N}{\delta_4} \qquad (422)$$

Power:

$$\frac{H_3-H_1}{(1-B_3)(1+f)N^2}+\frac{\mathscr{P}}{(1-B_3)(1+f)w_1N^2}=\frac{H_4-H_6}{N^2} \qquad (423)$$

Speed:

$$\frac{T_4}{T_1}=\left(\frac{\frac{N}{\sqrt{\theta_1}}}{\frac{N}{\sqrt{\theta_4}}}\right)^2 \qquad (424)$$

Matching maps and their superposition.—Compressor and turbine matching is achieved by graphically satisfying equations (422) to (424). The performance of the compressor is plotted as $(H_3-H_1)/N^2(1-B_3)(1+f)$ against w_4N/δ_4 for constant values of $N/\sqrt{\theta_1}$ (fig. 328(a)). The compressor variables are computed from

$$\frac{w_4N}{\delta_4}=\frac{(1-B_3)(1+f)}{\frac{P_3}{P_1}\frac{P_4}{P_3}}\frac{w_1\sqrt{\theta_1}}{\delta_1}\frac{N}{\sqrt{\theta_1}} \qquad (425)$$

$$\frac{H_3-H_1}{(1-B_3)(1+f)N^2}=\frac{518.7c_{p,C}\left[\left(\frac{P_3}{P_1}\right)^{\frac{\gamma c-1}{\gamma c}}-1\right]}{\eta_{ad,C}(1-B_3)(1+f)\left(\frac{N}{\sqrt{\theta_1}}\right)^2} \qquad (426)$$

For the purpose of this conversion, it is usually sufficient to assume constant values of fuel-air ratio f, compressor-exit-bleed ratio B_3, specific heat at constant pressure $c_{p,c}$, combustor pressure ratio P_4/P_3, and γ_C. (The variation of $c_{p,c}$ and γ_C with total temperature may be accounted for by using charts such as those presented in ref. 355.)

The turbine performance is plotted as $(H_4-H_6)/N^2$ against w_4N/δ_4 for constant values of $N/\sqrt{\theta_4}$ as in figure 328(b). The ordinate is computed from

$$\frac{H_4-H_6}{N^2}=\frac{\dfrac{H_4-H_6}{\theta_4}}{\left(\dfrac{N}{\sqrt{\theta_4}}\right)^2} \qquad (427)$$

The components are matched by superposing figures 328 (a) and (b) so as to satisfy the continuity and power relations (eqs. (422) and (423)). The abscissas are superposed directly, while the ordinates are offset by the value of the accessory power term in equation (423). In many instances the accessory power term is so small that it can be neglected. Sometimes the value of the accessory power term computed for one engine operating condition is assumed to prevail for all other operating conditions. With the compressor and turbine matching maps overlaid, each point common to both maps is a possible match point for the gas generator. At each such point, the turbine-inlet to compressor-inlet temperature ratio T_4/T_1 may be calculated by using equation (424) and the values of equivalent speed read from the overlaid maps.

Component parameters.—For each match point, the pressure and temperature ratios across the compressor and turbine may be calculated or read from appropriate component maps. The compressor pressure ratio and temperature ratio could be read from plots of these variables against w_4N/δ_4 with $N/\sqrt{\theta_1}$ as a parameter. After the turbine equivalent specific work is calculated from the values of $(H_4-H_6)/N^2$ and $N/\sqrt{\theta_4}$, the turbine pressure ratio can be read from the conventional performance map (fig. 327(b)). The turbine temperature ratio may be calculated from

$$\frac{T_6}{T_4}=1-\frac{H_4-H_6}{\theta_4}\frac{1}{c_{p,T}518.7} \qquad (428)$$

(a) Compressor.
(b) Turbine.
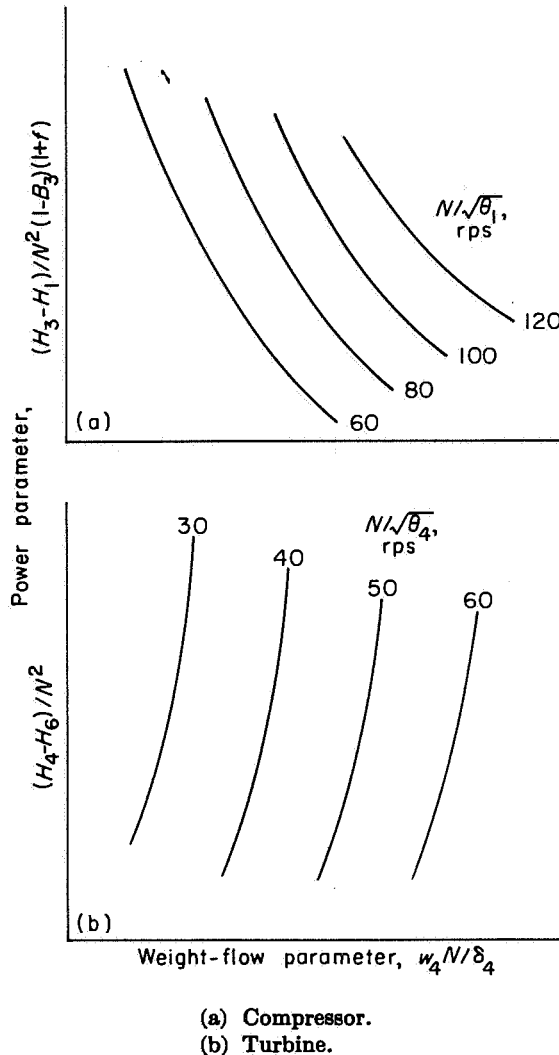
FIGURE 328.—Matching maps for one-spool gas generator.

The value of $c_{p,T}$ can be calculated from

$$c_p=\frac{\gamma}{\gamma-1}\frac{R}{J} \qquad (429)$$

The value of γ is usually based on the design values of fuel-air ratio and the arithmetic average of the turbine-inlet and -outlet temperatures. If more precise calculations are warranted, the charts of reference 355 may be used to find values of T_6/T_4.

For matching purposes, the value of f is usually assumed to be a constant (its design value). Once the compressor and turbine are matched, however, the equivalent fuel-air ratio f/θ_1 at each match point may be found by using the values of

T_3/T_1 and T_4/T_1, an assumed fuel, a combustor efficiency, and combustion charts such as those presented in reference 355. There is no need to rematch the compressor and turbine, because the term $(1+f)$ changes only slightly. The compressor equivalent weight flow $w_1\sqrt{\theta_1}/\delta_1$ may be calculated by using equation (425). The turbine-outlet equivalent weight flow may be calculated from

$$\frac{w_6\sqrt{\theta_6}}{\delta_6}=(1-B_3)(1+f)\frac{w_1\sqrt{\theta_1}}{\delta_1}\frac{\sqrt{\dfrac{T_4}{T_1}\dfrac{T_6}{T_4}}}{\dfrac{P_3}{P_1}\dfrac{P_4}{P_3}\dfrac{P_6}{P_4}} \quad (430)$$

The performance of the one-spool gas generator may be presented as plots of T_4/T_1, P_6/P_1, T_6/T_1, f/θ_1, P_3/P_1, and $w_1\sqrt{\theta_1}/\delta_1$ against $w_6\sqrt{\theta_6}/\delta_6$ with $N/\sqrt{\theta_1}$ as a parameter (fig. 329).

Compressor operations from gas-generator performance.—Compressor operating points for various flight conditions may be found from the gas-generator performance alone if engine operation is defined by setting values of mechanical speed N and turbine-inlet temperature T_4. For a particular flight condition (altitude and Mach number), values of T_1 and θ_1 can be found. From figure 329 and values of T_4/T_1 and $N/\sqrt{\theta_1}$, a value of $w_6\sqrt{\theta_6}/\delta_6$ is read. Then, from values of $w_6\sqrt{\theta_6}/\delta_6$ and $N/\sqrt{\theta_1}$, values of P_3/P_1 and $w_1\sqrt{\theta_1}/\delta_1$ are read. Thus, for each flight condition the compressor operating point can be located.

One-spool matching methods are applied to specific equilibrium problems in references 356 to 360.

TWO-SPOOL GAS GENERATOR

A schematic of a two-spool gas generator is shown in figure 326(b). The outer compressor and outer turbine are mounted on a common shaft. Hereafter, these components are called the outer spool. The inner compressor and the inner turbine are mounted on a second shaft that is not coupled mechanically to the shaft of the outer spool. In airplane engines, the outer-spool shaft is inside of and concentric with the hollow shaft of the inner spool. Between the inner compressor and inner turbine is the combustor; taken together, these components comprise the inner spool.

In matching the components of a two-spool gas generator, it is convenient to match the components of the inner spool and then match the

inner-spool with the outer-spool components. The inner-spool components are matched according to the procedures for matching the components of a one-spool gas generator. Notice that engine stations 1, 3, 4, and 6 for the one-spool gas generator are replaced by 2, 3, 4, and 5 for the inner spool of a two-spool gas generator (fig. 326). The manner in which inner-spool performance is presented is determined by the method employed to match the outer-spool components. Two procedures are discussed for matching the outer- and inner-spool components. In the first procedure, an inner-spool operating point is assigned and matching with the outer compressor and outer turbine is achieved directly. In the second procedure, which involves a trial-and-error step, an outer-compressor operating point is assigned so that the gas-generator performance for constant values of outer-spool equivalent speed results.

Direct method of matching outer and inner spools.—The two-spool matching problem becomes one of matching the outer spool with the inner spool. Because of the aerodynamic coupling between the two spools, specifying two independent conditions determines the operating points of all the components. If an operating point is assigned to the inner spool, outer-spool matching is achieved directly. For this approach it is convenient to express the power and continuity relations with regard to the outer compressor and outer turbine, respectively, as

$$\frac{H_2-H_1}{N_o^2}\frac{1}{(1-B_2)(1-B_3)(1+f)}$$
$$+\frac{\mathcal{P}}{w_1(1-B_2)(1-B_3)(1+f)N_o^2}=\frac{H_5-H_6}{N_o^2} \quad (431)$$

$$\log\frac{w_1 N_o}{\delta_2}=\log\left[\frac{\dfrac{P_5}{P_2}}{(1-B_2)(1-B_3)(1+f)}\right]+\log\frac{w_5 N_o}{\delta_5} \quad (432)$$

Constant values of compressor bleed at stations 2 and 3 and fuel-air ratio may be chosen. The matching map for the outer compressor is shown in figure 330(a). Here $\dfrac{H_2-H_1}{N_o^2(1-B_2)(1-B_3)(1+f)}$ is plotted against $\log(w_1 N_o/\delta_2)$ for lines of constant equivalent speed $N_o/\sqrt{\theta_1}$ and constant equivalent weight flow $w_2\sqrt{\theta_2}/\delta_2$. For the matching map of the outer turbine, $(H_5-H_6)/N_o^2$ is plotted against
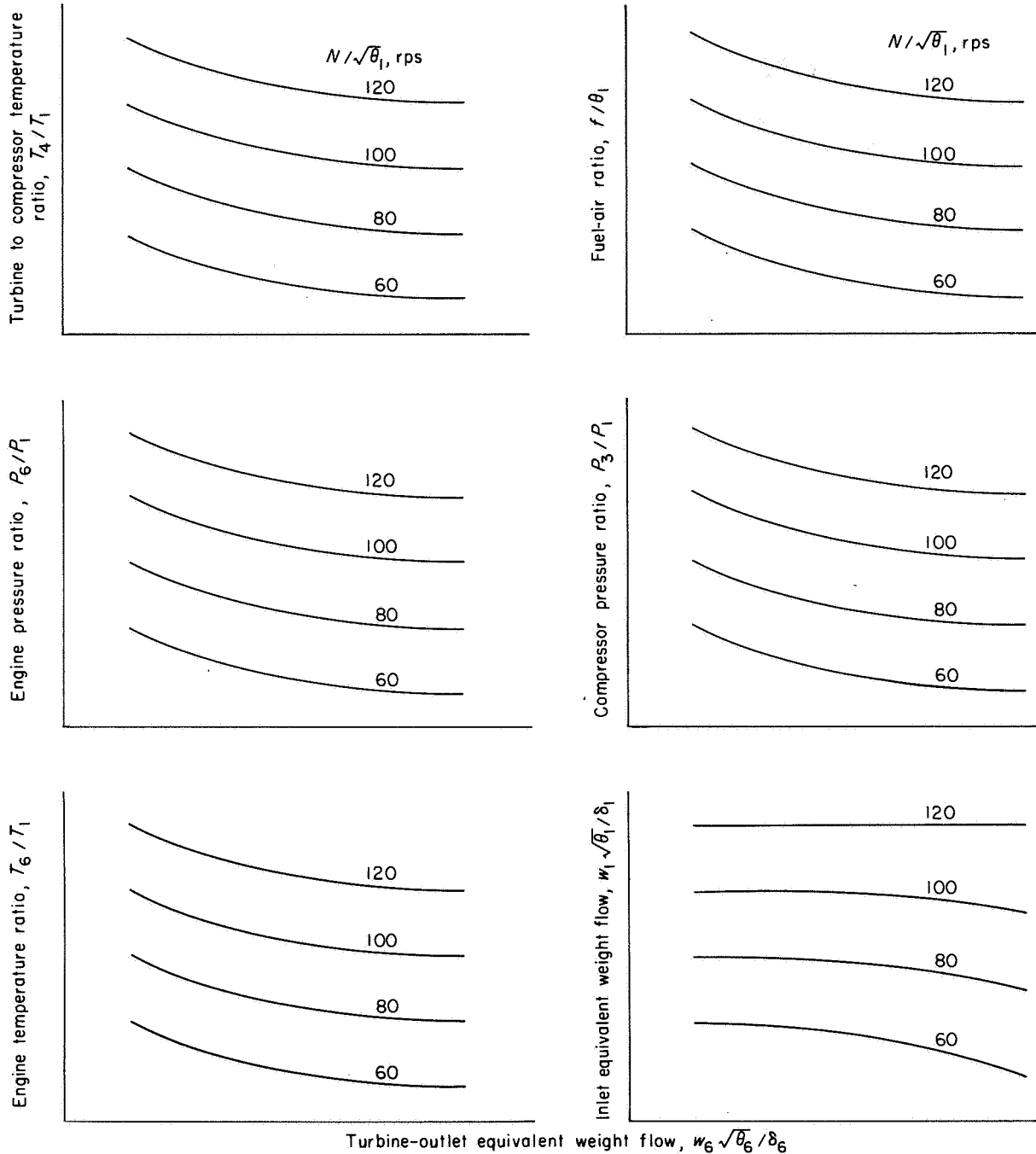
FIGURE 329.—One-spool gas-generator performance.

log $(w_5 N_o/\delta_5)$ with $w_5\sqrt{\theta_5}/\delta_5$ and $N_o/\sqrt{\theta_5}$ as parameters (fig. 330(b)). In order to match the outer-spool components with the inner spool, the matching map of the inner spool is plotted as in figure 330(c). Here, inlet equivalent weight flow $w_2\sqrt{\theta_2}/\delta_2$ is plotted against outlet equivalent weight flow $w_5\sqrt{\theta_5}/\delta_5$ with $N_4/\sqrt{\theta_2}$ and P_5/P_2 as parameters. Inner-spool operation is, of course, limited by the equivalent flow that can be passed by the outer turbine.

With these three matching maps (fig. 330), the match points of the two-spool gas generator can be
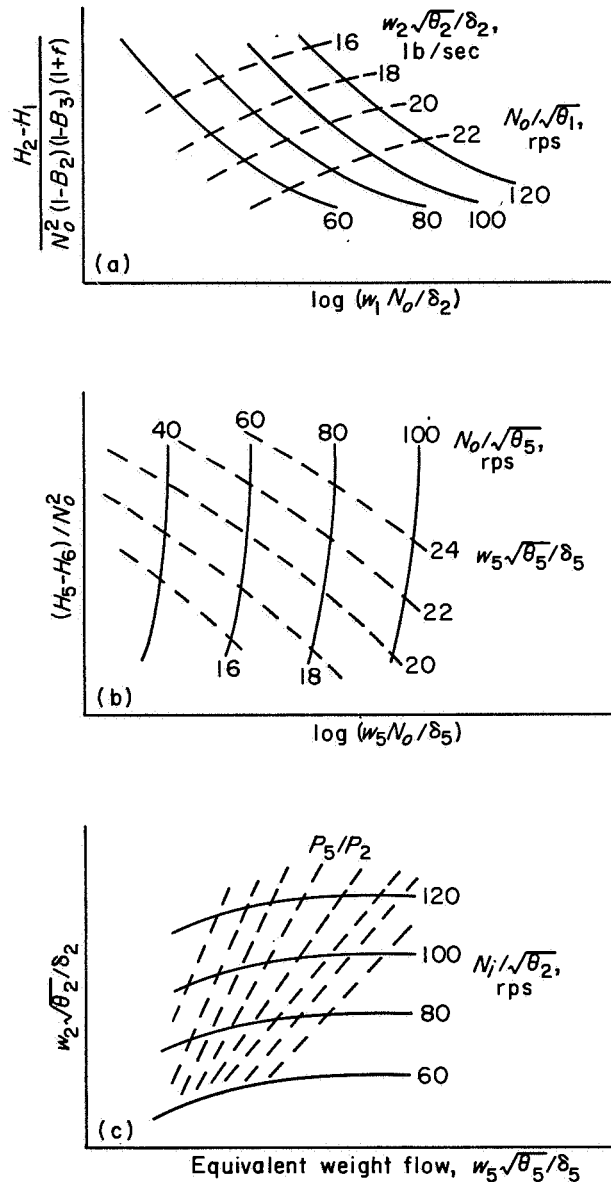
(a) Outer compressor.
(b) Outer turbine.
(c) Inner spool.

FIGURE 330.—Matching maps ford irect method of matching outer and inner spools of two-spool gas generator.

found. An inner-spool operating point is assigned on figure 330(c). The values of $w_2\sqrt{\theta_2}/\delta_2$, $w_5\sqrt{\theta_5}/\delta_5$, and $\frac{P_5}{P_2}$ are noted, and the value of log

$$\left[\frac{P_5/P_2}{(1-B_2)\,(1-B_3)\,(1+f)}\right]$$

is calculated. The outer-compressor and outer-turbine matching maps (figs. 330(a) and (b)) are

superposed so as to satisfy equations (431) and (432). The ordinates of figures 330(a) and (b) are offset by the value of the accessory power term in equation (431), and the abscissas are offset by the calculated value of the term

$$\log\left[\frac{P_5/P_2}{(1-B_2)\,(1-B_3)\,(1+f)}\right]$$

The operating points of the outer compressor and

the outer turbine corresponding to the assigned inner-spool operating point are at the intersection of the appropriate lines of constant $w_2\sqrt{\theta_2}/\delta_2$ and $w_5\sqrt{\theta_5}/\delta_5$. In using this procedure, it has been found convenient to assign several values of $w_5\sqrt{\theta_5}/\delta_5$ for each selected value of $w_2\sqrt{\theta_2}/\delta_2$ in figure 330(c). Choosing pairs of values for $w_2\sqrt{\theta_2}/\delta_2$ and $w_5\sqrt{\theta_5}/\delta_5$ in this way dictates the values of these parameters to be used in plotting lines of constant equivalent weight flow in figures 330(a) and (b). Use of this direct method of matching outer and inner spools or of the iterative method, which is described in the following paragraphs, is a matter of personal preference.

Iterative method of matching outer and inner spools. An alternative procedure for matching the outer-spool components with the inner spool may be employed by assigning the outer-compressor operating point rather than that of the inner spool. For this procedure, the matching maps of figure 331 are used. The outer-compressor performance is plotted as $(H_2-H_1)/N_o^2$ against $w_2\sqrt{\theta_2}/\delta_2$ with $N_o/\sqrt{\theta_1}$ as a parameter (fig. 331(a)); the performance of the outer turbine is plotted as (H_5-H_6) $/N_o^2$ against $w_5 N_o/\delta_5$ with $N_o/\sqrt{\theta_5}$ as parameter (fig. 331(b)); and inner-spool performance is plotted as $w_2\sqrt{\theta_2}/\delta_2$ against $w_5\sqrt{\theta_5}/\delta_5$ for constant values of $N_i/\sqrt{\theta_2}$ and T_5/T_2 (fig. 331(c)).

The inner- and outer-spool components may be matched by employing an iterative procedure in conjunction with the matching maps of figure 331:

(1) An operating point is assigned on the outer-compressor map (fig. 331(a)) from which values of $w_2\sqrt{\theta_2}/\delta_2$, $N_o/\sqrt{\theta_1}$, and $(H_2-H_1)/N_o^2$ are read.

(2) The value of $(H_5-H_6)/N_o^2$ is calculated from equation (431).

(3) The value of T_2/T_1 is calculated from

$$\frac{T_2}{T_1}=1+\frac{H_2-H_1}{N_o^2}\left(\frac{N_o}{\sqrt{\theta_1}}\right)^2\frac{1}{518.7c_{p,oC}} \qquad (433)$$

(4) A trial value of $N_o/\sqrt{\theta_5}$ is assigned.

Because assigning the outer-compressor operating point determines the operating points of all the other components, assuming a value of $N_o/\sqrt{\theta_5}$ is an overspecification and will lead to a contradiction if an incorrect value is assumed.

(5) A value of $w_5 N_o/\delta_5$ is read from figure 331(b) for the values of $(H_5-H_6)/N_o^2$ and $N_o/\sqrt{\theta_5}$.

(6) A value of $w_5\sqrt{\theta_5}/\delta_5$ is calculated from the values of $w_5 N_o/\delta_5$ and $N_o/\sqrt{\theta_5}$.

(7) A value of T_5/T_2, which depends on the inner-spool performance, is read from figure 331(c) for the values of $w_2\sqrt{\theta_2}/\delta_2$ and $w_5\sqrt{\theta_5}/\delta_5$.

(8) A second value of T_5/T_2, which depends on the relation between the outer compressor and outer turbine, is calculated from

$$\frac{T_5}{T_2}=\left(\frac{\frac{N_o}{\sqrt{\theta_1}}}{\frac{N_o}{\sqrt{\theta_5}}}\right)^2\frac{1}{\frac{T_2}{T_1}} \qquad (434)$$

If this does not equal the value from step (7), steps (4) to (8) are repeated until agreement is reached. In using this procedure, it has been found convenient to assign outer-compressor operating points along lines of constant outer-spool speed and to calculate first the match points for the higher values of $w_2\sqrt{\theta_2}/\delta_2$. As lower values of $w_2\sqrt{\theta_2}/\delta_2$ are assigned at a fixed speed $N_o/\sqrt{\theta_1}$, higher values of $w_5\sqrt{\theta_5}/\delta_5$ will result until the critical value is reached. From this point on, all lower selected values of $w_2\sqrt{\theta_2}/\delta_2$ will be accompanied by the critical value of $w_5\sqrt{\theta_5}/\delta_5$.

Variable pressure losses in primary combustor.—The matching procedure for the two-spool gas generator may also be applied for either a one-spool generator or the inner spool or a two-spool generator when large, variable pressure losses occur in the primary burner. For these conditions, curves analogous to figure 330(c) would represent the combuster characteristics.

Component parameters.—For each match point of a two-spool gas generator, the pressure and temperature ratios across the components may be calculated or read from appropriate component maps. If the iterative procedure is used for matching the inner spool with the outer components, the following values are known for each match point:

$$N_o/\sqrt{\theta_1},\ w_2\sqrt{\theta_2}/\delta_2,\ (H_5-H_6)/N_o^2,\ T_2/T_1,$$

$$w_5\sqrt{\theta_5}/\delta_5,\ T_5/T_2,\ \text{and}\ N_o/\sqrt{\theta_5}.$$

The outer-compressor pressure ratio may be read from a plot of P_2/P_1 against $w_2\sqrt{\theta_2}/\delta_2$ with $N_o/\sqrt{\theta_1}$ as parameter. Inner-compressor equivalent speed $N_i/\sqrt{\theta_2}$ may be read from figure 331(c). The values of P_3/P_2, T_3/T_2, T_4/T_2, and P_5/P_2 may be read from plots of these variables against
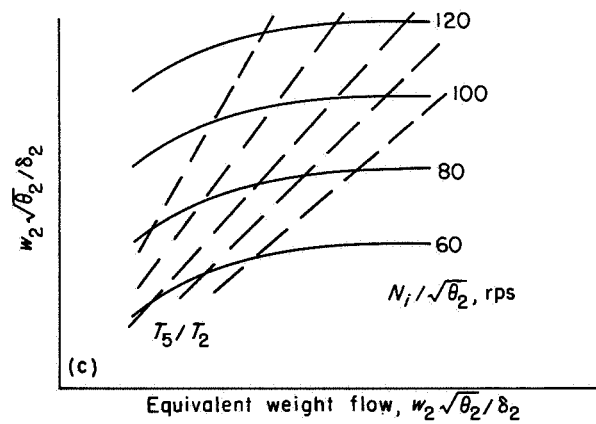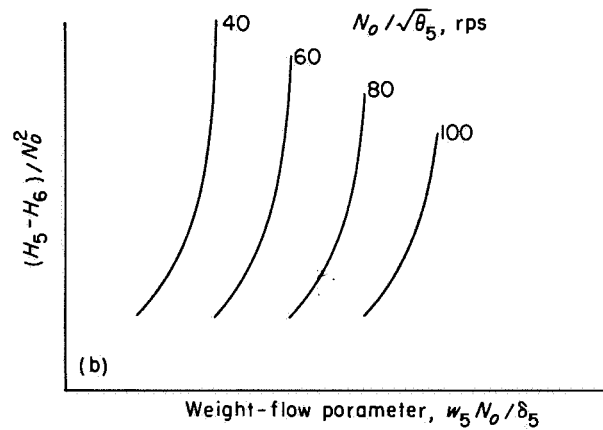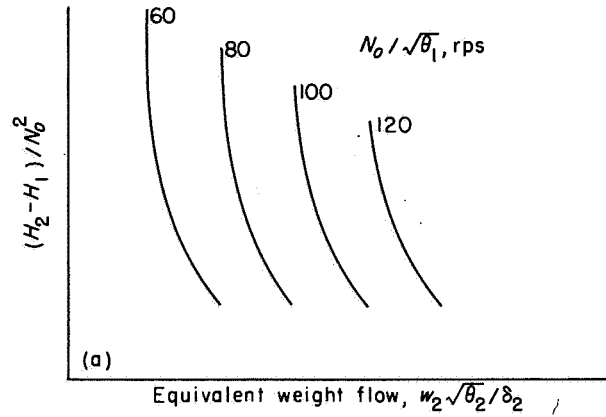
(a) Outer compressor.
(b) Outer turbine.
(c) Inner spool.

FIGURE 331.—Matching maps for iterative method of matching outer and inner spools of two-spool gas generator.

$w_5\sqrt{\theta_5}/\delta_5$ with $N_i/\sqrt{\theta_2}$ as a parameter. The outer-turbine pressure ratio may be read from a plot of P_5/P_6 against $(H_5-H_6)/N_o^2$ with $N_o/\sqrt{\theta_5}$ as a parameter. Outer-turbine temperature ratio may be calculated from

$$\frac{T_6}{T_5}=1-\frac{H_5-H_6}{N_o^2}\left(\frac{N_o}{\sqrt{\theta_5}}\right)^2\frac{1}{518.7c_{p,oT}} \quad (435)$$

The equivalent fuel-air ratio f/θ_1 at each match point may be found by using the values of T_4/T_1 and T_3/T_1, an assumed fuel, a combustor efficiency, and combustion charts such as those presented in reference 355.

The performance of the two-spool gas generator may be presented as plots of T_4/T_1, P_6/P_1, T_6/T_1, f/θ_1, and $w_1\sqrt{\theta_1}/\delta_1$ against $w_6\sqrt{\theta_6}/\delta_6$ with $N_o/\sqrt{\theta_1}$ as a parameter and a plot of $N_i/\sqrt{\theta_1}$ against T_4/T_1 with $N_o/\sqrt{\theta_1}$ as a parameter (fig. 332).

Compressor operation from gas-generator performance.—The outer- and inner-compressor operating points at an assigned flight condition may be found from the gas-generator performance if engine operation is specified by assigning values of outer- or inner-spool mechanical speed and inner-turbine-inlet temperature. From the assigned flight condition are found values of θ_1 and T_1. From the assigned engine operation, values of $N_o/\sqrt{\theta_1}$ or $N_i/\sqrt{\theta_1}$ and T_4/T_1 are calculated. If $N_o/\sqrt{\theta_1}$ and T_4/T_1 are known, a value of $w_6\sqrt{\theta_6}/\delta_6$ is read from figure 332(a). If $N_i/\sqrt{\theta_1}$ and T_4/T_1 are known, a value of $N_o/\sqrt{\theta_1}$ is read from figure 332(d); and then, using the values of $N_o/\sqrt{\theta_1}$ and T_4/T_1, a value of $w_6\sqrt{\theta_6}/\delta_6$ is read from figure 332(a). Values of P_2/P_1, $w_1\sqrt{\theta_1}/\delta_1$, P_3/P_2, and $w_2\sqrt{\theta_2}/\delta_2$ are read from plots of these variables against $w_6\sqrt{\theta_6}/\delta_6$ with $N_o/\sqrt{\theta_1}$ as a parameter. Thus, for each flight condition, the outer- and inner-compressor operating points may be found. In reference 26, two-spool matching methods are used to investigate the effect of design over-all compressor pressure ratio division on two-spool turbojet-engine performance and geometry.

MATCHING GAS GENERATORS WITH OTHER ENGINE COMPONENTS

To determine compressor operation when exhaust-nozzle area and mechanical speed are assigned, the gas generator must be matched with the other engine components. For either the one- or

the two-spool gas generator, the following gas-turbine engine configurations are possible:

(1) Simple turbojet, where gas generator is preceded by inlet diffuser and followed by tailpipe and exhaust nozzle (fig. 325(a))
(2) Afterburning turbojet, where afterburner replaces tailpipe of simple turbojet (fig. 325(b))
(3) Turboprop with coupled power turbine, where propeller is geared to gas-generator shaft (fig. 325(c))
(4) Turboprop with free-wheeling power turbine, where propeller is geared to shaft of free-wheeling power turbine (fig. 325(d))

Methods for matching the gas generator with the other engine components for each of these engine configurations are discussed. By using these methods, compressor operation can be determined for various flight conditions when engine operation is specified by assigning values of exhaust-nozzle area and mechanical speed.

Simple turbojet.—The gas generator of a simple turbojet may be matched with the other components by using three plots, one each for the inlet and the gas generator and a combined map for the tailpipe and exhaust nozzle. The performance of a fixed-geometry diffuser inlet is shown in figure 333(a), where pressure ratio P_1/p_0 is plotted against equivalent weight flow $w_1\sqrt{\theta_1}/\delta_1$ with free-stream Mach number M_0 as parameter. Gas-generator performance is plotted as log (P_6/P_1) against $w_6\sqrt{\theta_6}/\delta_6$ with $N_o/\sqrt{\theta_1}$ as parameter (fig. 333(b)). The combined map for the tailpipe and exhaust nozzle is shown in figure 333(c), where log (P_6/p_0) is plotted against $w_6\sqrt{\theta_6}/\delta_6$ for a fixed exhaust-nozzle area.

From figure 333(a), trial values of P_1/p_0 and $w_1\sqrt{\theta_1}/\delta_1$ are read for the assigned flight Mach number. Figures 333 (b) and (c) are superposed: the ordinates are offset by the value of log (P_1/p_0), while the abscissas are superposed directly. The value of $w_6\sqrt{\theta_6}/\delta_6$ is read from the overlaid maps at the intersection of the fixed-exhaust-nozzle-area curve and the appropriate constant-speed line. (The value of $N_o/\sqrt{\theta_1}$ may be calculated from the assigned value of M_0, altitude, and N_o.) A gas-generator plot of $w_1\sqrt{\theta_1}/\delta_1$ against $w_6\sqrt{\theta_6}/\delta_6$ with $N_o/\sqrt{\theta_1}$ as a parameter yields a value of $w_1\sqrt{\theta_1}/\delta_1$. If this value of $w_1\sqrt{\theta_1}/\delta_1$ is not equal to the trial value, the process is repeated. When the two

(a) Turbine to compressor temp. ratio, T_4/T_1 — $N_o/\sqrt{\theta_1}$, rps: 120, 100, 80, 60

(b) Fuel-air ratio, f/θ_1 — $N_o/\sqrt{\theta_1}$, rps: 120, 100, 80, 60

(c) Engine press. ratio, P_6/P_1 — 120, 100, 80, 60

(d) Inner-spool equivalent speed, $N_i/\sqrt{\theta_1}$, rps — 120, 100, 80, 60

(e) Engine temp. ratio, T_6/T_1 — 120, 100, 80, 60

(f) Inlet equivalent wt. flow, $w_1\sqrt{\theta_1}/\delta_1$ — 120, 100, 80, 60

Turbine-outlet equivalent weight flow, $w_6\sqrt{\theta_6}/\delta_6$
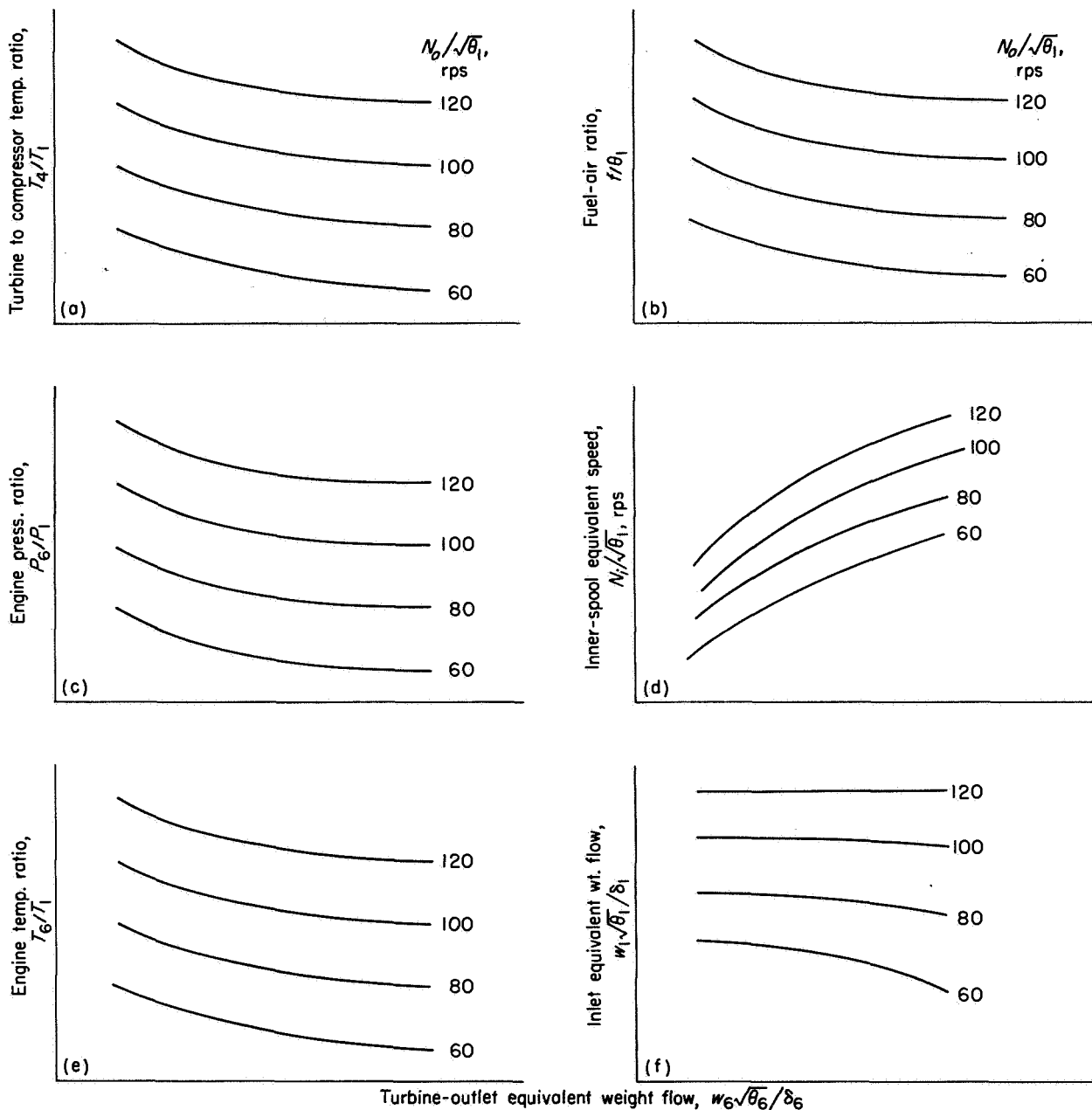
FIGURE 332.—Two-spool gas-generator performance.

values of $w_1\sqrt{\theta_1}/\delta_1$ agree, the gas generator is matched with the other engine components for the assigned flight condition and mode of engine operation. The outer- and inner-compressor operating points may now be found by reading values of P_2/P_1, P_3/P_2, and $w_2\sqrt{\theta_2}/\delta_2$ from plots of these variables against $w_6\sqrt{\theta_6}/\delta_6$ with $N_o/\sqrt{\theta_1}$ as a parameter.

Afterburning turbojet.—The procedures for the afterburning turbojet are the same as for the simple turbojet. The combined map for the tailpipe and exhaust nozzle is replaced by the combined map for the afterburner and exhaust nozzle.

Turboprop with coupled power turbine.—When the propeller is geared to the compressor shaft of
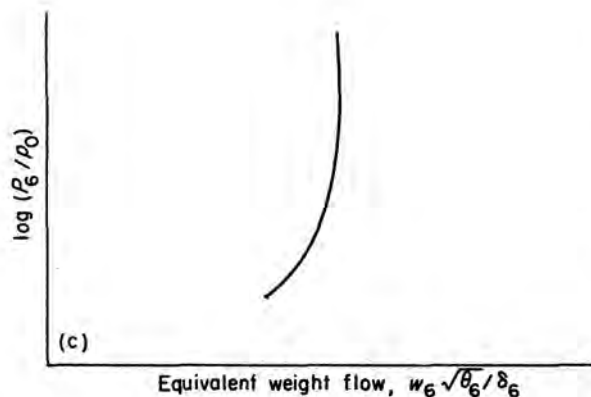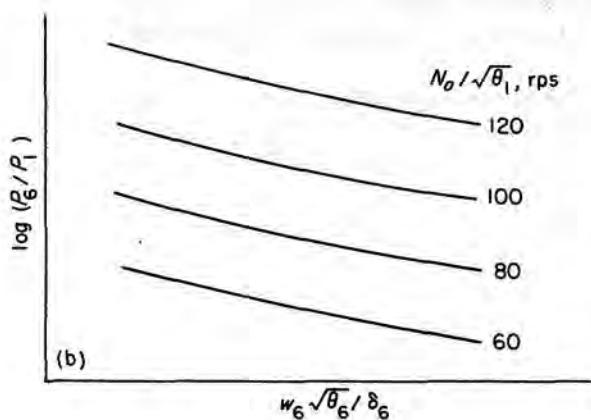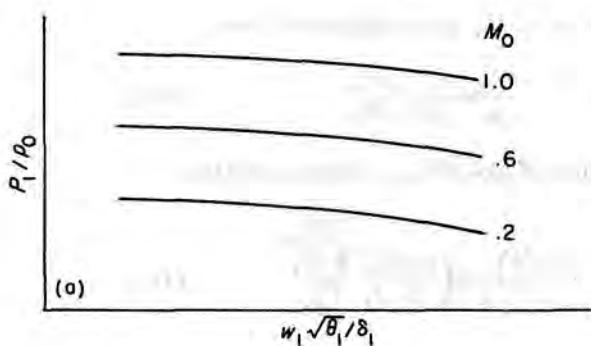
(a) Fixed-geometry inlet.
(b) Gas generator.
(c) Combined map for tailpipe and exhaust nozzle.

FIGURE 333.—Matching maps for simple turbojet.

a one-spool gas generator or to the outer-spool shaft of a two-spool engine, the propeller power must be added to the accessory power in equation

(423) or (431) before the gas-generator performance is obtained. For each value of propeller power, a distinct set of gas-generator performance curves will be obtained. Compressor operation can be found by assigning values of flight Mach number, altitude, mechanical speed, exhaust-nozzle area, and propeller power. The procedures for matching and for obtaining the compressor operating points are the same as those for a simple turbojet. One-spool turboprop problems are discussed in references 361 to 363.

Turboprop with free-wheeling power turbine.—For a turboprop with a free-wheeling power turbine, a procedure is discussed for finding the compressor operating points when the following are assigned: flight Mach number and altitude, propeller power $\mathcal{P}$, shaft speed of power turbine N_{PT}, and exhaust-nozzle area. The discussion is for a turboprop having a two-spool gas generator; the procedure is essentially the same for a turboprop having a one-spool gas generator.

(1) Values of T_1, θ_1, and p_0 are found for the assigned M_0 and altitude.

(2) A trial point is assigned in figure 333(a) for the assigned M_0, and values of P_1/p_0 and $w_1\sqrt{\theta_1}/\delta_1$ are read at this point.

(3) A value of $w_6\sqrt{\theta_6}/\delta_6$ is assumed. Over much of its operating range, the power turbine operates at a fixed value of $w_6\sqrt{\theta_6}/\delta_6$.

(4) A value of $N_o/\sqrt{\theta_1}$ is read from figure 332(f) for the values of $w_6\sqrt{\theta_6}/\delta_6$ and $w_1\sqrt{\theta_1}/\delta_1$.

(5) Values of P_6/P_1 and T_6/T_1 are read from figures 332 (c) and (e) for the values of $w_6\sqrt{\theta_6}/\delta_6$ and $N_o/\sqrt{\theta_1}$.

(6) The power-turbine equivalent speed $N_{PT}/\sqrt{\theta_6}$ is calculated from

$$\frac{N_{PT}}{\sqrt{\theta_6}}=N_{PT}\frac{1}{\sqrt{\theta_1}}\frac{1}{\sqrt{\dfrac{T_6}{T_1}}} \qquad (436)$$

(7) The power-turbine equivalent specific work is calculated from

$$\frac{H_6-H_{6a}}{\theta_6}=\frac{\mathcal{P}}{\dfrac{w_6\sqrt{\theta_6}}{\delta_6}\dfrac{P_6}{P_1}\dfrac{P_1}{p_0}\dfrac{p_0}{2116}\sqrt{\theta_1}\sqrt{\dfrac{T_6}{T_1}}} \qquad (437)$$

(8) A value of $w_6 N_{PT}/\delta_6$ is read from figure 334(a) for the values of $N_{PT}/\sqrt{\theta_6}$ and $(H_6-H_{6a})/\theta_6$.

(a) Power-turbine performance.
(b) Combined performance of tailpipe and exhaust nozzle.

FIGURE 334.—Matching maps for turboprop with free-wheeling power turbine.

(9) A value of $w_6\sqrt{\theta_6}/\delta_6$ is calculated from

$$\frac{w_6\sqrt{\theta_6}}{\delta_6}=\frac{w_6 N_{PT}}{\delta_6}\frac{1}{\dfrac{N_{PT}}{\sqrt{\theta_6}}} \qquad (438)$$

If this does not equal the assumed value of $w_6\sqrt{\theta_6}/\delta_6$ (step (3)), steps (3) to (9) are repeated until the two values do agree.

(10) A value of P_6/P_{6a} is read from figure 334(a) for the values of $N_{PT}/\sqrt{\theta_6}$ and $(H_6-H_{6a})/\theta_6$.

(11) A value of T_{6a}/T_6 is calculated from

$$\frac{T_{6a}}{T_6}=1-\frac{(H_6-H_{6a})}{\theta_6}\frac{1}{518.7c_{p,PT}} \qquad (439)$$

(12) A value of P_{6a}/p_0 is calculated from

$$\frac{P_{6a}}{p_0}=\frac{P_1}{p_0}\frac{P_6}{P_1}\frac{P_{6a}}{P_6} \qquad (440)$$

(13) A value of $(w\sqrt{\theta}/\delta)_{6a}$ is calculated from

$$\left(\frac{w\sqrt{\theta}}{\delta}\right)_{6a}=\left(\frac{w\sqrt{\theta}}{\delta}\right)_6\frac{\sqrt{\dfrac{T_{6a}}{T_6}}}{\dfrac{P_{6a}}{P_6}} \qquad (441)$$

(14) A value of $(w\sqrt{\theta}/\delta)_{6a}$ is read from figure 334(b) for the calculated value of P_{6a}/p_0 (step (12)). If this does not equal the value from step (13), steps (2) to (14) are repeated until agreement is reached.

(15) The compressor operating points can be found by reading values of P_2/P_1, P_3/P_2, and $w_2\sqrt{\theta_2}$ from gas-generator plots of these variables against $w_6\sqrt{\theta_6}/\delta_6$ for constant values of $N_o/\sqrt{\theta_1}$.

Turbojet- and turboprop-engine performance.— After the gas generator has been matched with the other turbojet-engine components, the airflow, the pressure, and the temperature at the exhaust nozzle are known. The jet thrust F_j can be found from the following equations (ref. 364), which relate F_j/w to P_8/p_0:

$$\frac{F_j}{\dfrac{w}{g}}=K_2\sqrt{T_8}(1+f) \qquad (442)$$

For a complete-expansion nozzle,

$$K_2=\sqrt{2gJc_p}\sqrt{1-\left(\frac{p_0}{P_8}\right)^{\frac{\gamma-1}{\gamma}}} \qquad (443)$$

and for the convergent nozzle at supercritical pressures,

$$K_2=\sqrt{2gJc_p}\left\{\sqrt{\frac{\gamma-1}{\gamma+1}}+\left(\frac{\gamma+1}{2}\right)^{\frac{\gamma+1}{2(\gamma-1)}}\frac{\sqrt{\frac{\gamma-1}{2}}}{\gamma}\right.$$
$$\left.\left[\left(\frac{2}{\gamma+1}\right)^{\frac{\gamma}{\gamma-1}}-\frac{p_0}{P_8}\right]\right\} \qquad (444)$$

A graph relating K_2 to the nozzle pressure ratio is given in figure 11 of reference 364. Net thrust is

found by deducting the momentum of the inlet air from the jet thrust.

Fuel flow can be computed by multiplying air-flow by fuel-air ratio. The fuel economy expressed as thrust specific fuel consumption is simply the ratio of fuel flow to thrust.

After the gas generator has been matched with the other turboprop-engine components, the shaft power, jet thrust, and specific fuel consumption can be calculated from the equations derived in appendix D of reference 348.

SIMPLIFIED METHODS FOR EQUILIBRIUM OPERATION

In this section, simplified methods are presented for obtaining the performance of one- and two-spool gas generators. The simplification consists in making several assumptions regarding turbine performance. The equivalent weight flow at the turbine inlet is assumed constant for all operating conditions. This implies that the turbine nozzles are choked. Most one-stage turbines operate at nearly constant equivalent weight flow for all turbine pressure ratios greater than 2.0, while many multistage turbines operate at nearly constant equivalent weight flow for all turbine pressure ratios greater than 2.5. Only during starting conditions are turbines normally required to operate at pressure ratios less than 2.0 or 2.5. The accessory power is assumed to be zero. Normally it is so small that negligible error is introduced by considering it to be zero. The turbine efficiency is assumed to vary according to the following equation:

$$\eta_{ad}=a+b\left(\frac{N}{\sqrt{\Delta H}}-c\right)^2 \tag{445}$$

where

a design value of turbine efficiency

b $-a/c^2$

c design value of $\left(\dfrac{N/\sqrt{\theta}}{\sqrt{\Delta H/\theta}}\right)_T$

This approximation is quite good over much of the turbine performance map. Near limiting loading, however, actual turbine efficiencies are much lower than those calculated from equation (445). Once the gas-generator performance is

obtained, the matching with the other engine components is achieved as described in the preceding section.

ONE-SPOOL GAS GENERATOR

Design point.—From a given compressor performance map, the compressor operating point is selected for the engine design conditions of the one-spool gas generator. The design value of turbine efficiency is specified as well as the design value of turbine to compressor temperature ratio T_4/T_1. Design values of $w_4\sqrt{\theta_4}/\delta_4$ and $N/\sqrt{H_4-H_6}$ are calculated from

$$\frac{w_4\sqrt{\theta_4}}{\delta_4}=\frac{w_1\sqrt{\theta_1}}{\delta_1}\frac{(1-B_3)(1+f)}{\dfrac{P_3}{P_1}\dfrac{P_4}{P_3}}\sqrt{\frac{T_4}{T_1}} \tag{446}$$

$$\frac{N}{\sqrt{H_4-H_6}}=\frac{\dfrac{N}{\sqrt{\theta_1}}\sqrt{(1-B_3)(1+f)}}{\sqrt{c_{p,c}\,518.7\left(\dfrac{T_3}{T_1}-1\right)}} \tag{447}$$

Constant values of B_3, f, and P_4/P_3 are usually adequate. The $w_4\sqrt{\theta_4}/\delta_4$ value from equation (446) is assumed to be constant for all operating conditions. The $N/\sqrt{H_4-H_6}$ value from equation (447) is equal to the constant c in equation (445).

Off-design points.—For each compressor operating point, the corresponding turbine operating point may be found by the following steps:

(1) A value of T_4/T_1 is calculated from equation (446).

(2) The turbine temperature ratio is calculated from

$$\frac{T_6}{T_4}=1-\frac{c_{p,C}\left(\dfrac{T_3}{T_1}-1\right)}{c_{p,T}(1+f)(1-B_3)\dfrac{T_4}{T_1}} \tag{448}$$

(3) A value of $N/\sqrt{H_4-H_6}$ is calculated from equation (447).

(4) A value of $\eta_{ad,T}$ is calculated from equation (445).

(5) The turbine pressure ratio is calculated from

$$\frac{P_6}{P_4}=\left(1-\frac{1-\dfrac{T_6}{T_4}}{\eta_{ad,T}}\right)^{\frac{\gamma_T}{\gamma_T-1}} \tag{449}$$

The gas-generator parameters $w_6\sqrt{\theta_6}/\delta_6$, P_6/P_1, and T_6/T_1 are calculated from

$$\frac{w_6\sqrt{\theta_6}}{\delta_6}=\frac{w_4\sqrt{\theta_4}}{\delta_4}\sqrt{\frac{T_6}{T_4}}\frac{1}{\frac{P_6}{P_4}} \qquad (450)$$

$$\frac{P_6}{P_1}=\frac{P_3}{P_1}\frac{P_4}{P_3}\frac{P_6}{P_4} \qquad (451)$$

$$\frac{T_6}{T_1}=\frac{T_4}{T_1}\frac{T_6}{T_4} \qquad (452)$$

As discussed previously, the equivalent fuel-air ratio f/θ_1 may be found from values of T_3/T_1 and T_4/T_1, an assumed fuel, a combustor efficiency, and combustion charts such as those presented in reference 355.

Thus, for a range of weight flow $w_1\sqrt{\theta_1}/\delta_1$ at each compressor speed $N/\sqrt{\theta_1}$, the values of $w_6\sqrt{\theta_6}/\delta_6$, T_4/T_1, T_6/T_1, P_6/P_1, P_3/P_1, and f/θ_1 may be found. The gas-generator performance can be represented by plots of $w_1\sqrt{\theta_1}/\delta_1$, T_4/T_1, T_6/T_1, P_6/P_1, P_3/P_1, and f/θ_1 against $w_6\sqrt{\theta_6}/\delta_6$ for constant values of $N/\sqrt{\theta_1}$ (fig. 329).

TWO-SPOOL GAS GENERATOR

For the two-spool gas generator, the outer- and inner-compressor performance maps are given, and the compressor operating points for the engine design conditions are selected. The design value of turbine to compressor temperature ratio T_4/T_1 is specified as well as the design values of outer- and inner-turbine efficiency.

Inner-spool matching.—The performance of the inner spool is obtained as described previously; engine stations, 1, 3, 4, and 6 for the one-spool gas generator are replaced by stations 2, 3, 4, and 5 for the inner spool of the two-spool gas generator. The design value of $w_5\sqrt{\theta_5}/\delta_5$ is read from the inner-spool performance plot for the design value of P_3/P_2 and $N_i/\sqrt{\theta_2}$. This value of $w_5\sqrt{\theta_5}/\delta_5$ is assumed to be constant for all operating conditions.

Because the inner-spool-outlet equivalent weight flow $w_5\sqrt{\theta_5}/\delta_5$ is assumed constant, inner-spool performance may be presented as plots of $w_2\sqrt{\theta_2}/\delta_2$, P_3/P_2, P_5/P_2, T_5/T_2, and T_4/T_2 against $N_i/\sqrt{\theta_2}$ for the design value of $w_5\sqrt{\theta_5}/\delta_5$.

Outer-spool matching.—The outer-spool components are matched with the inner-spool performance by first assigning values of $w_1\sqrt{\theta_1}/\delta_1$ at

each speed $N_o/\sqrt{\theta_1}$. At each point, the outer-compressor performance is known. The equivalent weight flow $w_2\sqrt{\theta_2}/\delta_2$, which is common to the outer compressor and inner spool, is calculated from

$$\frac{w_2\sqrt{\theta_2}}{\delta_2}=(1-B_2)\frac{w_1\sqrt{\theta_1}}{\delta_1}\frac{\sqrt{\frac{T_2}{T_1}}}{\frac{P_2}{P_1}} \qquad (453)$$

From the inner-spool performance curves, values of $N_i/\sqrt{\theta_2}$ and T_5/T_2 are read.

The outer-turbine temperature ratio T_6/T_5 is calculated from

$$\frac{T_6}{T_5}=1-\frac{w_1c_{p,oC}\left(\frac{T_2}{T_1}-1\right)}{w_5c_{p,oT}\frac{T_5}{T_2}\frac{T_2}{T_1}} \qquad (454)$$

where $w_5=w_1(1-B_2)(1-B_3)(1+f)$. From the design value of $\eta_{ad,oT}$ and the design value of $N_o/\sqrt{H_5-H_6}$, which is calculated from

$$\frac{N_o}{\sqrt{H_5-H_6}}=\frac{\frac{N_o}{\sqrt{\theta_1}}\sqrt{(1-B_2)(1-B_3)(1+f)}}{\sqrt{c_{p,oC}518.7\left(\frac{T_2}{T_1}-1\right)}} \qquad (455)$$

the constants of equation (445) can be evaluated for use with the outer turbine. Outer-turbine efficiency may be calculated from equation (445) after $N_o/\sqrt{H_5-H_6}$ is calculated from equation (455). Outer-turbine pressure ratio is calculated from

$$\frac{P_6}{P_5}=\left(1-\frac{1-\frac{T_6}{T_5}}{\eta_{ad,oT}}\right)^{\frac{\gamma_{oT}}{\gamma_{oT}-1}} \qquad (456)$$

From the component operating points, the two-spool gas-generator performance may be calculated and plotted as in figure 332.

If the assumption that outer-turbine-inlet equivalent weight flow is constant for all engine operation does not appear to be valid, an approximation such as that described in **EQUILIBRIUM OPERATING LINE OF ONE-SPOOL TURBO-JET** may be used. One of the curves representing the variation of turbine-inlet flow with turbine total-pressure ratio is selected. The value of equivalent weight flow at the outer-turbine inlet that is used in the matching procedures must

agree with the value read from the selected curve and the calculated turbine pressure ratio. If this approximation is used for the outer turbine, then the inner-spool performance must be presented as plots of $w_2\sqrt{\theta_2}/\delta_2$, P_3/P_2, P_5/P_2, T_5/T_2, and T_4/T_2 against $N_i/\sqrt{\theta_2}$ for constant values of $w_5\sqrt{\theta_5}/\delta_5$.

EQUILIBRIUM OPERATING LINE OF ONE-SPOOL TURBOJET

A method is given in reference 349 for locating a constant-exhaust-nozzle-area equilibrium operating line on the performance map of a compressor that is part of a one-spool turbojet engine operated at static sea-level conditions. In this method the performance characteristics of the combustor, turbine, and exhaust nozzle are simplified in order to obtain charts from which an equilibrium operating line can be obtained for specified design conditions and the compressor map.

The charts of reference 349 are shown in figures 335 to 338. In figure 335, turbine pressure ratio P_4/P_6 is plotted against $(P_3/P_1)(P_4/P_3)(P_1/p_0)$ (p_0/p_8) with P_8/p_8 and $(A_8/A_4)(w^*/w)_4(w_4/w_8)$ as parameters. This represents the combined performance of the turbine, tailpipe, and simple convergent exhaust nozzle. For this chart a turbine polytropic efficiency of 0.85 was assumed, and the total-pressure drop in the tailpipe was assumed to vary according to

$$P_6 - P_8 = K\frac{\rho_8 V_8^2}{2g} \qquad (457)$$

The value of K was set by assigning $P_6/P_8 = 1.05$ for sonic velocity at the exhaust-nozzle exit. A constant value of 4/3 was assigned to γ_4 and γ_8.

In figure 336, which relates the compressor with the rest of the engine, $(1-B_3)(1+f)(T_4/T_1)$ $\eta_{ad,c}\eta_{ad,T}$ is plotted against compressor pressure ratio P_3/P_1 with $(A_8/A_4)(w^*/w)_4(w_4/w_8)$, P_8/p_8, and P_4/P_6 as parameters. The bearing losses and accessory power are assumed to be negligible. The pressure ratio P_1/p_0 was taken equal to unity, and the combustor pressure ratio P_4/P_3 was taken equal to 0.97.

The compressor weight flow is related to the compressor pressure ratio and the performance of the combustor, turbine, tailpipe, and exhaust nozzle in figure 337, where P_3/P_1 is plotted against $\sqrt{(1-B_3)(1+f)/\eta_{ad,c}\eta_{ad,T}}(w_8/w_4)(A_1/A_8)(w_1\sqrt{\theta_1}/\delta_1 A_1)$ with $(1-B_3)(1+f)(T_4/T_1)\eta_{ad,c}\eta_{ad,T}$, $A_8/A_4(w^*/w)_4$ (w_4w_8), P_4/P_6, and P_8/p_8 as parameters.

In order to establish the compressor equilibrium operating line at pressure ratios less than design, it is necessary to estimate the variation in $(w/w^*)_4$ with turbine pressure ratio P_4/P_6. If actual turbine data are available, a good approximation to the variation in $(w/w^*)_4$ with turbine pressure ratio P_4/P_6 can be obtained by computing the value of $(w/w^*)_4$ for each value of P_4/P_6 at the best efficiency point. If turbine data are not available, a reasonably good approximation can be obtained from the curves of figure 338. The multistage curve represents the equation.

$$\left(\frac{w}{w^*}\right)_4 = \sqrt{1-\left(\frac{P_6}{P_4}\right)^2} \qquad (458)$$

The two single-stage curves are theoretical variations computed for two values of the turbine parameter $\psi_T\eta_{ad,T}/\sin^2\beta_4$ of 1.5 and 2.0. Operating lines for two- or three-stage turbines would be between those for the single-stage turbine and that for the multistage turbine.

USE OF CHARTS FOR DESIGN POINTS

The following procedure may be used to find the design values of A_8/A_4 and A_8 once the design conditions are specified:

(1) Design values are selected for P_3/P_1, $w_1\sqrt{\theta_1}/\delta_1$, T_4/T_1, w_4/w_8, $\eta_{ad,T}$, B_3, and f.

(2) Compressor efficiency $\eta_{ad,c}$ is read from the compressor map.

(3) The design value of $\overline{T} = (1-B_3)(1+f)$ $(T_4/T_1)\eta_{ad,c}\eta_{ad,T}$ is calculated.

(4) The design value of $\overline{A} = A_8/A_4(w^*/w)_4(w_4/w_8)$ is read from figure 336 for the known values of $\overline{T}$ and P_3/P_1.

(5) The design value of

$$\overline{w} = \sqrt{(1-B_3)(1+f)/\eta_{ad,c}\eta_{ad,T}}(w_8/w_4)$$

$$(A_1/A_8)(w_1\sqrt{\theta_1}/\delta_1 A_1)$$

is read from figure 337 for the known values of $\overline{A}$ and P_3/P_1.

(6) A value of $\overline{P}$ is calculated assuming $p_0/p_8 = 1.0$.

(7) If the point read from figure 335 for the known values of $\overline{A}$ and $\overline{P}$ lies to the left of the line $P_8/p_8 = 1.85$, a value of P_4/P_6 is read at this point.

If the point read from figure 335 for the known values of $\overline{A}$ and $\overline{P}$ lies to the right or on the line
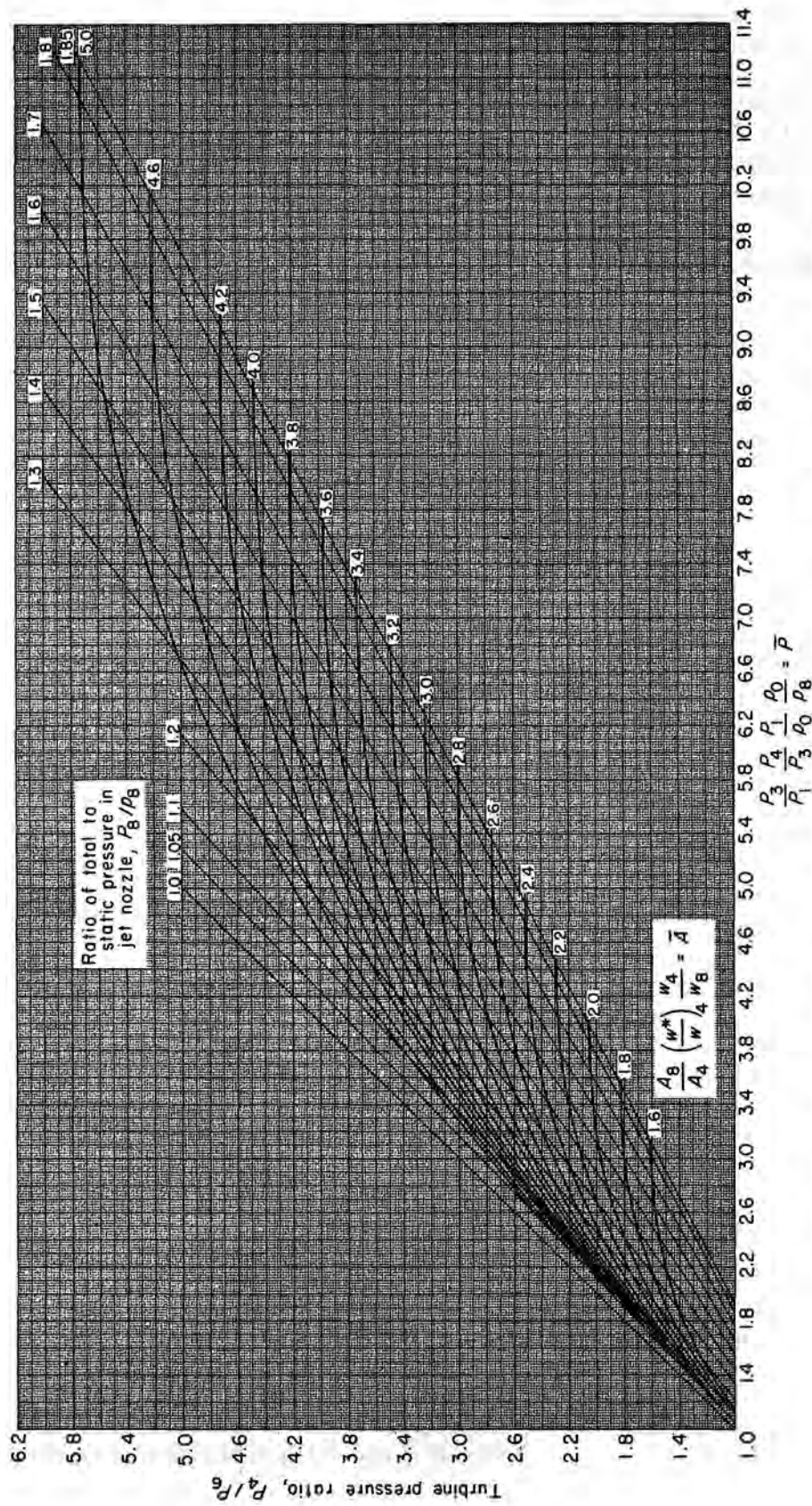
FIGURE 335.—Chart for estimating turbine pressure ratio. Turbine polytropic efficiency, 0.85; $\gamma_4 = \gamma_8 = 4/3$ (ref. 349).
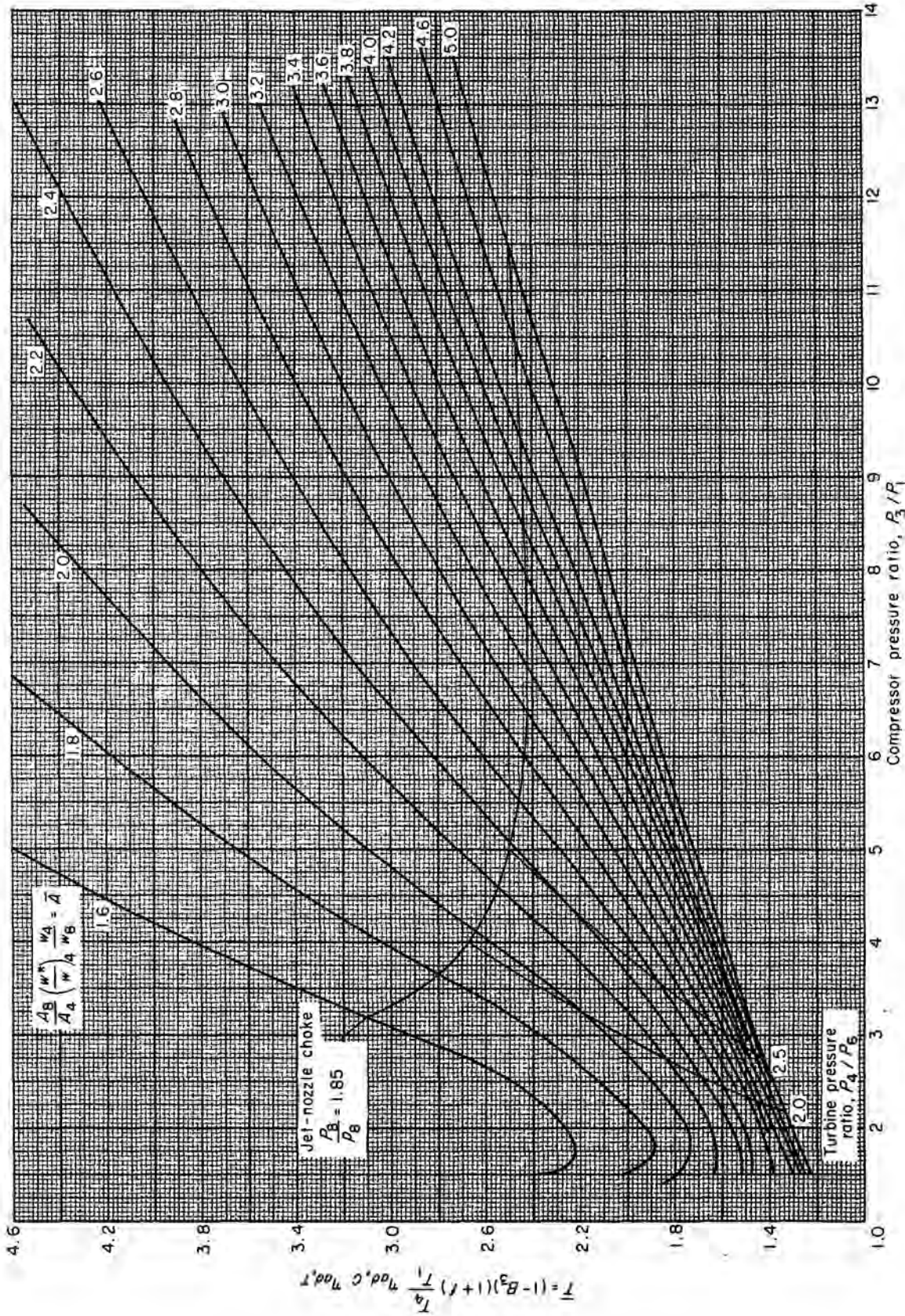
FIGURE 336.—Chart for estimating turbine-inlet temperature. Ram pressure ratio, P_1/p_0, 1; combustor pressure ratio, P_1/P_3, 0.97 (ref. 349).
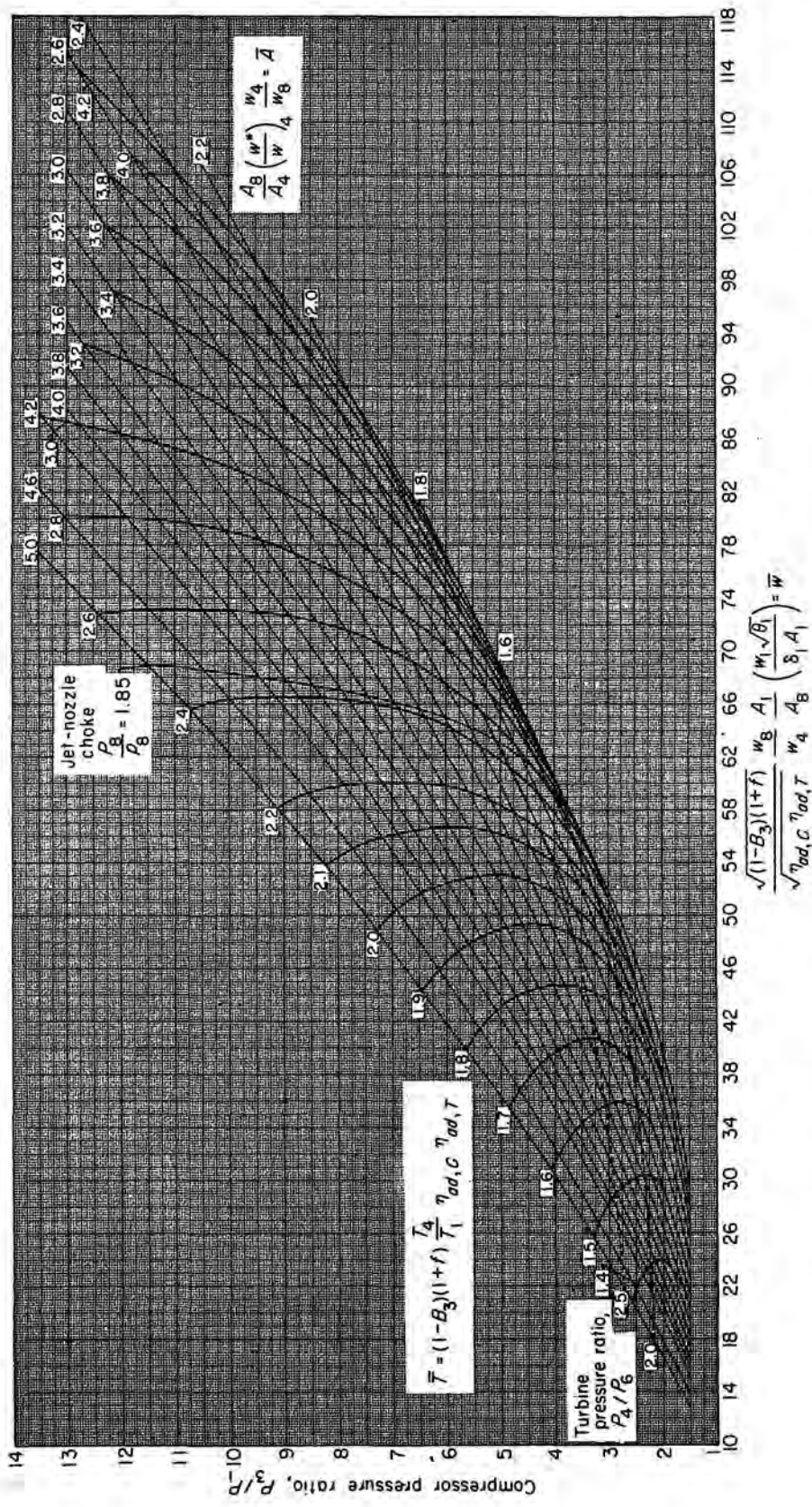
FIGURE 337.—Chart for estimating compressor equilibrium operating line. Ram pressure ratio, P_1/p_0, 1; combustor pressure ratio, P_4/P_3, 0.97; $\gamma_4 = \gamma_8 = 4/3$ (ref. 349).
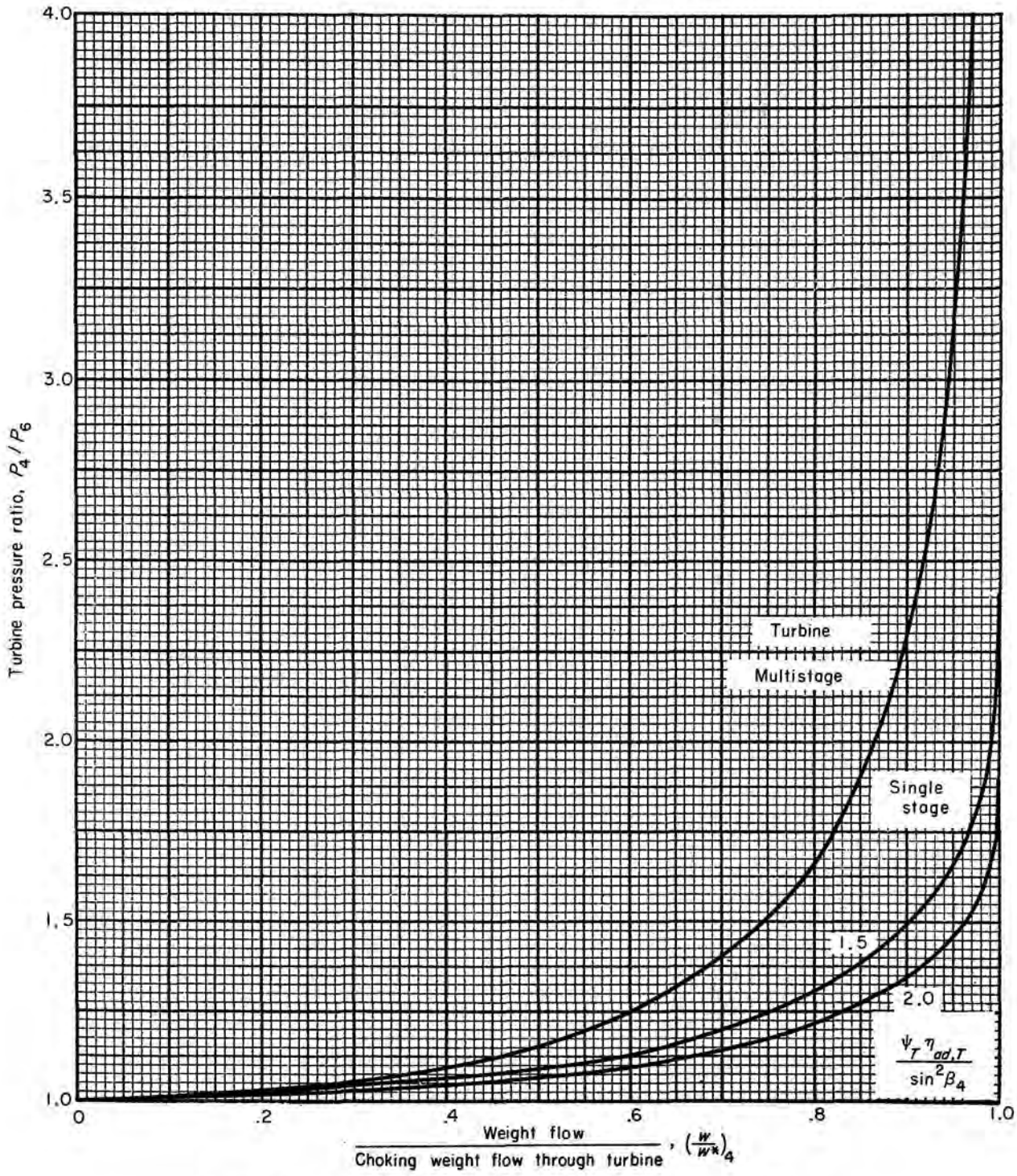
FIGURE 338.—Effect of turbine pressure ratio on weight flow (ref. 349).

$P_8/p_8 = 1.85$, a value of P_4/P_6 is read for the design value of $\overline{A}$ along the line $P_8/p_8 = 1.85$.

(8) The design value of $(w/w^*)_4$ is read from the proper curve in figure 338 for the design value of P_4/P_6.

(9) The design value of A_8/A_4 is calculated from known values of $\overline{A}$, $(w/w^*)_4$, and w_4/w_8.

(10) The design value of A_8 is calculated from known values of $\overline{w}$, $[(1-B_3)(1+f)]$, $\eta_{ad,c}\eta_{ad,T}$, (w_8/w_4), and $w_1\sqrt{\theta_1}/\delta_1$.

USE OF CHARTS FOR OFF-DESIGN POINTS

The following procedure may be used to locate equilibrium operating points on the compressor map for operation with the design values of A_8 and A_8/A_4 at compressor pressure ratios higher or lower than design:

(1) A value of P_3/P_1 is selected.

(2) A trial value of $\overline{A}$ is chosen. Although the values of A_8/A_4 and w_4/w_8 are known, the value of $(w/w^*)_4$ is not known.

(3) A value of $\overline{P}$ is calculated assuming $p_0/p_8 = 1.0$.

(4) If the point read from figure 335 for the values of $\overline{A}$ and $\overline{P}$ lies to the left of the line $P_8/p_8 = 1.85$, a value of P_4/P_6 is read at this point.

If the point read from figure 335 for the values of $\overline{A}$ and $\overline{P}$ lies to the right or on the line $P_8/p_8 = 1.85$, a value of P_4/P_6 is read for the value of $\overline{A}$ along the line $P_8/p_8 = 1.85$.

(5) A value of $(w/w^*)_4$ is read from figure 338 for the value of P_4/P_6.

(6) A value of $\overline{A}$ is calculated from the values of A_8/A_4, w_4/w_8, and $(w/w^*)_4$. If the calculated $\overline{A}$ does not equal the trial value of $\overline{A}$ from step (2), steps (2) to (6) are repeated until agreement is reached.

(7) The weight-flow parameter $\overline{w}$ is read from figure 337 for the known values of P_3/P_1 and $\overline{A}$.

(8) A value of $\eta_{ad,c}$ is estimated from the compressor map for the known value of P_3/P_1.

(9) The compressor weight flow $w_1\sqrt{\theta_1}/\delta_1$ is calculated from values of $\overline{w}$, $[(1-B_3)(1+f)]$, $\eta_{ad,c}\eta_{ad,T}$, (w_8/w_4), and A_8.

(10) A value of $\eta_{ad,c}$ is read from the compressor map for the values of P_3/P_1 and $w_1\sqrt{\theta_1}\delta_1$. If this does not equal the estimated value of $\eta_{ad,c}$ from step (8), steps (8) to (10) are repeated until agreement is reached.

(11) The desired equilibrium operating point can be located on the compressor map from the values of P_3/P_1 (step (1)) and $w_1\sqrt{\theta_1}/\delta_1$ (step (9)).

METHODS FOR TRANSIENT OPERATION

Two problems are treated in this section. A method is discussed whereby the compressor and turbine of a one-spool turbojet engine may be matched for a specified flight condition, a specified transient path on the compressor map, and a fixed exhaust-nozzle area (ref. 22). For a two-spool turbojet engine, procedures are discussed for finding the compressor paths during a transient for which the exhaust-nozzle area and inner-turbine-inlet temperature are held constant (ref. 27).

ONE-SPOOL TURBOJET

Up until now, compressor operation has been found for a specified flight condition and mode of engine operation. For a given flight condition, the compressor equilibrium operating point was fixed by assigning two quantities such as mechanical speed and turbine-inlet temperature or mechanical speed and exhaust-nozzle area. Now, compressor operation is scheduled. During a transient, the power-balance relation no longer is valid, so that three quantities must be assigned. For a given flight condition, the desired transient path on the compressor map is specified by assigning values for mechanical speed and compressor pressure ratio. The exhaust-nozzle area is assigned to be constant during the transient; this accounts for the third quantity.

At each speed, the excess torque is calculated after the turbine operating point has been found for the assigned compressor operating point. For known values of moment of inertia and excess torque at each speed, the time required to accelerate (or decelerate) along the specified path may be calculated. Such calculations indicate whether the specified path on the compressor map is acceptable with respect to transient operation. If, for a given engine configuration, the time to accelerate is found to be excessive, various schemes may be tried to improve the engine accelerating characteristics. These schemes will involve changes in component performance or a rematching between the compressor and turbine, or both. The effect of these changes on the engine accelerating characteristics may be calculated by rematching the compressor and turbine.

Compressor operation.—The steady-state compressor and turbine maps are assumed to be valid during transient operation. The aerodynamic
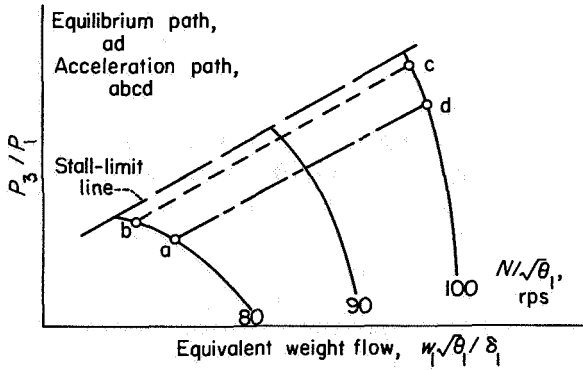
FIGURE 339.—Equilibrium and acceleration paths on compressor map.

adjustments are assumed to occur much faster than the mechanical adjustments. An acceleration is considered such that the compressor operates along the path abcd shown in figure 339. At a given speed $N/\sqrt{\theta_1}$, the compressor operating point is known, so that the value of w_4N/δ_4 may be calculated from

$$\frac{w_4N}{\delta_4}=\frac{w_1\sqrt{\theta_1}}{\delta_1}\frac{N}{\sqrt{\theta_1}}\frac{(1+f)(1-B_3)}{\dfrac{P_3}{P_1}\dfrac{P_4}{P_3}} \qquad (459)$$

where the fuel-air ratio and combustor pressure ratio are usually assumed constant.

Turbine operation.—At this point in the procedure, one turbine parameter is known. The second turbine parameter required to define turbine operation is found in an indirect manner. At the known value of w_4N/δ_4, several values of turbine pressure ratio P_4/P_6 are selected from the turbine performance map (fig. 340). For each P_4/P_6 selection, values of $N/\sqrt{\theta_4}$ and $(H_4-H_6)/\theta_4$ are read. The following calculations are made:

$$\frac{T_6}{T_4}=1-\frac{\dfrac{H_4-H_6}{\theta_4}}{c_{p,\,T}\,518.7} \qquad (460)$$

$$\frac{w_4\sqrt{\theta_4}}{\delta_4}=\frac{\dfrac{w_4N}{\delta_4}}{\dfrac{N}{\sqrt{\theta_4}}} \qquad (461)$$

$$\frac{T_4}{T_1}=\left[\frac{\dfrac{N}{\sqrt{\theta_1}}}{\dfrac{N}{\sqrt{\theta_4}}}\right]^2 \qquad (462)$$

The nozzle equivalent weight flow is calculated from

$$\frac{w_8\sqrt{\theta_8}}{\delta_8}=\frac{w_4\sqrt{\theta_4}}{\delta_4}\frac{\sqrt{\dfrac{T_6}{T_4}}\sqrt{\dfrac{T_8}{T_6}}\dfrac{P_4}{P_6}}{\dfrac{P_8}{P_6}} \qquad (463)$$

The values of T_8/T_6 and P_8/P_6 depend on the performance characteristics of the tailpipe and exhaust nozzle. A simplification that is satisfactory for many applications results from taking $T_8/T_6=1$ and $P_8/P_6=0.95$.

The exhaust-nozzle pressure ratio is calculated from

$$\frac{P_8}{p_0}=\frac{P_0}{p_0}\frac{P_1}{P_0}\frac{P_3}{P_1}\frac{P_4}{P_3}\frac{P_6}{P_4}\frac{P_8}{P_6} \qquad (464)$$

The value of P_0/p_0 is known from the specified flight Mach number. Inlet performance yields a value of P_1/P_0. For all values of P_8/p_0 less than or equal to the critical value $\left[\left(\dfrac{P}{p}\right)^{*}=\left(\dfrac{\gamma+1}{2}\right)^{\frac{\gamma}{\gamma-1}}\right]$, $\dfrac{P_8}{p_0}=\dfrac{P_8}{p_8}$; and the effective area of the convergent exhaust nozzle A_8 is found as follows:

(1) M_8 is found from

$$\frac{P}{p}=\left(1+\frac{\gamma-1}{2}M^2\right)^{\frac{\gamma}{\gamma-1}} \qquad (465)$$

(2) $(w\sqrt{\theta}/\delta A)_8$ is found from

$$\frac{w\sqrt{\theta}}{\delta A}=2116\cos\beta\sqrt{\frac{\gamma g}{R\,518.7}}M\left(1+\frac{\gamma-1}{2}M^2\right)^{-\frac{(\gamma+1)}{2(\gamma-1)}} \qquad (466)$$
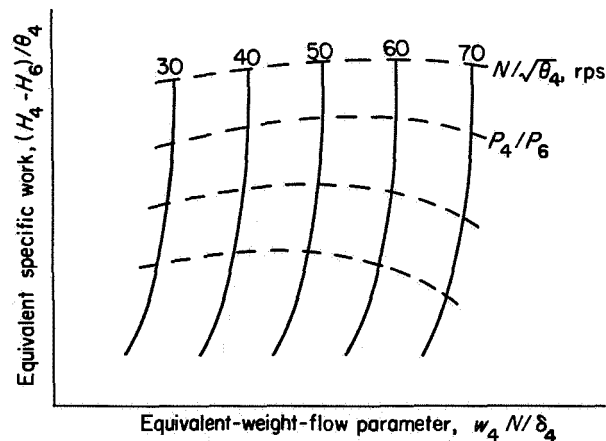

FIGURE 340.—Turbine performance map.

(3) Exhaust-nozzle area is calculated from

$$A_8 = \frac{\left(\dfrac{w\sqrt{\theta}}{\delta}\right)_8}{\left(\dfrac{w\sqrt{\theta}}{\delta A}\right)_8} \qquad (467)$$

When P_8/p_0 is greater than critical, the critical value of $w\sqrt{\theta}/\delta A$ is used in step (3). Nozzle area is plotted against turbine pressure ratio, and the value of P_4/P_6 for the assigned A_8 is read. Thus, the turbine operating point can be found for each compressor operating point along the assigned acceleration path.

Time to accelerate.—At each point along the assigned acceleration path, the excess torque available may be calculated from

$$Q_{xs} = \frac{778.2 w_1}{2\pi N}\left[(1+f)(1-B_3)c_{p,\,T}T_4 \right.$$
$$\left. \left(1 - \frac{T_6}{T_4}\right) - c_{p,\,c}T_1\left(\frac{T_3}{T_1} - 1\right)\right] \qquad (468)$$

The actual values of weight flow and speed are obtained from the equivalent values and the values of θ_1 and δ_1, which are known for the assigned flight condition and inlet performance.

The time to accelerate along the path b to c (fig. 339) is found from

$$\tau_c - \tau_b = 2\pi I \int_{N_b}^{N_c} \frac{1}{Q_{xs}}\,dN \qquad (469)$$

where the moment of inertia I is a physical constant of the engine. The acceleration of a high-pressure-ratio one-spool turbojet engine as determined from component performance characteristics is investigated in references 22, 23, and 365.

TWO-SPOOL TURBOJET

For a two-spool turbojet engine, procedures are discussed for finding the compressor paths during a transient for which the exhaust-nozzle area and inner-turbine-inlet temperature are held constant. The component performance maps for equilibrium operation are assumed to be valid for transient operation. For equilibrium operation of a two-spool turbojet, the specification of two quantities fixes its operation. For transient operation, four quantities are required, as the power-balance condition for each spool is no longer valid. At the beginning of a transient, the outer- and inner-spool

equivalent speeds are assumed to be the equilibrium values. These values of speed, together with the assigned values of inner-turbine-inlet temperature and exhaust-nozzle area, fix the operation of each of the components. The excess torque acting on each spool can then be calculated. The outer- and inner-spool speed increments occurring during a small time interval are found from the excess torque and moment of inertia for each spool. The new values of outer- and inner-spool speed, together with the constant values of inner-turbine-inlet temperature and exhaust-nozzle area, determine the operation of each of the components at the new time. The process is repeated until the desired end value of outer-spool speed is attained. It is a step-by-step procedure, then, and iterations are part of each step.

Thus for a specified flight condition and assigned values of inner-turbine-inlet temperature and exhaust-nozzle area, the transient paths on the compressor maps and the time required to traverse these paths may be calculated. From such calculations one can estimate whether or not an acceptable compromise can be reached between surge-free operation and time to accelerate for a given two-spool turbojet engine.

Compressor operation.—For a specified flight condition, initial values of $N_o/\sqrt{\theta_1}$, $N_i/\sqrt{\theta_1}$, T_4, and A_8, and the specification that T_4 and A_8 are maintained constant during an acceleration, the following procedures may be used to find the outer- and inner-compressor operating paths and the time required to accelerate to a higher engine speed:

(1) Values of $N_o/\sqrt{\theta_1}$, $N_i/\sqrt{\theta_1}$, T_4, and A_8 are specified.

(2) A trial value of $w_2\sqrt{\theta_2}/\delta_2$ is selected.

(3) A value of T_2/T_1 is read from a plot of T_2/T_1 against $w_2\sqrt{\theta_2}/\delta_2$ for constant values of $N_o/\sqrt{\theta_1}$.

(4) A value of $N_i/\sqrt{\theta_2}$ is calculated from values of $N_i/\sqrt{\theta_1}$ and T_2/T_1.

(5) A value of P_3/P_2 is read from a plot P_3/P_2 against $w_2\sqrt{\theta_2}/\delta_2$ for constant values of $N_i/\sqrt{\theta_2}$.

(6) A value of T_4 is calculated from

$$T_4 = T_1\left[\frac{\dfrac{w_4\sqrt{\theta_4}}{\delta_4}\dfrac{P_3}{P_2}\dfrac{P_4}{P_3}\sqrt{\dfrac{T_2}{T_1}}}{(1-B_3)(1+f)\dfrac{w_2\sqrt{\theta_2}}{\delta_2}}\right]^2 \qquad (470)$$

The value of T_1 is found from the specified flight condition. The assumption of constant values

for B_3, f, and P_4/P_3 is usually adequate. The value of $w_4\sqrt{\theta_4}/\delta_4$ is assumed to be the design value. (The validity of this assumption may be checked when the inner-turbine operating point is found.) If the value of T_4 calculated from equation (470) does not equal the assigned T_4 value (step (1)), steps (2) to (6) are repeated until agreement is reached.

Turbine operation.—

(7) A value of $N_i/\sqrt{\theta_4}$ is calculated from values of $N_i/\sqrt{\theta_1}$ and T_4/T_1.

(8) A trial value of P_4/P_6 is selected. If the proper value is chosen, the value of exhaust-nozzle area calculated later in the procedure will check with the specified value of A_8.

(9) A trial value of P_4/P_5 is selected.

(10) A value of T_4/T_5 is read from a plot of T_4/T_5 against $N_i/\sqrt{\theta_4}$ for constant values of P_4/P_5.

(11) A value of $N_o/\sqrt{\theta_5}$ is calculated from

$$\frac{N_o}{\sqrt{\theta_5}}=\frac{N_o}{\sqrt{\theta_1}}\frac{\sqrt{\dfrac{T_4}{T_5}}}{\sqrt{\dfrac{T_4}{T_1}}} \qquad (471)$$

(12) A value of P_5/P_6 is calculated from

$$\frac{P_5}{P_6}=\frac{\dfrac{P_4}{P_6}}{\dfrac{P_4}{P_5}} \qquad (472)$$

(13) A value of $w_5 N_o/\delta_5$ is calculated from

$$\frac{w_5 N_o}{\delta_5}=\frac{w_2\sqrt{\theta_2}}{\delta_2}\frac{N_o}{\sqrt{\theta_1}}\frac{(1-B_3)(1+f)}{\sqrt{\dfrac{T_2}{T_1}}\dfrac{P_3}{P_2}\dfrac{P_4}{P_3}\dfrac{P_5}{P_4}} \qquad (473)$$

(14) A value of $w_5 N_o/\delta_5$ is read from a plot of $w_5 N_o/\delta_5$ against $N_o/\sqrt{\theta_5}$ for constant values of P_5/P_6. If this does not equal the value of flow parameter calculated from equation (473) in step (13), steps (9) to (14) are repeated until agreement is reached.

(15) A value of T_6/T_5 is read from a plot of T_6/T_5 against $N_o/\sqrt{\theta_5}$ for constant values of P_5/P_6.

(16) A value of exhaust-nozzle area is found from the values of nozzle equivalent weight flow and nozzle equivalent specific weight flow as discussed for the one-spool turbojet. If the calculated value of A_8 does not equal the specified

value, steps (8) to (16) are repeated until agreement is reached. When the selection of P_4/P_6 is found to be compatible with the specified exhaust-nozzle area, the operating point of each of the two-spool components is known at the initial time.

Time to accelerate.—From the component operating points, the excess torques available for accelerating the outer and inner spools can be calculated. The specified flight condition and inlet performance yield values of θ_1 and δ_1 that can be used to convert equivalent-speed and equivalent-weight-flow values to actual values. Outer- and inner-spool excess torque are calculated from

$$Q_{xs,o}=\frac{778.2 w_1}{2\pi N_o}\left[(1+f)(1-B_2)(1-B_3)c_{p,oT}T_5\right.$$
$$\left.\left(1-\frac{T_6}{T_5}\right)-c_{p,oC}T_1\left(\frac{T_2}{T_1}-1\right)\right] \qquad (474)$$

$$Q_{xs,i}=\frac{778.2 w_2}{2\pi N_i}\left[(1+f)(1-B_3)c_{p,iT}T_4\right.$$
$$\left.\left(1-\frac{T_5}{T_4}\right)-c_{p,iC}T_2\left(\frac{T_3}{T_2}-1\right)\right] \qquad (475)$$

Speed increments in N_o and N_i for a specified time interval are defined by

$$\Delta N_o=(N_o)_b-(N_o)_a=\frac{1}{2\pi I_o}\int_{\tau_a}^{\tau_b}Q_{xs,o}\,d\tau \qquad (476)$$

$$\Delta N_i=(N_i)_b-(N_i)_a=\frac{1}{2\pi I_i}\int_{\tau_a}^{\tau_b}Q_{xs,i}\,d\tau \qquad (477)$$

Because the continuous variations of $Q_{xs,o}$ and $Q_{xs,i}$ with time are not known, an approximation is introduced. Trial increments in N_o and N_i are defined by

$$\Delta N_o=\frac{Q_{xs,o}}{2\pi I_o}\Delta\tau \qquad (478)$$

$$\Delta N_i=\frac{Q_{xs,i}}{2\pi I_i}\Delta\tau \qquad (479)$$

The time increment $\Delta\tau$ is selected so as to result in reasonable speed increments. If $\Delta\tau$ is made too large, the procedure becomes inaccurate, as evidenced by large irregularities in the points that define the transient paths on the compressor maps. If $\Delta\tau$ is made too small, more points will be calculated than are necessary to define the

transient paths. In reference 27, time increments of 0.1 and 0.2 second were used. At the new time (the initial time plus the time increment), trial values of N_o and N_i are defined to be equal to the initial values of N_o and N_i plus the incremental values calculated from the initial values of $Q_{zs,o}$ and $Q_{zs,i}$ and equations (478) and (479). For these trial values of N_o and N_i and the specified values of T_4 and A_8, the matching procedures are repeated to yield component operating points and excess-torque values. The actual increments in N_o and N_i occurring during the time interval are approximated by substituting in equations (478) and (479) average values of $Q_{zs,o}$ and $Q_{zs,i}$, which are defined to be the arithmetic means of the values corresponding to the initial and trial values of N_o and N_i. The actual values of N_o and N_i at the new time are equal to the initial values plus the actual speed increments.

The transient paths on the outer- and inner-compressor performance maps are found by repeating the matching procedures until the end value of engine speed is attained. The time required to reach this speed is found by summing up the time increments considered. The component operating trends during acceleration and deceleration of two hypothetical two-spool turbojet engines are discussed in reference 27.

REFERENCES

1. Supplee, H. H.: The Gas Turbine. J. B. Lippincott Co., 1910.
2. Howell, A. R.: Fluid Dynamics of Axial Compressors. War Emergency Issue No. 12 pub. by Inst. Mech. Eng. (London), 1945. (Reprinted in U.S. by ASME, Jan. 1947, pp. 441–452.)
3. Marks, L. S., and Weske, J. R.: The Design and Performance of an Axial-Flow Fan. Trans. ASME, AER–56–13, vol. 56, no. 11, Nov. 1934, pp. 807–813.
4. Constant, Hayne: The Early History of the Axial Type of Gas Turbine. War Emergency Issue No. 12 pub. by Inst. Mech. Eng. (London), 1945. (Reprinted in U.S. by ASME, Jan. 1947, pp. 411–426.)
5. Ruden, P.: Investigation of Single Stage Axial Fans. NACA TM 1062, 1944.
6. Sinnette, John T., Jr., Schey, Oscar W., and King, J. Austin: Performance of NACA Eight-Stage Axial-Flow Compressor Designed on the Basis of Airfoil Theory. NACA Rep. 758, 1943. (Supersedes NACA WR E–1.)
7. Howell, A. R.: Design of Axial Compressors. War Emergency Issue No. 12 pub. by Inst. Mech. Eng. (London), 1945. (Reprinted in U.S. by ASME, Jan 1947, pp. 452–462.)
8. Lieblein, Seymour, Lewis, George W., Jr., and Sandercock, Donald M.: Experimental Investigation of an Axial-Flow Compressor Inlet Stage Operating at Transonic Relative Inlet Mach Numbers. I—Over-All Performance of Stage with Transonic Rotor and Subsonic Stators Up to Rotor Relative Inlet Mach Number of 1.1. NACA RM E52A24, 1952.
9. Lieblein, Seymour, Schwenk, Francis C., and Broderick, Robert L.: Diffusion Factor for Estimating Losses and Limiting Blade Loadings in Axial-Flow-Compressor Blade Elements. NACA RM E53D01, 1953.
10. Sibulkin, Merwin: Theoretical and Experimental Investigation of Additive Drag. NACA Rep. 1187, 1954. (Supersedes NACA RM E51B13).
11. Esenwein, Fred T., and Valerino, Alfred S.: Force and Pressure Characteristics for a Series of Nose Inlets at Mach Numbers from 1.59 to 1.99. I—Conical Spike All-External Compression Inlet with Subsonic Cowl Lip. NACA RM E50J26, 1951.
12. Pinkel, Benjamin, and Karp, Irving M.: A Thermodynamic Study of the Turbojet Engine. NACA Rep. 891, 1947. (Supersedes NACA WR E–241.)
13. Pinkel, Benjamin, and Karp, Irving M.: A Thermodynamic Study of the Turbine-Propeller Engine. NACA Rep. 1114, 1953. (Supersedes NACA TN 2653.)
14. English, Robert E., and Wachtl, William W.: Charts of Thermodynamic Properties of Air and Combustion Products from 300° to 3500° R. NACA TN 2071, 1950.
15. Hauser, Cavour H., and Plohr, Henry W.: Two-Dimensional Cascade Investigation of the Maximum Exit Tangential Velocity Component and Other Flow Conditions at the Exit of Several Turbine-Blade Designs at Supercritical Pressure Ratios. NACA RM E51F12, 1951.
16. Alpert, Sumner, and Litrenta, Rose M.: Construction and Use of Charts in Design Studies of Gas Turbines. NACA TN 2402, 1951.
17. Cavicchi, Richard H., and English, Robert E.: Analysis on Limitations Imposed on One-Spool Turbojet-Engine Designs by Compressors and Turbines at Flight Mach Numbers of 0, 2.0, and 2.8. NACA RM E54F21a, 1954.
18. Klapproth, John F., Jacklitch, John J., Jr., and Tysl, Edward R.: Design and Performance of a 1400-Foot-per-Second-Tip-Speed Supersonic Compressor Rotor. NACA RM E55A27, 1955.
19. Huppert, Merle C., Calvert, Howard F., and Meyer, André J.: Experimental Investigation of Rotating Stall and Blade Vibration in the Axial-Flow Compressor of a Turbojet Engine. NACA RM E54A08, 1954.
20. Lucas, James G., Finger, Harold B., and Filippi, Richard E.: Effect of Inlet-Annulus Area Blockage on Over-All Performance and Stall Characteristics of an Experimental 15-Stage Axial-Flow Compressor. NACA RM E53L28, 1954.
21. Stockman, Norbert O.: Application of Stream-Filament Techniques to Design of Diffuser between

Compressor and Combustor in a Gas-Turbine Engine. NACA RM E55F06, 1955.

22. Rebeske, John J., Jr., and Rohlik, Harold E.: Acceleration of High-Pressure-Ratio Single-Spool Turbojet Engine As Determined from Component Performance Characteristics. I—Effect of Air Bleed at Compressor Outlet. NACA RM E53A09, 1953.

23. Rebeske, John J., Jr., and Dugan, James F., Jr.: Acceleration of High-Pressure-Ratio Single-Spool Turbojet Engine As Determined from Component Performance Characteristics. II—Effect of Compressor Interstage Air Bleed. NACA RM E53E06, 1953.

24. Wyatt, DeMarquis D.: An Analysis of Turbojet-Engine-Inlet Matching. NACA TN 3012, 1953.

25. Dugan, James F., Jr.: Two-Spool Matching Procedures and Equilibrium Characteristics of a Two-Spool Turbojet Engine. NACA RM E54F09, 1954.

26. Dugan, James F., Jr.: Effect of Design Over-All Compressor Pressure Ratio Division on Two-Spool Turbojet-Engine Performance and Geometry. NACA RM E54F24a, 1954.

27. Dugan, James F., Jr.: Component Operating Trends During Acceleration and Deceleration of Two Hypothetical Two-Spool Turbojet Engines. NACA RM E54L28, 1955.

28. Davison, Elmer H.: Compressor and Turbine Matching Considerations in Turboprop Engines. Preprint No. 695, SAE, 1956.

29. Sorensen, Harry A.: Gas Turbines. Ronald Press Co., 1951.

30. Wislicenus, George F.: Fluid Mechanics of Turbomachinery. McGraw-Hill Book Co., Inc., 1947.

31. Howell, A. R.: The Present Basis of Axial Flow Compressor Design. Pt. I—Cascade Theory and Performance. R. & M. 2095, British ARC, June 1942; Pt. II—Compressor Theory and Performance. Rep. No. E. 3961, British RAE, Dec. 1942.

32. Bowen, John T., Sabersky, Rolf H., and Rannie, W. Duncan: Theoretical and Experimental Investigations of Axial Flow Compressors. Mech. Eng. Lab., C.I.T., Jan. 1949. (Navy Contract N6-ORI-102.)

33. Zucrow, Maurice Joseph: Principles of Jet Propulsion and Gas Turbines. John Wiley & Sons, Inc., 1948.

34. Stanitz, John D.: Effect of Blade-Thickness Taper on Axial-Velocity Distribution at the Leading Edge of an Entrance Rotor-Blade Row with Axial Inlet, and the Influence of This Distribution on Alinement of the Rotor Blade for Zero Angle of Attack. NACA TN 2986, 1953.

35. Sinnette, John T., Jr.: Analysis of Effect of Basic Design Variables on Subsonic Axial-Flow-Compressor Performance. NACA Rep. 901, 1948. (Supersedes NACA RM E7D28.)

36. Stanitz, John D., and Ellis, Gaylord O.: Flow Surfaces in Rotating Axial-Flow Passages. NACA TN 2834, 1952.

37. Stewart, Warner L.: Investigation of Compressible Flow Mixing Losses Obtained Downstream of a Blade Row. NACA RM E54I20, 1954.

38. Savage, Melvyn: Analysis of Aerodynamic Blade-Loading-Limit Parameters for NACA 65-($C_{lo}A_{10}$) 10 Compressor-Blade Sections at Low Speeds. NACA RM L54L02a, 1955.

39. Herrig, L. Joseph, Emery, James C., and Erwin, John R.: Systematic Two-Dimensional Cascade Tests of NACA 65-Series Compressor Blades at Low Speeds. NACA TN 3916, 1957. (Supersedes NACA RM L51G31.)

40. Andrews, S. J.: Tests Related to the Effect of Profile Shape and Camber Line on Compressor Cascade Performance. R. & M. 2743, British ARC, 1949.

41. Klapproth, John F.: General Considerations of Mach Number Effects on Compressor-Blade Design. NACA RM E53L23a, 1954.

42. Beatty, Loren A., Savage, Melvyn, and Emery, James C.: Experimental Investigation of Flow through Three Highly Loaded Inlet Guide Vanes Having Different Spanwise Circlation Gradients. NACA RM L52D25a, 1952.

43. Lieblein, Seymour, and Ackley, Richard H.: Secondary Flows in Annular Cascades and Effects on Flow in Inlet Guide Vanes. NACA RM E51G27, 1951.

44. Mahoney, John J., Dugan, Paul D., Budinger, Raymond E., and Goelzer, H. Fred: Investigation of Blade-Row Flow Distributions in Axial-Flow-Compressor Stage Consisting of Guide Vanes and Rotor-Blade Row. NACA RM E50G12, 1950.

45. Westphal, Willard R., and Godwin, William R.: Comparison of NACA 65-Series Compressor-Blade Pressure Distributions and Performance in a Rotor and in Cascade. NACA TN 3806, 1957. (Supersedes NACA RM L51H20.)

46. Johnsen, Irving A.: Investigation of a 10-Stage Subsonic Axial-Flow Research Compressor. I—Aerodynamic Design. NACA RM E52B18, 1952.

47. Budinger, Ray E., and Thomson, Arthur R.: Investigation of a 10-Stage Subsonic Axial-Flow Research Compressor. II—Preliminary Analysis of Over-All Performance. NACA RM E52C04, 1952.

48. Budinger, Ray E.: Investigation of a 10-Stage Subsonic Axial-Flow Research Compressor. VI—Performance Evaluation and Flow Distributions in the First, Fifth, and Tenth Stages. NACA RM E54F28, 1954.

49. Hatch, James E., Giamati, Charles C., and Jackson, Robert J.: Application of Radial-Equilibrium Condition to Axial-Flow Turbomachine Design Including Consideration of Change of Enthropy with Radius Downstream of Blade Row. NACA RM E54A20, 1954.

50. Sandercock, Donald M., Kovach, Karl, and Lieblein, Seymour: Experimental Investigation of a Five-Stage Axial-Flow Research Compressor with Transonic Rotors in All Stages. I—Compressor Design. NACA RM E54F24, 1954.

51. Kovach, Karl, and Sandercock, Donald M.: Experimental Investigation of a Five-Stage Axial-Flow Research Compressor with Transonic Rotors in All Stages. II—Compressor Over-All Performance. NACA RM E54G01, 1954.

52. Dugan, Paul D., Mahoney, John J., and Benser, William A.: Effect of Mach Number on Performance of an Axial-Flow Compressor Rotor-Blade Row. NACA RM E8D29, 1948.

53. Geye, Richard P., Budinger, Ray E., and Voit, Charles H.: Investigation of a High-Pressure-Ratio Eight-Stage Axial-Flow Research Compressor with Two Transonic Inlet Stages. II—Preliminary Analysis of Over-All Performance. NACA RM E53J06, 1953.

54. Felix, A. Richard: Summary of 65-Series Compressor-Blade Low-Speed Cascade Data by Use of the Carpet-Plotting Technique. NACA TN 3913, 1957. (Supersedes NACA RM L54H18a.)

55. Lewis, George W., Jr., Schwenk, Francis C., and Serovy, George K.: Experimental Investigation of a Transonic Axial-Flow-Compressor Rotor with Double-Circular-Arc Airfoil Blade Sections. I—Design, Over-All Performance, and Stall Characteristics. NACA RM E53L21a, 1954.

56. Savage, Melvyn, Erwin, John R., and Whitley, Robert P.: Investigation of an Axial-Flow Compressor Rotor Having NACA High-Speed Blade Sections (A_2I_{8b} Series) at Mean Radius Relative Inlet Mach Numbers Up to 1.13. NACA RM L53G02, 1953.

57. Montgomery, John C., and Glaser, Frederick W.: Experimental Investigation of a 0.4 Hub-Tip Diameter Ratio Axial-Flow Compressor Inlet Stage at Transonic Inlet Relative Mach Numbers. II—Stage and Blade-Element Performance. NACA RM E54I29, 1955.

58. Hamrick, Joseph T., Ginsburg, Ambrose, and Osborn, Walter M.: Method of Analysis for Compressible Flow Through Mixed-Flow Centrifugal Impellers of Arbitrary Design. NACA Rep. 1082, 1952. (Supersedes NACA TN 2165.)

59. Stodola, A.: Steam and Gas Turbines. Vols. I and II. McGraw-Hill Book Co., Inc., 1927. (Reprinted by Peter Smith (New York), 1945.)

60. Withee, Joseph R., Jr., and Beede, William L.: Design and Test of Mixed-Flow Impellers. II—Experimental Results, Impeller Model MFI-1A. NACA RM E52E22, 1952.

61. Smith, Kenneth J., and Osborn, Walter M.: Design and Test of Mixed-Flow Impellers. VI—Performance of Parabolic-Bladed Impeller with Shroud Redesigned by Rapid Approximate Method. NACA RM E55F23, 1955.

62. Stewart, Warner L.: Analytical Investigation of Flow Through High-Speed Mixed-Flow Turbine. NACA RM E51H06, 1951.

63. Stewart, Warner L., Whitney, Warren J., and Monroe, Daniel E.: Investigation of Turbines for Driving Supersonic Compressors. III—First Configuration with Four Nozzle Settings and One Nozzle Modification. NACA RM E53A20, 1953.

64. Stewart, Warner L., Whitney, Warren J., and Heaton, Thomas R.: Effect of Certain Combinations of Wall Contouring and Design Exit Velocity Distribution on Prediction of Turbine-Nozzle Mass Flow. NACA RM E53E14, 1953.

65. Stewart, Warner L., Wong, Robert Y., and Evans, David G.: Design and Experimental Investigation of Transonic Turbine with Slight Negative Reaction Across Rotor Hub. NACA RM E53L29a, 1954.

66. Standahar, Raymond M.: Investigation of Three Highly Loaded Subsonic-Inlet-Stage Axial-Flow Compressors Employing Varying Radial Gradients of Energy Addition. NACA RM E54G20, 1954.

67. Giacomelli, R., and Pistolesi, E.: Historical Sketch. Vol. I of Aerodynamic Theory, div. D, ch. III, W. F. Durand, ed., Durand Reprinting Comm. (C.I.T.), 1943, pp. 336–394.

68. Munk, Max M.: General Theory of Thin Wing Sections. NACA Rep. 142, 1922.

69. Glauert, H.: A Theory of Thin Aerofoils. R. & M. 910, British ARC, Feb. 1924.

70. Birnbaum, W.: Die Tragende Wirbelfläche als Hilfsmittel zur Behandlung des ebenen Problems der Tragflügeltheorie. Z.A.M.M., Bd. 3, Heft 4, 1923, pp. 290–297.

71. Glauert, H.: The Elements of Aerofoil and Airscrew Theory. Univ. Press (Cambridge), 1926.

72. Allen, H. Julian: General Theory of Airfoil Sections Having Arbitrary Shape or Pressure Distribution. NACA Rep. 833, 1945. (Supersedes NACA ACR 3G29.

73. Theodorsen, Theodore: Theory of Wing Sections of Arbitrary Shape. NACA Rep. 411, 1931.

74. Theodorsen, T., and Garrick, I. E.: General Potential Theory of Arbitrary Wing Sections. NACA Rep. 452, 1933.

75. Naiman, Irven: Numerical Evaluation of the ϵ-Integral Occurring in the Theodorsen Arbitrary Airfoil Potential Theory. NACA WR L-136, 1944. (Supersedes NACA ARR L4D27a.)

76. Naiman, Irven: Numerical Evaluation by Harmonic Analysis of the ϵ-Function of the Theodorsen Arbitrary-Airfoil Potential Theory. NACA WR L-153, 1945. (Supersedes NACA ARR L5H18.)

77. Warschawski, S. E.: On Theodorsen's Method of Conformal Mapping of Nearly Circular Regions. Quart. Appl. Math., vol. III, no. 1, Apr. 1945, pp. 12–28.

78. Collar, A. R.: The Flow of a Perfect Fluid Through Cascades of Aerofoils. Rep. 4589, British ARC, July 4, 1940.

79. Merchant, W., and Collar, A. R.: Flow of an Ideal Fluid Past a Cascade of Blades, pt. II. R. & M. 1893, British ARC, May 26, 1941.

80. Weinig, F.: Die Strömung und die Schaufeln von Turbomaschinen. Johann Ambrosius Barth (Leipzig), 1935.

81. Pistolesi, E.: On the Calculation of Flow Past an Infinite Screen of Thin Airfoils. NACA TM 968, 1941.
82. Lieblein, V. (Wilhelm Bente, trans.): The Calculation of the Lift Characteristics of an Aerofoil Section in a Cascade. Rep. and Trans. 442, M.O.S. Volkenrode, Feb. 1947.
83. Erwin, John R., and Yacobi, Laura A.: Method of Estimating the Incompressible-Flow Pressure Distribution of Compressor Blade Sections at Design Angle of Attack. NACA RM L53F17, 1953.
84. Woolard, Henry W.: The Incompressible Flow about a Cascade of Airfoils. Rep. AF-734-A-1, Cornell Aero. Lab., Nov. 1950.
85. Scholz, N.: On an Extension of Glauert's Theory of Thin Airfoils to Profiles in Cascade. Jour. Aero. Sci., vol. 18, no. 9, Sept. 1951, pp. 637-638.
86. Katzoff, S., Finn, Robert S., and Laurence, James C.: Interference Method for Obtaining the Potential Flow Past an Arbitrary Cascade of Airfoils. NACA Rep. 879, 1947. (Supersedes NACA TN 1252.)
87. Howell, A. R.: A Theory of Arbitrary Airfoils in Cascade. Phil. Mag., vol. 39, no. 299, Dec. 1948, pp. 913-927.
88. Carter, A. D. S., and Hughes, Hazel P.: A Theoretical Investigation into the Effect of Profile Shape on the Performance of Aerofoils in Cascade. R. & M. 2384, British ARC, Mar. 1946.
89. Vazsonyi, Andrew: On the Aerodynamic Design of Axial-Flow Compressors and Turbines. Jour. Appl. Mech., vol. 15, no. 1, Mar. 1948, pp. 53-64.
90. Garrick, I. E.: On the Plane Potential Flow Past a Lattice of Arbitrary Airfoils. NACA Rep. 788, 1944. (Supersedes NACA WR L-313.)
91. Kawada, S.: A Contribution to the Theory of Latticed Wings. Proc. Third Int. Cong. Appl. Mech., vol. I, pt. I, Aug. 24-29, 1930.
92. von Kármán, Th., and Burgers, J. M.: Flow Through a Lattice Composed of Airfoils. Vol. II of Aerodynamic Theory, div. E, ch. II, pt. B, sec. 23, W. F. Durand, ed., Julius Springer (Berlin), 1935, pp. 91-96.
93. Traupel, W.: Die Berechnung der Potentialströmung durch Schaufelgitter. Schweizer Archiv f. Angewandte Wiss. und Tech., Bd. 10, Heft 12, 1944.
94. Calderwood, James: Some Researches on Internal Combustion Prime Movers. Trans. North East Coast Inst. Eng. and Shipbuilders, vol. 62, 1945-1946, pp. 283-310; Appendix by W. Traupel, pp. 311-328.
95. Mutterperl, William: The Conformal Transformation of an Airfoil into a Straight Line and Its Application to the Inverse Problem of Airfoil Theory. NACA WR L-113, 1944. (Supersedes NACA ARR L4K22a.)
96. Mutterperl, William: A Solution of the Direct and Inverse Potential Problems for Arbitrary Cascades of Airfoils. NACA WR L-81, 1944. (Supersedes NACA ARR L4K22b.)
97. Resnick, Robert, and Green, L. J.: Velocity Distributions and Design Data for Ideal Incompressible Flow through Cascades of Airfoils. Jour. Appl. Mech., vol. 18, no. 3, Sept. 1951, pp. 253-259.
98. Katzoff, S., and Hannah, Margery E.: Further Comparisons of Theoretical and Experimental Lift and Pressure Distributions on Airfoils in Cascade at Low-Subsonic Speed. NACA TN 2391, 1951.
99. Betz, Albert: Diagrams for Calculation of Airfoil Lattices. NACA TM 1022, 1942.
100. Goldstein, Arthur W., and Jerison, Meyer: Isolated and Cascade Airfoils with Prescribed Velocity Distribution. NACA Rep. 869, 1947. (Supersedes NACA TN 1308.)
101. Betz, A.: Modification of Wing-Section Shape to Assure a Predetermined Change in Pressure Distribution. NACA TM 767, 1935.
102. Theodorsen, Theodore: Airfoil-Contour Modifications Based on ε-Curve Method of Calculating Pressure Distribution. NACA WR L-135, 1944. (Supersedes NACA ARR L4G05.)
103. Gebelein, H.: Theory of Two-Dimensional Potential Flow about Arbitrary Wing Sections. NACA TM 886, 1939.
104. Peebles, Glenn H.: A Method for Calculating Airfoil Sections from Specifications on the Pressure Distributions. Jour. Aero. Sci., vol. 14, no. 8, Aug. 1947, pp. 451-456.
105. Hansen, Arthur G., and Yohner, Peggy L.: A Numerical Procedure for Designing Cascade Blades with Prescribed Velocity Distributions in Incompressible Potential Flow. NACA TN 2101, 1950.
106. Lighthill, M. J.: A Mathematical Method of Cascade Design. R. & M. 2104, British ARC, June 1945.
107. Southwell, R. V.: Relaxation Methods in Theoretical Physics. Clarendon Press (Oxford), 1946.
108. Emmons, Howard W.: The Numerical Solution of Partial Differential Equations. Quart. Appl. Math., vol. II, no. 3, Oct. 1944, pp. 173-195.
109. Shaw, F. S.: Introduction to Relaxation Methods. Dover Pub., 1953.
110. Chaplygin, S.: Gas Jets. NACA TM 1063, 1944.
111. Garrick, I. E., and Kaplan, Carl: On the Flow of a Compressible Fluid by the Hodograph Method. I—Unification and Extension of Present-Day Results. NACA Rep. 789, 1944. (Supersedes NACA ACR L4C24.)
112. Demtchenko, B.: Quelques problèmes d'hydrodynamique bidimensionelle des fluides compressibles. Pub. Scientifique et Techniques du Ministère de l'Air (France), No. 144, 1939.
113. von Kármán, Th.: Compressibility Effects in Aerodynamics. Jour. Aero. Sci., vol. 8, no. 9, July 1941, pp. 337-356.
114. Tsien, Hsue-Shen: Two-Dimensional Subsonic Flow of Compressible Fluids. Jour. Aero. Sci., vol. 6, no. 10, Aug. 1939, pp. 399-407.
115. Costello, George R.: Method of Designing Cascade Blades with Prescribed Velocity Distributions in

Compressible Potential Flows. NACA Rep. 978, 1950. (Supersedes NACA TN's 1913 and 1970.)

116. Costello, George R., Cummings, Robert L., and Sinnette, John T., Jr.: Detailed Computational Procedure for Design of Cascade Blades with Prescribed Velocity Distributions in Compressible Potential Flows. NACA Rep. 1060, 1952. (Supersedes NACA TN 2281.)

117. Clauser, Francis H.: Two-Dimensional Compressible Flows Having Arbitrarily Specified Pressure Distributions for Gases with Gamma Equal to Minus One. Rep. NOLR 1132, Symposium on Theoretical Compressible Flow, U.S. Naval Ord. Lab., June 28, 1949, pp. 1–33.

118. Lin. C.C.: On the Subsonic Flow through Circular and Straight Lattices of Airfoils. Jour. Math and Phys., vol. XXXVIII, no. 2, July 1949, pp. 117–130.

119. Lin, C. C.: On an Extension of the von Kármán-Tsien Method to Two-Dimensional Subsonic Flows with Circulation around Closed Profiles. Quart. Appl. Math., vol. IV, no. 3, Oct. 1946, pp. 291–297.

120. Sauer, Robert: Introduction to Theoretical Gas Dynamics. J. W. Edwards (Ann Arbor), 1947.

121. Woolard, Henry W.: A Note on the Subsonic Compressible Flow about Airfoils in a Cascade. Jour. Aero. Sci., vol. 17, no. 6, June 1950, pp. 379–381.

122. Briggs, William B.: Effect of Mach Number on the Flow and Application of Compressibility Corrections in a Two-Dimensional Subsonic-Transonic Compressor Cascade Having Varied Porous-Wall Suction at the Blade Tips. NACA TN 2649, 1952.

123. Erwin, John R., Savage, Melvyn, and Emery, James C.: Two-Dimensional Low-Speed Cascade Investigation of NACA Compressor Blade Sections Having a Systematic Variation in Mean-Line Loading. NACA TN 3817, 1956. (Supersedes NACA RM L53I30b.)

124. Huppert, M. C., and MacGregor, Charles: Comparison between Predicted and Observed Performance of Gas-Turbine Stator Blade Designed for Free-Vortex Flow. NACA TN 1810, 1949.

125. Stanitz, John D., and Prian, Vasily D.: A Rapid Approximate Method for Determining Velocity Distribution on Impeller Blades of Centrifugal Compressors. NACA TN 2421, 1951.

126. Wu, Chung-Hua, and Brown, Curtis A.: A Theory of the Direct and Inverse Problems of Compressible Flow Past Cascade of Arbitrary Airfoils. Jour. Aero. Sci., vol. 19, no. 3, Mar. 1952, pp. 183–196.

127. Wu, Chung-Hua, and Brown, Curtis A.: Method of Analysis for Compressible Flow Past Arbitrary Turbomachine Blades on General Surface of Revolution. NACA TN 2407, 1951.

128. Milne, William Edmund: Numerical Calculus. Princeton Univ. Press, 1949.

129. Wu, Chung-Hua: Formulas and Tables of Coefficients for Numerical Differentiation with Function Values Given at Unequally Spaced Points and

Application to Solution of Partial Differential Equations. NACA TN 2214, 1950.

130. Wu, Chung-Hua: Matrix and Relaxation Solutions that Determine Subsonic Through Flow in an Axial-Flow Gas Turbine. NACA TN 2750, 1952.

131. Stanitz, John D.: Design of Two-Dimensional Channels with Prescribed Velocity Distributions along the Channel Walls. NACA Rep. 1115, 1953. (Supersedes NACA TN's 2593 and 2595.)

132. Stanitz, John D., and Sheldrake, Leonard J.: Application of a Channel Design Method to High-Solidity Cascades and Tests of an Impulse Cascade with 90° of Turning. NACA Rep. 1116, 1953. (Supersedes NACA TN 2652.)

133. Ackeret, J. (V. P. Akimoff, trans.): The Design of Closely Spaced Blade Grids. R.T.P. Trans. No. 2007, British M.A.P.

134. Sawyer, William T.: Experimental Investigation of a Stationary Cascade of Aerodynamic Profiles. Mitt. aus d. Inst. f. Aero., Heft 17, Zurich, 1949.

135. Alpert, Sumner: Design Method for Two-Dimensional Channels for Compressible Flow with Application to High-Solidity Cascades. NACA TN 1931, 1949.

136. Stanitz, John D.: Approximate Design Method for High-Solidity Blade Elements in Compressors and Turbines. NACA TN 2408, 1951.

137. Orlin, W. James, Lindner, Norman J., and Bitterly, Jack G., Application of the Analogy between Water Flow with a Free Surface and Two-Dimensional Compressible Gas Flow. NACA Rep. 875, 1947. (Supersedes NACA TN 1185.)

138. Portisky, H., Sells, B. E., and Danforth, C. E.: Graphical, Mechanical, and Electrical Aids for Compressible Fluid Flow. Jour. Appl. Mech., vol. 17, no. 1, Mar. 1950, pp. 37–46.

139. Westphal, Willard R., and Dunavant, James C.: A Compressible-Flow Plotting Device and Its Application to Cascades Flows. NACA TN 2681, 1952.

140. Westphal, Willard R., and Dunavant, James C.: Application of the Wire-Mesh Plotting Device to Incompressible Cascade Flow. NACA TN 2095, 1950.

141. Taylor, G. I., and Sharman, C. F.: A Mechanical Method for Solving Problems of Flow in Compressible Fluids. R. & M. No. 1195, British ARC, Aug. 1928.

142. Malavard, L.: Use of Rheoelectrical Analogies. Jour. Roy. Aero. Soc., vol. 51, no. 441, 1947.

143. Peres, J.: Les methodes d'analogie en mecanique appliquee. Proc. Fifth Int. Cong. Appl. Mech., 1938, pp. 9–19.

144. Preiswerk, Ernst: Application of the Methods of Gas Dynamics to Water Flows with Free Surface. I—Flows with No Energy Dissipation. NACA TM 934, 1940.

145. Hargest, T. J.: The Theoretical Pressure Distributions around Some Related Aerofoils in Cascade. Memo. M.68, British NGTE, Nov. 1949.

146. Hargest, T. J.: The Theoretical Pressure Distributions around Some Conventional Turbine Blades in Cascade. R. & M. 2765, British ARC, 1949.

147. deHaller, P.: Application of Electrical Analogy to the Investigation of Cascades. Sulzer Tech. Rev., No. 3/4, 1947, pp. 11–17.

148. Vandrey, F.: Investigations of Plane Subsonic Flow with the Help of an Electrical Analogy. LFA Völkenrode Trans. No. 34, British M.O.S.

149. Bieberbach, L.: Conformal Mapping. Chelsea Pub. Co. (New York), 1953.

150. Schilhansl, Max J.: Survey of Information on Two-Dimensional Cascades. Tech. Rep. 54–322, WADC, Mar. 1955.

151. Schlichting, H.: Lecture Series "Boundary Layer Theory." Pt. I—Laminar Flows. Pt. II—Turbulent Flows. NACA TM's 1217 and 1218, 1949.

152. Goldstein, Sydney, ed.: Modern Developments in Fluid Dynamics. Vols. I and II. Clarendon Press (Oxford), 1938.

153. Dryden, Hugh L.: Recent Advances in the Mechanics of Boundary Layer Flow. Advances in Appl. Mech., vol. 1, 1948.

154. Howarth, L., ed.: Modern Developments in Fluid Dynamics; High Speed Flow. Vols. I and II. Clarendon Press (Oxford), 1953.

155. Squire, H. B., and Young, A. D.: The Calculation of the Profile Drag of Aerofoils. R. & M. 1838, British ARC, Nov. 1937.

156. Lieblein, Seymour, and Roudebush, William H.: Theoretical Loss Relations for Low-Speed Two-Dimensional-Cascade Flow. NACA TN 3662, 1956.

157. Pohlhausen, K.: Zur naherungsweisen Integration der Differentialgleichung der laminaren Grenzschicht. Z.A.M.M., Bd. 1, Heft 4, Aug. 1921 pp. 252–268.

158. Clauser, Francis H.: Turbulent Boundary Layers in Adverse Pressure Gradients. Jour. Aero. Sci., vol. 21, no. 2, Feb. 1954, pp. 91–108.

159. Ludwieg, H., and Tillmann, W.: Investigations of the Wall-Shearing Stress in Turbulent Boundary Layers. NACA TM 1285, 1950.

160. Maskell, E. C.: Approximate Calculation of the Turbulent Boundary Layer in Two-Dimensional Incompressible Flow. Rep. AERO 2443, British RAE, Nov. 1951.

161. Schubauer, G. B., and Skramstad, H. K.: Laminar-Boundary-Layer Oscillations and Transition on a Flat Plate. NACA Rep. 909, 1948. (Supersedes NACA WR W-8.)

162. Bussmann, K., and Ulrich, A.: Systematic Investigations of the Influence of the Shape of the Profile upon the Position of the Transition Point. NACA TM 1185, 1947.

163. Taylor, G. I.: Some Recent Developments in the Study of Turbulence. Proc. Fifth Int. Cong. Appl. Mech., 1938, pp. 294–310.

164. Dryden, Hugh L., Schubauer, G. B., Mock, W. C., Jr., and Skramstad, H. K.: Measurements of Intensity and Scale of Wind-Tunnel Turbulence and Their Relation to the Critical Reynolds Number of Spheres. NACA Rep. 581, 1937.

165. Seiferth, R., ed.: D_1—Model Testing Technique. I—Test Installations. Measurement of the Tunnel Turbulence by Means of a Sphere and Its Relation to the Hot-Wire Measurement. Rep. and Trans. No. 994, M.A.P. Volkenrode, June 15, 1947.

166. Bursnall, William J., and Loftin, Laurence K., Jr.: Experimental Investigation of Localized Regions of Laminar-Boundary-Layer Separation. NACA TN 2338, 1951.

167. Blight, F. G., and Howard, W.: Tests on Four Airfoil Cascades. Pt. I—Deflection, Drag, and Velocity Distribution. Pt. II—Boundary Layer Characteristics. Reps. E.74 and E.75, Dept. Supply, Aero. Res. Labs., Melbourne (Australia), July 1952.

168. Carter, A. D. S., Andrews, S. J., and Shaw, H.: Some Fluid Dynamic Research Techniques. Proc. Inst. Mech. Eng. (London), vol. 163, 1950, pp. 249–263.

169. von Kármán, Th.: On Laminar and Turbulent Friction. NACA TM 1092, 1946.

170. Loitsianskii, L. G.: Approximate Method of Integration of Laminar Boundary Layer in Incompressible Fluid. NACA TM 1293, 1951.

171. Thwaites, B.: Approximate Calculation of the Laminar Boundary Layer. Aero. Quarterly, vol. 1, Nov. 1949, pp. 245–280.

172. Owen, P. R., and Klanfer, L.: On the Laminar Boundary Layer Separation from the Leading Edge of a Thin Aerofoil. Rep. AERO. 2508, British RAE, Oct. 1953.

173. Crooks, P. V., and Howard, W.: Low Speed Tests on Three Aerofoil Cascades Designed for Prescribed Surface Velocity Distributions. Rep. ME.76, Res. & Dev. Branch, Aero. Res. Labs., Melbourne (Australia), June 1954.

174. von Doenhoff, Albert E., and Tetervin, Neal: Determination of General Relations for the Behavior of Turbulent Boundary Layers. NACA Rep. 772, 1943. (Supersedes NACA WR L–382.)

175. Persh, Jerome: The Behavior of the Boundary Layer in the Region of Transition from Laminar to Turbulent Flow. Jour. Aero. Sci., vol. 22, no. 6, June 1955, pp. 443–444.

176. Braslow, Albert L., and Visconti, Fioravante: Investigation of Boundary-Layer Reynolds Number for Transition on an NACA $65_{(215)}$-114 Airfoil in the Langley Two-Dimensional Low-Turbulence Pressure Tunnel. NACA TN 1704, 1948.

177. Katzoff, S., Bogdonoff, Harriet E., and Boyet, Howard: Comparisons of Theoretical and Experimental Lift and Pressure Distributions on Airfoils in Cascade. NACA TN 1376, 1947.

178. Preston, J. H.: The Calculation of the Lift Taking Account of the Boundary Layer. R. & M. 2725, British ARC, 1949.

179. Loitsianskii, L. G.: Soprotivlenie Reshetki Profilei Obtekaemoi Viazkoi Neszhimaemoi Zhidkost'iu. Prik. Mate. i Mikh., vol. XI, no. 4, 1947. (Resistance of Cascade of Airfoils in Viscous Incompressible Fluid.) (Trans. available from NASA Headquarters.)

180. Loitsianskii, L. G.: Resistance of Cascade of Airfoils in Gas Stream at Subsonic Velocity. NACA TM 1303, 1951.

181. Schlichting, H., und Scholz, N.: Über die theoretische Berechnung der Stromungsverluste eines ebenen Schaufelgitters. Ing.-Archiv., Bd. XIX, Heft 1, 1951, pp. 42–65.

182. Platt, Robert C.: Turbulence Factors of NACA Wind Tunnels as Determined by Sphere Tests. NACA Rep. 558, 1936.

183. Lawson, T. V.: An investigation into the Effect of Reynolds Number on a Cascade of Blades With Parabolic Arc Camber Line. Memo. M.195, British NGTE, Nov. 1953.

184. Kantrowitz, Arthur, and Daum, Fred L.: Preliminary Experimental Investigation of Airfoils in Cascade. NACA WR L–231, 1942. (Supersedes NACA CB.)

185. Bogdonoff, Seymour M., and Bogdonoff, Harriet E.: Blade Design Data for Axial-Flow Fans and Compressors. NACA WR L–635, 1945. (Supersedes NACA ACR L5F07a.)

186. Constant, H.: Note on Performance of Cascades of Aerofoils. Note E–3696, British RAE, 1939.

187. Davis, Hunt: A Method of Correlating Axial-Flow-Compressor Cascade Data. ASME Trans., vol. 70, no. 8, Nov. 1948, pp. 951–955.

188. Howell, A. R., and Carter, A. D. S.: Fluid Flow Through Cascades of Aerofoils. Rep. R.6, British NGTE, Sept. 1946.

189. Carter, A. D. S., and Hounsell, A. F.: General Performance Data for Aerofoils Having C.1, C.2, or C.4 Base Profiles on Circular Arc Camber Lines. Memo. M.62, British NGTE, Aug. 1949.

190. Carter, A. D. S.: The Low Speed Performance of Related Aerofoils in Cascade. Rep. R.55, British NGTE, Sept. 1949. (See also C.P. 29, British M.O.S., Sept. 1949.)

191. Erwin, John R., and Emery, James C.: Effect of Tunnel Configuration and Testing Technique on Cascade Performance. NACA Rep. 1016, 1951. (Supersedes NACA TN 2028.)

192. Fletcher, P. J.: Low Speed Tests on Compressor Cascades of Parabolic Cambered Aerofoils. Pt. I—Pitch/Chord Ratio = 1.0. Pt. II—Pitch/Chord Ratio = 0.75. Memos. M.81 and M.159, British NGTE, Mar. 1950 and Nov. 1952.

193. Schlichting, Herman: Problems and Results of Investigations on Cascade Flow. Jour. Aero. Sci., vol. 21, no. 3, Mar. 1954, pp. 163–178.

194. Blight, F. G., Howard, W., and McCallum, H.: The Design and Performance of a Low-Speed Cascade Tunnel. Eng. Note 133, Aero. Lab., Fishermen's Bend, Melbourne (Australia), June 1949.

195. Korbacher, G. K.: A Test on a Compressor Cascade of Aerofoils Having Their Position of Maximum Thickness 40% of the Chord from the Leading Edge and a Pitch/Chord Ratio of 0.75. Memo. M.89, British NGTE, June 1950.

196. Jeffs, R. A., Hounsell, A. F., and Adams, R. G.: Further Performance Data for Aerofoils Having C.1, C.2, or C.4 Base Profiles on Circular Arc Camber Lines. Memo. M.139, British NGTE, Dec. 1951.

197. Howell, A. R.: A Note on Compressor Base Aerofoils C.1, C.2, C.3, C.4, C.5, and Aerofoils Made Up of Circular Arcs. Memo. M.1011, Power Jets (Res. and Dev.), Ltd., Sept. 1944.

198. Hughes, Hazel P.: Base Profiles C.7. Memo. M.1210, British NGTE, May 1946.

199. Felix, A. Richard, and Emery, James C.: A Comparison of Typical National Gas Turbine Establishment and NACA Axial-Flow Compressor Blade Sections in Cascade at Low Speed. NACA TN 3937, 1957. (Supersedes NACA RM L53B26a.)

200. Andrews, S. J., Andrews, Patricia M., and Baines, Margaret: A Comparison Between Two Compressor Cascades Using C.4 Profile on Parabolic and Circular Arc Camber Lines. Memo. M.6, British NGTE, Sept. 1946.

201. Carter, A. D. S.: Some Tests on Compressor Cascades of Related Aerofoils Having Different Positions of Maximum Camber. Rep. R.47, British NGTE, Dec. 1948.

202. Herrig, L. Joseph, Emery, James C., and Erwin, John R.: Effect of Section Thickness and Trailing-Edge Radius on the Performance of NACA 65-Series Compressor Blades in Cascade at Low Speeds. NACA RM L51J16, 1951.

203. Bailey, W., and Jefferson, J. L.: Compressibility Effects on Cascades of Low Cambered Compressor Blades. Rep. E. 3972, British RAE, May 1943.

204. Reeman, J., and Simonis, E. A.: The Effect of Trailing Edge Thickness on Blade Loss. Tech. Note 116, British RAE, Mar. 1943.

205. Todd, K. W.: An Experimental Study of Three-Dimensional High-Speed Air Conditions in a Cascade of Axial-Flow Compressor Blades. R. & M. 2792, British ARC, Oct. 1949.

206. Bogdonoff, Seymour M.: NACA Cascade Data for the Blade Design of High-Performance Axial-Flow Compressors. Jour. Aero. Sci., vol. 15, no. 2, Feb. 1948, pp. 89–95.

207. Savage, Melvyn, Felix, A. Richard, and Emery, James C.: High-Speed Cascade Tests of a Blade Section Designed for Typical Hub Conditions of High-Flow Transonic Rotors. NACA RM L55F07, 1955.

208. Carter, A. D. S., and Hughes, Hazel P.: A Note on the High Speed Performance of Compressor Cascades. Memo. M.42, British NGTE, Dec. 1948.

209. Staniforth, R.: A Note on Compressor Operation at Transonic Relative Inlet Mach Numbers. Memo. M.224, British NGTE, July 1954.

210. Carter, A. D. S.: Throat Areas of Compressor Blade Cascades Derived for the Base Aerofoil C.4. Memo. M.1025, Power Jets, Ltd., Oct. 1944.

211. Hughes, Hazel P.: Throat Areas for the Parabolic Arc Cambered Aerofoil C.4 in Cascade. Memo. M.157, British NGTE, Aug. 1952.

212. Wright, Linwood C., and Schwind, Richard: Throat-Area Determination for a Cascade of Double-Circular-Arc Blades. NACA RM E55H25a, 1955.

213. Dunavant, James C.: Cascade Investigation of a Related Series of 6-Percent-Thick Guide-Vane Profiles and Design Charts. NACA TN 3959. (Supersedes NACA RM L54I02.)

214. Alsworth, Charles C., and Iura, Toru: Theoretical and Experimental Investigations of Axial Flow Compressors. Pt. 3—Progress Report on Loss Measurements in Vortex Blading. Mech. Eng. Lab., C.I.T., July 1951. (Navy Contract N6-ORI-102.)

215. Mankuta, Harry, and Guentert, Donald C.: Some Effect of Solidity on Turning through Constant-Thickness Circular-Arc Guide Vanes in Axial Annular Flow. NACA RM E51E07, 1951.

216. Korbacher, G. K.: A Test on a Compressor Cascade of Aerofoils Having Their Position of Maximum Thickness 40% of the Chord and a Position of Maximum Camber of 45% of the Chord from the Leading Edge. Memo. M.80, British NGTE, Mar. 1950.

217. Wilson, Robert E.: Turbulent Boundary-Layer Characteristics at Supersonic Speeds—Theory and Experiment. Jour. Aero. Sci., vol. 17, no. 9, Sept. 1950, pp. 585–594.

218. Schulze, Wallace M., Erwin, John R., and Ashby, George C., Jr.: NACA 65-Series Compressor Rotor Performance with Varying Annulus-Area Ratio, Solidity, Blade Angle, and Reynolds Number and Comparison with Cascade Results. NACA TN 4130, 1957. (Supersedes NACA RM L52L17.)

219. Ashby, George C., Jr.: Comparison of Low-Speed Rotor and Cascade Performance for Medium-Camber NACA 65—$(C_{lo}A_{10})$10 Compressor-Blade Sections Over a Wide Range of Rotor Blade-Setting Angles at Solidities of 1.0 and 0.5. NACA RM L54I13, 1954.

220. Andrews, S. J., and Ogden, H.: A Detailed Experimental Comparison of Blades Designed for Free Vortex Flow and Equivalent Untwisted Constant Section Blades. Rep. R.123, British NGTE, Aug. 1952.

221. Lieblein, Seymour: Review of High-Performance Axial-Flow-Compressor Blade-Element Theory. NACA RM E53L22, 1954.

222. Schwenk, Francis C., Lieblein, Seymour, and Lewis, George W., Jr.: Experimental Investigation of an Axial-Flow Compressor Inlet Stage Operating at Transonic Relative Inlet Mach Numbers. III—Blade-Row Performance of Stage with Transonic Rotor and Subsonic Stator at Corrected Tip Speeds of 800 and 1000 Feet per Second. NACA RM E53G17, 1953.

223. Moses, Jason J., and Serovy, George K.: Effect of Blade-Surface Finish on Performance of a Single-Stage Axial-Flow Compressor. NACA RM E51C09, 1951.

224. Moses, J. J., and Serovy, G. K.: Some Effects of Blade Trailing-Edge Thickness on Performance of a Single-Stage Axial-Flow Compressor. NACA RM E51F28, 1951.

225. Thurston, Sidney, and Brunk, Ralph E.: Performance of a Cascade in an Annular Vortex-Generating Tunnel Over Range of Reynolds Numbers. NACA RM E51G30, 1951.

226. Wallner, Lewis E., and Fleming, William A.: Reynolds Number Effect on Axial-Flow Compressor Performance. NACA RM E9G11, 1949.

227. Mühlemann, E. (John Perl, trans.): Experimental Investigations on an Axial Blower Stage. Lockheed Aircraft Corp., Burbank (Calif.).

228. Voit, Charles H., Guentert, Donald C., and Dugan, James F.: Effect of Mach Number on Over-All Performance of Single-Stage Axial-Flow Compressor Designed for High Pressure Ratio. NACA RM E50D26, 1950.

229. Robbins, William H., and Glaser, Frederick W.: Investigation of an Axial-Flow-Compressor Rotor with Circular-Arc Blades Operating Up to a Rotor-Inlet Relative Mach Number of 1.22. NACA RM E53D24, 1953.

230. Jackson, Robert J.: Effects on the Weight-Flow Range and Efficiency of a Typical Axial-Flow Compressor Inlet Stage That Result from the Use of a Decreased Blade Camber or Decreased Guide-Vane Turning. NACA RM E52G02, 1952.

231. Jackson, Robert J.: Analysis of Performance of Four Symmetrical-Diagram-Type Subsonic Inlet-Stage Axial-Flow Compressors. NACA RM E53K03, 1954.

232. Standahar, Raymond M., and Serovy, George K.: Some Effects of Changing Solidity by Varying the Number of Blades on Performance of an Axial-flow Compressor Stage. NACA RM E52A31, 1952.

233. Serovy, George K., Robbins, William H., and Glaser, Frederick W.: Experimental Investigation of a 0.4 Hub-Tip Diameter Ratio Axial-Flow Compressor Inlet Stage at Transonic Inlet Relative Mach Numbers. I—Rotor Design and Over-All Performance at Tip Speeds from 60 to 100 Percent of Design. NACA RM E53I11, 1953.

234. Tysl, Edward R., Schwenk, Francis C., and Watkins, Thomas B.: Experimental Investigation of a Transonic Compressor Rotor with a 1.5-Inch Chord Length and an Aspect Ratio of 3.0. I—Design, Over-All Performance, and Rotating-Stall Characteristics. NACA RM E54L31, 1955.

235. Sandercock, Donald M., Lieblein, Seymour, and Schwenk, Francis C.: Experimental Investigation of an Axial-Flow Compressor Inlet Stage Operating at Transonic Relative Inlet Mach Numbers. IV—Stage and Blade-Row Performance of Stage

with Axial-Discharge Stators. NACA RM E54C26, 1954.

236. Wu, Chung-Hua, and Wolfenstein, Lincoln: Application of Radial-Equilibrium Condition to Axial-Flow Compressor and Turbine Design. NACA Rep. 955, 1950. (Supersedes NACA TN 1795.)

237. Eckert, and Korbacher: The Flow Through Axial Turbine Stages of Large Radial Blade Length. NACA TM 1118, 1947.

238. Marble, Frank E.: The Flow of a Perfect Fluid Through an Axial Turbomachine with Prescribed Blade Loading. Jour. Aero. Sci., vol. 15, no. 8, Aug. 1948, pp. 473–485.

239. Marble, Frank E., and Michelson, Irving: Analytical Investigation of Some Three Dimensional Flow Problems in Turbomachines. NACA TN 2614, 1952.

240. Eckert, B.: Axialkompressoren und Radialkompressoren. Springer-Verlag (Berlin), 1953.

241. Wu, Chung-Hua: Subsonic Flow of Air Through a Single-Stage and a Seven-Stage Compressor. NACA TN 2961, 1953.

242. Wu, Chung-Hua: A General Theory of Three-Dimensional Flow in Subsonic and Supersonic Turbomachines of Axial-, Radial-, and Mixed-Flow Types. NACA TN 2604, 1952.

243. Novak, R. A.: Notes on the Fundamentals of the Design of Multi-Stage Axial Compressors. Lecture No. 6, Gas Turbine Lectures, Dept. Mech. and Ind. Eng., Univ. Mich., June 29–July 10, 1953.

244. Smith, L. H., Jr., Traugott, S. C., and Wislicenus, G.F.: A Practical Solution of a Three-Dimensional Flow Problem of Axial-Flow Turbomachinery. Trans. ASME, vol. 75, no. 5, July 1953, pp. 789–803.

245. Holmquist, Carl O., and Rannie, W. Duncan: An Approximate Method of Calculating Three-Dimensional Flow in Axial Turbomachines. Paper presented at meeting Inst. Aero. Sci., New York, Jan. 24–28, 1955.

246. Carter, A. D. S., Andrews, S. J., and Fielder, E. A.: The Design and Testing of an Axial Compressor Having a Mean Stage Temperature Rise of 30° C. Rep. R. 148, British NGTE, Nov. 1953.

247. Briggs, William B., and Giamati, Charles C.: Interstage Surveys and Analysis of Viscous Action in Latter Stages of a Multistage Axial-Flow Compressor. NACA RM E52I12, 1953.

248. Finger, Harold B., and Dugan, James F., Jr.: Analysis of Stage Matching and Off-Design Performance of Multistage Axial-Flow Compressors. NACA RM E52D07, 1952.

249. Finger, Harold B.: Method of Experimentally Determining Radial Distributions of Velocity Through Axial Flow Compressor. NACA TN 2059, 1950.

250. Ames Research Staff: Equations Tables, and Charts for Compressible Flow. NACA Rep. 1135, 1953. (Supersedes NACA TN 1428.)

251. Hagen, H.: Compressor Characteristics and Starting Powers of Jet Propulsion Power Plants. BuShips 338, vol. 8, pt. A, May 1946, pp. 1–20.

252. Bogdonoff, Seymour M.: The Performance of Axial-Flow Compressors As Affected by Single-Stage Characteristics. Jour. Aero. Sci., vol. 18, no. 5, May 1951, pp. 319–328.

253. Medeiros, Arthur A., Benser, William A., and Hatch, James E.: Analysis of Off-Design Performance of a 16-Stage Axial-Flow Compressor With Various Blade Modifications. NACA RM E52L03, 1953.

254. Geye, Richard P., and Voit, Charles H.: Investigation of a High-Pressure-Ratio Eight-Stage Axial-Flow Research Compressor With Two Transonic Inlet Stages. IV—Modification of Aerodynamic Design and Prediction of Performance. NACA RM E55B28, 1955.

255. Standahar, Raymond M., and Geye, Richard P.: Investigation of a High-Pressure-Ratio Eight-Stage Axial-Flow Research Compressor With Two Transonic Inlet Stages. V—Preliminary Analysis of Over-All Performance of Modified Compressor. NACA RM E55A03, 1955.

256. Howell, A. R., and Bonham, R. P.: Over-All and Stage Characteristics of Axial-Flow Compressors. Proc. Inst. Mech. Eng., vol. 163, 1950, pp. 235–248.

257. Budinger, Ray E., and Serovy, Geroge K.: Investigation of a 10-Stage Subsonic Axial-Flow Research Compressor. IV—Individual Stage Performance Characteristics. NACA RM E53C11, 1953.

258. Voit, Charles H., and Geye, Richard P.: Investigation of a High-Pressure-Ratio Eight-Stage Axial-Flow Research Compressor with Two Transonic Inlet Stages. III—Individual Stage Performance Characteristics. NACA RM E54H17, 1954.

259. Cheshire, L. J.: The Design and Development of Centrifugal Compressors for Aircraft Gas Turbines. War Emergency Issue No. 12 pub. by Inst. Mech. Eng. (London), 1945. (Reprinted in U.S. by ASME, Jan. 1947, p. 438.)

260. Schulze, Wallace M., Erwin, John R., and Westphal, Willard R.: Investigation of an Impulse Axial-Flow Compressor Rotor Over a Range of Blade Angles. NACA RM L50F27a, 1950.

261. Grant, Howard P.: Hot Wire Measurements of Stall Propagation and Pulsating Flow in an Axial Flow Inducer-Centrifugal Impeller System. Pratt and Whitney Res. Rep. No. 133, June 1951.

262. Ossofsky, Eli: Constant Temperature Operation of the Hot-Wire Anemometer at High Frequency. Rev. Sci. Instr., vol. 19, no. 12, Dec. 1948, pp. 881–889.

263. Laurence, James C., and Landes, L. Gene: Auxiliary Equipment and Techniques for Adapting the Constant-Temperature Hot-Wire Anemometer to Specific Problems in Air-Flow Measurements. NACA TN 2843, 1952.

264. Lowell, Herman H.: Design and Application of Hot-Wire Anemometers for Steady-State Measurements at Transonic and Supersonic Airspeeds. NACA TN 2117, 1950.

265. Huppert, Merle C.: Preliminary Investigation of Flow Fluctuations During Surge and Blade Row

Stall in Axial-Flow Compressors. NACA RM E52E28, 1952.

266. Huppert, Merle C., Costilow, Eleanor L., and Budinger, Ray E.: Investigation of a 10-Stage Subsonic Axial-Flow Research Compressor. III—Investigation of Rotating Stall, Blade Vibration, and Surge at Low and Intermediate Compressor Speeds. NACA RM E53C19, 1953.

267. Delio, G. J., and Stiglic, P. M.: Experimental Investigation of Control Signals and the Nature of Stall and Surge Behavior in a Turbojet Engine. NACA RM E54I15, 1954.

268. Iura, T., and Rannie, W. D.: Observations of Propagating Stall in Axial-Flow Compressors. Rep. 4, Mech. Eng. Lab., C.I.T., Apr. 1953. (Navy Contract N6-ORI-102.)

269. Johnson, Donald F., and Costilow, Eleanor L.: Experimental Determination of Aerodynamic Forces Normal to the Chord Due to Rotating Stall Acting on Compressor Blading. NACA RM E54F14, 1954.

270. Huppert, Merle C., Johnson, Donald F., and Costilow, Eleanor L.: Preliminary Investigation of Compressor Blade Vibration Excited by Rotating Stall. NACA RM E52J15, 1952.

271. Graham, Robert W., and Prian, Vasily D.: Rotating Stall Investigation of 0.72 Hub-Tip Ratio Single-Stage Compressor. NACA RM E53L17a, 1954.

272. Emmons, H. W., Pearson, C. E., and Grant, H. P.: Compressor Surge and Stall Propagation. Trans. ASME, vol. 77, no. 4, May 1955, pp. 455–467; discussion, pp. 467–469.

273. Costilow, Eleanor L., and Huppert, Merle C.: Rotating-Stall Characteristics of a Rotor with High Hub-Tip Radius Ratio. NACA TN 3518, 1955.

274. Stenning, Alan H., Kriebel, Anthony R., and Montgomery, Stephen R.: Stall Propagation in Axial-Flow Compressors. NACA TN 3580, 1956.

275. Sears, W. R.: On Asymmetric Flow in an Axial-Flow Compressor Stage. Jour. Appl. Mech., vol. 20, no. 3, Sept. 1953, pp. 442–443.

276. Mendelson, Alexander: Effect of Aerodynamic Hysteresis on Critical Flutter Speed at Stall. NACA RM E8B04, 1948. (See also Jour. Aero. Sci., vol. 16, no. 11, Nov. 1949, pp. 645–654.)

277. Sears, W. R.: A Theory of "Rotating Stall" in Axial Flow Compressors. Graduate School Aero. Eng., Cornell Univ., Ithaca (N.Y.). (Contract AF 33(038)-21406.)

278. Graham, Robert W., and Prian, Vasily D.: Experimental and Theoretical Investigation of Rotating-Stall Characteristics of Single-Stage Axial-Flow Compressor with Hub-Tip Ratio of 0.76. NACA RM E53I09, 1953.

279. Marble, Frank E.: Propagation of Stall in a Compressor Blade Row. Tech. Rep. No. 4, GALCIT, Jan. 1954. (Office Sci. Res., Air Res. and Dev. Command Contract AF 18(600)-178.) (See also Jour. Aero. Sci., vol. 22, no. 8, Aug. 1955, pp. 541–554.)

280. Pearson, H.: The Aerodynamics of Compressor Blade Vibration. Fourth Anglo-American Aero. Conf. (London), Sept. 15–17, 1953, pp. 127–162; discussion, pp. 162A–162J. (Publ. by Roy. Aero. Soc. (London).) (Summarized in The Engineer, Oct. 9, 1953, pp. 473–476.)

281. Bollay, William, and Brown, Charles D.: Some Experimental Results on Wing Flutter. Jour. Aero. Sci., vol. 8, no. 8, June 1941, pp. 313–318.

282. Howell, A. R., and Carter, A. D. S.: Note on Stalling Flutter of Compressor Blades. Memo. 131, British NGTE, Oct. 1951.

283. Bellenot, C., and d'Epinay, J. Laline: Self-Induced Vibrations of Turbo-Machine Blades. Brown-Boveri Rev., vol. XXXVII, no. 10, Oct. 1950, pp. 368–376.

284. Schnittger, Jan R.: Single Degree of Freedom Futter of Compressor Blades in Separated Flow. Jour. Aero. Sci., vol. 21, no. 1, Jan. 1954, pp. 27–36.

285. Sisto, F.: Stall-Futter in Cascades. Jour. Aero. Sci., vol. 20, no. 9, Sept. 1953, pp. 598–604.

286. Smith, A.G., and Fletcher, P. J.: Observations on the Surging of Various Low-Speed Fans and Compressors. Memo. M.219, British NGTE, July 1954.

287. Bullock, Robert O., Wilcox, Ward W., and Moses, Jason J.: Experimental and Theoretical Studies of Surging in Continuous-Flow Compressors. NACA Rep. 861, 1946. (Supersedes NACA TN 1213.)

288. Pearson, H., and Bower, T.: Surging of Axial Compressors. The Aero. Quarterly, vol. 1, pt. III, Nov. 1949. (Pub. by Roy. Aero. Soc. (London).)

289. Doherty, Robert E., and Keller, Ernest G.: Mathematics of Modern Engineering. Vol. I. John Wiley & Sons, Inc., 1936.

290. Trimmer, John Dezendorf: Response of Physical Systems. John Wiley & Sons, Inc., 1950.

291. Brainerd, J. G., Koehler, Glenn, Reich, Herbert J., and Woodruff, L. L.: Ultra High Frequency Techniques. D. Van Nostrand Co., Inc., 1942.

292. Foster, D. V.: The Performance of the 108 Compressor Fitted with Low Stagger Free Vortex Blading. Rep. R.116, British NGTE, June 1952.

293. Lucas, James G., and Filippi, Richard E.: Multiple Over-All Performance and Rotating-Stall Characteristics of a 15-Stage Experimental Axial-Flow Compressor at an Intermediate Speed. NACA RM E54C29, 1954.

294. Benser, William A.: Analysis of Part-Speed Operation for High-Pressure-Ratio Multistage Axial-Flow Compressors. NACA RM E53I15, 1953.

295. Huppert, Merle C., and Benser, William A.: Some Stall and Surge Phenomena in Axial-Flow Compressors. Jour. Aero. Sci., vol. 20, no. 12, Dec. 1953, pp. 835–845.

296. Budinger, Ray E., and Serovy, George K.: Investigation of a 10-Stage Subsonic Axial-Flow Research Compressor. V—Effect of Reducing Inlet-Guide-Vane Turning on Over-All and Inlet-Stage Performance. NACA RM E53H10, 1954.

297. Budinger, Ray E., and Kaufman, Harold R.: Investigation of the Performance of a Turbojet Engine with Variable-Position Compressor Inlet Guide Vanes. NACA RM E54L23a, 1955.

298. Reissner, Hans: Blade Systems of Circular Arrangement in Steady, Compressible Flow. Studies and Essays. Courant Anniversary Vol., Interscience Pub., Inc. (New York), 1948, pp. 307–327.

299. Reissner, H. J., and Meyerhoff, L.: Analysis of an Axial Compressor Stage with Infinitesimal and Finite Blade Spacing. NACA TN 2493, 1951.

300. Reissner, Hans J., Meyerhoff, L., and Bloom, Martin: Two-Dimensional Steady Nonviscous and Viscous Compressible Flow through a System of Equidistant Blades. NACA TN 2718, 1952.

301. Wu, Chung-Hua: A General Through-Flow Theory of Fluid Flow with Subsonic or Supersonic Velocity in Turbomachines of Arbitrary Hub and Casing Shapes. NACA TN 2302, 1951.

302. Wu, Chung-Hua, and Costilow, Eleanor L.: A Method of Solving the Direct and Inverse Problem of Supersonic Flow Along Arbitrary Stream Filaments of Revolution in Turbomachines. NACA TN 2492, 1951.

303. Marble, Frank E.: Some Problems Concerning the Three-Dimensional Flow in Axial Turbomachines. Preprint No. 182, Inst. Aero. Sci., 1949.

304. Torda, T. P., Hilton, H. H., and Hall, F. C.: Analysis of Viscous Laminar Incompressible Flow Through Axial-Flow Turbomachines with Infinitesimal Blade Spacing. Rep. C–TR–1, Eng. Exp. Station, Aero. Eng. Dept., Univ. Ill., Feb. 24, 1953. (Contract AF 33 (616)–52.)

305. Born, P. W., Hall, F. C., Hilton, H. H., and Torda, T. P.: Analysis of Viscous Laminar Incompressible Flow Through Axial Flow Turbomachines with Finite Blade Spacing. Rep. C–TR–2, Eng. Exp. Station, Aero. Eng. Dept., Univ. Ill., Mar. 18, 1953. (Contract AF 33(616)–52.)

306. Torda, T. P.: Analysis of Viscous Laminar Incompressible Flow Through Axial Flow Turbomachines. Annual Summary Rep. C–TR–3, Eng. Exp. Station, Aero. Eng. Dep., Univ. Ill., July 15, 1953. (Contract AF 33(616)–52.)

307. Wu, Chung-Hua, Brown, Curtis A., and Prian, Vasily D.: An Approximate Method of Determining the Subsonic Flow in an Arbitrary Stream Filament of Revolution Cut by Arbitrary Turbomachine Blades. NACA TN 2702, 1952.

308. Bragg, Stephen L., and Hawthorne, William R.: Some Exact Solutions of the Flow through Annular Cascade Actuator Discs. Jour. Aero. Sci., vol. 17 no. 4, Apr. 1950, pp. 243–249.

309. Weske, John R.: Fluid Dynamic Aspects of Axial-Flow Compressors and Turbines. Jour. Aero. Sci., vol. 14, no. 11, Nov. 1947, pp. 651–656.

310. Carter, A. D. S.: Three-Dimensional-Flow Theories for Axial Compressors and Turbines. War Emergency Issue No. 41, pub. by Inst. Mech Eng. (London). (Reprinted in U.S. by ASME, Apr. 1949, pp. 255–268.)

311. Rohlik, Harold E., Kofskey, Milton G., Allen, Hubert W., and Herzig, Howard Z.: Secondary Flows and Boundary-Layer Accumulations in Turbine Nozzles. NACA Rep. 1168, 1954. (Supersedes NACA TN's 2871, 2909, and 2989.)

312. Smith, Leroy H., Jr.: Three-Dimensional Flow in Axial-Flow Turbo-machinery. Pt. I—Theoretical Determination of Secondary Flow. Rep. 1–14, Mech. Eng. Dept. Internal Flow Res., The Johns Hopkins Univ., Nov. 1953. (Air Force Contract AF–33(616)–152.)

313. von Kármán, Th., and Sears, W. R.: Airfoil Theory for Non-Uniform Motion. Jour. Aero. Sci., vol. 5, no. 10, Aug. 1938, pp. 379–390.

314. Sears, William R.: Some Aspects of Non-Stationary Airfoil Theory and Its Practical Application. Jour. Aero. Sci., vol. 8, no. 3, Jan. 1941, pp. 104–108.

315. Kemp, Nelson H., and Sears, W. R.: Aerodynamic Interference between Moving Blade Rows. Jour. Aero. Sci., vol. 20, no. 9, Sept. 1953, pp. 585–597.

316. Kemp, Nelson H., and Sears, W. R.: Aerodynamic Interference between Moving Blade Rows. Grad. School Aero. Eng., Cornell Univ., Dec. 1, 1952. (Contract AF 33(038)–21406.)

317. Keller, C. (C. Keller, Trans.): Kinetic Energy Losses Behind Blade Grids as a Result of Periodic Variation in the Circulation. Rep. Inst. Aero., Tech. Hochschule (Zurich), 1934, pp. 167–187. (Available as R.T.P. Trans. 1883, British M.A.P.)

318. Herzig, Howard Z., Hansen, Arthur G., and Costello, George R.: A Visualization Study of Secondary Flows in Cascades. NACA Rep. 1163, 1954. (Supersedes NACA TN 2947.)

319. Herzig, Howard Z., and Hansen, Arthur G.: A Survey of Unclassified Axial-Flow-Compressor Literature. NACA RM E55H11, 1955.

320. Kofskey, Milton G., and Allen, Hubert W.: Smoke Study of Nozzle Secondary Flows in a Low-Speed Turbine. NACA TN 3260, 1954.

321. Michal, Aristotle D.: Matrix and Tensor Calculus. John Wiley & Sons, Inc., 1947.

322. Dean, W. R.: Note on the Motion of Fluid in a Curved Pipe. Phil. Mag., ser. 7, vol. 4, no. XX, July 1927, pp. 208–223.

323. Dean, W. R.: The Stream-Line Motion of Fluid in a Curved Pipe. Phil. Mag., ser. 7, vol. 5, no. XXX, April 1928, pp. 673–695.

324. Kito, Fumiki: On the Secondary Vortex Generated in a Bent-Pipe of Elliptical Cross-Section. Jour. Japan Soc. Appl. Mech., 1950, pp. 73–75.

325. Ito, Hidesato: Theory of Laminar Flows through Curved Pipes of Elliptic and Rectangular Cross Sections. Inst. High Speed Mech., Tohoku Univ., Sendai (Japan), vol. I, 1951, pp. 1–16.

326. Squire, H. B., and Winter, K. G.: The Secondary Flow in a Cascade of Airfoils in a Nonuniform Stream. Jour. Aero. Sci., vol. 18, no. 4, Apr. 1951, pp. 271–277.

327. Hawthorne, William R.: Secondary Circulation in Fluid Flow. Proc. Roy. Soc. (London), ser. A, vol. 206, no. A1086, May 7, 1951, pp. 374–387.

328. Eichenberger, Hans P.: Shear Flow in Bends. Tech. Rep. 2, Office Naval Res., Gas Turbine Lab., M.I.T., Apr. 15, 1952. (Contract N5ori07848.)

329. Kronauer, Richard E.: Secondary Flows in Fluid Dynamics. Pratt and Whitney Res. Rep. 132, Gordon McKay Lab., Harvard Univ., Apr. 1951.

330. Prandtl, L.: On Boundary Layers in Three-Dimensional Flow. Rep. and Trans. 64, British RAE, May 1, 1946.

331. Mager, Artur: Laminar Boundary Layer Problems Associated with Flow through Turbomachines. Tech. Rep. 2, GALCIT, June 1953. (Contract AF 18(600)–178.)

332. Howarth, L.: The Boundary Layer in Three-Dimensional Flow. I—Derivation of the Equations for Flow along a General Curved Surface. Phil. Mag., ser. 7, vol. 42, no. 326, Mar. 1951, pp. 239–243.

333. Hayes, Wallace D.: The Three-Dimensional Boundary Layer. NAVORD Rep. 1313, NOTS 384, U.S. Naval Ord. Test Station (Inyokern), May 9, 1951. (Bur Ord Task Assignment NOTS–36–Re3d–441–3.)

334. Moore, Franklin K.: Three-Dimensional Compressible Laminar Boundary-Layer Flow. NACA TN 2279, 1951.

335. Burgers, J. M.: Some Considerations on the Development of Boundary Layers in the Case of Flows Having a Rotational Component. Nederl. Akad. van Wetenschappen, vol. XLIV, nos. 1–5, 1941, pp. 12–25.

336. Mager, Artur: Generalization of Boundary-Layer Momentum-Integral Equations to Three-Dimensional Flows Including Those of Rotating System. NACA Rep. 1067, 1952. (Supersedes NACA TN 2310.)

337. Bödewadt, U. T.: Die Drehströmung über festem Grunde. Z.A.M.M., Bd. 20, Heft 5, Oct. 1940, pp. 241–253.

338. Mager, Artur, and Hansen, Arthur G.: Laminar Boundary Layer Over Flat Plate in a Flow Having Circular Streamlines. NACA TN 2658, 1952.

339. Loos, H. G.: A Simple Laminar Boundary Layer with Secondary Flow. Tech. Rep. 1, GALCIT, June 1953. (Contract AF 18(600)–178.)

340. Sowerby, L.: Secondary Flow in a Boundary Layer. Rep. AERO. 2512, British RAE, Mar. 1954.

341. Mager, A.: Thick Laminar Boundary Layer Under Sudden Lateral Perturbation. Tech. Rep. 5, GALCIT, Apr. 1954. (Contract AF 18(600)–178.)

342. Carrier, G. F.: The Boundary Layer in a Corner. Quart. Appl. Math., vol. IV, no. 4, Jan. 1947, pp. 367–370.

343. Loitsianskii, L. G., and Bolshakov, V. P.: On Motion of Fluid in Boundary Layer Near Line of Intersection of Two Planes. NACA TM 1308, 1951.

344. Ainley, D. G., and Jeffs, R. A.: Analysis of the Air Flow through Four Stages of Half-Vortex Blading in Axial Compressors. R. & M. 2383, British ARC, Apr. 1946.

345. Wilson, Edwin Bidwell: Advanced Calculus. Ginn and Co., 1912.

346. Dean, Robert C., Jr.: Aerodynamic Measurements. Gas Turbine Lab., M.I.T., 1953.

347. Yates, A. H.: 'Carpets' and 'Lattices.' Aircraft Eng., vol. XVIII, no. 203, Jan. 1946, pp. 8–9.

348. Sutor, Alois T., and Zipkin, Morris A.: Method of Matching components and predicting Performance of a Turbine-Propeller Engine. NACA TN 2450, 1951.

349. Huppert, Merle C.: Approximate Method for Determining Equilibrium Operation of Compressor Component of Turbojet Engine. NACA TN 3517, 1955.

350. Goldstein, Arthur W.: Analysis of Performance of a Jet Engine from Characteristics of Components. I—Aerodynamic and Matching Characteristics of the Turbine Component Determined with Cold Air. NACA Rep. 878, 1947. (Supersedes NACA TN 1459.)

351. Goldstein, Arthur W., Alpert, Sumner, Beede, William, and Kovach, Karl: Analysis of Performance of Jet Engine from Characteristics of Components. II—Interaction of Components as Determined from Engine Operation. NACA Rep. 928, 1949. (Supersedes NACA TN 1701.)

352. Goldstein, Arthur W.: Interaction of Components of Gas Turbines for Aircraft. Paper Presented at ASME meeting, New London (Conn.), Apr. 28–May 5, 1949.

353. Woodworth, L. R.: Performance Analysis Methods for the Twin-Spool, High Pressure Ratio, Turbojet Engine. RM 1039, U.S. Air Force Proj. RAND, The RAND Corp., Oct. 15, 1952.

354. Gist, W. B., and Woodworth, L. R.: Approximate Methods for Determining the Performance of Gas Turbine Engines at Off-Design Conditions. RM 1205, U.S. Air Force Proj. RAND, The RAND Corp., Mar. 5, 1954.

355. Esgar, Jack B., and Ziemer, Robert R.: Methods for Rapid Graphical Evaluation of Cooled or Uncooled Turbojet and Turboprop Engine or Component Performance (Effects of Variable Specific Heat Included). NACA TN 3335, 1955.

356. Hensley, Reece V., Rom, Frank E., and Koutz, Stanley L.: Effect of Heat and Power Extraction of Turbojet-Engine Performance. I—Analytical Method of Performance Evaluation with Compressor-Outlet Air Bleed. NACA TN 2053, 1950.

357. Rom, Frank E., and Koutz, Stanley L.: Effect of Heat and Power Extraction on Turbojet-Engine Performance. II—Effect of Compressor-Outlet Air Bleed for Specific Modes of Engine Operation. NACA TN 2166, 1950.

358. Koutz, Stanley L., Hensley, Reece V., and Rom, Frank E.: Effect of Heat and Power Extraction on Turbojet-Engine Performance. III—Analytical Determination of Effects of Shaft-Power Extraction. NACA TN 2202, 1950.

359. Koutz, Stanley L.: Effect of Heat and Power Extraction on Turbojet-Engine Performance. IV—Analytical Determination of Effects of Hot-Gas Bleed. NACA TN 2304, 1951.

360. Rebeske, John J., Jr., and Dugan, James F., Jr.: Matched Performance Characteristics of a 16-Stage Axial-Flow Compressor and a 3-Stage Turbine. NACA RM E52H18, 1953.

361. Davison, Elmer H.: Turbine Design Considerations for Turbine-Propeller Engine Operating Over a Range of Flight Conditions. NACA RM E53D16, 1953.

362. Davison, Elmer H.: Turboprop-Engine Design Considerations. I—Effect of Mode of Engine Operation on Performance of Turboprop Engine with Current Compressor Pressure Ratio. NACA RM E54D19, 1955.

363. Davison, Elmer H., and Stalla, Margaret C.: Turboprop-Engine Design Considerations. II—Design Requirements and Performance of Turboprop Engines with a Single-Spool High-Pressure-Ratio Compressor. NACA RM E55B18, 1955.

364. Sanders, Newell D., and Behun, Michael: Generalization of Turbojet-Engine Performance in Terms of Pumping Characteristics. NACA TN 1927, 1949.

365. Rohlik, Harold E., and Rebeske, John J.: Acceleration of High-Pressure-Ratio Single-Spool Turbojet Engine as Determined from Component Performance Characteristics. III—Effect of Turbine Stator Adjustment. NACA RM E54F04, 1954.